HEAT AND MASS TRANSFER THROUGH DISTURBED SOIL: MULTISCALE EXPERIMENTAL AND MODELING INVESTIGATION

by

Benjamin M. Wallen

A thesis submitted to the Faculty and Board of Trustees of the Colorado School of Mines in partial fulfillment of the requirements for the degree of Doctor of Philosophy (Civil and Environmental Engineering).

Golden, Colorado

Date: _____

Signed: _____
Benjamin M. Wallen

Signed: _____
Dr. Kathleen M. Smits
Thesis Advisor

Golden, Colorado

Date: _____

Signed: _____
Dr. John E. McCray
Professor and Head
Department of Civil and Environmental Engineering

ABSTRACT

Landmines are one of the most prolific, human-made environmental hazards impacting the world. Although there are numerous technologies used to detect buried landmines, none enable a perfect find rate, in part, due to the heterogeneous nature of the environment in which they are buried. Variations in environmental conditions such as soil moisture and climate (e.g., temperature, diurnal fluctuations) impact detection performance. Improved understanding of the environmental conditions associated with minefield emplacement is needed to enable improvement in the algorithms used by detection technologies (e.g., infrared, ground penetrating radar), thus increasing their performance and probability of detection rates. However, there is a lack of understanding of the effect of the mine placement on the heat and mass transfer dynamics in the vicinity of the mine. More specifically, very little is known about how soil disturbance, a process that changes the soil thermal and hydraulic properties of the soil surrounding the mine, due to the placement and burial of the mine effects the soil moisture and temperature conditions in the vicinity of the mine. This is important because understanding these impacts enables increased ability to compare progressively complex models to measured aspects of interest specific to landmine emplacement conditions. The purpose of this research is to better understand the effect of soil disturbance (i.e., loosening the soil) and mixing (i.e., combining different soil types) on heat and mass transfer behavior in the vicinity of buried landmines. The aim is that this knowledge can help future research efforts to improve algorithms associated with various detection technologies. This research integrates a field experiment and numerous laboratory experiments with analytical modeling. In the first task, the thermal conductivity of mixed sands are evaluated at the small scale, providing critical knowledge of the unique behavior. Results indicate that for the test sands studied, knowledge of soil density enables identification of both saturated and dry

thermal conductivity which enhances modeling of the thermal conductivity-saturation relationships. Experimental data were used to test thermal conductivity-saturation models. The analytical models varied in their ability to capture the thermal behavior, demonstrating the need for a physically based thermal conductivity-saturation model. The second task compares several approaches used to determine evaporation with several laboratory evaporation and evapotranspiration experiments in an effort to determine an appropriate method that can be applied to studies of landmine detection, specifically, disturbed soil conditions. Results demonstrate that the methods vary in their ability to capture atmospheric versus diffusion dominated evaporative stages for the test soils and boundary conditions studied. Although no one method is applicable for all boundary and initial conditions, the sensible heat balance and heat pulse method enabled the highest level of agreement between measured and modeled evaporation from bare soil experiments. Additionally, the ability of this method to isolate evaporation under evapotranspiration conditions has the potential to isolate transpiration which is significant for many agricultural applications as well as modeling efforts. The third task investigates the impact of soil disturbance and mixing on heat and mass transfer behavior under varying climate conditions at the laboratory scale. Using the methods established in Task 2, I could quantitatively understand the evaporation rates from soils under different conditions (e.g. disturbed or loose conditions compared to undisturbed or tight conditions) using both in-situ and remotely sensed temperature and soil moisture data. Results demonstrate that the disturbance and mixing cause a significant increase in evaporation compared to undisturbed soil conditions. Under disturbed conditions without mixing, the increase evaporation occurred in part to due capillary pumping from the loose soil into the tight soil. Additionally, higher evaporation rates were observed from the upstream tight region compared to the downstream tight region. Finally, the fourth task is a field scale proof

of concept demonstration. The purpose of this task is to obtain a data set that includes aspects of tasks 1-3, thus testing our understanding of soil disturbance at the field scale. Experimental results demonstrate distinct behaviors in soil moisture and temperature distributions above and around buried objects that change with climate forcings (i.e., temperature and rain events).

TABLE OF CONTENTS

ABSTRACT ..... **iii**

LIST OF FIGURES ..... **xi**

LIST OF TABLES ..... **xvi**

MATHEMATICL NOMENCLATURE ..... **xvii**

ABBREVIATIONS ..... **xix**

ACKNOWLEDGEMENTS ..... **xx**

CHAPTER 1 INTRODUCTION **1**

1.1 Motivation 1

1.2 Problem Description 2

1.3 Research Objectives and Hypotheses 4

1.3.1 Research Objectives 5

1.3.2 Overarching Hypothesis 5

1.3.3 Individual Hypotheses based upon Specific Objectives 6

1.4 Research Scope and Specific Tasks 9

1.5 Thesis Outline 13

1.6 References 14

CHAPTER 2 LITERATURE REVIEW **18**

2.1 Mine Detection Technologies 18

2.1.1 Ground Penetrating Radar (GPR) 19

2.1.2 Infrared (IR) Thermography 21

2.2 Environmental Considerations Applicable to Landmine Detection 23

2.3 Data Collection Considerations Applicable to Modeling of Landmine Scenarios 28

2.4 Analytical Models of Consideration 30

2.5 References 38

CHAPTER 3 THERMAL CONDUCTIVITY OF BINARY SAND MIXTURES EVALUATED THROUGH FULL WATER CONTENT RANGE **42**

3.1 Abstract 43

3.2 Introduction 44

3.3 Material and Methods 48

3.3.1 Experimental Apparatus 48

3.3.2 Sand Materials 51

3.3.3 Experimental Procedure 53

3.3.4 Statistical Analysis 53

3.4 Results and Discussion 54

3.5 Applicability of λ-θ Models to Binary Mixtures 60

3.6 Conclusions 70

3.7 Acknowledgements 72

3.8 References 72

CHAPTER 4 ESTIMATING SOIL WATER EVAPORATION: AN INTERCOMPARISON OF ENERGY BALANCE, WATER BALANCE AND WATER FLUX BASED MODELS USING LABORATORY MEASUREMENTS OVER BARE AND VEGETATED SURFACE 79

4.1 Abstract 80

4.2 Introduction 81

4.3 Material and Methods 91

4.3.1 Experimental Apparatus 91

4.3.2 Sand and Vegetation Materials 95

4.3.3 Experimental Procedure 97

4.4 Results and Discussion 99

4.5 Applicability of Evaporation Models 105

4.6 Conclusions 117

4.7 Acknowledgements 120

4.8 References 121

CHAPTER 5 HEAT AND MASS TRANSFER BEHAVIOR FROM DISTURBED AND MIXED SOILS: LABORATORY SCALE EXPERIMENTAL AND ANALYTICAL INVESTIGATION 126

5.1 Abstract 127

5.2 Introduction 128

5.3 Material and Methods 131
5.3.1 Experimental Apparatus 131
5.3.2 Sand Materials 137
5.3.3 Experimental Procedure 139
5.3.4 Experimental Summary 141
5.4 Experimental Results and Discussion 143
5.4.1 Evaporation based on Weight Data for EX1 (Ambient Conditions) 144
5.4.2 Evaporation based on Drying Front Visualization for EX1 (Ambient Conditions) 145
5.4.3 Surface Temperature of EX1 (Ambient Conditions) 147
5.4.4 Relative Humidity of EX1 (Ambient Conditions) 148
5.4.5 Saturation of EX1 (Ambient Conditions) 149
5.4.6 Subsurface Temperature of EX1 (Ambient Conditions) 149
5.4.7 Experimental Results Comparison with EX-2, EX-3, and EX-4 152
5.4.8 Evaporation Comparison based upon Weight Analysis 152
5.4.9 Drying Front Visualization Comparison 153
5.4.10 Surface Temperature Comparison 156
5.4.11 Relative Humidity Comparison 156
5.4.12 Saturation Comparison 158
5.4.13 Subsurface Temperature Comparison 159
5.4.14 Soil Mixing Experimental Highlights 160
5.5 Analytical Model based on Surface Energy Balance (SEB) Theory 167
5.6 Analytical Modeling Results and Discussion 168
5.6.1 Evaporation based upon SEB Method for EX1 (Ambient Conditions) 169
5.6.2 Evaporation Analysis based upon Surface Temperature Measurements Comparison 170
5.7 Conclusions 171
5.8 Acknowledgements 172
5.9 References 173

CHAPTER 6 FIELD SCALE EXPERIMENTAL AND NUMERICAL INVESTIGATION OF DIURNAL FLUCTUATIONS OF HEAT AND WATER DISTRIBUTIONS AROUND LANDMINES IN NATURAL SOIL 177

6.1 Abstract 178

6.2 Introduction 178

6.3 Mass and Heat Flow Theory Fundamentals 185

6.3.1 Mass Flow in Soils 186

6.3.2 Heat Flow in Soils 187

6.4 Material and Methods 188

6.4.1 Site Selection 188

6.4.2 Description of Soil 188

6.4.3 Experimental Design 189

6.4.4 Experimental Methods 193

6.5 Experimental Results 194

6.5.1 Temperature 195

6.5.2 Soil Moisture 202

6.6 Conclusions 207

6.7 Acknowledgements 208

6.8 References 208

CHAPTER 7 CONCLUSIONS 214

7.1 Lessons Learned 215

7.1.1 Chapter 3 Key Findings 216

7.1.2 Chapter 4 Key Findings 217

7.1.3 Chapter 5 Key Findings 219

7.1.4 Chapter 6 Key Findings 221

7.2 Recommendations for Future Research 222

7.3 References 223

APPENDIX A SENSOR USER GUIDES 225

APPENDIX B PROCEDURES TO DETERMINE EFFECTIVE RADIUS OF HEAT PULSE PROBES 226

B.1 Theory.....226

B.2 Procedure.....228

B.2.1. Heat-Pulse Probe (3 mm needle spacing) Dry Experiment (Probe C2036, C2037, C2038, C2039).....228

B.2.2. Heat-Pulse Probe (6 mm needle spacing) Dry Experiment (Probe C2040, 2041) 230

B.2.3. Heat-Pulse Probe (3 mm needle spacing) Saturated Experiment (Probe C2036, C2037, C2038, C2039) 231

B.2.4. Heat-Pulse Probe (6 mm needle spacing) Saturated Experiment (Probe C2040, 2041).....233

B.3 Data Analysis.....234

B.4 References 235

APPENDIX C PERMISSIONS 236

APPENDIX D DETAILS OF SOILS USED IN EXPERIMENTATION 237

APPENDIX E SUPPLEMENTAL ELECTRONIC FILES 241

LIST OF FIGURES

Figure 1.1 Impact of landmines resulting in associated socio-politico-ecological problems (Berhe, 2007). 2

Figure 1.2 Conceptual model of coupled processes and interactions between subsurface and near surface environments influenced by landmine burial when focused on (a) binary soil mixtures, (b) heat and mass transfer as well as energy budget considerations regarding fluxes, (c) impact of soil disturbance on mass and heat flux with a homogeneous soil prior to landmine emplacement, (d) impact of mixing on mass and heat flux with a layered soil prior to landmine emplacement, and (e) emplacement of a surrogate mine as part of a field experiment proof of concept. 11

Figure 2.1 Conceptual sketch of the zones below the surface, regimes, fundamental relationships, interactions, and properties of interest that are required for consideration to improve landmine detection technologies. 24

Figure 2.2 Conditions of consideration regarding (a) disturbance associated with field experiments and (b) mixing associated with laboratory experiments to guide sensor selections for collecting data essential for input of modeling effort. 25

Figure 2.3 Representative SWRC and λ-S relationship for a well sorted sand depicting four regimes associated with saturation, the boundary and transition points between the regimes, the associated soil saturation at each point, and the relative water energy level spectrum (amended based on Lu and Likos, 2004). ... 27

Figure 3.1 Experimental setup (not to scale). The inside volume of cell excluding sensors and porous cup for drainage is 510 cm^3. All sensors were positioned at 3 cm below the surface so that all measurements represent those within the same horizontal plane. Note that the water reservoir is sufficiently large and long so that drainage through the syringe needle induces a slow drainage (discussed in Section 3.3.3) at a nearly constant rate in the pressure range of interest. 49

Figure 3.2 Sieve analysis for each binary mixture with C0F10, C9F1, and C10F0 measured and the remainder predicted based upon percent of the base sands (C0F10 and C10F0). 52

Figure 3.3 Porosity of binary mixtures (tightly packed) compared with predictions made using the partial mixing model developed by Kamann et al. (2007). 54

Figure 3.4 Soil water retention curve for all binary mixtures. 56

Figure 3.5 Thermal conductivity as a function of water content for binary mixtures highlighting the impact of changes in porosity and density within the four saturation regimes (I: hydration, II: pendular, III: funicular, and IV: capillary). ... 58

Figure 3.6 Dry and saturated thermal conductivity as a function of the volumetric fraction of fine particles. 59

Figure 3.7 Correlation between soil bulk density and thermal conductivity for (a) saturated mixtures and (b) dry mixtures. 60

Figure 3.8 Sensitivity analysis of the Campbell model four soil-specific parameters for (a) λ_m, (b) x_{wo}, (c) g_a, and (d) q_o. 64

Figure 3.9 Comparison of measured to modeled thermal conductivity based on the Campbell model with all parameters determined empirically for (a) coarse-controlled mixtures and (b) fine-controlled mixtures. 66

Figure 3.10 Comparison of measured to modeled thermal conductivity (λ) based on the Lu and Dong model using experimentally measured saturated and dry λ and empirically determined parameters (θ_f and m) for (a) coarse-controlled mixtures and (b) fine-controlled mixtures. 69

Figure 4.1 Sketch of Tank 1 and Tank 2 interfaced with Wind Tunnel 1 providing a side view and top view of the experimental apparatus. 92

Figure 4.2 Sketch of Tank 3 interfaced with Wind Tunnel 2 providing a side view, top view, and view of primary instrumentation locations similar for all tanks. Tank is used with bare soil. 93

Figure 4.3 Lysimeter analysis for all four experiments providing a comparison of evaporation or evapotranspiration rate based upon ground cover and boundary conditions. 100

Figure 4.4 Average saturation at 2.5 cm (blue), 7.5 cm (red), and 12.5 cm (green) below ground surface for a) EX1, b) EX2, c) EX3, and d) EX4. 102

Figure 4.5 Temperature difference between air and surface temperature for EX1 (denoted by circles), EX2 (denoted by squares), EX3 (denoted by diamonds), and EX4 (denoted by triangles). 103

Figure 4.6 Relative humidity difference between surface and air measurements for EX1 (denoted by circles), EX2 (denoted by squares), EX3 (denoted by diamonds), and EX4 (denoted by triangles). 104

Figure 4.7 Evaporation model comparison associated with ambient conditions (EX1) comparing (a) evaporation rates modeled compared to lysimeter data, and (b) direct comparison between measured and modeled evaporation rates. 112

Figure 4.8 Evaporation model comparison associated with elevated air temperature (EX2) comparing (a) evaporation rates modeled compared to lysimeter data, and (b) direct comparison between measured and modeled evaporation rates. 113

Figure 4.9 Evaporation model comparison associated with diurnal heating of bare soil (EX3) comparing (a) evaporation rates modeled compared to lysimeter data, and (b) direct comparison between measured and modeled evaporation rates. ... 114

Figure 4.10 Evaporation model comparison associated with diurnal heating of grass covered soil (EX4) comparing (a) evapotranspiration rates modeled compared to lysimeter data, and (b) direct comparison between measured and modeled evapotranspiration rates. ... 116

Figure 4.11 Surface energy balance resolved by infrared thermography for different sampling frequencies. ... 117

Figure 5.1 Sketch of Tank 1 and Tank 2 interfaced with Wind Tunnel 1 providing a side view and top view of the experimental apparatus. The top layer of #12/20 coarse sand is shown as the darkest shading, the underlying #110 sand is shown as the lightest shading, and the disturbed, loose mixture of #12/20 and #110 sand is shown in the center of Tank 1. ... 135

Figure 5.2 Sketch of Tank 3 interfaced with Wind Tunnel 2 providing a side view, top view, and view of primary instrumentation locations similar for all tanks. Tank is used with #30/40 sand. Tight and loose packing (disturbed sand conditions) are shown. ... 136

Figure 5.3 Soil water retention curve (SWRC) for #30/40 Accusand for tight and loose packing conditions. ... 138

Figure 5.4 Soil water retention curve (SWRC) for tight packing conditions for #12/20 and #110 sands and for loose packing conditions of the mixture of the two sands. ... 139

Figure 5.5 Tank 1 preparation for experimentation showing the (a) tight packed regions of #110 sand in the bottom 25 cm of the tank overlain by #12/20 sand in the top 5 cm of the tank and the (b) loose packed, disturbed inclusion of the C3F7 binary mixture in the center of the tank. Note that the metal baffles used to separate the tight and loose packed regions were removed prior to the beginning of the experiment. ... 141

Figure 5.6 Cumulative water loss from EX-1. ... 145

Figure 5.7 Drying front propagation within a heterogeneously packed sand tank under ambient conditions. Porosities shown for different packed regions. Arrows below the surface indicate direction of capillary pumping. ... 146

Figure 5.8 Surface and atmospheric temperature. Temperature measured across the surface length, head space, influent and effluent air upstream and downstream of the soil surface, and outside on the front of the tank. ... 147

Figure 5.9 Relative humidity at the soil surface and above the soil surface for EX-1. 148

Figure 5.10 Soil moisture profiles across the length of the soil tank at varying depths within the heterogeneous packed region at (a) 2.5 cm bgs, (b) 7.5 cm bgs, and (c) 12.5 cm bgs. 150

Figure 5.11 Measured temperature as a function of time for different packing regions within the soil tank for EX-1. Each graph (a-c) is associated with a column of sensors: (a) downstream tight packed region downstream, (b) center loose packed region, and (c) upstream tight packed region. 151

Figure 5.12 Cumulative water loss comparison between the different boundary conditions associated with all four experiments. 153

Figure 5.13 Drying front visualization across the length and throughout the depth of the sand tank over the duration of the experiments for (a) EX-2, (b) EX-3, and (c) EX-4. The constant water table and air entry head, h_d, for the tight (T) and loose (L) packed regions are shown in (c). 155

Figure 5.14 Surface relative humidity profile comparisons between differently packed regions between all four experiments. 157

Figure 5.15 Soil moisture profile comparisons between differently packed regions at varying depths within the heterogeneous packing region at (a) 2.5-cm bgs (b) 7.5-cm bgs (c) 12.5-cm bgs. 159

Figure 5.16 Cumulative water loss comparison between the different subsurface conditions associated with EX-5 and EX-6. 161

Figure 5.17 Drying front visualization of the propagation over the 20-day experiment for EX-5 and EX-6. 162

Figure 5.18 Average surface temperatures measured using infrared thermography for each surface soil type (EX-5: tight packed, #12/20; EX6: tight packed, #12/20 and loose packed C3F7 mixture). 163

Figure 5.19 Comparison of the soil moisture profile at depths ranging from 2.5 to 12.5 cm below the surface for (a) EX-5 with layered soils and (b) EX-6 with layered soils and a loose binary mixture. 164

Figure 5.20 Average soil water retention curve (SWRC) based on location and depth (EX-5: triangles / EX-6: circles = tight packed soil & squares = loose packed mixture). 165

Figure 5.21 Measured thermal conductivity-saturation relationships based upon soil type and location (all measured at 2.5 cm bgs except for #110 sand at 7.5 cm bgs). .. 166

Figure 5.22 Cumulative water loss comparison between measured and calculated values based upon the surface energy balance method under ambient conditions. 170

Figure 6.1 Sketch illustrating the experimental set-up to include buried object and sensor locations (cross sectional view). 191

Figure 6.2 Schematic of (a) plan view of site showing emplacement locations, points of temperature acquired via laser thermometer, and infrared camera field of view, and (b) top view of the soil bed. Scale shown on figure. 192

Figure 6.3 Experimental conditions: (a) wind speed, (b) relative humidity, (c) temperature. Note: time zero is 12 pm on day one of the experiment. 195

Figure 6.4 Soil surface temperature comparison for emplacement locations: (a) direct temperature measurement, (b) thermal contrast. 196

Figure 6.5 Infrared thermography of emplacement locations prior to, immediately following, and multiple days after rain events at specific representative times of 7 a.m., 2 p.m., and 9 p.m. Rain events are noted as (1), (2), and (3) with the numbers placed next to the image closest to the rain event occurrence. 200

Figure 6.6 Temperature profiles for each emplacement location: (a) disturbed soil, (b) shallow mine, (c) deep mine, and (d) limestone block. 202

Figure 6.7 Saturation and temperature at 2.5 cm below the surface for comparison of emplacement locations. 205

Figure 6.8 Saturation profiles for each emplacement location: (a) disturbed soil, (b) shallow mine, (c) deep mine, and (d) limestone block. 207

Figure B.1 “Heat-pulse probe design modeled after Heitman et al. (2008). The probe consists of three needles arranged in parallel that project from an epoxy body. Each needle contains a thermister for measuring temperature; the center needle also has a heating element.” (Trautz et al., 2014). 226

Figure D.1 Thermal conductivity and capillary pressure as a function of water content for (a) #12/20 – tight, (b) #110 – tight, (c) C9F1 – tight, (d) C9F1 – loose, (e) C8F2 – tight, (f) C8F2 – loose, (g) C7F3 – tight, (h) C7F3 – loose, (i) C5F5– tight, (j) C5F5 – loose, (k) C2F8 – tight, (l) C2F8 – loose, (m) #30/40 – tight, (n) #30/40 – loose, (o) #50/70 – tight, (p) C7F3 {#12/20 & #50/70} – tight. Unless otherwise stated, the binary mixtures are comprised of parent sands #12/20 and #110. The notation for the binary mixtures denote % coarse followed by % fine sand. 239

LIST OF TABLES

Table 2.1 Environmental conditions impacting detection technology capabilities 22

Table 3.1 Sand properties obtained from sieve analysis. 52

Table 3.2 Properties of component sands and binary mixtures under tightly packed condition. 55

Table 3.3 Campbell model parameter values associated with scenario 1 and model to measured λ agreement based upon all four scenarios. 64

Table 3.4 Campbell model parameters based upon empirically determined λ_m, x_{wo}, g_a and q_o obtained through calibration. 67

Table 4.1 Evaporation methods selected for comparison and evaluation. 88

Table 4.2 Sand properties for #30/40 Accusand. 96

Table 4.3 Vegetation properties of Bermuda grass. 96

Table 4.4 Experimental boundary and initial conditions. 98

Table 4.5 Comparison of evaporation models regarding sensor location, property measured, and number of inputs for model operation. 111

Table 5.1 Sand properties as characterized by Smits and Limsuwat (2009) for #30/40 Accusand and for the loose mixture of #12/20 and #110 parent sands. 138

Table 5.2 Average characteristics and conditions of Experiments 1-6. 142

Table 5.3 Summary of final soil porosities for disturbed and mixed experiments. 143

Table 5.4 Other fluid properties applied in surface energy balance (SEB). 169

Table 6.1 Key field soil properties. 189

Table 6.2 Properties of surrogate mines and limestone block. 191

Table 6.3 Summary of diurnal experimental conditions for field experiment. 194

Table D.1 Select measured properties of investigated sands. 238

MATHEMATICL NOMENCLATURE

C_p	heat capacity	(J kg^{-1} K^{-1})
$C_{p,eff}$	effective soil heat capacity	(J kg^{-1} K^{-1})
c_v	vapor concentration	(kg m^{-3})
c_{veq}	equilibrium vapor concentration	(kg m^{-3})
D	drainage rate	(mm d^{-1})
D_v*	effective vapor diffusion coefficient	(m^2 s^{-1})
d_g	geometric mean particle diameter	(mm)
E	evaporation rate	(mm d^{-1})
ET	evapotranspiration rate	(mm d^{-1})
f_c	dimensionless condensation coefficient	(-)
f_e	dimensionless evaporation coefficient	(-)
G	heat flux into the ground	(W m^{-2})
H	sensible heat flux into the atmosphere	(W m^{-2})
h_c	capillary pressure	(cm of H_2O)
h_d	air entry pressure (AKA: displacement pressure)	(cm of H_2O)
I	irrigation rate	(mm d^{-1})
K_s	saturated hydraulic conductivity	(cm s^{-1})
$k_{r,g}$	gas relative permeability	(-)
$k_{r,l}$	liquid water relative permeability	(-)
L	latent heat of vaporization	(J kg^{-1})
L_v	latent heat of vaporization of liquid water	(J kg^{-1})
$\dot{m}$	rate of phase change	(kg m^{-3} s^{-1})
M_w	molecular weight of water	(kg mol^{-1})
n	van Genuchten model parameter	(-)
p_c	capillary pressure	(Pa)
p_g	gas phase pressure	(Pa)
p_l	water pressure	(Pa)
Q_{loss}	heat loss	(W m^{-3})
R	ideal gas constant	(Pa m^3 mol^{-1} K^{-1})
RH	relative humidity	(%)
R_n	net radiation	(W m^{-2})
R_{off}	runoff rate	(mm d^{-1})
r_d	radius of interface curvature of air entry	(m)
S	soil storage rate	(mm d^{-1})
S_g	gas saturation	(m^3 m^{-3})
S_l	liquid water saturation	(m^3 m^{-3})
T	temperature	(K)
t	time	(s)
T_{atm}	atmospheric temperature	(K)
T_g	moist air temperature	(K)
u	wind speed	(m s^{-1})
w_v	mass fraction of water vapor in the gas phase	(K)
z	elevation relative to a defined datum	(m)

α	van Genuchten model parameter	(cm^{-1})
α_{BJ}	Beavers-Joseph slip parameter	(-)
ϕ	porosity	($cm^3\ cm^{-3}$)
λ	thermal conductivity	($W\ m^{-1}\ K^{-1}$)
λ_{dry}	thermal conductivity under dry conditions	($W\ m^{-1}\ K^{-1}$)
λ_{eff}	effective soil thermal conductivity	($W\ m^{-1}\ K^{-1}$)
λ_g	gas thermal conductivity	($W\ m^{-1}\ K^{-1}$)
λ_{sat}	thermal conductivity under saturated conditions	($W\ m^{-1}\ K^{-1}$)
μ_g	dynamic viscosity of gas	(Pa s)
ρ	density	($g\ cm^{-3}$)
ρ_B	dry bulk density	($g\ cm^{-3}$)
ρ_g	gas (air) density	($g\ cm^{-3}$)
ρ_l	temperature dependent density of liquid water	($g\ cm^{-3}$)
ρ_p	particle density (AKA: specific gravity, SG)	($g\ cm^{-3}$)
θ	volumetric water content	($cm^3\ cm^{-3}$)
θ_r	residual volumetric water content	($cm^3\ cm^{-3}$)

Subscripts:

a	denotes air
m	denotes mineral
w	denotes water

ABBREVIATIONS

ABL	Atmospheric Boundary Layer
ADC	Analog to Digital Count
AEV	Air Entry Value
bgs	below ground surface
CDFS	Context-Dependent Feature Selection
CESEP	Center for Experimental Study of Subsurface Environmental Processes
EC	Eddy Covariance
ENWATBAL	Energy and Water Balance
GPR	Ground Penetrating Radar
GSL	Geotechnical and Structures Laboratory
IR	Infrared
LBNL	Lawrence Berkeley National Laboratory
LRM	Live Mine Risk
M-BREB	Micro-Bowen Ratio Energy Balance
RH	Relative Humidity
SEB	Surface Energy Balance
SHB+HP	Sensible Heat Balance and Heat Pulse
SP	Poorly graded concrete Sand
SWRC	Soil Water Retention Curve
TD	Temperature Difference
USCS	Unified Soil Classification
WRC	Water Retention Curve

ACKNOWLEDGEMENTS

First and foremost, I wish to thank my wife, Cara, who empowered me to succeed in the endeavor of completing this Ph.D. dissertation via her superb support of me and simply being an incredible mother to our wonderful children: Alec, Jack and Sadie.

I also thank all my family for their support throughout this Ph.D. process. This includes highlights of lunches together, a place to stay in the greater Golden area, and all those that came to my Ph.D. dissertation defense.

My advisor, Dr. Kathleen Smits, provided continual support and guidance regarding all aspect of my Ph.D. This included providing me the motivation to come to Colorado School of Mines and work with her on landmine detection. She was a consummate professional and demanded the same from all of her students which pushed us all to do our best.

My Ph.D. committee members, Dr. Tissa Illangasekare, Dr. Ning Wu, Dr. Julia Regnery, and Dr. Stacy Howington, provided essential candid feedback and challenged me to strive for deeper learning of the fundamentals required throughout my Ph.D. work.

The professors, Dr. Tissa Illangasekare, Dr. Ning Wu, and Dr. Ning Lu, from whom I had the pleasure of attending their classes taught me quintessential material required for my research.

Dr. Abdullah Cihan and Dr. Stacy Howington hosted me for two week internships at Lawrence Berkeley National Laboratory and the Engineer Research and Development Center, respectively. Their time and support greatly enhanced my Ph.D. experience.

The internships, conference attendance and presentations, and equipment used throughout my research was made possible by the Edna Bailey Sussman Foundation Environmental Intership, Dorothy Bertine Internship, Society of American Military Engineers Denver Metro Post, G.A.

Harris Research Instrumentation Fellowship, Colorado School of Mines Graduate Student Government Travel Grants, and additional funding from Dr. Kathlene Smits.

My classmates, Ali Moradi and Andrew Trautz, who gave freely of their time to help me understand difficult concepts made the entire Ph.D. experience more successful and enjoyable. Other current and former members of the Center for Experimental Study of Subsurface Environmental Processes (CESEP) research group deserve my thanks for their help and friendship over the years: Elif Agartan, Zach Drumheller, Victoria Eagan, Ariel Esposito, Jack Massey, Ben Petri, Mike Plampin, Amy Rice, Luca Trevisan, Javier Vargas, Jack Wu, Inge Hill, Alec Wallen, Kristen Hietala, Chamindu Deepagoda, Toshi Sakaki, Steve Byers, Logan Forsythe, Hao Wu, Jamie Ramirez, Paul Schulte, and Yi Dong.

The Civil and Environmental Engineering administrative team of Tim VanHaverbeke, Angela Knighton, and Kathryn Lowe helped me successfully navigate graduation requirements and building/laboratory access all while maintaining a wonderfully positive, helpful disposition.

The leadership at the Colorado School of Mines Army ROTC Detachment, CPT Bill Fehrenbach and Frances Aguilar, provide me with the opportunity to give a number of presentations to ROTC cadets of each class as well as be an active member in the student chapter of the Society of American Military Engineers.

Finally, I would like to thank the Department of Geography and Environmental Engineering at the United States Military Academy who provided me with the opportunity to pursue a Ph.D. in Environmental Engineering. Without their trust and confidence in my abilities, this Ph.D. adventure would not have been possible.

To my wonderful wife and children

Cara, Alec, Jack, and Sadie Wallen

CHAPTER 1 INTRODUCTION

Chapter 1 provides the motivation and problem description associated with this work. The overarching research goals and objectives follow. This chapter concludes with an outline of this dissertation.

1.1 Motivation

Over 100 million landmines and other explosive remnants of war are man-made environmental threats affecting more than 80 countries around the world (Miles, 1998; ICRC, 2011; Shire et al., 2015). The Red Cross estimates that landmines kill about 800 people and injure thousands each month (Andersson et al., 2015). The use of modern explosive landmines has accompanied every major conflict since the American Civil War. The termination of these conflicts leave large parcels of land with embedded landmines. National militaries typically have the responsibilities to perform mine clearance or demining operations upon the resolution of hostilities; however, these efforts cannot proceed in regions without functioning national militaries (e.g., Afghanistan when Soviet troops departed the country around 1988). As a result, a humanitarian response has accompanied military efforts around the world in demining operations. Although there is a combined effort to remove these hazards, there is much needed improvement regarding the technologies used to identify the buried landmines. A report in 2003 listed the cost of removal as US$ 300-1000 per mine and the personnel cost as one mine disposal expert killed and two injured for every 5000 mines cleared (Walsh and Walsh, 2003). Research regarding the impact of landmines continues to be a point of international concern (e.g., Arcand et al., 2014). A comprehensive report regarding landmines and land action is provided by Keeley (2003) and a holistic model of the effects of landmines is presented by Berhe (2007) and shown in Figure 1.1.

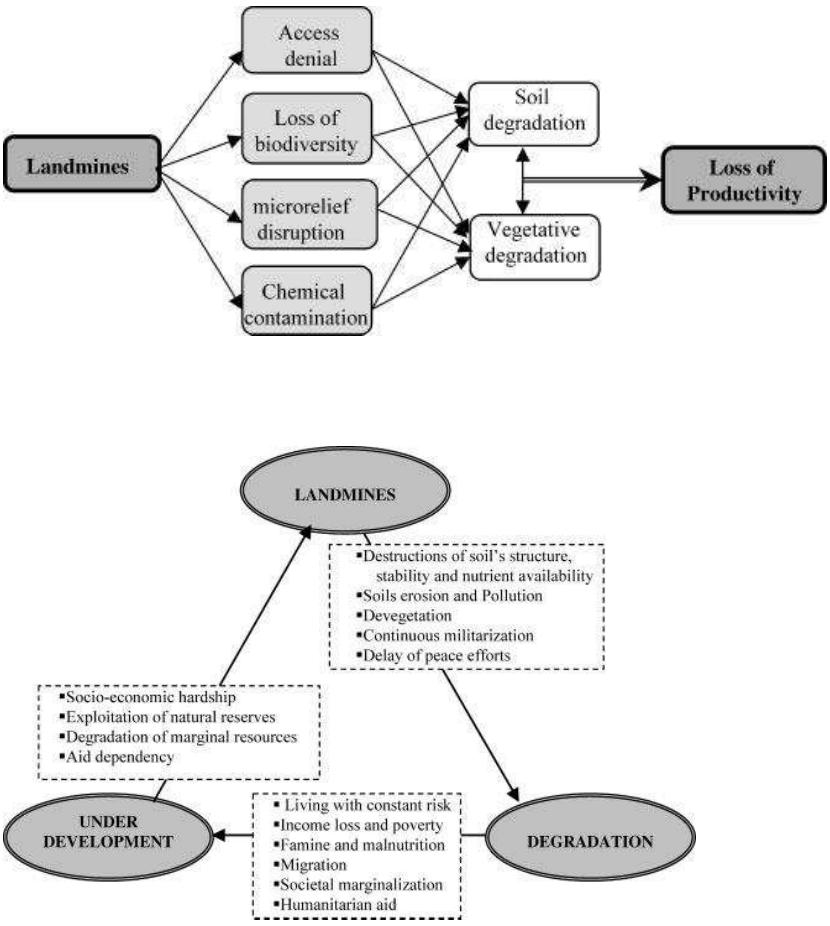

Figure 1.1. Impact of landmines resulting in associated socio-politico-ecological problems (Berhe, 2007).

1.2 Problem Description

The prolific nature of the hazard caused by landmines and the associated cost of demining operations necessitates improved technologies for these efforts. There are a variety of landmine detection techniques such as ground penetrating radar (GPR) (Krueger et al., 2015), radar bullet (Shire et al., 2015), metal detection through electromagnetic induction (EMI), infrared imaging (Bruschini and Gros, 1998; Deans et al., 2001), trace vapor explosive detection (Phelan and Webb, 1997), and biological methods of detection by mine detection dogs (English, 2000) or rats

(Edwards et al., 2015). No one detection technique performs with perfect accuracy. The demand for improvement in technology to increase the find rate or probability of detection (PD) and reduce the false alarm rate (FAR) drives current research efforts. Typically, nonthreatening subsurface objects, environmental effects, sensor vibration, or system noise contributes to FARs (Ratto et al., 2011). MacDonald et al. (2003) stated that innovative mine detection technology optimization and integration will occur through the development of algorithms for advanced signal processing. Advancements in algorithms comes from improved understanding of the changes in heat and mass flow impacted by burying landmines.

Landmine emplacement occurs through following a series of steps. The general concepts involve (1) digging a hole resulting in creating loose disturbed soil, (2) placing the mine in the dug hole, (3) arming the mine, and (4) carefully covering the mine with the loose disturbed soil. The loose disturbed soil is comprised of the local material and has the potential to be a mixture of the top soil material in contact with the surface and the underlying material dependent on the depth of the top layer. There is no one standard soil profile as weathering and geologic events alter soils and layering events for the various soil horizons. With numerous environments to consider, the work of this research focuses on desert areas (e.g., Iraq and Afghanistan) which occupy approximately 31.5% of the Earth's land surface (Dregne, 1976). Soils in deserts experience less weathering and leaching resulting in coarse textures, shallow soils, coarse weathered mantles, and abrupt soil boundaries (Cooke et al., 1993). In arid regions (less than 10 cm of annual precipitation), the soil profile contains a shallow A horizon (topsoil) consisting of a coarse top layer of a few centimeters in depth followed by finer material below in a B horizon, and concluding with a C horizon which is the underlying rock (Tekstu et al., 1991; McAuliffe, 2015).

Altered soil properties and processes of the disturbed soil near the surface above a buried object may persist for months if not years (Koh and Ballard, 2004). Once soil properties are altered, they do not return to pre-disturbed conditions. Research conducted to improve understanding of the interacting physical processes behind temperature contrasts and changes in soil moisture may result in an increase in the probability of successful detection of buried landmines (Garcia-Padron et al., 2002). Therefore, a variety of mine detection efforts focus on identifying localized soil disturbance compared to their surroundings. It is a well-designed multisensory system that has the highest probability to increase performance of demining operations (MacDonald et al., 2003). In order to make improvements in the algorithms used by these systems, robust data sets are essential and required. Data sets obtained from detailed experiments enable comparison with modeling efforts designed to relate to specific technology platforms. Examples of data required for algorithmic fusion include soil moisture, temperature, relative humidity, and thermal conductivity. Out of these and other characteristics such as dielectric properties, water content is the most important soil property that affects most mine detection sensors (Hendrickx et al., 2001). Therefore, deliberate experiments are required to obtain a clear understanding of the essential changes that take place concerning properties of interest (e.g., soil moisture, temperature) as a result of mine emplacement.

1.3 Research Objectives and Hypotheses

The goal of this research is to improve our understanding of the environmental conditions in which landmines are placed. Burying landmines results in soil disturbance and soil mixing that in effect alters the heat and mass transfer behavior in the vicinity of the mines. This research integrates field and laboratory experimentation with analytical modeling to systematically investigate how heat and mass transfer around and above a landmine changes as a result of changes

in environmental conditions. The experiments and analytical modeling effort focus on the individual components of change (e.g. mixing, disturbance, depth of burial) due to landmine emplacement.

1.3.1 Research Objectives

The objectives of this research are to (1) systematically evaluate the effect of binary mixtures on soil thermal conductivity in order to better predict the spatial and temporal distribution of heat, (2) evaluate the performance of different models to estimate evaporation using laboratory data collected at high spatial and temporal resolutions to determine the ability of the models to work for areas of localized soil disturbance due to landmine emplacement, (3) experimentally explore the spatial and temporal effects of (3a) soil disturbance and (3b) mixing on evaporation to evaluate the contribution from the various soil conditions created as a function of landmine emplacement on the overall evaporation, and (4) to simultaneously evaluate the impact of soil disturbance, burial depth, and object properties (i.e., shallow buried mine, deep buried mines, buried limestone block, and a disturbed hole location) on soil moisture and temperature distributions in the vicinity of a buried object to enable a field proof of concept incorporating lessons learned from the prior three objectives.

1.3.2 Overarching Hypothesis

This research is designed to test an overarching hypotheses: The differences in the local hydrological conditions and thermal properties of buried objects results in distinct spatial and temporal differences in water saturation and temperature in the direct vicinity of the buried object, especially under natural environmental conditions (e.g. precipitation, wind, diurnal temperature changes). MacDonald et al. (2003) stated that innovative mine detection technology optimization

and integration will occur through the development of algorithms for advanced signal processing. However, as stated by Ratto et al. (2011), this cannot be done without an improvement in our understating of subsurface objects, environmental effects, sensor vibration, and system noise as well as the properties of the soil that surrounds the mine (e.g. Garcia-Padron et al., 2002; Van Dam et al., 2005).

1.3.3 Individual Hypotheses based upon Specific Objectives

In order to accomplish this overarching hypothesis, three individual hypotheses were developed. As with the overarching hypothesis discussed above, the individual hypothesis is listed followed by presenting supporting background used in the hypothesis development.

Hypothesis 1: **The thermal properties of binary soil mixtures is distinct from that of the parent materials comprising the mixtures and cannot be described by current λ-θ models.**

In the shallow subsurface, soil is expected to follow complex drainage and wetting paths due to transient water flux on the land surface and water table conditions. The mixing of different sized soil particles is known to affect soil properties such as density, porosity, hydraulic conductivity, and soil water retention curves (SWRCs) (Sakaki and Smits, 2015). Sakaki and Smits (2015) determined that none of the SWRCs for mixtures of the two constituent sands could be well described by a weighted superposition of two SWRC subfunctions for the unmixed uniform particles weighted by the mixing fractions. Therefore, the same theory may apply to the λ-θ relationship. The validity of this hypothesis identifies the necessity to experimentally determine binary mixture impacts on the λ-θ relationship of soils in regions in which landmines are buried and soil horizons include two distinct layers in the near surface region that is disturbed during the landmine burial process.

Hypothesis 2: **Error associated with soil water evaporation estimates can be overcome through independent observations of both water and energy cycle variables rather than relying on a single-process or single-variable.**

Because it is very difficult to measure evaporation from soil, with the exception of using a lysimeter (Evett et al., 1995), numerous formulations have been proposed (e.g., Penmann 1948, Monteith, 1965, Brutsaert and Stricker, 1979; see Mahfouf and Noilhan, 1991 for a review) to establish a relationship between evaporation and soil moisture. These formulations consist of two approaches: a bulk aerodynamic method and threshold formulation method; the methods vary in how they partition the available energy (Mahfouf and Noilhan, 1991). The bulk aerodynamic method relates evaporation and water content explicitly by using a parameterization of the surface relative humidity (e.g., Kondo et al., 1990). The threshold formulation method is based on water supply and demand (Mahfouf and Noilhan, 1991). In this method, the surface relative humidity is not needed but rather detailed information about the hydraulic properties in a thin layer close to the soil surface, making the method very sensitive to the depth of the dry surface layer. Mahfouf and Noilhan (1991) found that the bulk aerodynamic formulations method overestimated evaporation flux from bare soil while the threshold method underestimates surface evaporation.

Another less well known method to determine evaporation relies on heat pulse sensors (Heitman et al., 2008), to measure soil temperature and thermal properties. Soil thermal properties play a significant role in the dynamic behaviors of soil moisture distributions in the shallow subsurface (e.g., Saito et al., 2007) and are strongly influenced by the fractions of water content, air phase and solid phase in the soil (e.g., Ochsner et al., 2001). This method can determine, in situ, the latent heat component of subsurface evaporation based on the sensible heat balance determined from vertical soil temperature measurements and estimated soil thermal properties

(Heitman et al., 2008; Sakai et al., 2011). However, previous studies do not compare the accuracy of the heat-pulse approach to more traditional methods of calculating evaporation using experimental data, nor do they consider an approach that uses a combination of the above listed methods.

In order to assess this hypothesis, a variety of models are required in which the inputs for the different models are associated with different mediums (e.g., porous medium, free flow medium, or both). The validity of this hypothesis enables increased accuracy between measured and modeled evaporation for future studies that may impact water management and predictions of evaporation required as part of landmine detection technology algorithms. Additionally, selection of an optimal evaporation model provides clarity regarding essential sensors required to collect data necessary as model inputs.

Hypothesis 3: **Soil moisture and temperature distributions are significantly altered by soil disturbance/mixing, especially in the shallow subsurface where transient boundary conditions at the land/atmospheric interface (e.g. temperature, wind speed, pressure, humidity and evapotranspiration) play a role.**

The drying behavior of vertical and horizontally texturally contrasting soils is more complex than those of homogeneous or horizontally layered heterogeneous soils (Lehmann and Or, 2009; Shahraeeni and Or, 2010; Shahraeeni and Or, 2011; Nachshon et al., 2011a; Nachshon et al., 2011b). The change in capillary pressure across the vertical disturbance layer can lead to evaporation enhancement by increasing the equilibrium vapor pressure (Kozak and Ahuja, 2003; Ho, 2006). Lehmann and Or (2009) showed that a heterogeneous soil packing consisting of fine and coarse soils have higher total evaporation rates than a homogeneous soil packing configuration. The validity of this hypothesis enables better understand the mechanisms of liquid

water and water vapor transport within a disturbed soil profile consisting of a tight and loosely packed soil created as a function of the landmine burial process. The effect of this packing configuration on momentum, thermal, and mass concentration boundary layers development is possible to analyze. Additionally, the added complexity of a layered soil with a localized disturbance that creates a mixture enhances the ability to investigate condition from a more robust number of environments in which landmines may be found.

1.4 Research Scope and Specific Tasks

In order to address the hypotheses/objectives described above, four specific research tasks were developed as shown in Figure 1. Components of the figure will be described within each task description below. Each tasks builds upon the previous task in gaining additional understanding regarding the environment in which landmines are buried. Task 1 involves understanding the impact of the disturbed soil mixture portrayed in Figure 1.2a and d. A variety of homogeneous soil conditions under varying boundary conditions are evaluated for Task 2. Task 3 addresses a condition where the subsurface is homogenous (Figure 1.2c) and the added complexity of a natural system which includes a coarse top layer and the resulting disturbed soil mixture (Figure 1.2d). Finally, conditions shown in Figure 1.2e are evaluated in a field environment as part of Task 4. It is important to be clear that all findings associated with this research are for quartz sand materials. Therefore, conclusions do not necessarily apply to all soil types or conditions not evaluated within this dissertation.

Task 1: **Characterization of thermal conductivity of binary sand mixtures**

Soil horizons typically include a layer of coarse top soil over a finer subsurface environment. Therefore, the landmine burial process of digging a hole to emplace the landmine causes the creation of a mixture of the coarse and fine soil, which can be considered a binary soil

mixture (Figure 1.2a). The depth of the interface between the coarse and fine soil results in a variety of different mixing fractions between the two soils. In the first task, the hydraulic and thermal characteristics of soil mixtures were evaluated. Characterization of the binary mixtures was essential to understand the environmental response expected within the disturbed soil environments. Two analytical thermal conductivity models were investigated in their ability to use easily-measured soil properties that changed for each binary mixture to predict the measured thermal conductivity-water content relationship specific to each mixture. In order for the agreement between the modeled and measured relationships to be statistically significant, all model parameters that could have been based upon physical measurements were required to be used as fitting parameters. The knowledge obtained as part of Task 1 is not only important to research on buried landmines dealing with binary mixtures, but also applicable to research incorporating heat transfer in soil focused on such areas as micrometeorological phenomena, soil borehole thermal energy storage, and agricultural production.

Task 2: **Comparison of methods used to calculate evaporation**

As discussed in the background and motivation sections, several methods can express aspects of the relationship between soil moisture or temperature and evaporation. These methods may be based on either the hydraulic or thermal properties of the soils as well as the atmospheric conditions. For this analysis, I assessed the bulk aerodynamic, threshold formulation and heat pulse methods. Numerical results were compared with laboratory experimental data collected under varying boundary and initial conditions. Knowledge obtained is not only applicable to landmine detection research focused on arid regions with homogenous, high-quartz content soils (e.g., Israel, Egypt), but is also applicable to land-atmospheric research focused on the interaction between the shallow subsurface and near surface free flow medium.

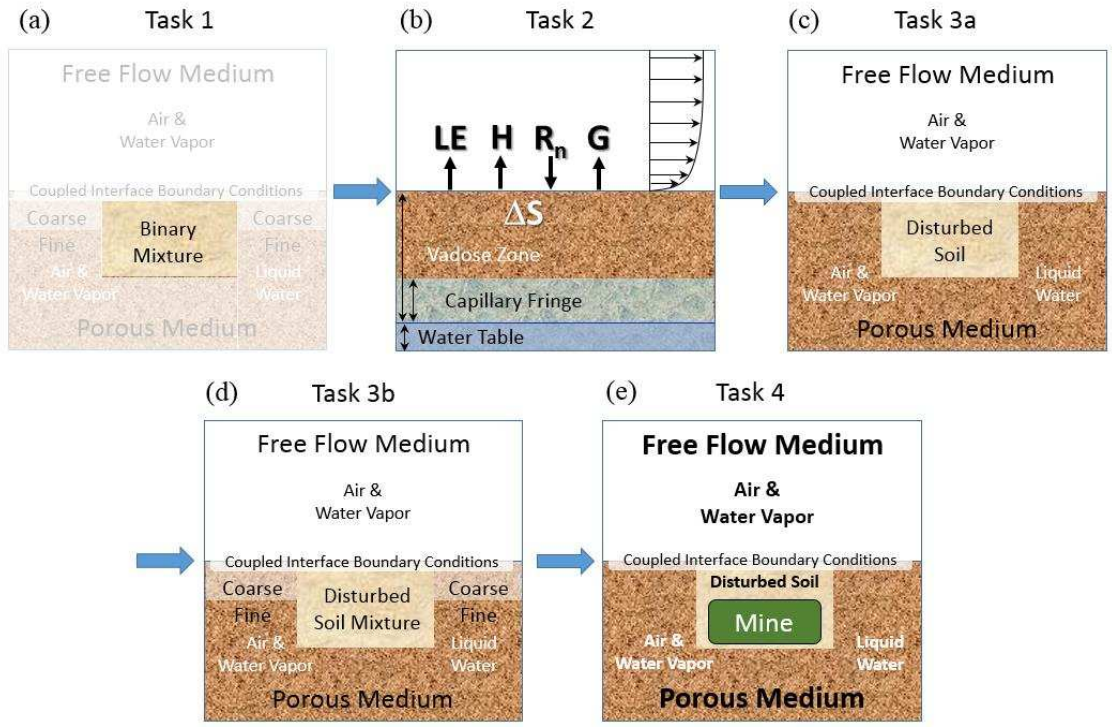

Figure 1.2. Conceptual model of coupled processes and interactions between subsurface and near surface environments influenced by landmine burial when focused on (a) binary soil mixtures, (b) heat and mass transfer as well as energy budget considerations regarding fluxes, (c) impact of soil disturbance on mass and heat flux with a homogeneous soil prior to landmine emplacement, (d) impact of mixing on mass and heat flux with a layered soil prior to landmine emplacement, and (e) emplacement of a surrogate mine as part of a field experiment proof of concept.

Task 3: **Impact of soil disturbance and mixing on heat and mass transfer behavior in soil at the land-atmosphere interface**

The process of landmine emplacement creates a physical contrast between parent, undisturbed soil and the disturbed soil used to cover a buried mine. Depending on soil characteristics, the emplacement process either leads to a disturbed soil in the case of a homogeneous soil region or a mixed soil in the case of a layered soil region. No research was identified that has investigated the impact of landmine emplacement disturbance and mixing on

heat and mass transfer behavior under varying boundary conditions. This type of research improves our understanding of the ensuing changes from burying landmines which provides new data for comparison in future research efforts designed to improve the algorithms of different mine detection platforms.

Six experiments were performed under varying boundary conditions occurred as part of this task and included both homogeneous soil under tight packed conditions with a center, loose packed disturbed region as well as a layered soil under tight packed conditions with a center, loose packed mixture region. Results indicated preferential subsurface flow based upon the interaction of the various subsurface regions. The robust, experimental data collected enables use by future research efforts to validate numerical models in their ability to accurately predict temperature and soil moisture changed as influenced by mine emplacement activities (i.e., creation of a loose soil based upon the characteristics of the parent material due to digging a hole, creation of a loose soil surrounded by a tight soil due to filling the hole compared to the undisturbed surrounding soil). The added complexity associated with this analysis more appropriately simulated natural conditions found in arid climates in which landmines may be buried. In the case of the disturbed soil, an analytical model investigation was pursued which identified the relative contribution to total evaporation of each packed region across the surface. This research is significant for landmine detection and any research in which soil disturbance and mixtures may be of importance in the shallow subsurface to capture conditions at a subsurface boundary interface between difference quartz-based sands.

Task 4: **Field investigation of the effect of soil disturbance on heat and moisture transfer behavior around buried objects**

Numerical modeling of actual conditions associated with landmine emplacement requires data collected from field investigations. Prior to a model's use for predictive purposes, the model must be validated based upon experimental measurement. The purpose of this task was to collect high temporal and spatial resolution experimental data from a field site for model validation associated with future research. The field experiment investigated the relationship between surrogate landmines buried at different depths (e.g., shallow and deep), a shallow buried limestone block similar in size to the landmine, and a hole dug with similar dimensions for landmine burial that was filled only with disturbed soil. The impact of soil conditions (e.g., porosity, saturation) and atmospheric conditions (e.g., velocity, temperature, relative humidity) were measured to determine the level of agreement between the disturbed soil and conditions existing for the buried landmines. Although other field experiments have been conducted, no one research effort has simultaneously evaluated the impact of soil disturbance, burial depth, and object properties on soil moisture and temperature distributions in the vicinity of buried objects as is done as part of this task. This knowledge is not only important for landmine research, but is also applicable to research which is concerned with the impact of near surface natural and man-made heterogeneities on heat and mass transfer.

1.5 Thesis Outline

The structure of this thesis is organized into 7 chapters and 4 appendices. A literature review on topics relevant to this dissertation is located in Chapter 2. Each of the four tasks noted above are organized into the following chapters:

Chapter 3: Thermal conductivity of binary sand mixtures evaluated through full water content range.

Chapter 4: Estimating soil water evaporation: an intercomparison of energy balance, water balance and water flux based models using laboratory measurements over bare and vegetated surfaces.

Chapter 5: Heat and mass transfer behavior from disturbed and mixed soils: laboratory scale experimental and analytical model investigation.

Chapter 6: Field scale experimental investigation of diurnal fluctuations of heat and water distributions around landmines in natural soil.

The significant conclusions and findings of this research are presented in Chapter 7. Appendix A contains a list of the user guides that were developed for all sensors and systems used throughout the extensive experimental period of research for this dissertation. These guides sit in a repository for easy reference and use by the Center for Experimental Study of Subsurface Environmental Processes (CESEP) research group members. A procedure developed to determine the effective radius of heat pulse sensors is presented in Appendix B. Permissions granted for publishing material presented in this dissertation are located in Appendix C. Finally, Appendix D contains the complete data sets created as part of the work associated with Chapters 3 to 6.

1.6 References

Andersson, Neil, Sergio Paredes, and Cesar Palha da Sousa. "Social cost of land mines in four countries: Afghanistan, Bosnia, Cambodia, and Mozambique." *British Medical Journal* 16 Sept. 1995: 718+. *Academic OneFile*. Web. 19 May 2015.

Arcand, J.L., A.S. Rodella-Boitreaud, and M. Rieger. 2014. The impact of land mines on child health: evidence from Angola. Economic development and cultural change. 63(2):249-279.

Berhe, A.A. 2007. The contribution of landmines to land degradation. Land Degrad. Develop. 18:1-15. doi:10.1002/ldr.754.

Bruschini, C. and B. Gros. 1998. A survey of current sensor technology research for the Q7 detection of landmines, in sustainable humanitarian demining: trends, techniques and technologies, edited by the Humanitarian Demining Information Center, James Madison University (Co-Editors: D. Barlow, C. Bowness, A. Craib, G. Gately, J.D. Nicoud, J. Trevelyan), Mid Vally Press, Verona, VA. 172-187.

Brutsaert, W., and J. Stricker. 1979. An advection-aridity approach to estimating actual regional evaporation. Water Resour. Res. 15:443-450.

Cooke, R.U., A. Warren, and A.S. Goudie. 1993. Desert geomorphology. CRC Press. Frome, England.

Deans, J., G. Schmithals, and L.J. Carter. 2001. An analysis of the thermal imaging method for landmine detection using microwave heating. J. Appl. Geophys. 47(2):123-133.

Dregne, H.E. 1976. Soils of arid regions. Elsevier, New York, p. 250.

Edwards, T.L., C. Cox, B. Weetjens, T. Tewelde, and A. Poling. 2015. Giant African pouched rates (Cricetomys gambianus) that work on tilled soil accurately detect land mines. J. Applied Behavior Analysis. doi:10.1002/jaba.214

English, T.L. 2000. The quiet Americans: a history of military working dogs. Office of History. 37th Training Wing, Lackland AFB, Texas.

Evett, S.R., A.W. Warrick, and A.D. Matthias. 1995. Wall material and capping effects on microlysimeter temperatures and evaporation. Soil Sci. Soc. Am. J. 59:329-336.

Garcia-Padron, R., D. Loyd, and S. Sjökvist. 2002. Heat and moisture transfer in wet sand exposed to solar radiation – models and experiments concerning buried objects. Subsurface Sensing Technologies and Applications. 3(2):125-150.

Heitman, J.L., X. Xiao, R. Horton, and T.J. Sauer. 2008. Sensible heat measurements indicating depth and magnitude of subsurface soil water evaporation. Water Resour. Res. 44:7.

Hendrickx, J.M.H., B. Borchers, J. Woolslayer, L.W. Dekker, C. Ritsema, and S. Paton. 2001. Spatial variability of dielectric properties in field soils. Proceedings of SPIE. 4394:398-408.

Ho, J. 2006. Vapor transport processes, Theory Appli. Transp. Por. Med. 20:27-46.

International Committee of the Red Cross. Explosive remnants of war. Geneva: ICRC Publications, 2011.

Keeley, R. 2003. Understanding landmines and mine action. http://web.mit.edu/demining/assignments/understanding-landmines.pdf; Accessed July 14, 2015.

Koh, G., and J.R. Ballard. 2004. Disturbed soil signatures for mine detection. Engineer Research and Development Center Hanover NH Cold Regions Research and Engineering Lab.

Kondo, J., N. Saigusa, and T. Sato. 1990. A parameterization of evaporation from bare soil surfaces. J. Appl. Meteorol. 29:385-389.

Kozak, J.A., and L.R. Ahuja. 2005. Scaling of infiltration and redistribution of water across soil textural classes, Soil Sci. Soc. Am. J. 69(3):816-827.

Krueger, K.R., McClellan, J.H., and W.R. Scott, Jr. 2015. Efficient algorithm design for GPR imaging of landmines. IEEE Transactions on Geoscience and Remote Sensing. 53(7):4010-4021. doi:10.1109/TGRS.2015.2388786

Lehmann, P. and D. Or. 2009. Preferential evaporation and capillary coupling in porous media with textural contrasts, Phys. Rev. E. 80. 046318.

MacDonald, J., J.R. Lockwood, J. McFee, T. Altshuler, T. Broach, L. Carin, R. Harmon, C. Rappaport, W. Scott, and R. Weaver. 2003. Alternatives for landmine detection. RAND Science and Technology Policy Institute.

McAuliffe, J.R. 2015. Desert Soils. Arizona-Sonora Desert Museum. Tucson, AZ.

Miles, D. 1998. Confronting the land mine threat. American Forces Press Service.

Mahfouf, J.F., and J. Noilhan. 1991. Comparative-study of various formulations of evaporation from bare soil using insitu data. J. Appl. Meteorol. 30:1354-1365.

Monteith, J.L. 1965. Evaporation and environment. *In* Symp. Soc. Exp. Biol. 19:205-223.

Nachshon, U., N. Weisbrod, M.I. Dragila, and A. Grader. 2011a. Combined evaporation and salt precipitation in homogeneous and heterogeneous porous media, Water Resour. Res., 47, W03513, doi:10.1029/2010WR009677

Nachshon, U., E. Shahraeeni, D. Or, M. Dragila, and N. Weisbrod. 2011b. Infrared thermograpy of evaporative fluxes dynamics of salt deposition on heterogeneous porous surfaces, Water Resour. Res., 47, W12519, doi:10.1029/2011WR010776

Ochsner, T.E., R. Horton, and T.H. Ren. 2001. A new perspective on soil thermal properties. Soil Sci. Soc. Am. J. 65:1641-1647.

Penmann, H.L. 1948. Natural evaporation from open water, bare soil, and grass. *Proc. R. Soc. London A.* 193:120-145.

Phelan, J.M., and S.W. Webb. 1997. Environmental fate and transport of chemical signatures from buried landmines: screening model formulation and initial simulations, Sandia National Laboratories Report SAND97-1426, Albuquerque, NM.

Ratto, C.R., P.A. Torrione, and L.M. Collins. 2011. Exploiting ground-penetrating radar phenomenology in a context-dependent framework for landmine detection and discrimination. IEEE Transactions on Geoscience and Remote Sensing. 49(5):1689-1700. doi:10.1109/TGRS.2010.2084093.

Saito, H., J. Simunek, J.W. Hopmans, and A. Tuli. 2007. Numerical evaluation of alternative heat pulse probe designs and analyses. Water Resour. Res. 43:W07408. doi:10.1029/2006WR005320

Sakai, M., S.B. Jones, and M. Tuller. 2011. Numerical evaluation of subsurface soil water evaporation derived from sensible heat balance. Water Resour. Res. 47:W02547. doi:10.1029/2110WR009866.

Sakaki, T., and K.M. Smits. 2015. Water retention characteristics and pore structure of binary mixtures. Vadose Zone J. 14(2). doi:10.2136/vzj2014.06.0065

Shahraeeni, E., and D. Or. 2010. Thermo-evaporative fluxes from heterogeneous porous surfaces resolved by infrared thermography, Water Resour. Res. 46. W09511, doi:10.1029/2009WR008455

Shahraeeni, E., and D. Or. 2011. Quantification of subsurface thermal regimes beneath evaporating porous surfaces, Int. J. Heat Mass Transf. 54:4193-4202.

Shire, A., U. Jawarkar, and S. Chavhan. 2015. Overview of buried mines detection using radar bullet. Int. J. Eng. Sci. and Resear. Technol. 4(2):250-254.

Tekstu, S., I.S. Atdalit, and N. Izcelsana. 1991. Food from dryland gardens – an ecological, nutritional, and social approach to small-scale household food production. CPFE.

Van Dam, R.L., B. Borchers, and J.M. Hendrickx. 2005. Strength of landmine signatures under different soil conditions: implication for sensor fusion. International J. Systems Sci. 36(9):573-588.

Walsh, N.E. and W.S. Walsh. 2003. Rehabilitation of landmine victims – the ultimate challenge. Bulletin of the World Health Organization. 83:665-670.

CHAPTER 2 LITERATURE REVIEW

This chapter provides more detailed information regarding the problem description and motivation from Chapter 1. Previous research is discussed and includes consideration of mine detection technologies followed by fundamental processes of consideration for the experiments conducted throughout this research effort. Each subsequent chapter includes its own literature review as well. The chapter concludes with a discussion of data collection considerations and analytical model considerations with respect to Task 1.

2.1 Mine Detection Technologies

There are numerous technologies currently employed with the purpose of detecting buried landmines. As mentioned in Chapter 1, some of these technologies include single sensor metal detectors, ground penetrating radar, acoustic/seismic detection, infrared/hyperspectral methods, and biological method based upon chemical odor sensing. Although there are numerous technologies to discuss, this section focuses on fundamental concepts associated with ground penetrating radar (GPR) and infrared (IR) methods after introducing points of interest regardless of detection technology employed. The strength of landmine signature measured by these different technologies is significantly affected by different soil conditions (Van Dam et al., 2005).

Synthesis from the literature review leads to considerations regarding detecting buried landmines including diverse sizes, shapes, composition, and burial depth (Koh and Ballard, 2004; Moukalled et al., 2006). Surface roughness, subsurface heterogeneity, and soil moisture are environmental conditions that impact landmine detection (Khanafer and Vafai, 2002; Ratto et al., 2011). Soil moisture impacts the permittivity, conductivity, and dielectric contrast of the subsurface environment (Ratto et al., 2011). Diurnal thermal fluctuations impact thermal contrast at the soil surface to a depth of about 10 cm resulting from the energy exchange with the

environment (Garcia-Padron et al., 2002; Moukalled et al., 2006). Landmine material makeup (i.e., metal, plastic, wood, fiberglass, bakelite, ceramic, cardboard, concrete, neoprene, and resin) are other characteristics that impact detection probability based upon the detection technology employed (Sai et al., 1998, Estes et al., 2011). The contrast between mine and environment increases as the thermal diffusivity and conductivity of a mine decreases (Moukalled et al., 2006).

Estes et al. (2011) provided a summary of considerations regarding both the landmine structure and the environmental conditions in which the landmine is buried. The structure of the landmine is discussed regarding casing material (metal and plastic) and the inner material considerations that can degrade over time. Discussion regarding landmine degradation and environmental indicators or factors (soil, climate, etc.) that may allow predictive changes in landmine functionality are presented. The research does not to discuss different ways landmines may be detected based upon environmental conditions and the associated technology best suited for removal of various mines based upon composition. Instead, the literature review conducted by Estes et al. (2011) lead to recommending Eq. (2.1) illustrating that the rate of degradation consists of the vulnerability index (VI) for a mine to degrade, time (t), and environment (ENV) effects that may alter degradation.

$$Live\ Mine\ Risk\ (LMR) = \frac{VI \times ENV}{t} \tag{2.1}$$

2.1.1 Ground Penetrating Radar (GPR)

With an understanding of overarching concepts, the discussion of two specific technologies continues with GPR. GPR operates by measuring the reflection of an electromagnetic pulse from discontinuities in subsurface dielectric properties (Ratto et al., 2011). GPR performance is very sensitive to local environmental conditions (English, 2000; Hendrickx et al., 2001; Garcia-Padron et al., 2002; Estes et al., 2011; Ratto et al., 2011; Edwards et al., 2015). The ability to properly

measure or model environmental conditions such as soil water content is essential to GPR use. Uncertainty in soil water content leads to substantial uncertainty in the strength of GPR reflections and attenuation (Hendrickx et al., 2001). The maximum detection depth in clayey soil is 25 cm and up to 50 cm in sandy soil (Sai et al., 1998).

Ratto et al. (2011) presented a technique for making landmine detection using a GPR sensor more robust to fluctuations in environmental conditions via both physics-based and statistical methods for obtaining features form GPR data to characterize surface texture and subsurface electrical properties. Context-dependent feature selection (CDFS) was evaluated on a large set of GPR data collected over several years in dry to wet conditions for dirt, gravel and asphalt. CDFS technique was shown to improve landmine discrimination performance over conventional fusion of several currently fielded algorithms from the recent literature. Surface roughness, subsurface heterogeneity, and soil moisture are environmental conditions that impact landmine detection. Algorithm fusion for mine/clutter discrimination results from specific GPR detection algorithms versus measurements of moisture and temperature. However, Ratto et al. (2011) state that a potential improvement for results using CDFS would include using quantitative measurements (e.g., soil moisture, dielectric properties, etc.) to define the contexts of the data. One challenge includes the potential for soil measurements to be logistically difficult in the field.

Hendricks et al. (2001) researched how the variability of soil water content, both spatially and temporally, from field measurements in the Netherlands (water repellent soil), Panama (tropical forest soil), and New Mexico (desert soil) affects dielectric soil properties and the resulting response of a GPR system. Multiple samples were collected from various depths at each site over a period at least one year and a statistical analysis was employed to determine the coefficient of variability based on the soil moisture measured at each site and each depth. The

connection is made between the predicted variability in GPR response due to the variability in soil moisture as a means to highlight this relationship to GPR sensor designers. See Table 2.1 for more considerations specific to GPR technology.

2.1.2 Infrared (IR) Thermography

With a brief discussion of GPR technology complete, our discussion turns to two studies and finding of interest with respect to infrared (IR) thermography. As soil properties change, the fidelity of landmine detection using IR technology also changes. For example, the most favorable thermal contrast on the surface occurs with 5 wt.% moisture level (Carter et al., 1998). Garcia-Padron et al. (2002) used optical systems for detecting contrasts in surface temperature through analyzing reflected and natural energy that all objects continuously emit and absorb due to their temperature and energy exchange with the environment. This study was based on indoor experiments on wet and dry sand exposed to radiation from a solar panel. The optical system used operated within the thermal infrared wavelengths of 8-14 μm. The objective of the work was to improve the understanding of heat and moisture transfer mechanisms above a buried object in sand (without actual buried objects present), and the changes in surface temperature during a drying process of the sand. The models used based up de Vries (1963) did not include consideration of effects of heat generation, heat transfer from the evaporation-condensation processes, effects of thermal gradients on mass transport, and gravitational effects in order to simplify calculations.

Koh and Ballard (2004) investigated soil spectral signatures at the UV/VNIR regions to identify difference between disturbed and undisturbed sections of a mine test lane. The impact of soil disturbance above the mine masked a limestone signature found in the undisturbed soil based upon the relationship measured between emissivity and wavelength (μm). Soil disturbance resulted in lower backscatter intensity at normal incident angle as measured by a high-frequency radar

responding to the differences in soil roughness. The location of soil disturbed during mine emplacement is possible through spectral and radar signatures. However, IR technology is best suited for shallowly buried objects (e.g., antipersonnel mines) (Moukalled et al., 2006). A primary reason for this is because an increase in burial depth results in increased importance of the soil volume above a mine compared to the specific properties of the mine (Garcia-Padron et al., 2002). See Table 2.1 for more considerations specific to IR technology.

Some of the key considerations regarding GPR and IR technologies related to surface characteristics, subsurface characteristics, and soil moisture considerations are provided in Table 2.1. The items listed impact detection performance.

Table 2.1. Environmental conditions impacting detection technology capabilities.

Technology	Surface Characteristics	Subsurface Characteristics	Soil Moisture
GPR[1]	roughness serves as a source of radar clutter (may increase FAR)	heterogeneity causes radar clutter, distortion of signature	Increase in SM causes: 1) electromagnetic waves to propagate more slowly, hyperbolic GPR signature located further down the time axis = appears deeper 2) permittivity increase that alters dielectric contrast between targets and surrounding soil, contributes to slower propagation speed 3) conductivity increase that attenuates GPR pulse, reduces energy of target's GPR signature
IR[2]	back ground clutter (reduces thermal contrast clarity) causes irregular surface emissivity & reflectivity, shadows on surface, vegetation	irregular homogeneity, rocks, roots	Increase in SM causes: 1) altered surface temperature due to major influence on thermal properties of soil 2) increase in thermal conductivity

[1]Ratto et al., 2011
[2]Garcia-Padron et al., 2002

2.2 Environmental Considerations Applicable to Landmine Detection

Environmental conditions in which mines are likely encountered are diverse (Koh and Ballard, 2004) with considerations including redox potential, pH, acidity, soil moisture content, rainfall, heat, cold, fire, shrink/swell soils, saltwater degradation, and plant interferences (Estes at al., 2011). Some of the fundamental properties of consideration, interactions and coupled processes that must be considered as part of this research are shown in Figure 2.1. Heat and diffusion parameters of a soil are disturbed through mine emplacement (Garcia-Padron et al., 2002). Each detection technique applies differently based upon landmine case, explosive material, and soil (Kasban et al., 2010). Additionally, the aging of the environment in which the landmine is placed impacts the landmine casing as well as differentiation between buried object and surrounding soil (Estes et al., 2011). If the landmine casing has been compromised, then contact with water and heat may degrade the explosive material within the mine (e.g., TNT) as well as the geophysics associated with the subsurface soil elements present and their potential reaction (e.g., redox potential) with the emplaced mines (Estes et al., 2011). Consideration of landmine degradation may enable more focused removal efforts in areas where degradation is less likely. These considerations can help the prioritization of demining operations in areas with greater threat to human life. However, unless a landmine has been exposed to extreme environmental conditions, significant degradation is not expected (Estes et al., 2011). Therefore, the majority of research to date is still focused on detection and removal versus research focused on better understanding of the impact of soil disturbance and mixture on heat and mass transfer processes in the vicinity of buried landmines.

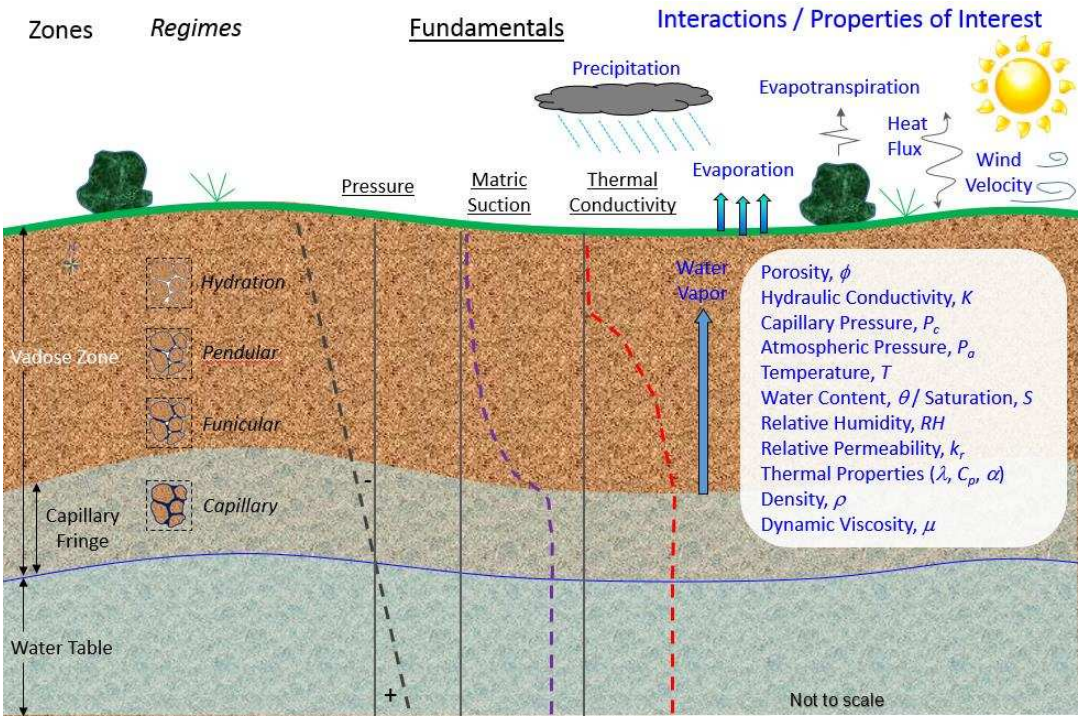

Figure 2.1. Conceptual sketch of the zones below the surface, regimes, fundamental relationships, interactions, and properties of interest that are required for consideration to improve landmine detection technologies.

The variety of environmental conditions that impact mine detection lead to a host of data required for collection during both field and laboratory experiments. Field conditions in which a landmine is buried is shown in Figure 2.2a and conditions of consideration associated with laboratory experiments are shown in Figure 2.2b. Consideration for sensors used to collect data in order to account for mass and heat transfer include being able to measure properties associated with air, water vapor, and liquid water in both the porous and free flow mediums as well as characteristics of the boundary between the two domains (Figure 2.2). The soil texture must be known regarding percent sand, silt, clay, and organic matter content. Both precipitation and potential evaporation are significant characteristics to know as well. The strength of landmine signature measured by different technologies is significantly affected by different soil conditions (Van Dam et al., 2005). Therefore, subsurface soil moisture and temperature are required as well

as relative humidity and temperature on the soil surface. Variations in soil moisture within soils composed of different degrees of sand, silt, clay and organic matter impact soil material properties (e.g., soil water retention, thermal conductivity, and hydraulic conductivity) (Qin et al., 2002). With a dry surface, surface temperatures rise with a decrease in moisture content (matric potential) due to less heat required for evaporation resulting in less sensible heating of the soil and a reduced thermal contrast (Moukalled et al., 2006). Regardless of soil moisture content, the need to measure and compare a variety of other properties with soil moisture cannot be overstated.

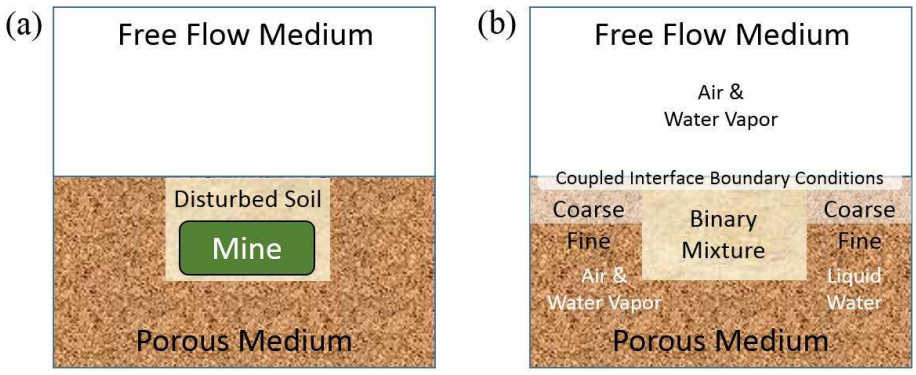

Figure 2.2. Conditions of consideration regarding (a) disturbance associated with field experiments and (b) mixing associated with laboratory experiments to guide sensor selections for collecting data essential for input of modeling effort.

The correlation of the regimes between the soil water retention curve (SWRC) and the relative saturation in a soil profile is shown in Figure 2.3. The fundamental relationships depicted are essential to understand for a more complete appreciation of the interconnected response between saturation, capillarity and thermal conductivity. Point (a) represents initial saturated conditions where saturation, *S*, is equal to 1 corresponding to θ equal to porosity, ϕ. Point (b) is the transition between the capillary (fully saturated yet under negative pore water pressure) and funicular (hydraulic connection to the soil surface) regimes. This transition occurs as the matric

suction approaches the air entry pressure. At point (b), the largest pores within the soil experience breakthrough of air resulting in the initiation of significant decrease in water content during small increases in matric suction, ψ. Point (c) denotes the transition between the funicular and pendular (pore water existing in pockets or thin films) regimes where water flow reduces to water lens connectivity. The physical point on the SWRC is the point of inflection. Within the pendular regime, there is a lack of hydraulic connection from the water table to the soil surface which results in pore water transport occurring primarily by vapor transport mechanisms (Lu and Likos, 2004). Although there is no flow of water, between different soil grains, water may connect two or more grains with these connections referred to as water bridges in nearly dry soil (Sakaguchi et al., 2007). Point (d) is the transition point between the pendular and hydration regime (structural ordering of water molecules as a function of properties of the minerals at the soil surface). At point (d), ψ increases significantly with very little decrease in *S*. Point (e) represents the residual saturated conditions where *S* remains almost constant and ψ reaches its peak.

The transition points relate to the change in slope regarding the λ-*S* relationship. In the capillary regime, λ is relatively constant due to the interconnection between soil grains via direct contact or water interfaces. At high *S* values, the water phase is continuous and heat is therefore transferred primarily through the grain and water phases and contacts between grains, resulting in high and relatively constant λ values. The λ value of water and air are typically 0.58 W m^{-1} K^{-1} (at 20^{o}C) and 0.024 W m^{-1} K^{-1} (at 20^{o}C), respectively, demonstrating that the water pathways are more conductive than the air pathways. Within the funicular regime bound by points (b) and (c), λ decreases gradually at an even rate. The small change in λ indicates that air begins to displace the water in a few of the larger pores. The rate of decrease in λ increases at point (c) and continues to decrease while in the pendular regime (between points c and d). In the pendular regime, the grain-

water paths become less continuous and more tortuous. This results in heat flow through less and longer thermally conductive grain-water pathways and therefore λ decreases. Thermal conductivity significantly decreases within the hydration regime approaching a residual value after water content decreases to residual conditions as discussed by Smits et al. (2010). In the hydration regime, the water is disconnected and can no longer form continuous grain-water paths. Heat conduction occurs predominately through grain-air pathways and grain to grain contacts and only partly though long tortuous grain-water paths, resulting in very few thermally conductive pathways and hence a pronounced decrease in λ down to a minimum value when only grain-air pathways exist.

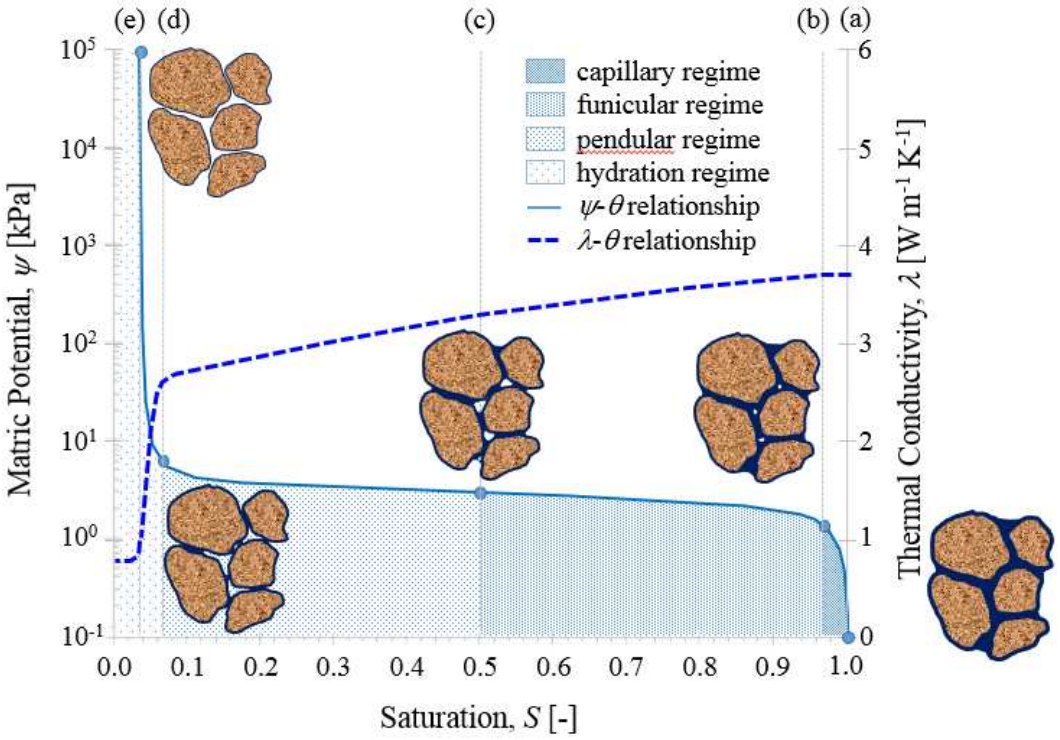

Figure 2.3. Representative SWRC and λ-S relationship for a well sorted sand depicting four regimes associated with saturation, the boundary and transition points between the regimes, the associated soil saturation at each point, and the relative water energy level spectrum (amended based on Lu and Likos, 2004).

2.3 Data Collection Considerations Applicable to Modeling of Landmine Scenarios

The discussion in the section above enables insight into significant relationship that require measurement of various properties throughout the conduct of an experiment. However, the specifics of which data to collect is best determined through consideration of data required as inputs for specific models of interest. This in turn enables proper data collection for future research efforts with the aim of algorithmic fusion to improve mine detection technology platforms. Therefore, the model inputs must be identified prior to field work and experimentation in order to set the conditions for essential data collection. For example if the Peplinski et al. (1995) model is used to estimate dielectric soil properties, inputs required include volumetric water content θ, frequency f, fraction of sand particles S, fraction of clay particles C, density of soil particles ρ_s (a typical value is 2.66 g cm^{-3}), and bulk soil density ρ_B (Hendrickx et al., 2001). To consider a phenomenological formulation for the heat and mass transfer coupled processes between the subsurface environment in which a landmine is buried and that adjacent free flow air stream above the ground, a comprehensive numerical model is required. An unsteady two-dimensional model for these transfer processes was developed via a finite-volume-based numerical method by Moukalled and Saleh (2006).

Moukalled and Saleh (2006) present research focused on increasing capabilities to predict moisture and temperature distribution in soil considered as a nonhomogeneous and nonisotropic porous material composed of a mixture of liquid moisture, vapor, and air in the pores. A finite-volume method is used to implement a matric potential ψ (pressure head)-based conservative equation to analyze heat and moisture transfer in soil. Properly estimating the soil's moisture content is essential for modeling the soil's thermal and hydraulic properties. The moisture and energy conservation equations require input for numerous variables. The physical properties of the

soil (e.g., moisture retention, hydraulic conductivity, thermal conductivity, and specific heat) are obtained by either laboratory experiments to characterize the soil or through estimates of fundamental parameters (e.g., van Genuchten, 1980; Brooks and Corey, 1964; etc.) to derive correlations for evaluating the physical properties. The essential properties required for analysis include porosity, water content, and temperature of the soil and air. The numerical method developed for predicting moisture and temperature distributions is verified through solving several test problems of increasing complexity and comparing the results against available theoretical values. However, no comparison occurs with actual experimental results.

Moukalled et al. (2006) build upon the work of Moukalled and Saleh (2006) and employ use of the numerical method developed to predict thermal signatures of buried landmines. Their research is used to determine the maximum temperature difference between the surface above the mine and the adjacent soil for different types of soils (Yolo light clay, sandy clay loam, and heavy clay), mines (TNT and Tetryl), and the times of its occurrence (6 a.m., 10 a.m., 2 p.m., and 8 p.m.). Although there is a lack of actual experimentation with this work, the model employed to evaluate a landmine (10 cm diameter x 5 cm thickness) buried at depths of 1, 2, 4, 6, and 8 cm identifies key considerations for landmine detection. As burial depth increases, the thermal contrast (temperature difference between surface temperatures above a mine compared to surface temperature where no mine is buried) decreases and the magnifying effects of soil moisture content disappear. Shallow buried mines (up to 2 cm) may be identified more readily through the addition of moisture. However, high moisture content in heavy clay soil results in degrading thermal contrast. Increasing soil moisture content shifts the time of day when the maximum thermal contrast occurs. The discussion regarding governing equations in both papers is complete and a good reference to ensure consideration of the variety of coupled processing involved.

2.4 Analytical Models of Consideration

Prior to numerical modeling efforts to enable verification of the coupled-integrated processes measured from experimental data, analytical modeling efforts are required for isolated interactions of interest (e.g., λ-θ, p_c-θ). For clarity of the reader, research presented in this dissertation is not focused on numerical modeling. The focus is on a variety of analytical modeling associated with Tasks 1, 2 and 3. The robust data sets collected from the various experiments as part of this dissertation are the legacy left for future research efforts. These data sets that have high spatial and temporal resolution will enable verification of numerical modeling. In so doing, those numerical models (once verified) may then change environmental conditions (i.e., temperature, relative humidity, soil moisture) for predictive analysis.

The discussion of analytical models of interest is presented in Chapters 3, 4, and 5. However, a variety of other models were investigated for each task which ultimately were not included in the subsequent chapters. The primary reason stems from the model's inability to function under the conditions associated with landmine emplacement. Presented below is an example of the analytical models initially included in the full analysis associated with Task 1. However, these models were filtered out of the discussion included in Chapter 3 and that reason is presented below.

The analytical models of concern relate to the λ-θ relationship. Empirical models provide one of three primary categories associated with modeling λ. Dong et al. (2015) provided a thorough, detailed description of mixing, empirical and mathematical models from the 1950s through 2008. Their discussion focused on the significance of the presented models, applicable operation range in terms of saturation, temperature, and soil type, and potential for each model to accurately predict the thermal conductivity to saturation, λ-S, relationships. Other examples of

detailed investigations of multiple models are provided by Lu et al. (2007), Smits et al. (2012), and Haigh (2012). Additional models continue to be developed across the spectrum of categories signifying that a universal equation to determine λ from the full saturation range has not been determined.

More recent models developed (e.g., Balland and Arp, 2005; Coté and Konrad, (2005); Lu et al., (2007)) have built upon the foundation of others (de Vries 1963, Johansen 1975, Campbell 1985) in efforts to further the model applicability. Each subsequent model addressed an area or areas with which to improve upon previous models. For example, Balland and Arp (2005) improved upon the Johansen (1975) model through inclusion of soils containing organic matter, soils with particle density < 2.7 g cm^{-3}, and θ < 0.1. Coté and Konrad (2005) improved upon the Johansen (1975) model incorporating a soil texture dependent parameter and two additional parameters encompassing particle shape effects. These improvements require knowledge of soil mineral composition regarding the soil of concern. Lu et al. (2007) endeavored to advance the Coté and Konrad (2005) model to incorporate fine-textured soils at lower θ.

One of the analytical models used in the analysis associated with Task 1 is the Campbell et al., (1994) model. A discussion focused on the fitting parameters is included in Chapter 3. Therefore, the discussion located herein provides the specifics of the variety of equations that are incorporated into the model. The semi-empirical Campbell et al. (1994) model is based upon the de Vries (1963) λ model.

$$\lambda = \frac{k_w x_w \lambda_w + k_a x_a \lambda_a + k_m x_m \lambda_m}{k_w x_w + k_a x_a + k_m x_m} \tag{2.2}$$

where the components of the soil derive from the mixture of water *w*, gas *a*, and mineral *m* regarding the weighting factor, *k*, the volume fractions, *x*, and the associated λ of each. The weighting factors are determined using Eqs. 2.3, 2.4, and 2.5.

$$k_w = \frac{1}{3}\left[\frac{2}{1+\left(\frac{\lambda_w}{\lambda_f}-1\right)g_a} + \frac{1}{1+\left(\frac{\lambda_w}{\lambda_f}-1\right)g_c}\right] \tag{2.3}$$

$$k_a = \frac{1}{3}\left[\frac{2}{1+\left(\frac{\lambda_a}{\lambda_f}-1\right)g_a} + \frac{1}{1+\left(\frac{\lambda_a}{\lambda_f}-1\right)g_c}\right] \tag{2.4}$$

$$k_m = \frac{1}{3}\left[\frac{2}{1+\left(\frac{\lambda_m}{\lambda_f}-1\right)g_a} + \frac{1}{1+\left(\frac{\lambda_m}{\lambda_f}-1\right)g_c}\right] \tag{2.5}$$

where g_a and g_c are shape factors with g_c defined in relation to g_a in Eq. 2.6, g_a serving as the first physical based fitting parameter, and λ_f defined as a "fluid" thermal conductivity in Eq. 2.7.

$$g_c = 1 - 2g_a \tag{2.6}$$

$$\lambda_f = \lambda_a + f_w(\lambda_w - \lambda_a) \tag{2.7}$$

where f_w is an empirical weighting function shown in Eq. 2.8 ranging from 0 to 1 for dry to saturated soil conditions.

$$f_w = \frac{1}{1+\left(\frac{x_w}{x_{wo}}\right)^{-q}} \tag{2.8}$$

where x_w is defined in Eq. 2.9, the volume fraction for gas and mineral is provided in Eqs. 2.10 and 2.11, x_{wo} is the cutoff water content for water recirculation or water content at which water starts to affect λ serving as the second physical based fitting parameter, and q is the soil property denoting the transition from air to water dominated conductivity given by Eq. 2.12.

$$x_w = \theta = S\phi \tag{2.9}$$

$$x_a = \phi - x_w = \phi - S\phi = \phi(1-S) \tag{2.10}$$

$$x_m = 1-\phi \tag{2.11}$$

$$q = q_o\left(\frac{\Gamma}{303}\right)^2 \tag{2.12}$$

where q_o is the power for the recirculation function and serves as the third physical based fitting parameter, and Γ is the soil temperature in Kelvin. The λ determined for water and gas is calculated using Eqs. 2.13 and 2.14, respectively.

$$\lambda_w = 0.554 + 2.24x10^{-3}T - 9.87x10^{-6}T^2 \tag{2.13}$$

$$\lambda_a = \lambda_{da} + \lambda_v \tag{2.14}$$

where T is the soil temperature in Celsius, λ_{da} is the dry air thermal conductivity given by Eq. 2.15, and λ_v is the vapor thermal conductivity as a function of latent heat transfer given in Eq. 2.16.

$$\lambda_{da} = 0.024 + 7.73x10^{-5}T - 2.6x10^{-8}T^2 \tag{2.15}$$

$$\lambda_v = \frac{H_v h f_w \hat{\rho} D_v s}{P - hp^*} \tag{2.16}$$

where H_v is latent heat of vaporization (J mol^{-1}) determined using Eq. 2.17, h is measured relative humidity without a provided equation, $\hat{\rho}$ is molar density of air (mol m^{-3}) determined using Eq. 2.18, D_v is vapor diffusivity in air (m^2 s^{-1}) calculated via Eq. 2.19, s is slope of the saturation vapor pressure vs. temperature function (Pa K^{-1}) using Eq. 2.20, P is measured atmospheric pressure (Pa), and p^* is saturated vapor pressure of water in the pore (Pa) given by Eq. 2.21.

$$H_v = 45144 - 48T \tag{2.17}$$

$$\hat{\rho} = \hat{\rho}_o \left(\frac{P}{P_o}\right)\left(\frac{\Gamma_o}{\Gamma}\right) \tag{2.18}$$

$$D_v = D_{vo}\left(\frac{P_o}{P}\right)\left(\frac{\Gamma}{\Gamma_o}\right)^{1.75} \tag{2.19}$$

$$s = 373.15p^*\left(13.3015 - 4.082t + 0.78t^2 + 10.76t^3\right)/\Gamma^2 \tag{2.20}$$

$$p^* = 101325\exp\left(13.3016t - 2.042t^2 + 0.26t^3 + 2.69t^4\right) \tag{2.21}$$

where $\hat{\rho}_o$ is molar density of air at sea level = 44.65 mol m^{-3}, P_o is atmospheric pressure at sea level = 101325 Pa, Γ_o is standard temperature = 273.15 K, D_{vo} is vapor diffusivity in air at 0 ^{o}C and sea level pressure = 2.12 x 10^{-5} m^2 s^{-1}, and t is given by Eq. 2.22.

$$t = 1 - \frac{373.15}{\Gamma} \tag{2.22}$$

One minor modification to the Campbell et al. (1994) model included calculating the relative humidity through the use of Eq. 2.23 presented in Lu and Likos (2004).

$$h = \exp\left[-\frac{(u_a - u_w)v_w}{R\Gamma} \right] \tag{2.23}$$

where $(u_a - u_w)$ is measured capillary pressure or matric suction (kPa), v_w is partial molar volume of water vapor = 1.8 x 10^{-5} m^3 mol^{-1}, and R is the universal gas constant = 8.314 J mol^{-1} K^{-1}. The final variable to define includes λ determined for the mineral component of the soil mixture, λ_m, which serves as the fourth and final physical based fitting parameter.

The Campbell et al. (1994) model along with the Lu and Dong (2015) model are used for comparison in Task 1. Other models were investigated, such as the Lu et al. (2007) model, the Chen (2008) model, and the Haigh (2012) model. The Lu et al. (2007) empirical model is evaluated using Eq. 2.24:

$$\lambda = \left(\left(\left(\lambda_q^q \lambda_o^{1-q}\right)^{1-\phi} \lambda_w^{\phi}\right) - (b - a\phi)\right)\exp\left\{\alpha\left[1 - S^{(\alpha - 1.33)}\right]\right\} + (b - a\phi) \tag{2.24}$$

where q is the quartz content of the total solids, λ_q is the thermal conductivity of quartz (= 7.7 W m^{-1} K^{-1}), λ_o is the thermal conductivity of other minerals (= 2.0 W m^{-1} K^{-1} for soils with $q > 0.2$ and = 3.0 W m^{-1} K^{-1} for soils with $q \leq 0.2$), a and b are empirical parameters, α is a soil texture dependent parameter (0.96 for coarse-textured soils and 0.27 for fine-textured soils), and 1.33 is a shape parameter. Lu et al. (2007) calculated values of 0.56 and 0.51 in their study for a and b, respectively.

The Chen (2008) empirical model incorporates the use of Eq. 2.25:

$$\lambda = \lambda_w^{\phi}\lambda_q^{1-\phi}\left[(1-0.0022)S + 0.0022\right]^{0.78\phi} \tag{2.25}$$

where λ_w is the thermal conductivity of water (= 6.096 W m^{-1} K^{-1}) and other variables previously defined.

The Haigh (2012) model is a purely analytical model, derived from simplified geometrical idealization of microstructure in soils. The model assessed one-dimensional heat flow between two equally sized spherical soil particles. The overall thermal conductivity of the soil is:

$$\lambda = \left[2(1+\xi)^2 \left\{ \frac{\alpha_w}{(1-\alpha_w)^2} \ln\left[\frac{(1+\xi)+(\alpha_w-1)x}{\xi+\alpha_w} \right] + \frac{\alpha_a}{(1-\alpha_a)^2} \ln\left[\frac{(1+\xi)}{(1+\xi)+(\alpha_a-1)x} \right] \right\} + \frac{2(1+\xi)}{(1-\alpha_w)(1-\alpha_a)}\left[(\alpha_w-\alpha_a)x - (1-\alpha_a)\alpha_w\right] \right] \lambda_q \tag{2.26}$$

where α_w and α_a are the thermal conductivities, normalized by that of the soil solids (λ_q = 7.69 W m^{-1} K^{-1}), of water (λ_w = 0.6096 W m^{-1} K^{-1}) and air (λ_a = 0.0219 W m^{-1} K^{-1}) respectively, as shown in Eq. 2.27. ξ is a geometric parameter specific to the soil (Eq. 2.28) based upon the voids ratio, e (Eq. 2.29), and x is a parameter defined through Eqs. 2.30 and 2.31.

$$\alpha = \frac{\lambda_{fluid}}{\lambda_{solid}} \tag{2.27}$$

$$\xi = \frac{2e-1}{3} \tag{2.28}$$

$$e = \frac{V_{void}}{V_{solid}} = \frac{V_{void}}{V_{total}-V_{void}} = \frac{\phi}{1-\phi} \tag{2.29}$$

$$x = \left(\frac{1+\xi}{2}\right)\left(1+\cos\varphi-\sqrt{3}\sin\varphi\right) \tag{2.30}$$

$$\varphi = \left[\arccos\left(\frac{2(1+3\xi)(1-S)-(1+\xi)^3}{(1+\xi)^3}\right)\right]\frac{1}{3} \tag{2.31}$$

Although the Haigh (2012) model was shown in the literature to provide better prediction of λ compared to nine other models for over 120 data points evaluated with each model for quartz sands, the model does not work for binary mixtures. The Haigh (2012) analytical model does not apply to binary mixtures due to geometric restrictions for ϕ less than 0.276 based upon the equations used to calculate λ. It is important that the basis of analytical models are considered prior to use. The Chen (2008) and Lu et al. (2007) model are shown in literature to provide good agreement to measured λ; however, both employ non-physically based fitting parameters. Therefore, with the focus of this research extensively based upon laboratory experiments where all aspects of soil boundary conditions are measured, empirical models selected for use with all tasks were chosen based on having fitting parameters that could be identified through physically measured properties impacted by disturbance and mixing associated with landmine emplacement activities.

There is more discussion regarding analytical models of concern for this dissertation which accompanies each chapter associated with Tasks 1, 2, and 3. Task 4 (Chapter 6) is focused entirely on experimental results. As this dissertation does not include numerical modeling, the reader is referred to a Smits et al. (2011), Smits et al. (2012), and Davarzani et al. (2014) for details regarding macroscopic flow and mass and energy balance equations in the free flow (gas) and porous medium domains as well as equations necessary for coupling the two domains. Some fundamental concept to keep in mind include that heat in soil is transported by conduction through

soil particles, through the water present in pores or adsorbed on solid particles, and through the air spaces (Shiozawa and Campbell, 1990). Gas flow in the free flow domain may be modeled using the Navier-Stokes equations. Energy transfer in both domains may be based upon incorporation of change in enthalpy with time, conduction, convection, and viscous heat generation portions of the overall energy equation. Flow of liquid in the porous medium may be modeled using Richards equation based upon the combined influence of Darcy's law and the continuity equation. Vapor transport must also be considered. Domain coupling occurs through continuity of normal stresses of the gas phase (Whitaker, 1999). There is much more to consider regarding numerical modeling; however, for the purposes of this dissertation, this discussion is closed.

2.5 References

Balland, V., and P.A. Arp. 2005. Modeling soil thermal conductivities over a wide range of conditions. J. Env. Eng. Sci. 4:549-558.

Brooks, R.H., and A.T. Corey. 1964. Hydraulic properties of porous media, Hydrological Papers (Colorado State University), 3.

Campbell, G.S. 1985. Soil Physics with BASIC. Elsevier, New York.

Campbell, G. S., J. D. Jungbauer, W. R. Bidlake, and R. D. Hungerford. 1994. Predicting the effect of temperature on soil thermal-conductivity. Soil Sci. 158:307–313.

Carter, L.L., M.J. O'Sullivan, Y.J. Hung, and J.C-C. Teng. 1998. Thermal imaging for landmine detection. Detection of abandoned land mines. IEE Conference Publication Number 458:110-114.

Chen, S.X. 2008. Thermal conductivity of sands. Heat Mass Transfer. 44(10):1241-1246.

Coté, J., and J.M. Konrad. 2005. A generalized thermal conductivity model for soils and construction materials. Canadian Geotech. J. 42:443-458.

Davarzani, H., K. Smits, R.M. Tolene, and T. Illangasekare. 2014. Study of the effect of wind speed on evaporation from soil through integrated modeling of the atmospheric boundary layer and shallow subsurface, Water Resour. Res., 50, doi:10:10.1002/2013WR013952

de Vries, D.A. 1963. Thermal properties of soils. In: W.R. van Wijk, editor, Physics of plant environment. North-Holland Publ. Co., Amsterdam. p. 210-235.

Dong, Y., J.S. McCartney, and N. Lu. 2015. Critical review of thermal conductivity models for unsaturated soils. Geotechnical Geological Engineering. 33(2):207-221. doi:10.1007/s10706-015-9843-2

Edwards, T.L., C. Cox, B. Weetjens, T. Tewelde, and A. Poling. 2015. Giant African pouched rates (Cricetomys gambianus) that work on tilled soil accurately detect land mines. J. Applied Behavior Analysis. doi:10.1002/jaba.214

English, T.L. 2000. The quiet Americans: a history of military working dogs. Office of History. 37th Training Wing, Lackland AFB, Texas.

Estes, E.J.III, T. Hartshorn, and J. Vallotton. 2011. Landmine materials and environmental soils literature review. Scoping study on the effects of aging on landmines phase 2 presented to the United States Department of State Office of Weapons Removal and Abatement, March 7, 2011.

Garcia-Padron, R., D. Loyd, and S. Sjökvist. 2002. Heat and moisture transfer in wet sand exposed to solar radiation – models and experiments concerning buried objects. Subsurface Sensing Technologies and Applications. 3(2):125-150.

Haigh, S.K. 2012. Thermal conductivity of sands. Geotechnique. 62(7):617-625.

Hendrickx, J.M.H., B. Borchers, J. Woolslayer, L.W. Dekker, C. Ritsema, and S. Paton. 2001. Spatial variability of dielectric properties in field soils. Proceedings of SPIE. 4394:398-408.

Johansen, O. 1975. Thermal conductivity of soils. Ph.D. Dissertation. Norwegian University of Science and Technology. Trondheim (CRREL draft transl. 637, 1977).

Kasban, H., O. Zahran, S.M. Elaraby, M. El-Kordy, and F.E.A. El-Samie. 2010. A comparative study of landmine detection techniques. Sens Imaging. 11:89-112. doi:10.1007/s11220-010-0054-x

Khanafer, K. and K. Vafai. 2002. Thermal analysis of buried land mines over a diurnal cycle. IEEE Trans. Geosci. Remote Sensing. 40(2):461-473.

Koh, G., and J.R. Ballard. 2004. Disturbed soil signatures for mine detection. Engineer Research and Development Center Hanover NH Cold Regions Research and Engineering Lab.

Lu, N., and W.J. Likos. 2004. Unsaturated soil mechanics. John Wiley & Sons, Inc., Hoboken. p. 429-431.

Lu, S., T. Ren, and Y. Gong. 2007. An improved model for predicting soil thermal conductivity from water content at room temperature. Soil Sci. Soc. Am. J. 71(1):8-14.

Moukalled, F., and Y. Saleh. 2006. Heat and mass transfer in moist soil, Part I. Formulation and testing. Numerical Heat Transfer, Part B, 49:467-486. doi:10.1080/10407790500510866.

Moukalled, F., N. Ghaddar, Y. Saleh, and Z. Fawaz. 2006. Heat and mass transfer in moist soil, Part II. Application to predicting thermal signatures of buried landmines, numerical heat transfer, Part B: Fundamentals. Int. J. Computation and Methodology, 49:5, 487-512, doi:10.1080/10407790500510965.

Peplinski, N.R., F.T. Ulaby, and M.C. Dobson. 1995. Dielectric properties of soils in the 0.3-1.3-GHz range. Geoscience and Remote Sensing. 33(3):803-807. doi:10.1109/36.387598.

Qin, Q., P. Berliner, and A. Karnieli. 2002. Numerical solution of a complete surface energy balance model for simulation of heat fluxes and surface temperature under bare soil environment. Appl. Math. Comput. 130:171-200.

Ratto, C.R., P.A. Torrione, and L.M. Collins. 2011. Exploiting ground-penetrating radar phenomenology in a context-dependent framework for landmine detection and discrimination. IEEE Transactions on Geoscience and Remote Sensing. 49(5):1689-1700. doi:10.1109/TGRS.2010.2084093.

Sai, B., I. Morrow, and P. van Genderen. 1998. Limits of detection of buried landmines based on local echo contrasts. Proceedings of 28th European Microwave Conf. Amsterdam, Netherlands.

Sakaguchi, I., T. Momose, and T. Kasubuchi. 2007. Decrease in thermal conductivity with increasing temperature in nearly dry sandy soil. Eur. J. Soil Sci. 58(1):92-97. doi:10.1111/j.1365-2389.2006.00803.x

Shiozawa, S., and G.S. Campbell. 1990. Soil thermal conductivity. Remote Sensing Reviews. 5(1):301-310.

Sakaki, T., and K.M. Smits. 2015. Water retention characteristics and pore structure of binary mixtures. Vadose Zone J. 14(2). doi:10.2136/vzj2014.06.0065

Smits, K.M., T. Sakaki, A. Limsuwat, and T.H. Illangasekare. 2010. Thermal conductivity of sands under varying moisture and porosity in drainage-wetting cycles. Vadose Zone J. 9(1):1-9. doi:10.2136/vzj2009.0095.

Smits, K.M., A. Cihan, T. Sakaki, and T.H. Illangasekare. 2011. Evaporation from soils under thermal boundary conditions: Experimental and modeling investigation to compare equilibrium- and nonequilibrium-based approaches, Water Resour. Res., 47, W05540.

Smits, K.M., A. Cihan, T. Sakaki, S.E. Howington, J.F. Peters, and T.H. Illangasekare. 2012. Soil moisture and thermal behavior in the vicinity of buried objects affecting remote sensing detection: Experimental and modeling investigation. IEEE Transactions on Geosci. Remote Sensing. 51(5):2675-2688.

Van Dam, R.L., B. Borchers, and J.M. Hendrickx. 2005. Strength of landmine signatures under different soil conditions: implication for sensor fusion. International J. Systems Sci. 36(9):573-588. doi:10.1080/00207720500147800

van Genuchten, M. T. 1980. A closed-form equation for predicting the hydraulic conductivity of unsaturated soils, Soil Sci. Soc. Am. J., 44:892–898.

Whitatker, S. 1999. The method of volume averaging. Kluwer, Dordrecht.

CHAPTER 3 THERMAL CONDUCTIVITY OF BINARY SAND MIXTURES EVALUATED THROUGH FULL WATER CONTENT RANGE

Manuscript published in *Soil Science Society American Journal*[1]

Benjamin M. Wallen[2,3], Kathleen M. Smits[3], Toshihiro Sakaki[3], Stacy E. Howington[4], and Chamindu Deepagoda T.K.K.[5]

Prior to discussion regarding the specifics of this chapter, the intellectual contribution is specified along with identification of the author's contribution to the work. This research increased knowledge in the field of research regarding thermal conductivity-water content (λ-θ) relationships. Prior to this effort, no research existed that reviewed the impact of binary sand mixtures on the λ-θ relationship. Specific contributions included identifying the significance of porosity (ϕ) in controlling the λ-θ relationship and identifying a strong correlation between density and both dry (λ_{dry}) and saturated (λ_{sat}) thermal conductivity values for the sands tested. These finding enable estimation of λ_{dry} and λ_{sat} which are inputs for models (e.g., Lu and Dong, 2015). Analytical modeling identified that neither the Campbell et al. (1994) or Lu and Dong (2015) model are able to use easily-measureable characteristics for binary mixtures as input for the parameters of either model to obtain a statistically significant agreement between measured and modeled λ. This finding is significant because both models were established on the fact that their fitting parameters are physically based which is not accurate for application with binary mixtures. Therefore, further model development is required to enable a λ model to be physically based for

[1] Reprinted with permission, Soil Sci. Soc. Am. J., 2016, doi:10.2136/sssaj2015.11.0408
[2] Primary researcher and author
[3] Center for Experimental Study of Subsurface Environmental Processes (CESEP), Department of Civil and Environmental Engineering, Colorado School of Mines, Golden, CO, U.S.A.
[4] U.S. Army Engineer Research and Development Center, Vicksburg, MS, U.S.A.
[5] Department of Civil Engineering, University of Peradeniya, Peradeniya 20400, Sri Lanka.

binary sand mixtures. These findings apply to binary mixtures of poorly graded, well sorted sand of high quartz content (>98%). All experimental and analytical modeling work was completed by the author of this dissertation. Additional work associated with this chapter involved developing a user's guide for all sensors and systems used for the experiments, also completed by the author. These user guides are listed in Appendix A and available through CESEP.

3.1 Abstract

A soil's grain size distribution affects its physical and hydraulic properties; however, little is known about its effect on soil thermal properties. To better understand how grain size distribution affects soil thermal properties, specifically the effective thermal conductivity, a set of laboratory experiments was performed using binary mixtures of two uniform sands tightly-packed with seven different mixing fractions over the full range of saturation. For each binary mixture, the effective thermal conductivity, λ, capillary pressure, h_c, and volumetric water content, θ, were measured. Results demonstrated that the λ-θ relationship exhibited distinct characteristics based upon the percentage of fine and coarse grained sands. We further compared measured λ-θ properties with independent estimates from two semi-empirical models (Campbell model and Lu and Dong model) to evaluate the models' applicability in relation to physically based parameters associated with changes in soil mixing (e.g. porosity and grain size). Both models were able to fit experimental data but to varying degrees based on the number of physically based parameters used. In general, model improvements are needed to capture the λ-θ relationship solely on physically based parameters.

3.2 Introduction

Understanding soil thermal properties is important to properly determine the impact of heat transfer on the distribution, circulation and evaporation of water in soil. Heat transfer within soil influences micrometeorological phenomena (Hanks et al., 1967), engineering efforts such as cooling electronic devices with heat pipes and insulating buildings (Bussing and Bart, 1997; Sakaguchi et al., 2009; Moradi et al., 2015), agricultural production (Al Nakshabandi and Kohnke, 1965; Usowicz et al., 1996; Lipiec et al., 2007), and landmine detection efforts that rely on thermal contrast (e.g., Garcia-Padron et al., 2002; Martínez et al., 2004). Previous studies provide insight into the effect of soil moisture, temperature and soil physical characteristics on soil thermal properties, specifically the effective thermal conductivity, λ (W $m^{-1}K^{-1}$) (e.g., de Vries, 1963; Johansen, 1975; Hopmans and Dane, 1986; Ochsner et al., 2001; Tarnawski and Gori, 2002). However, to our knowledge, none of the studies to date has investigated the effect of mixing differently-sized particles on controlling the λ behavior under varying soil water contents (θ, cm^3 cm^{-3}). Knowledge of the λ-θ relationship for differently-sized soil fractions is particularly important in many engineering applications such as soil borehole thermal energy storage (SBTES), landfill covers, and engineered material stabilization.

Previous research provides strong evidence that λ is affected by a wide range of parameters including θ (e.g., Philip and de Vries, 1957; de Vries, 1963; Yadav and Saxena, 1977; Tarnawski and Leong, 2000), porosity (ϕ, cm^3 cm^{-3}) (e.g., Terzaghi, 1952; Skaggs and Smith, 1968), soil type (Van Rooyen and Winterkorn, 1959; Adivarahan et al., 1962; Haigh, 2012), grain size (e.g., Sepaskhah and Boersma, 1979; Tavman, 1996; Midttømme and Roaldset, 1998), and temperature (e.g., Campbell et al., 1994; Hiraiwa and Kasubuchi, 2000; Sakaguchi et al., 2007). In general, λ increases with an increase in θ (Philip and de Vries, 1957; de Vries, 1963); this is because λ of

water (~0.58 W m^{-1} K^{-1}) is over an order of magnitude larger than that of air (~0.02 W m^{-1} K^{-1}). Increasing the contact between soil grains lowers ϕ enabling higher heat transfer through the grain lattice structure which yields a higher λ (Yadav and Saxena, 1977; Midttømme and Roaldset, 1998; Smits et al., 2010; Tarnawski et al., 2013). Past studies focused on the effect of porosity on thermal conductivity for specific field locations or unimodal soils rather than soil mixtures. Soil type also affects λ. Soils with relatively flat grain surfaces, such as silts and clays, have more contact points between grains and higher λ than do more rounded particles like sands and gravels, which have smaller contact area and lower λ (Becker et al., 1992). Grain size also affects λ where coarse-grained materials often maintain a higher λ than fine grained materials (Al Nakshabandi and Kohnke, 1965; Côté and Konrad, 2009). The increase in λ for coarse grained materials is due to the larger grains' ability to enable a more continuous length of high conductivity material (fewer gaps filled with air or water). As shown by de Vries (1963) and confirmed by Smits et al. (2010), this effect is small compared to changes in moisture contact and soil packing conditions (i.e., ϕ). Finally, increases in temperature result in an increase in bulk λ, behavior which is more pronounced for the intermediate saturation range (Campbell et al., 1994). This increase is due to the increase in the transfer of latent heat with decreasing air pressure or increasing temperature (Momose and Kasubuchi, 2002; Sakaguchi et al., 2009; Smits et al., 2013).

Soil mixtures with two differently-sized components, referred commonly as binary mixtures, are often described by the volume fraction of each particle size and the ratio of the particle diameters. When the smaller grains are sufficiently small as compared to the larger grains, the smaller particles can "fill" the voids created by larger grains, thus producing a lower ϕ. The difference in the particle packing is oftentimes referred to as coarse or fine packing (Clarke, 1979) based on which fraction dominates the mixture - the packing of a soil mixture shifts from coarse-

dominated to fine-dominated when the volume fraction of fines exceeds a critical value (Koltermann and Gorelick, 1995). The critical volume fraction of fines, f_{crit}, denotes the transition between coarse controlled and fine controlled mixtures which occurs near 30% fines as shown in the literature (e.g., Koltermann and Gorelick, 1995; Sakaki and Smits, 2015). Coarse-controlled mixtures exist as long as coarse grains make up the load-bearing skeleton. As more fine particles are added to the mixture, the fines keep filling the voids between the coarse grains until the coarse material no longer comprises the load-bearing skeleton. When the volume fraction of fines is equal to the ϕ of the coarse-grained component, the fines completely fill the voids in the coarser grains (Koltermann and Gorelick, 1995). Previous research demonstrates the effect of soil mixing on soil water retention behavior. For example, the soil water retention curve (SWRC) depends on the distribution and continuity of the pore sizes of the mixture and cannot simply be defined by a weighted algebraic superposition of the two soil water retention curves (Sakaki and Smits, 2015). Therefore, the SWRC oftentimes cannot be reproduced using a dual porosity model such as those developed by Gerke and van Genuchten (1993), Zimmerman et al. (1993), and Larsson and Jarvis (1999) and requires a multimodal model like that of Durner (1994).

Although much effort has been invested in the development of λ-θ models (e.g., de Vries, 1963; Johansen, 1975; McCumber and Pielke, 1981; Campbell, 1985; Campbell et al., 1994; Tarnawski et al., 2000; Lu et al., 2007; Chen, 2008; Côté and Konrad, 2005, 2009; Tarnawski and Leong, 2012; Haigh, 2012; Lu and Dong, 2015), none of the models specifically address the applicability to soils that are mixed, including binary mixtures. Additionally, few λ–θ models are physically based and rely on the use of fitting parameters. For example, the Lu et al. (2007) model incorporates two empirical parameters *a* and *b* and only one soil texture dependent parameter, α. The Tarnawski et al. (2000) model incorporates seven fitting parameters unique to each soil type.

The Côté and Konrad (2005) model includes a single dimensionless empirical fitting parameter associated with the combined impacts of grain size, pore size, and pore water. The Haigh (2012) model is based upon the assumption of perfectly spherical soil grain geometrically restricting the model to $\phi > 0.276$. The focus for this research was to obtain experimental data on λ-θ for binary mixtures whose soil water retention relationships are well characterized and examine how the λ-θ relationships are affected by mixing fractions. Therefore, two physically based models, the Campbell et al. (1994) and Lu and Dong (2015) models were selected to obtain insight on how existing models can or cannot reproduce the λ-θ relationships for binary mixtures.

The Campbell et al. (1994) model (hereafter referred to as the Campbell model) employs four soil-specific empirically determined parameters (thermal conductivity of mineral fraction λ_m, volumetric water content at which water starts to affect thermal conductivity x_{wo}, shape factor of the soil g_a, and rapidity of transition from air- to water- dominated conductivity q_o). The first three parameters listed are based on physical properties with λ_m requiring knowledge of the mineral fraction of the soil, x_{wo} relying on knowledge of the mean particle diameter, and g_a based upon soil grain geometry. The fourth parameter q_o is not linked to a measurable property of the soil. Campbell et al. (1994) state that ideally, one could predict all parameters from basic physical properties of the soil so that no fitting of parameters would be necessary. However, Campbell et al. (1994) compared experimental measurements to model predictions based upon some fitted parameters (i.e. nonlinear least square fits to data) rather than physically based parameters.

The Lu and Dong (2015) model (hereafter referred to as the Lu and Dong model) employs two soil-specific parameters (i.e., the onset of the funicular regime when menisci on soil particles are interconnected with each other θ_f, and the pore fluid network connectivity parameter m). Both of these parameters are based on physical properties of the soil and related to the soil water

retention behavior with θ_f based upon the residual volumetric water content θ_r, which is associated with the maximum rate of increase in λ when transitioning from dry to saturated conditions. Modeling of the soil water retention behavior using the van Genuchten (1980) model based upon measured capillary pressure and θ enables knowledge of the pore-size distribution parameter, *n*, which is related empirically to *m*. Therefore, it can be hypothesized that both the Campbell model and Lu and Dong model can estimate λ based upon their associated physical based measureable parameters to enable specific identification of the impact of binary mixtures.

The main objective of this work is to generate λ-θ relationship data for well-characterized binary mixtures under well-controlled conditions and systematically evaluate the effect of binary mixtures on soil thermal conductivity. Based on two uniform sands with different particle sizes (i.e., a coarse and fine grained sand), we generated a set of binary mixture samples with different mixing fractions identical to those used by Sakaki and Smits (2015). For each mixture, λ, θ and capillary pressure (P_c,) were measured over the entire range of saturation (S). The λ measured in the study were then compared with independent estimates made using the Campbell model and the Lu and Dong model in order to obtain insight on the applicability of the existing models to soils such as the binary mixtures.

3.3 Material and Methods

In this section, the experimental apparatus is described, sand materials, and experimental procedure. A discussion on statistical analysis concludes at the end of this section.

3.3.1 Experimental Apparatus

The experimental apparatus used in this study is shown in Figure 3.1. A small cell consisting of a network of sensors was hydraulically connected to a long water column. The cell

and water column were constructed out of 4-mm thick acrylic (specific heat = 1464 J kg^{-1} K^{-1}, λ = 0.2 W m^{-1} K^{-1}, and density = 1150 kg m^{-3}).

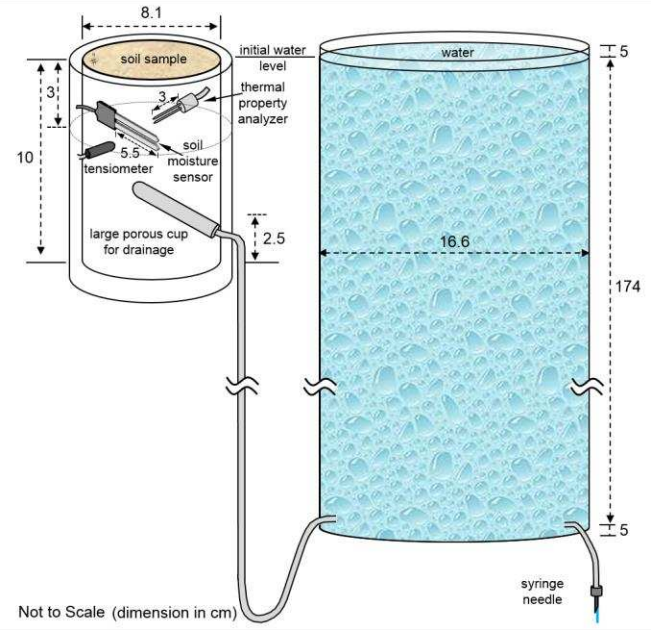

Figure 3.1. Experimental setup (not to scale). The inside volume of cell excluding sensors and porous cup for drainage is 510 cm^3. All sensors were positioned at 3 cm below the surface so that all measurements represent those within the same horizontal plane. Note that the water reservoir is sufficiently large and long so that drainage through the syringe needle induces a slow drainage (discussed in Section 3.3.3) at a nearly constant rate in the pressure range of interest.

The cell was outfitted with three sensors for measuring soil moisture, thermal properties, and capillary pressure. Soil moisture was continuously monitored using an ECH_2O EC-5 dielectric soil moisture sensor (Decagon Devices, Inc., Pullman, WA; sensor length = 5.5 cm, measurement frequency = 70 MHz) at 1 minute intervals; the moisture sensor was connected to an Em50 data logger (Decagon Devices, Inc., Pullman, WA). The EC-5 sensor measured the dielectric constant of the soil, which was converted to a digital count (ADC count, dimensionless). ADC counts were then used to estimate θ (m^3 m^{-3}) based upon the empirical two-point α-mixing model developed

by Sakaki et al. (2008; 2011). The bulk sampling of the ECH_2O EC-5 sensor is ~ 1 to 2 cm volume around the electrodes (Limsuwat et al., 2009).

A thermal property SH-1 sensor (Decagon Devices, Inc., Pullman, WA; dual needle, length = 3 cm, spacing = 6 mm, sample volume = 7.2 mm for saturated conditions transitioning to 6.5 mm for dry conditions (Knight and Kluitenberg, 2004)) connected to a KD2 Pro™ thermal property analyzer was used to measure λ (W m^{-1} K^{-1}) and soil temperature (^oC). Soil thermal measurements were made at 15 minute intervals to allow thermal gradients to dissipate, per the manufacturer's recommendation. The SH-1 sensor consists of two needles containing a thermistor in one needle and a heating element in the other. A current is passed through the heating element in one needle while the time-dependent temperature response is monitored in the second needle, 6 mm away. The λ of the soil is calculated based upon temperature measurements and knowledge of the heat generated (~22.3 W m-1) during heating (1 min) and cooling (1 min) cycles (Decagon Devices, 2014). The calculations derive from a dual needle algorithm based on the line heat source analysis (Carslaw and Jaeger, 1959; Abramowitz and Stegun, 1972; Kluitenberg et al., 1993, 1995; Bristow et al., 1994).

Water pressure was continuously monitored using a tensiometer. The tensiometer included a small porous cup (Soilmoisture Equipment Corp., Goleta, CA; diameter = 0.64 cm, length = 2 cm, air-entry value = 51 kPa, sample volume = 6.4 mm in the vertical direction) connected to a differential pressure transducer (Validyne Engineering Corp., Northridge, CA; Model P55D, range + 14 kPa. Measurements were made every minute. To allow for water drainage, a large porous cup (Soilmoisture Equipment Corp., Goleta, CA; diameter = 1.0 cm, length = 7.2 cm, air-entry value = 51 kPa) located near the bottom of the small cell was used. The porous cup was connected to a 174 cm long water reservoir (Figure 3.1).

3.3.2 Sand Materials

The two different sands used in the experiments were a fine-grained sand (Ottawa sand #110, US Silica Co., Ottawa, MN; uniformity coefficient = 1.7, mean diameter = 0.12 mm, dry bulk density = 1.79 g cm^{-3} when tightly packed) and a coarse grained sand (Accusand #12/20, Accusands, Unimin Corps., Ottowa, MN; uniformity coefficient = 1.2, mean diameter = 1.04 mm, dry bulk density = 1.81 g cm^{-3} when tightly packed). Both sands have a particle density (ρ_p) or specific gravity of 2.65 g cm^{-3} and mineralogical composition of 99.8% quartz as provided by the manufacturer. High sphericity (0.9), similar uniformity coefficients (d_{60}/d_{10}), batch-to-batch consistency, and purity with negligible amount of organic matter are among other important physical properties of the two sand types. These characteristics increase experimental reproducibility by minimizing porosity variations between consecutive packings (Schroth et al., 1996).

In addition to testing the fine and coarse grained sands separately, mixtures of the two sands were created based upon a mass-weighted fraction of each component. The two sands were mixed at seven different coarse to fine (C:F) ratios; 10:0, 9:1, 8:2, 7:3, 5:5, 2:8 and 0:10, respectively, identical to those evaluated by Sakaki and Smits (2015). These samples are referred to as C10F0, C9F1, C8F2, C7F3, C5F5, C2F8 and C0F10, respectively. Samples were well mixed to ensure homogeneity of the binary mixture. The cumulative particle size distribution associated with each binary mixture was obtained by conducting a series of sieve analyses.

The sieve analysis is shown in Figure 3.2. The particle size distribution for each binary mixture (except for the two parent sands) shows distinct two-region (bimodal) characteristics, thus showing the effect of mixing differently-sized particles on the characteristic size distribution. The sieve analysis enables identification of the uniformity coefficient and the geometric mean particle

diameter to further understand the physical impact of coarse- and fine-controlled mixtures. Table 3.1 provides the sand properties obtained from the sieve analysis for all binary mixtures.

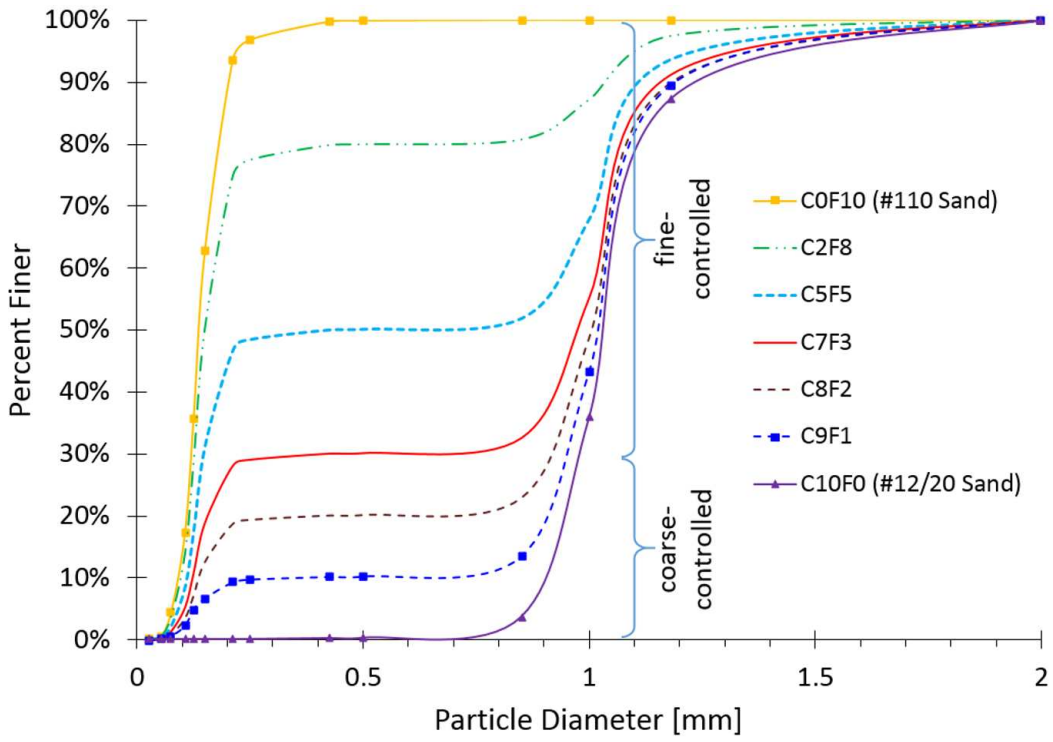

Figure 3.2. Sieve analysis for each binary mixture with C0F10, C9F1, and C10F0 measured and the remainder predicted based upon percent of the base sands (C0F10 and C10F0).

Table 3.1. Sand properties obtained from sieve analysis.

Binary Mixture	Mean Grain Size d_{50} [mm]	d_{60} [mm]	d_{10} [mm]	Uniformity Coefficient d_{60}/d_{10}	d_{16} [mm]	d_{84} [mm]	Geometric Mean Particle Diameter† $d_g = (d_{16}+d_{50}+d_{84})/3$ [mm]
C10F0	1.03	1.04	0.91	1.15	0.91	1.14	1.03
C9F1	1.02	1.04	0.50	2.07	0.88	1.12	1.01
C8F2	1.01	1.03	0.14	7.62	0.18	1.11	0.76
C7F3	0.97	1.02	0.12	8.42	0.14	1.09	0.73
C5F5	0.57	0.95	0.11	8.59	0.12	1.06	0.58
C2F8	0.15	0.17	0.10	1.73	0.11	0.94	0.40
C0F10	0.14	0.15	0.09	1.63	0.10	0.19	0.14

† used in the Campbell et al., 1994 model

3.3.3 Experimental Procedure

Each sample was wet packed using degassed-deionized water into the small cell based on the method described in Smits et al. (2010). Sand was poured into the cell in 2.5 cm increments ensuring maximum compaction and contact with the sensors by gently tapping the cell wall at each increment (e.g., Sakaki and Illangasekare, 2007). The saturated sample was subsequently drained by lowering the water level at a rate of ~3.4 cm^3 min^{-1} (0.016 cm of H_2O min^{-1}) through a syringe needle (21G1½ PrecisionGlide® Needle) connected at the outlet of the reservoir near the bottom of the water column (Figure 3.1) to slowly drain the mixture over a period of seven to ten days to achieve residual water contents in each sample. After the completion of each experiment, the residual water content was confirmed using destructive sampling. Each experiment associated with the various binary mixtures was conducted at least twice to confirm the repeatability.

3.3.4 Statistical Analysis

An appropriate statistical analysis tool is needed to compare nonlinear, curved relationships, such as an *F*-test (Motulsky and Ransnas, 1987; Spiess and Neumeyer, 2010). The *F*-test enables comparison of the variance associated with two data sets (e.g., experimental and modeled) and the ability to determine if the difference is statistically significant. *F* is determined as the ratio between two variances with the larger variance in the numerator. This ratio provides the percentage difference between the variance of the two compared data sets (i.e. experimental and modeled λ-θ data). *F* is compared to F_{crit} where F_{crit} is determined based upon the degrees of freedom for the sample and the desired confidence level which is typically set at 95%. If $F > F_{crit}$, then there is 95% confidence that the variance between the two data sets are significantly different. However, if $F < F_{crit}$, then one cannot conclude that a significant difference between variances exists (i.e., measured and modeled λ-θ relationships are in agreement).

3.4 Results and Discussion

Figure 3.3 shows the measured porosity of the binary mixtures compared with predictions from the partial mixing model developed by Kamann et al., (2007). Consistent with previous findings (Westman and Hugill, 1930; Holts and Lowitz, 1957; Garga and Madureira, 1985; Fragaszy et al., 1990; and Koltermann and Gorelick, 1995), the minimum ϕ (or equivalently, maximum bulk density) occurs when the small particles completely fill the voids of the load-bearing, larger particles, corresponding to a fine fraction of ~30% (C7F3) (i.e., f_{crit}). Although not the focus of this work, the partial mixing model described by Kamann et al. (2007) well described the data as in Figure 3.3 through setting the minimum total porosity to the observed value associated with the C7F3 mixture.

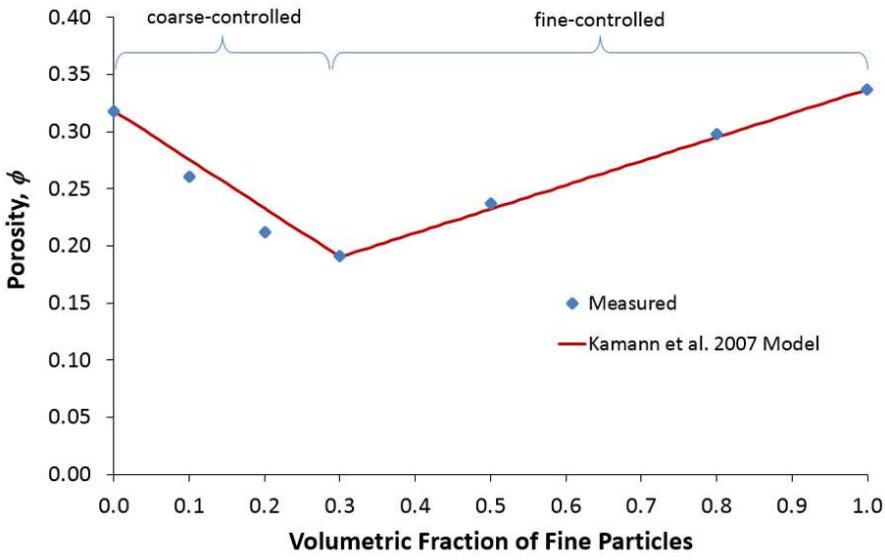

Figure 3.3. Porosity of binary mixtures (tightly packed) compared with predictions made using the partial mixing model developed by Kamann et al. (2007).

Important physical, water retention and thermal properties of the binary mixtures considered in this study are given in Table 3.2. Many properties shown in the table (e.g., ϕ, ρ, λ_{dry},

and λ_{sat}) exhibit a departure from similar values associated with the parent or base sands (#12/20 sand and #110 sand) and are discussed in further detail below. The measured h_c and θ_r values are in good agreement with the work of Sakaki and Smits (2015) in which identical binary mixtures were studied and are required as with λ_{dry}, and λ_{sat} for various modeling efforts. Comparing λ_{sat} from two sands with similar ϕ values (e.g., C10F0 and C0F10), shows the minimal dependence of thermal conductivity on the percentage of fine sand. deVries (1963) demonstrated that grain size does not significantly influence λ, assuming the grains have similar mineralogical properties, shape and packing. Although past researchers have found that λ decreases with a decrease in grain size (e.g., Tavman, 1996; Midttømme and Roaldset, 1998), consistent with the findings here, Smits et al. (2010) showed that there is only a slight correlation between λ and grain size for the sands used in this study.

Table 3.2. Properties of component sands and binary mixtures under tightly packed condition.

Sand	Porosity ϕ (-)	Bulk Density ρ (g cm^{-3})	Air Entry Pressure† h_c (cm H_2O)	Residual Water Content‡ θ_r (m^3 m^{-3})	Thermal Conductivity	
					Dry λ_{dry} (W m^{-1} K^{-1})	Saturated λ_{sat} (W m^{-1} K^{-1})
#12/20 (C10F0)	0.318	1.806	10.8	0.004	0.287	3.383
C9F1	0.261	1.959	10.7	0.013	0.427	4.396
C8F2	0.212	2.088	10.5	0.015	0.558	4.833
C7F3	0.190	2.145	52.1	0.006	0.529	5.010
C5F5	0.237	2.022	72.0	0.007	0.419	4.815
C2F8	0.298	1.860	78.0	0.007	0.332	3.947
#110 (C0F10)	0.337	1.757	72.8	0.009	0.282	3.241

† Based upon graphical interpretation of the SWRC corresponding to the pressure reached when water content transitioned from a constant value to decreasing significantly with small increases in pressure.

‡ Measured based upon destructive sampling method for each binary mixture.

The soil water retention curves for each mixture are shown in Figure 3.4. Results mirror those of Sakaki and Smits (2015) demonstrating the repeatability of the experimental results and high degree of confidence regarding data obtained during experimental procedures. It has to be emphasized here that the shape of the SWRCs is significantly affected by the mixing fraction. The coarse-controlled mixtures depict a similar displacement pressure close to that of the base coarse material (#12/20 sand) and the fine-controlled mixtures depict a larger displacement pressure closer to that of the base fine material (#110 sand). The displacement pressure, also known as air entry pressure or bubbling pressure (Brooks and Corey, 1964), is the pressure at which air first enters the soil matrix in the largest pores. A complete discussion regarding the water retention characteristics and pore structure of binary mixtures is found in Sakaki and Smits (2015).

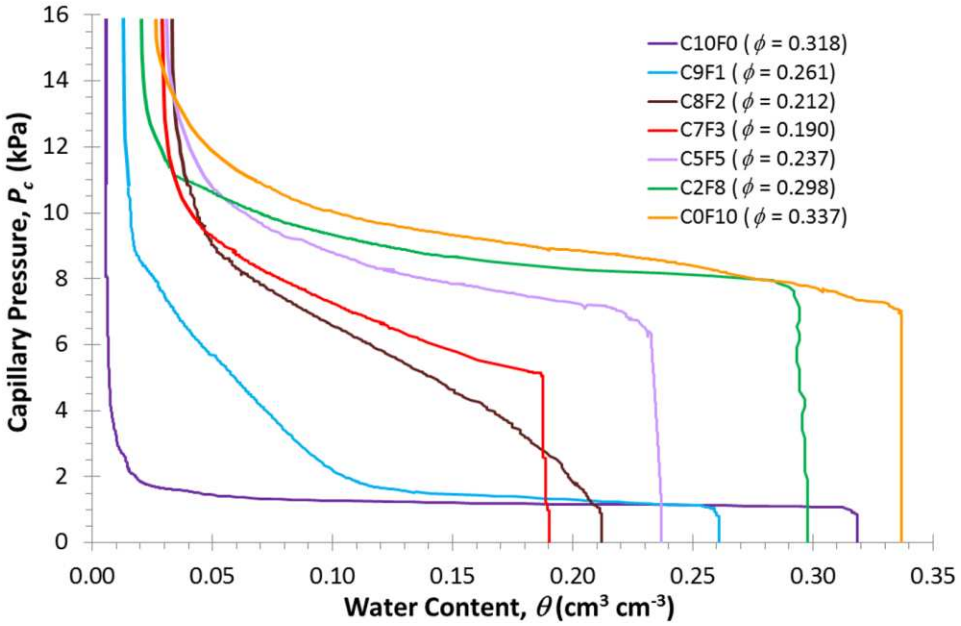

Figure 3.4. Soil water retention curve for all binary mixtures.

The impact of the binary mixtures on the λ-θ relationship is shown in Figure 3.5. The typical λ-θ behavior from fully saturated to completely dry conditions is characterized by the four saturation regimes; capillary, funicular, pendular, and hydration (Lu and Likos, 2004). In the capillary regime (Figure 3.5 – Region IV), the soil remains fully saturated (i.e., $\theta \approx \phi$) and the heat primarily transfers through the grain and water phases and contacts between grains resulting in a high and relatively constant λ. The typical values of λ for water and air (at 20^{o}C) are 0.58 W m^{-1} K^{-1} and 0.024 W m^{-1} K^{-1} respectively, demonstrating that the water pathways are more conductive than the air pathways. As the air entry pressure is reached (i.e. transition to the funicular regime (Figure 3.5 – Region III)) and the largest pores become air-filled, λ decreases slightly as water content decreases. Within the pendular regime (Figure 3.5 – Region II), the lower hydraulic connectivity makes the grain-water paths more tortuous, resulting in heat flow through less and longer thermally conductive grain-water pathways. Consequently, λ shows a steep and abrupt decrease at or around the residual saturation where the heat flow is essentially limited to water bridges randomly connected with nearly dry sand grains (Philip and de Vries, 1957; Sakaguchi et al., 2007). In the hydration regime (Figure 3.5 – Region I), the water is disconnected and can no longer form continuous grain-water paths. Heat conduction occurs predominately through grain-air pathways and grain to grain contacts, resulting in very resistive thermally conductive pathways and hence a pronounced decrease in λ. After the abrupt and pronounced decrease, λ continues to decrease slightly until a minimum value is reached corresponding to λ under dry soil conditions.

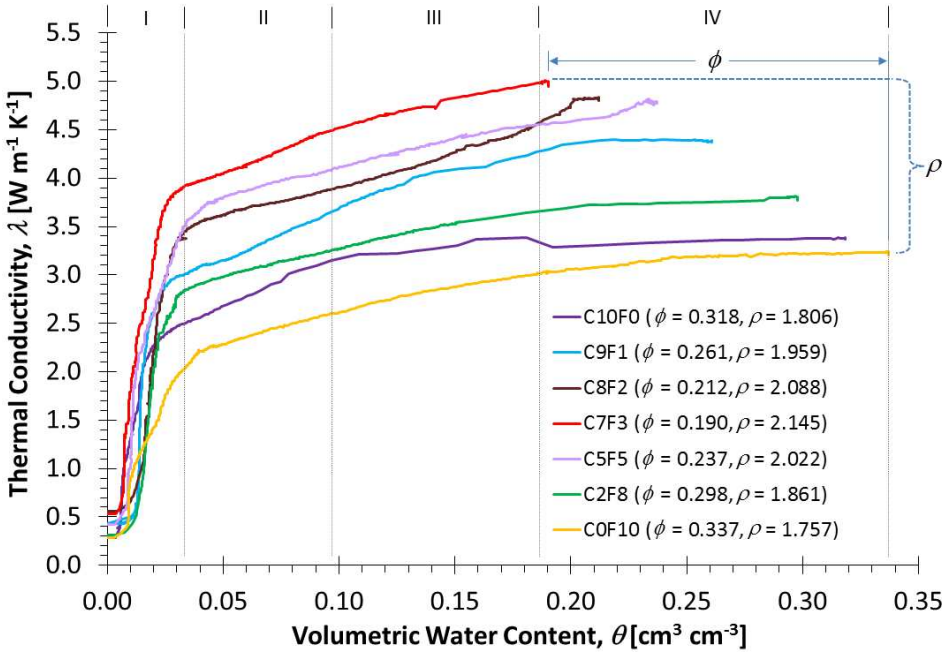

Figure 3.5. Thermal conductivity as a function of water content for binary mixtures highlighting the impact of changes in porosity and density within the four saturation regimes (I: hydration, II: pendular, III: funicular, and IV: capillary).

The general behavior described above is observed for all mixtures, consistent with previous findings (e.g., de Vries, 1963; Horton and Wierenga, 1984; Hopmans and Dane, 1986); however, the specific impact of binary mixtures on the λ-θ relationship is better understood through considering the influence of the systematic change in ϕ and bulk density, ρ, due to mixture characteristics. Binary mixtures with less than 30% fines exhibited coarse-controlled characteristics with a rapid rate of decrease in λ with a decrease in θ. Fine-controlled binary mixtures (percent fines $\geq$ 30%) portrayed a slower, more gradual rate of decrease in λ with a decrease in θ due to buffering capacity by more tortuous water pathways resulting from a decrease in large interconnected pore spaces as compared to coarse-controlled mixtures. However, these nuances between fine- and coarse-controlled binary mixtures are relatively small.

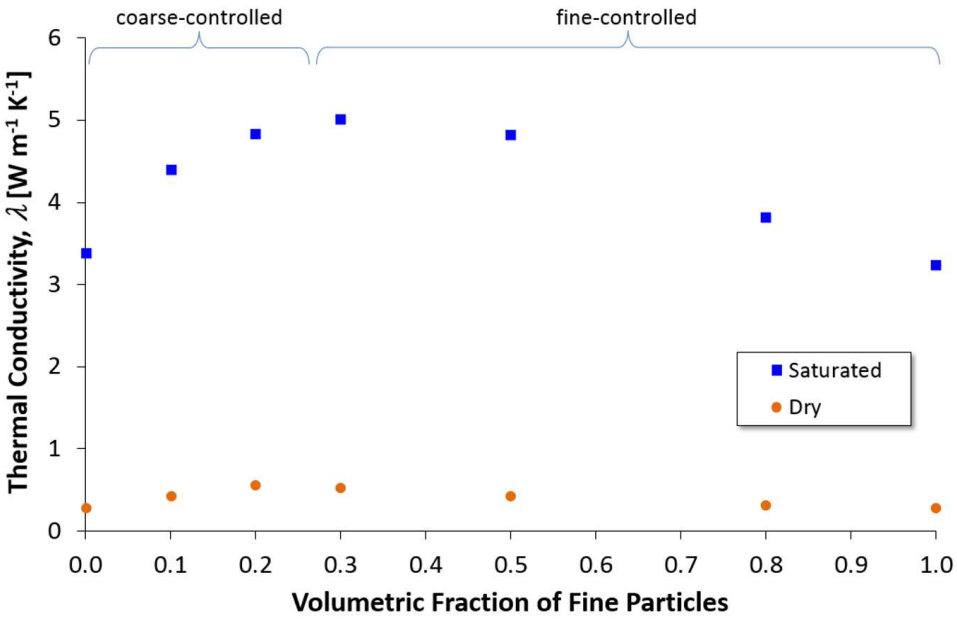

Figure 3.6. Dry and saturated thermal conductivity as a function of the volumetric fraction of fine particles.

Figure 3.5 shows that as ϕ decreases, at any given θ, λ increases. This is better illustrated by examining the saturated and dry λ for each mixture (λ_{sat} and λ_{dry}, respectively) (Table 3.2). As expected, the lowest λ_{sat} occurs with the soils with the highest ϕ (i.e., C10F0 and C0F10) while the highest λ_{sat} occurs with the soil with the lowest ϕ (i.e., C7F3). Figure 3.6 shows λ_{dry} and λ_{sat} as a function of the fraction of fine sand. The results demonstrate that the systematic change in volume fraction of fine particles, which of course affects the bulk density, also systematically changes λ_{dry} and $\lambda_{sat.}$ There is a significant change in λ for the saturated sands ($\Delta\lambda_{sat}$ approx. 1.77 W m^{-1} K^{-1}) where Δ refers to the difference between the maximum and minimum observed values of saturated or dry λ. Although the influence of the volume fraction of fine particles (hence ϕ) are considerably less for λ_{dry}, slight effects are still present ($\Delta\lambda_{dry}$ approx. 0.28 W m^{-1} K^{-1}). As previously discussed, this is because the air pathways are less conductive than the water pathways.

The less conductive pathways do not alter the strong positive correlation between both λ_{sat} and λ_{dry} with ρ. Shown in Figure 3.7, when λ_{sat} and λ_{dry} are each plotted against ρ, there is a distinct linear response (stronger for λ_{sat}) between an increase in ρ that occurs as the fraction of fines approaches f_{crit} and the corresponding increase in λ (R^2 >92%) demonstrating the large influence ρ has on λ. Changing the mixing fraction of the two sands in a systematic manner results in a predictable thermal behavior.

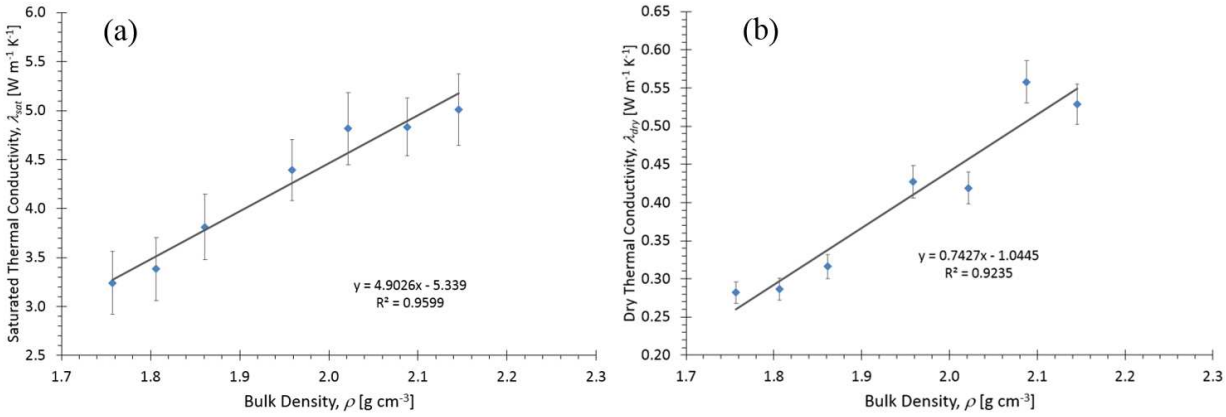

Figure 3.7. Correlation between soil bulk density and thermal conductivity for (a) saturated mixtures and (b) dry mixtures.

3.5 Applicability of λ-θ Models to Binary Mixtures

This section addresses whether existing predictive models describing the λ-θ relationship based on easily-measurable soil parameters are able to capture the behavior of soil mixtures. The Campbell model is based upon the de Vries (1963) model and posits that λ of soil can be determined from a volume-weighted sum of the λ of the mixture components:

$$\lambda = \frac{k_w x_w \lambda_w + k_a x_a \lambda_a + k_m x_m \lambda_m}{k_w x_w + k_a x_a + k_m x_m} \quad (3.1)$$

where k is the weighting factor, x is the volume fractions of each component, and the mixture components of water, gas, and mineral are denoted by subscripts w, a, and m, respectively. The model incorporates four soil-specific empirical model parameters to determine λ. For detailed information on model development and parameters, readers are referred to Campbell et al. (1994), however, key equations and parameters will be discussed here.

As mentioned above, Campbell et al. (1994) stated that ideally one could derive all four model parameters from basic physical properties without fitting to observed data. For example, λ_m can be estimated if the mineral fraction and soil composition is known. λ_m controls saturated λ where an increase in λ_m increases λ_{sat} and increases the difference between λ_{sat} and λ_{dry}. However, with Campbell's model, it has to be noted that λ_{dry} remains constant and is not influenced by λ_m. Based upon the physical properties of sands used in this research, λ_m is associated with the λ of quartz which has a range in literature of 3 to 13.9 W m^{-1} K^{-1} (e.g., Farouki, 1981; Clauser and Huenges, 1995; Bristow, 2002). The value selected in this study was 7.69 W m^{-1} K^{-1} based on previous works (e.g., Lu et al., 2007; Chen, 2008).

The second parameter, x_{wo}, impacts the λ at the transition between the pendular and hydration regimes. An increase in x_{wo} increases the residual water content, θ_r, and decreases the rapidity of λ reduction to the λ_{dry} value. Campbell et al. (1994) empirically developed a relationship between x_{wo} and the geometric mean particle diameter, d_g (μm):

$$x_{wo} = 0.267 d_g^{-0.2} \quad (3.2)$$

The geometric mean for each binary mixture was determined graphically based upon Folk and Ward (1957) and using Figure 3.2 and Eq. 3-3:

$$d_g = \frac{d_{16}+d_{50}+d_{84}}{3} \tag{3.3}$$

where d_{16}, d_{50}, and d_{84} are cumulative percentile values (grain size at which a specified percentage of the grains are coarser). For our mixtures, these values were determined based on the particle size distribution (Figure 3.2 and Table 3.1). From Table 3.1, the values of d_g for the binary mixtures transitions from 1.026 for C10F0 to 0.143 for C0F10 resulting in x_{wo} ranging from 0.067 to 0.099 with an increase in x_{wo} as the percent fines increases.

The magnitude of λ across the entire range of θ is controlled by g_a (shape factor of the soil) where an increase in g_a shifts the entire λ-θ relationship upward. Knowledge of the soil texture (coarse or fine) can be used to determine g_a based upon de Vries (1963) where a perfect sphere corresponds to a g_a value of 0.333. Shape data from the sand manufacturer leads to a g_a value of 0.2997 for #12/20 and 0.3830 for #110 sand. Therefore, a weighted average for each binary mixture based upon the percentage of coarse and fine sand can be estimated for all binary mixtures and falls within the range reported by Campbell et al. (1994).

As with x_{wo}, q_o has a similar, inverse impact on the λ-θ relationship with respect to the transition between the pendular and hydration regimes. An increase in q_o (versus a decrease in x_{wo}) results in an increase in the rapidity of λ reduction to the λ_{dry} value. With the previous three parameters, there was a means to predict the parameters from basic physical properties from the binary mixtures. However, there is not a clear means to predict q_o; therefore, q_o is employed strictly as a soil-specific empirically determined model parameter. Although not shown in the above equations, the Campbell model was developed to take into account the effect of temperature on λ.

Previous works have tested the applicability of the model to wide ranges of temperatures (e.g. Smits et al., 2013). As this was not the focus of this work, ambient conditions were maintained throughout all experiments to focus analysis on the impact of binary mixtures.

To identify the Campbell model parameters that have the most significant influence on the modeled λ, a sensitivity analysis was conducted as shown in Figure 3.8. Each parameter was adjusted by ±40% while keeping the others unchanged. When considering the impact of each parameter, λ_m had the most significant impact on λ followed by g_a, x_{wo}, and q_o in the given order. An increase in g_a results in more agreement between modeled and measured λ in the near-dry region.

To investigate the ability for the Campbell model to incorporate characteristics that change specifically due to the mixing of two different particles, the parameters associated with the Campbell model were varied based upon measured mixture characteristics and empirically determined properties. Four scenarios were conducted for each mixture in which the number of empirically determined parameters increased by one (e.g., scenario 1 - q_o served as the only empirically determined parameter; scenario 2 - g_a and q_o were determined through calibration; scenario 3 - q_o, g_a, and λ_m were determined through calibration; and scenario 4 - q_o, g_a, λ_m, and x_{wo} were all used as fitting parameters). The initial parameter values for scenario 1 and the F ratio between measured and modeled λ for all four scenarios is shown in Table 3.3.

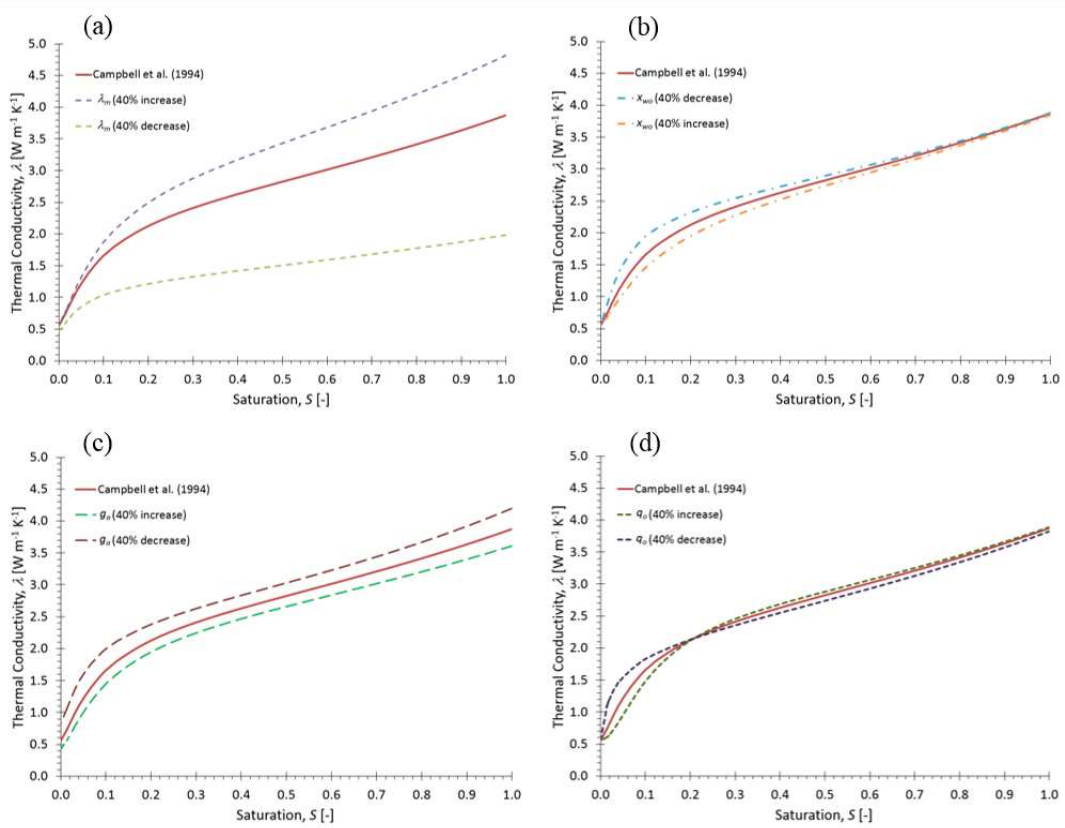

Figure 3.8. Sensitivity analysis of the Campbell model four soil-specific parameters for (a) λ_m, (b) x_{wo}, (c) g_a, and (d) q_o.

Table 3.3. Campbell model parameter values associated with scenario 1 and model to measured λ agreement based upon all four scenarios.

	Scenario 1 - Parameters Determined by Measured Characteristics			Calibration	*F* ratio based Upon Varying Calibrated Parameters†			
					1 Parameter	2 Parameters	3 Parameters	4 Parameters
Binary Mixture	g_a [-]	x_{wo} [-]	λ_m [W m^{-1} K^{-1}]	q_o [-]	q_o	q_o, λ_m	q_o, λ_m, g_a	q_o, λ_m, g_a, x_{wo}
C10F0	0.2997	0.0667	7.69	0.6295	4.26	4.36	1.48	1.02
C9F1	0.3080	0.0670	7.69	0.6574	7.50	4.41	1.36	1.03
C8F2	0.3164	0.0708	7.69	0.5175	4.65	3.73	1.23	1.02
C7F3	0.3247	0.0714	7.69	0.9900	1.85	2.30	1.24	1.02
C5F5	0.3413	0.0747	7.69	0.2515	6.88	4.13	1.19	1.03
C2F8	0.3663	0.0805	7.69	1.1000	1.41	3.80	1.23	1.04
C0F10	0.3830	0.0990	7.69	0.1565	3.24	1.02	1.04	1.00

† The shaded values indicate statistically significant difference between the variance of the measured and modeled λ.

In scenario 1, using only q_o as an unknown parameter, the difference in variance between measured and modeled λ was statistically significant (F=1.41-7.50 with F_{crit}=1.11-1.15). The Campbell model underestimates λ for all binary mixtures in the capillary and funicular regimes and overestimates for all mixtures in the lower end of the pendular regime and hydration regimes.

Despite the ability to independently estimate Campbell model parameters, Bristow (2002) recommended to obtain both g_a and q_o through calibration (scenario 2). With two best-fit model parameters (g_a and q_o), the F-test identified the difference between measured and modeled λ as statistically significant for all mixtures except for the base fine-grained sand (C0F10) (F=1.00-4.41 with F_{crit}=1.11-1.15). Although there is a slight increase in the level of model agreement, the Campbell model underestimated λ_{sat} and λ_{dry} for all binary mixtures.

To achieve an improvement in model agreement, λ_m accompanies g_a and q_o as best-fit model parameters in scenario 3. Scenario 3 reduced the F ratio by greater than 45% compared to scenario 2 in all binary mixtures (except C0F10); however, the percent difference in variance between modeled and measured λ remained statistically significant (F=1.04-1.48 with F_{crit}=1.11-1.15). The C0F10 sample remained the only mixture in which there was 95% confidence that the variance of the measured λ is not significantly different from the modeled λ. The incorporation of λ_m as a fitting parameter results in a significant improvement in estimated λ_{sat}; however, λ_{dry} is overestimated by at least 75% in all mixtures. With three of the four model parameters used to enhance agreement between modeled and experimental λ, the Campbell model is not able to effectively predict λ for binary mixtures.

Employing the Campbell model with all four model parameters (q_o, g_a, λ_m, and x_{wo}) used as best-fit parameters results in the Campbell model achieving a significant improvement in ability

to model λ for binary mixtures (scenario 4). Coarse-controlled and fine-controlled mixtures all exhibit F ratios denoting less than 5% percent significance in difference between measured and modeled λ (F=1.00-1.04 with F_{crit}=1.11-1.15). This higher level of model agreement is shown in Figure 3.9 and exhibits good estimation of λ_{sat} and λ_{dry} for both coarse-controlled (Figure 3.9a) and fine-controlled (Figure 3.9b) mixtures. Therefore, the Campbell model is limited to requiring the calibration of all four parameters versus enabling the use of physical based, measured quantities in order to effectively model binary mixtures. The calibrated value for each parameter and associated F ratio for each binary mixture for scenario 4 is provided in Table 3.4. For all scenarios, the values for q_o, g_a, and x_{wo} are within the ranges determined by Campbell et al. (1994). However, the value for λ_m for binary mixtures C10F0 and C9F1 are outside the range found in literature for λ of quartz (3 to 13.9 W m^{-1} K^{-1}). Therefore, there may be a need to constrain λ_m for sandy soils. Empirically determining all parameters enables an increased agreement between modeled and measured λ versus using physically determined values for x_{wo}, g_a, and λ_m demonstrating a need for an improved λ model for binary mixtures that can effectively capture the full range of saturation.

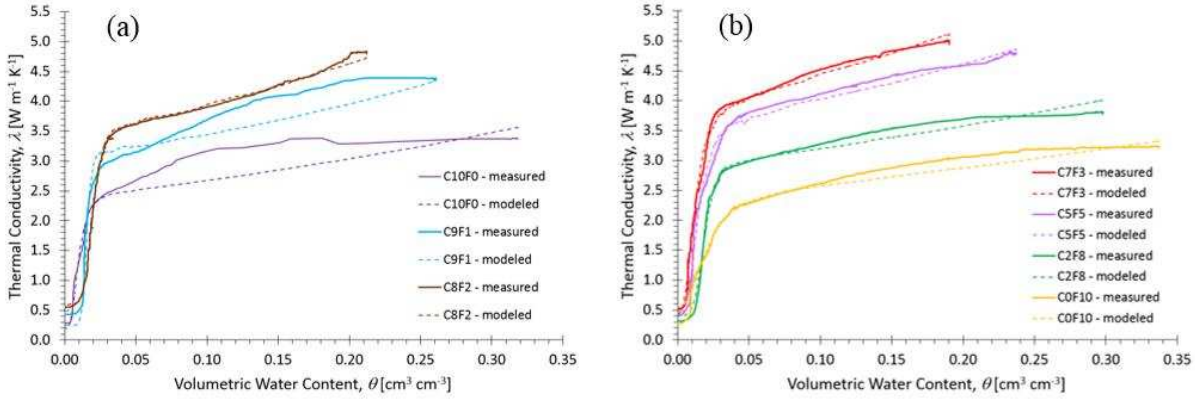

Figure 3.9. Comparison of measured to modeled thermal conductivity based on the Campbell model with all parameters determined empirically for (a) coarse-controlled mixtures and (b) fine-controlled mixtures.

Table 3.4. Campbell model parameters based upon empirically determined λ_m, x_{wo}, g_a and q_o obtained through calibration.

Sand	λ_m [W m^{-1} K^{-1}]	x_{wo} [m^3 m^{-3}]	g_a [-]	q_o [-]	F ratio
C10F0	17.33	0.011	0.272	3.52	1.02
C9F1	20.50	0.016	0.333	9.26	1.03
C8F2	8.42	0.023	0.110	6.66	1.02
C7F3	11.20	0.015	0.200	2.97	1.02
C5F5	12.44	0.018	0.448	3.16	1.03
C2F8	9.83	0.023	0.469	5.18	1.04
C0F10	7.29	0.034	0.485	2.73	1.00

The recently developed semi-empirical Lu and Dong model is a closed-form equation for the λ-θ relationship. The Lu and Dong model was demonstrated to accurately (R^2~98%) predict λ from saturated to dry for ambient conditions from 20-25 ^{o}C for 27 soils ranging from clay to silt to sand as compared to other models (e.g., Lu et al., 2007; Coté and Konrad, 2005) with a similar foundation (i.e., stemming from the Johansen (1975) model). The Lu and Dong model states:

$$\lambda = \lambda_{dry} + \left(1 - \left[1 + \left(\frac{\theta}{\theta_f}\right)^m\right]^{(1/m-1)}\right)\left(\lambda_{sat} - \lambda_{dry}\right) \tag{3.4}$$

where m is the pore fluid network connectivity parameter related to the pore-size parameter n in the van Genuchten (1980) model, and θ_f is the onset of funicular water content corresponding to the highest rate of change in water content between the pendular and hydration regimes. Both m and θ_f are fitting parameters with all other variables defined previously. For sandy soils, m values range between 1.4 and 2.9 and θ_f between 0.01 and 0.06 (Lu and Dong 2015). The best fit functional relationship for both parameters can be found by:

$$\theta_f = 1.84\theta_r \tag{3.5}$$

$$m = 3.0 - 0.2n \tag{3.6}$$

where θ_r is the residual volumetric water content and n is the van Genuchten (1980) empirical parameter that is dependent on the pore-size distribution. Both θ_r and n can be experimentally determined and are based upon the water retention behavior specific to each soil of interest.

The Lu and Dong model enables incorporation of experimentally determined hydraulic properties (θ_r and n) through Eqs. 3.5 and 3.6 as well as incorporation of experimentally determined thermal properties (λ_{sat} and λ_{dry}) to estimate λ for each binary mixture. As with the Campbell model, the Lu and Dong model's ability to incorporate characteristics that change specifically due to the soil mixing was evaluated. The parameters of the Lu and Dong model were obtained through experimental data (i.e., θ_r, λ_{sat} and λ_{dry}) and empirically determined properties (i.e., m). The use of all experimentally determined parameters results in statistically significant differences between measured and modeled λ for all binary mixtures except for C8F2 and C7F3 (F=1.02-3.96 with F_{crit}=1.11-1.15). The F ratio approaches the highest level of agreement between variances as the mixtures transition from the base sands (i.e., C0F10 and C10F0) towards f_{crit} (C7F3). As with the Campbell model, the modeled to experimental fit increases with use of the soil-specific empirically determined parameters (θ_f and m) as fitting parameters rather than using θ_r and m as in Eqs. 3.5 and 3.6. Using θ_f and m as fitting parameters, the variation of modeled λ of all binary mixtures compared to experimental λ are all within 7% agreement (F=1.03-1.07 with F_{crit}=1.11-1.15) as shown in Figure 3.10.

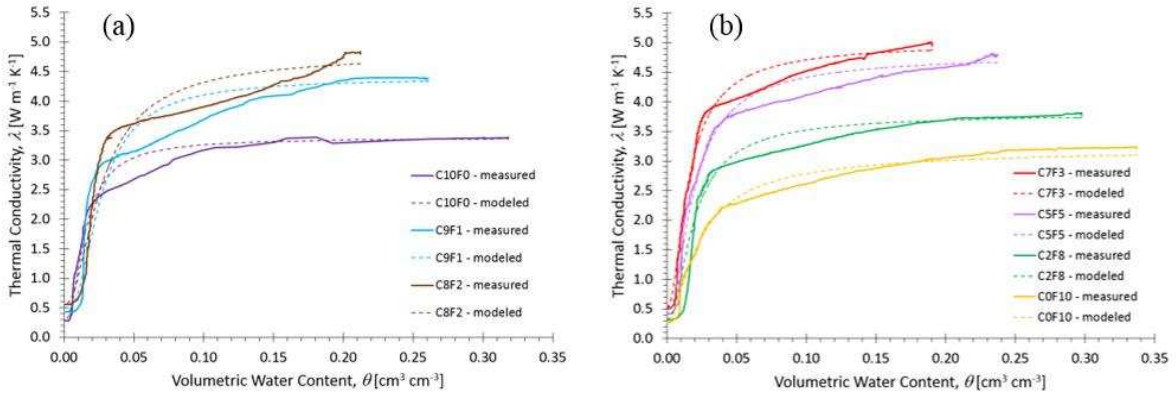

Figure 3.10. Comparison of measured to modeled thermal conductivity (λ) based on the Lu and Dong model using experimentally measured saturated and dry λ and empirically determined parameters (θ_f and m) for (a) coarse-controlled mixtures and (b) fine-controlled mixtures.

In an effort to further assess the Lu and Dong model's ability to incorporate physical properties of the binary mixtures, components of the Johansen (1975) model (hereafter referred to as the Johansen model) are incorporated into the Lu and Dong model. The Johansen model enables estimation of λ_{sat} and λ_{dry} with λ_{sat} determined using Eqs. 3.7 and 3.8 and λ_{dry} determined using Eq. 3.9 as:

$$\lambda_{sat} = \lambda_s^{1-\phi}\lambda_w^{\phi} \tag{3.7}$$

$$\lambda_s = \lambda_q^{q}\lambda_o^{1-q} \tag{3.8}$$

$$\lambda_{dry} = \frac{0.135\rho_b + 0.0647}{\rho_p - 0.947\rho_b} \tag{3.9}$$

where λ_s is effective thermal conductivity of soil solids, λ_w is thermal conductivity of water (0.594 W m^{-1} K^{-1} at 20^{o}C), λ_q is thermal conductivity of quartz (7.69 W m^{-1} K^{-1} as used in the Campbell model), q is quartz content of total solids, λ_o is thermal conductivity of other minerals (2.0 W m^{-1} K^{-1} for soils with q > 0.2), and all other variables previously defined. Use of Eq. 3.7 effectively

predicts λ_{sat} within an average of 6.8% for all mixtures and Eq. 3.9 predicts λ_{dry} within an average of 5.3% for all mixtures based upon the physical properties of the soils used to create the mixtures.

Evaluation of the Lu and Dong model proceeded next through incorporation of the same experimentally determined hydraulic properties (θ_r and n) through Eqs. 3.5 and 3.6. However, the thermal properties (λ_{sat} and λ_{dry}) were determined using the Johansen model through Eqs. 3.7 and 3.9 to estimate λ for each binary mixture. The use of the Johansen model yielded similar results to the Lu and Dong model with measured λ_{sat} and λ_{dry} (F=1.13-4.03 with F_{crit}=1.11-1.15). Only the predicted λ for the C8F2 mixture was not statistically different from the measured λ for all mixtures. Therefore, use of the Johansen model in conjunction with the Lu and Dong model or use of the Lu and Dong model independently with measured physical properties of the binary mixtures cannot properly predict λ-θ for binary mixtures. The Lu and Dong model was only able to effectively predict λ-θ for binary mixtures with the use of θ_r and m as fitting parameters. Additionally, the Lu and Dong model requires increased agreement in the low water content region to accurately capture the entire λ relationship from fully saturated to residual saturation.

3.6 Conclusions

This study generated thermal conductivity data for well-characterized binary mixtures under well-controlled conditions and investigated the impact of binary sand mixtures on thermal conductivity for the full range of saturation. The applicability and behavior of the Campbell and Lu and Dong models in predicting λ based upon those mixtures was also examined. Seven different mixing factions resulted in a wide range of ϕ. The obtained λ-θ relationships for seven tightly-packed mixtures varied significantly depending on the volume fraction of the fine particles and can be divided into two categories; fine- and coarse-controlled. Results demonstrate that λ–θ is

highly dependent on ϕ and that systematic changes in the volume fraction of fine particles also systematically changes λ. The change in ρ due to the fine fraction or percentage of fines associated with each mixture was shown to affect λ more significantly under saturated conditions with the effect diminishing in the hydration regime.

Binary mixtures with less than 30% fines exhibited coarse-controlled characteristics with a rapid rate of decrease in λ with a decrease in θ. Fine-controlled binary mixtures (percent fines $\geq$ 30%) portrayed a slower, more gradual rate of decrease in λ with a decrease in θ due to buffering capacity by more tortuous water pathways resulting from a decrease in large interconnected pore spaces as compared to coarse-controlled mixtures. However, these nuances between fine- and coarse-controlled binary mixtures are relatively small.

The Campbell model did not enable the incorporation of experimentally measured soil properties for the model parameters (F=1.41-7.50 with F_{crit}=1.11-1.15) but rather worked best when the parameters were fitted to experimental data (F=1.00-1.04 with F_{crit}=1.11-1.15). Similarly, the Lu and Dong model worked best when the physically based soil specific parameters were used as best fit parameters (F=1.03-1.07 with F_{crit}=1.11-1.15). Despite the fact that the models were able to capture the behavior for the binary mixtures when properly fitted with experimental data, model improvements are needed to capture the relationship focused on physically based soil parameters. Future work studying the effect of binary mixtures from a variety of soils with more grain sizes and at different temperatures is required to enhance our understanding of the impact of binary mixtures on λ.

3.7 Acknowledgements

This research was funded by the U. S. Army Research Office Award W911NF-04-1-0169, the Engineering Research and Development Center (ERDC), and the National Science Foundation (CMMI-1230544 and EAR-1447533). The authors wish to thank John Peters from ERDC for conversations that improved this research and L. Scott Baggett and William J. Massman from the USDA Forest Service whose careful review and comments significantly improved the manuscript.

3.8 References

Abramowitz, M., and I.A. Stegun. 1972. Handbook of mathematical functions. Dover Publications, Inc., New York.

Adivarahan, P., D. Kunli, and J.M. Smith. 1962. Heat transfer in porous rocks through which single phase fluids are flowing. Soc. Pet. Eng. J. 2(3):290-296. doi:10.2118/368-PA

Al Nakshabandi, G., and H. Kohnke. 1965. Thermal conductivity and diffusivity of soils as related to moisture tension and other physical properties. Agric. Meteorol. 2(4):271-279. doi:10.1016/0002-1571(65)90013-0

Becker, B.R., A. Misra, and B.A. Fricke. 1992. Development of correlations for soil thermal conductivity. Int. Communications in Heat and Mass Transfer. 19(1):59-68.

Bristow, K.L., G.J. Kluitenberg, and R. Horton. 1994. Measurement of soil thermal properties with a dual-probe heat-pulse technique. Soil Sci. Soc. Am. J. 58:1288-1294.

Bristow, K.L. 2002. Thermal conductivity. p. 1209-1225. *In* J.H. Dane and G.C. Topp (ed.) Methods of soil analysis. Part 4. Physical methods. SSSA Book Ser. 5, SSSA, Madison, WI.

Brooks, R.H., and A.T. Corey. 1964. Hydraulic properties of porous media: *Hydrol. Pap. 3*, Colo. State Univ., Fort Collins.

Bussing, W., and H.J. Bart. 1997. Thermal conductivity of unsaturated packed beds – comparison of experimental results and estimation methods. Chem. Eng. Process. 36(2):119-132. doi:10.1016/S0255-2701(96)04176-1

Campbell, G.S., 1985, Soil physics with BASIC. Elsevier, New York.

Campbell, G.S., J.D. Jungbauer, W.R. Bidlake, and R.D. Hungerford. 1994. Predicting the effect of temperature on soil thermal conductivity. Soil Sci. 158(5):307-313. doi:10.1097/00010694-199411000-00001

Carslaw, H.S., and J.C. Jaeger. 1959. Conduction of heat in soils. 2nd ed. Oxford Univ. Press, London.

Chen, S.X. 2008 Thermal conductivity of sands. Heat Mass Trans. 44(10):1241-1246. doi:10.1007/s00231-007-0357-1

Clarke, R.H. 1979. Reservoir properties of conglomerates and conglomeratic sandstones. AAPG bull. 63(5):799-803.

Clauser, C., and E. Huenges. 1995. Thermal conductivity of rocks and minerals. p. 105-126. *In* T.J. Ahrens (ed.) Rock physics and phase relations: A handbook of physical constants. Am. Geophys. Union, Washington, DC.

Côté, J., and J.M. Konrad. 2005. A generalized thermal conductivity model for soils and construction materials. Can. Geotech. J. 42(2):443-458. doi:10.1139/t04-106

Côté, J., and J.M. Konrad. 2009. Assessment of structure effects on the thermal conductivity of two-phase porous geomaterials. Int. J. Heat Mass Trans. 52(3-4):769-804. doi:10.1016/j.ijheatmasstransfer.2008.07.037

Decagon Devices. 2014. KD2 Pro thermal properties analyzer operator's manual, version 20 June 2014 – 09:11:40. Decagon Devices, Inc., Pullman, WA.

de Vries, D.A. 1963. Thermal properties of soils. In: W.R. van Wijk, editor, Physics of plant environment. North-Holland Publ. Co., Amsterdam. p. 210-235.

Durner, W. 1994. Hydraulic conductivity estimation for soils with heterogeneous pore structure. Water Resour. Res. 30(2):211-223.

Farouki, O.T. 1981. Thermal properties of soils (No. CRREL-MONO-81-1). Cold Regions Research and Engineering Lab Hanover NH.

Folk, R.L., and W.C. Ward. 1957. Brazos River bar: a study in the significance of grain size parameters. J. Sedimentary Petrology. 27:3-26.

Fragaszy, R.J., W. Su, and F.H. Siddiqi. 1990. Effects of oversize particles on the density of clean granular soils. Geotech. Test. J., 13(2):106-114. doi:10.1520/GTJ10701J

Garcia-Padron, R., D. Loyd, and S. Sjökvist. 2002. Heat and moisture transfer in wet sand exposed to solar radiation – models and experiments concerning buried objects. Subsurface Sensing Technologies and Applications. 3(2):125-150.

Garga, V.K., and C.J. Madureira. 1985. Compaction characteristics of river terrace gravel. J. Geotech. Eng. 111(8):987-1007. doi:10.1061/(ASCE)0733-9410(1985)111:8(987)

Gerke, H.H., and M.T. van Genuchten. 1993. A dual-porosity model for simulating the preferential movement of water and solutes in structured porous media. Water Resour. Res. 29(2):305-319. doi:10.1029/92WR02339

Haigh, S.K. 2012. Thermal conductivity of sands. Géotech. 62(7):617-625. doi:10.1680/geot.11.P.043

Hanks, R.J., H.R. Gardner, and M.L. Fairbourn. 1967. Evaporation of water from soils as influenced by drying with wind or radiation. Soil Sci. Soc. Am. Proc. 31(5):593-598. doi:10.2136/sssaj1967.03615995003100050001x

Hiraiwa, Y., and T. Kasubuchi. 2000. Temperature dependence of thermal conductivity of soil over a wide range of temperature (5-75ºC). Eur. J. Soil Sci. 51(2):211-218. doi:10.1046/j.1365-2389.2000.00301.x

Holtz, W.G., and C.W. Lowitz. 1957. Compaction characteristics of gravelly soils. Special Tech. Pub. No. 232, ASTM, Philadelphia, PA, 70-83.

Hopmans, J.W., and J.H. Dane. 1986. Thermal conductivity of two porous media as a function of water content, temperature, and density. Soil Sci. 143:187-195. doi:10.1097/00010694-198610000-00001

Horton, R., and P.J. Wierenga. 1984. The effect of column wetting on soil thermal conductivity. Soil Sci. 138(2):102-108.

Johansen, O. 1975. Thermal conductivity of soils. Ph.D. diss. Norwegian Univ. of Science and Technol., Trondheim (CRREL Draft Transl. 637, 1977).

Kaman, P.J., R.W. Ritzi, D.F. Dominic, and C.M. Conrad. 2007. Porosity and permeability in sediment mixtures. Groundwater. 45(4):429-438. doi:10.1111/j.1745-6584.2007.00313.x

Kluitenberg, G.J., J.M. Ham, and K.L. Bristow. 1993. Error analysis of the heat pulse method for measuring soil volumetric heat capacity. Soil Sci. Soc. Am. J. 57(6):1444-1451. doi:10.2136/sssaj1993.03615995005700060008x

Kluitenberg, G.J., K.L. Bristow, and B.S. Das. 1995. Error analysis of heat pulse method for measuring soil heat capacity, diffusivity, and conductivity. Soil Sci. Soc. Am. J. 59:719-726.

Knight, J.H., and G.J. Kluitenberg. 2004. Simplified computational approach for dual-probe heat-pulse method. Soil Sci. Soc. Am. J. 68:447-449. doi:10.2136/sssaj2004.0447.

Koltermann, C.E., and S.M. Gorelick. 1995. Fractional packing model for hydraulic conductivity derived from sediment mixtures. Water Resour. Res. 31(12):3283-3297. doi:10.1029/95WR02020

Larsson, M.H., and N.J. Jarvis. 1999. Evaluation of a dual-porosity model to predict field-scale solute transport in a macroporous soil. J. Hydrol. 215(1-4):153-171. doi:10.1016/S0022-1694(98)00267-4

Limsuwat, A., Sakaki, T., & Illangasekare, T. H. (2009). Experimental quantification of bulk sampling volume of ECH2O soil moisture sensors. *Proceedings of the 29th Annual American Geophysical Union Hydrology Days*, 25-27.

Lipiec, J., B. Usowicz, and A. Ferrero. 2007. Impact of soil compaction and wetness on thermal properties of sloping vineyard soil. Int. J. Heat Mass Trans. 50(19-20):3837-3847. doi:10.1016/j.ijheatmasstransfer.2007.02.008

Lu, N., and Y. Dong. 2015. Closed-form equation for thermal conductivity of unsaturated soils at room temperature. J. Geotech. Geoenviron. Eng., doi:10.1061/(ASCE)GT.1943-5606.0001295, 04015016.

Lu, N., and W.J. Likos. 2004. Unsaturated soil mechanics. John Wiley & Sons, Inc., Hoboken. p. 429-431.

Lu, S., T. Ren, Y. Gong, and R. Horton. 2007. An improved model for predicting soil thermal conductivity from water content at room temperature. Soil Sci. Soc. Am. J. 71(1):8-14. doi:10.2136/sssaj2006.0041

Martínez, P.L., L. van Kempen, H. Sahli, and D.C. Ferrer. 2004. Improved thermal analysis of buried landmines. IEEE Transactions on Geoscience and Remote Sensing. 42(9):1965-1975. doi:10.1109/TGRS.2004.831884

McCumber, M.C., and R.A. Pielke. 1981. Simulation of the effects of surface fluxes of heat and moisture in a mesoscale numerical model. J. Geophys. Res. 86:9929-9938. doi:10.1029/JC086iC10p09929

Midttømme, K., and E. Roaldset. 1998. The effect of grain size on thermal conductivity of quartz sands and silts. Pet. Geosci. 4(2):165-172. doi:10.1144/petgeo.4.2.165

Momose, T. and T. Kasubuchi. 2002. Effect of reduced air pressure on soil thermal conductivity over a wide range of water content and temperature. European J. Soil Sci. 53:599-606. doi:10.1046/j.1365-2389.2002.00474.x

Moradi, A., K.M. Smits, J. Massey, A. Cihan, and J. McCartney. 2015. Impact of coupled heat transfer and water flow on soil borehole thermal energy storage (SBTES) systems: experimental and modeling investigation. Geothermics. doi:10.1016/j.geothermics.2015.05.007

Motulsky, H.J., and L.A. Ransnas. 1987. Fitting curves to data using nonlinear regression: a practical and nonmathematical review. Federation Am. Soc. Exp. Biology J. 1:365-374.

Ochsner, T.E., R. Horton, and T. Ren. 2001. A new perspective on soil thermal properties. Soil Sci. Soc. Am. J. 65(6):1641-1647. doi:10.2136/sssaj2001.1641

Philip, J.R., and D.A. de Vries. 1957. Moisture movement in porous materials under temperature gradients. Trans. Am. Geophy. Union. 38(2):222-232. doi:10.1029/TR038i002p00222

Sakaguchi, I., T. Momose, and T. Kasubuchi. 2007. Decrease in thermal conductivity with increasing temperature in nearly dry sandy soil. Eur. J. Soil Sci. 58(1):92-97. doi:10.1111/j.1365-2389.2006.00803.x

Sakaguchi, I., T. Momose, H. Mochizuki, and T. Kasubuchi. 2009. Heat pipe phenomenon in soil under reduced air pressure. Eur. J. Soil Sci. 60(1):110-115. doi:10.1111/j.1365-2389.2008.01095.x

Sakaki, T., and T.H. Illangasekare. 2007. Comparison of height-averaged and point-measured capillary pressure-saturation relations for sands using a modified Tempe cell. Water Resour. Res. 43(12):W12502. doi:10.1029/2006WR005814.

Sakaki, T., A. Limsuwat, K.M. Smits, and T.H. Illangasekare. 2008. Empirical two-point α-mixing model for calibrating the ECH2O EC-5 soil moisture sensor in sands. Water Resour. Res. 44(4):W00D08. doi:10.1029/2008WR006870

Sakaki, T., A. Limsuwat, and T. H. Illangasekare. 2011. A simple method for calibrating dielectric soil moisture sensors: Laboratory validation in sands, Vadose Zone J. 10:526-531, doi:10.2136/vzj2010.0036

Sakaki, T., and K.M. Smits. 2015. Water retention characteristics and pore structure of binary mixtures. Vadose Zone J. 14(2). doi:10.2136/vzj2014.06.0065.

Schroth, M.H., J.D. Istok, S.J. Ahearn, and J.S. Selker. 1996. Characterization of Miller-similar sands for laboratory hydrologic studies. Soil Sci. Soc. Am. J. 60:1331-1339.

Sepaskhah, A.R., and L. Boersma. 1979. Thermal conductivity of soils as a function of temperature and water content. Soil Sci. Soc. Am. J. 43(3):439-444. doi:10.2136/sssaj1979.03615995004300030003x

Skaggs, R.W., and E.M. Smith. 1968. Apparent thermal conductivity of soil as related to soil porosity. Soil Sci. Soc. Am. Proc. 38:504-507. doi:10.13031/2013.39451

Smits, K.M., T. Sakaki, A. Limsuwat, and T.H. Illangasekare. 2010. Thermal conductivity of sands under varying moisture and porosity in drainage-wetting cycles. Vadose Zone J. 9(1):172-180. doi:10.2136/vzj2009.0095

Smits, K.M., T. Sakaki, S.E. Howington, J.F. Peters, T.H. Illangasekare. 2013. Temperature dependence of thermal properties of sands across a wide range of temperatures (30-70oC). Vadose Zone J. doi:10.2136/vzj2012.0033

Spiess, A.N., and N. Neumeyer. 2010. An evaluation of R2 as an inadequate measure for nonlinear models in pharmacological and biochemical research: a Monte Carlo approach. BMC Pharmacology. 10:6. doi:10.1186/1471-2210-10-6

Tarnawski, V.R., and F. Gori. 2002. Enhancement of the cubic cell soil thermal conductivity model. Int. J. Energy Res. 26(2):143-157. doi:10.1002/er.772

Tarnawski, V.R., and W.H. Leong. 2000. Thermal conductivity of soils at very low moisture content and moderate temperatures. Transp. Porous Media. 41(2):137-147.

Tarnawski, V.R., and W.H. Leong. 2012. A series-parallel model for estimating the thermal conductivity of unsaturated soils. Int. J. Thermophys. doi:10.1007/s10765-012-1281-1

Tarnawski, V.R., W.H. Leong, and K.L. Bristow. 2000. Developing a temperature-dependent Kersten function for soil thermal conductivity. Int. J. Energy Res. 24(15):1335-1350. doi:10.1002/1099-114X(200012)24:15<1335::AID-ER652>3.0.CO;2-X

Tarnawski, V.R., M.L. McCombie, T. Momose, I. Sakaguchi, and W.H. Leong. 2013. Thermal conductivity of standard sands. Part III. Full range of saturation. Int. J. of Thermophys. 34(6):1130-1147. doi:10.1007/s10765-013-1455-6

Tavman, I.H. 1996. Effective thermal conductivity of granular porous materials. Int. Commun. Heat Mass Transfer. 23(2):169-176. doi:10.1016/0735-1933(96)00003-6

Terzaghi, K. 1952. Permafrost. J. Boston Soc. Civil Eng. 39:1-50.

Usowicz, B., J. Kossowski, and P. Baranowski. 1996. Spatial variability of soil thermal properties in cultivated fields. Soil Tillage Res. 39(1-2):85-100. doi:10.1016/S0167-1987(96)01038-0

van Genuchten, M.T. 1980. A closed-form equation for predicting the hydraulic conductivity of unsaturated soils. Soil Sci. Soc. Am. J. 44(5):892-897.

Van Rooyen, M., and H.F. Winterkorn. 1959. Structural and textural influences on thermal conductivity of soils. High Res. Board Proc. 39:576-621.

Westman, A.E.R., and H.R. Hugill. 1930. The packing of particles. J. Am. Ceramic Soc. 13(10):767-779. doi:10.1111/j.1151-2916.1930.tb16222.x

Yadav, M.R., and G.S. Saxena. 1977. Thermal characteristics of the soils in relation to their physical parameters and moisture content. J. Indian Soc. Soil Sci. 25:1-6.

Zimmerman, R.W., G. Chen, T. Hadgu, and G.S. Bodvarsson. 1993. A numerical dual-porosity model with semianalytical treatment of fracture/matrix flow. Water Resour. Res. 29(7):2127-2137. doi:10.1029/93WR00749

CHAPTER 4 ESTIMATING SOIL WATER EVAPORATION: AN INTERCOMPARISON OF ENERGY BALANCE, WATER BALANCE AND WATER FLUX BASED MODELS USING LABORATORY MEASUREMENTS OVER BARE AND VEGETATED SURFACE

As with Chapter 3, prior to any discussion regarding the specifics of this chapter, the intellectual contribution of this portion of the research is specified along with identification of the author's contribution to the work. This research increases knowledge in the field of research regarding analysis of evaporation models and their applicability for use at the laboratory bench scale. Although there have been many studies comparing the performance of different evaporation models, a comparison for the purpose of selection based upon input approach (i.e., surface and free flow, porous and free flow mediums, or strictly porous medium) was not identified. Therefore, four different energy and water balance methods used to determine evaporation from soil were compared. Four different experiments were performed that included varying boundary and initial conditions as well as soil surface conditions enabling comparison between measured evaporation and evapotranspiration with modeled rates. The methods vary in their ability to capture atmospheric versus diffusion dominated evaporative stages. Specific contributions included identifying that although no one method is applicable for all boundary and initial conditions, the sensible heat balance and heat pulse (SHB+HP) method (Heitman et al., 2008a; Trautz et al., 2014; Xiao et al., 2014) enabled the highest level of agreement between measured and modeled evaporation from bare soil experiments. This finding is significant because the SHB+HP method is directly applicable to large field experiments as well as laboratory experiments. Additionally, the ability of the SHB+HP method to isolate evaporation under evapotranspiration conditions has the potential to isolate transpiration which is significant for many agricultural applications as well

as modeling efforts. It is important to not extend these finding too generously to all soil mixtures. The disclaimer is that these findings do apply to poorly graded, well sorted sand of high quartz content (>98%) both with bare soil and vegetated surface conditions. All experimental and analytical work was completed by the author of this dissertation. The experimental work enabled direct comparison of modeled evaporation. Additional work by the author, involved developing a user's guide for all sensors used in all experiments. These user guides were made available to all members of the CESEP research group and are listed in Appendix A. A laboratory procedure was developed to determine the effective radius of each individual heat pulse probe used in the experiments and that procedure is included in Appendix B.

4.1 Abstract

Evaporation is a key component of land surface models and general circulation models used to explore climate change, predict weather, and influence water management policies. In field and laboratory studies, remotely sensed and in-situ thermal and soil moisture data are often used to estimate evaporative fluxes based upon a variety of different water and sensible energy balance formulations. Although many methods are available, to date there is no standardized approach for determining evaporation. Identical atmospheric forcing terms can be applied to different modeling approaches, yielding widely varying estimations of evaporation. Comparison of these methodologies has only been performed for field data which inherently have a high degree of uncertainty. The purpose of this work is to compare different methods used to quantify evaporative fluxes based on remotely sensed and in-situ temperature and soil moisture data under carefully controlled laboratory conditions. A series of laboratory experiments were performed under ambient and elevated atmospheric air temperatures for homogeneous soil packing configurations with bare and grass covered soil in a two dimensional soil tank interfaced with a wind tunnel

apparatus. The soil tank and wind tunnel were outfitted with a suite of sensors that measured wind speed, relative humidity, air and soil temperature, soil moisture, and weight. Air and soil temperature measurements were obtained using infrared thermography, heat pulse sensors and thermistors. Data collected from these sensors were in turn used in five different analytical energy balance models. Outputs were compared directly with evaporation rate data determined through weight scale measurements in a direct water balance approach. Results demonstrate the applicability of different methods under varying surface boundary conditions to predict behavior and rates during the two stages of evaporation. The in-situ combined heat-pulse and sensible heat balance method provided the best prediction of evaporation under bare soil conditions with the other methodologies showing varying degrees of agreement. This ability of this method to isolate evaporation under evapotranspiration conditions has the potential to identify transpiration occurring which is significant for many agricultural applications as well as modeling efforts. Additional analysis showed that sampling frequency significantly impacts each method's ability to capture evaporation. These findings can be used in future laboratory and field scale evaporative studies to help guide the selection of the most appropriate energy balance method based on available data.

4.2 Introduction

The ability to accurately evaluate evaporation is increasingly important as the effects of climate change become more apparent. Models used on the global scale (e.g., global climate models (GCMs)) required a variety of inputs to properly account for mass and energy transfer within soils, canopies, and the atmosphere. From the multitude of methods available to determined evaporation, many are compared against other models or lysimeters placed in the field.

In the absence of vegetation, evaporation occurs entirely from the soil. It is a process that can lead to considerable water losses on the order of 30% to 75% depending on the geographic location and climate conditions (Peters, 1960; Riou, 1977; Floret et al., 1982; Cooper et al., 1987; Stewart and Burnett, 1987). With respect to agricultural applications, these areas often remain bare for the majority of the year due to both farming activity and crop rotation. This includes periods of tillage, planting, germination and early growth where the soil is effectively bare (Hillel, 1998). Understanding soil water evaporation (*E*) is critical for the long term health and growth of vegetation as evaporation can rapidly decrease the water in the vicinity of seedlings during one of the most critical stages in plant maturity. Understanding *E* is also important for sparse crops to include orchards and vineyards, in which the soil is oftentimes kept bare around the trees and vines. Methods are needed to quickly asses the variability of evaporation and resulting moisture status in fields to improve the uniformity of water use (Ben-Asher et al., 1983). Proper planning of cropping systems and irrigation management depends on accurately accounting for evaporation as a component of the field water budget (Xiao et al., 2014).

For vegetated surfaces, *E* has been shown to act as a regulator for transpiration (*T*) by enhancing (Kustas and Agam, 2013) or suppressing (Tolk et al., 1995) *T* to improve irrigation efficiency. Understanding separate estimates of *E* is applicable to evapotranspiration (*ET*) partitioning studies and validating remote sensing models of *ET*. In addition to agricultural applications, bare soil evaporation is relevant to natural environments, especially considering the increase of water limited environments throughout the world and their potential for expansion over the coming years (Newman et al., 2006). The ability to properly assess and predict moisture in soil due to evaporation processes is important to a variety of other research areas some of which include landmine detection (e.g., Das et al., 2001; Ratto et al., 2011; Smits et al., 2012) and coupled heat

transfer and water flow on soil borehole thermal energy storage systems (e.g., Moradi et al., 2015) to name a few.

For evaporation to occur, there must be three conditions present (Jones, 1991). First, a continual heat supply is needed to fulfill the requirements for latent heat of vaporization. This heat can be supplied externally from radiation or advected energy or internally from the soil itself (Hillel, 1998). Secondly, there must be a gradient in vapor pressure between the atmosphere and the soil and third, a supply of water. The rate of evaporation is determined based on the combination of the conditions present and oftentimes described in stages (Idso et al., 1974). Stage I evaporation occurs during a period of high, relatively constant evaporation rate based upon atmospheric demand in which a primary drying front is established (Lehmann et al., 2008). Transition occurs to a vapor diffusion limited Stage II evaporation rate which is indicative of a much lower evaporation rate due to supplied liquid water becoming limited (Or et al., 2012).

Evapotranspiration (*ET*) occurs in conjunction with the stages of evaporation due to the fundamental relationship that $ET = E + T$. There are a number of methods available to determine system level *ET* to include remote sensing and ground based methods; however, very few techniques exist to independently determine *E*, especially for under canopy *E* as shown by Holland et al. (2013) and Kool et al. (2014). In terms of *ET*, there are three comprehensive literature reviews from Glenn et al. (2007), Kalma et al. (2008) and Li et al. (2009) that summarize the advantages, limitations, errors and uncertainties in many of the different methods. However, as pointed out by Kool et al. (2014), no single model exists for independently estimating *E* and therefore models simulate combined *E* and *T*. Although some of these methods can then be used to partition the contribution of *E* and *T* or in the case of bare soil, the models can be used without employing *T*, validation of *E* is difficult. In addition, methods vary in their ability to capture evaporative stages.

For example, some methods are applicable over the entire range of evaporation (e.g., Ben-Asher et al., 1983) while others are only applicable for evaporation from wet (e.g., Blight, 2002) or dry (e.g., Lascano et al., 1987) soils.

Methods that can be used to estimate *E* include direct methods such as micro-lysimeters and soil moisture balance methods and indirect methods such as micrometerological, deterministic, empirical and remote sensing approaches. Although direct methods provide good estimates of evaporation, they are often timely to install in the field (Trambouze et al., 1998), not feasible for large scale use (Daamen and Simmonds, 1996), and can require manual weighing (in the case of a lysimeter). Therefore, the use of indirect methods such as micrometerological methods via flux tower measurements (e.g., eddy covariance (EC) method (Brutsaert, 1982) and Bowen ratio (Bowen 1926; Brutsaert, 1982)) are often employed. These methods rely on the measurement of many parameters to include air temperature, CO_2, moisture content of air at two heights, wind speed, etc. over an area having adequate fetch (~200 – 1000m, depending on the crop size) and have high estimates of uncertainty (15-30%) (Glenn et al., 2007; Kalma et al., 2008). Micrometerological methods are advantageous in that they take continuous measurements over wide areas but cannot be used to determine *E* separate from *ET*. In addition, most methods use meteorological data at 2m screening heights to determine the atmospheric demand. However, this is not indicative of the conditions under-canopy or at the soil surface and often results in wrong estimations of *E*.

Evaporation can be quantified in three different ways (1) determining the amount of latent heat in a system using an energy balance, (2) by determining the removal of liquid water from a system using a water balance or (3) by assessing the water vapor fluxes (Kool et al., 2014).

First, the surface energy balance (SEB) is defined as:

$$R_n - LET - H - G + \Delta S = 0 \quad (4.1)$$

where R_n is net radiation (incoming minus outgoing long and short wave radiation), L is the latent heat of vaporization (J kg^{-1}), H is the sensible heat flux from the surface to the atmosphere, G is the soil heat flux, ΔS is the physical energy stored (all in units of W m^{-2} unless otherwise specified).

Most methods that involve the surface energy balance calculate ET as the residual for Eq. 4.1, once H, G and R_n are determined through a combination of both remote sensing and ground based measurements. R_n is determined by subtracting the incoming from the outgoing long and short wave radiation. G is generally only 5-10% of R_n for vegetated surface and it can be between 30-50% for bare soil (Choudhury et al., 1986). However, over a diurnal 24hr cycle, G is usually zero and hence many ET models ignore G. The most difficult term to obtain is H as it is the most difficult to measure or estimate. The heat flux is usually estimated from the difference in temperature between the soil surface and the atmosphere at some reference height above the surface. However, the height selected could have a significant impact on H when calculating it for bare soil or under canopy.

Another issue in determining H includes difficulties in temporal and spatial scaling issues such as instantaneous estimates of H (and ultimately ET) to daily or longer time steps (Glenn et al., 2007). Kalma et al. (2008) noted that improved temporal scaling procedures are needed to extrapolate instantaneous estimates of temperature that are recorded via remote sensing (IR imagery). For example, longer time periods and gap-filling procedures are needed when the temporal scaling is affected by intermittent coverage from satellites. One option for this is using data fusion approaches (e.g., use the IR data along with soil surface temperature measurements).

Spatial scaling is also an issue. Formulations require being compared with data at different scales prior to implementation in meteorological models (Ge et al., 2015).

The energy balance shown in Eq. (4.1) has a complementary water balance. Evaporation can be quantified in three different ways (1) by determining the removal of liquid water from a system using a water balance (2) determining the amount of latent heat in a system using an energy balance or (3) by assessing the water vapor fluxes (Kool et al., 2014). The water balance is the sum of inputs and outputs to the defined system:

$$P + I - R_{off} - D - \Delta S - ET = 0 \quad (4.2)$$

where P is precipitation, I is irrigation, R_{off} is runoff, D is drainage or deep percolation and ΔS is change in soil storage and ET is the evaporated mass (all in units of mm d^{-1}). The water balance is only practical to estimate ET when ET is large as small measurement errors of components can cause large errors in ET (Hillel, 1998).

A water balance using soil moisture data is possible as described in (Hillel, 1998). It is important to note that the energy balance of a soil surface depends significantly on its water content (Ben-Asher et al., 1983). Using soil moisture measurements in the top 15 cm of soil, one can calculate the water loss from the system and hence evaporation rate over time by applying mass balance to convert changes in soil moisture to estimates of E fluxes from the respective layers/system through applying Eq. (4.2). Note that ΔS is a measure of the water gain or loss from the soil storage within the top 15 cm below ground surface (bgs) as obtained from soil moisture measurements. With all other aspects of Eq. (4.2) determined, it is possible to calculate ET.

Although the water balance does provide a means to determine ET, there are literally hundreds of other models employed to determine ET. Many methods rely on a single process (e.g., Bowen ratio energy balance) or single variable (e.g., temperature). Error associated with single

inputs could be overcome through independent observations of both water and energy cycle variables rather than relying on a single-process or single-variable (McCabe et al., 2008). For example, when using both lysimeters and meteorological data, error decreases significantly (to about 10%) compared to using one of the methods alone (McCabe et al., 2008). Developing and testing approaches that combine both energy and water balance components may decrease the error or uncertainty associated with current prediction methods. One such method is the energy and water balance methods (Lascano et al., 1987).

A few methods that have shown promise to understand *E* separate from *ET* are summarized in Table 4.1 and include sensible heat balance measurements combined with the soil heat pulse method (Heitman et al., 2008a; Trautz et al., 2014; Xiao et al., 2014), the micro Bowen ratio energy balance (Ashktorab et al., 1989; Holland et al., 2013), a relative evaporation method developed by Ben-Asher et al. (1983), and an energy and water balance model developed by Lascano et al. (1987). These methods incorporate approaches that require measurements from the surface and atmosphere or below the surface and some that require measurements from both below the surface and the surface and atmosphere. These methods were selected over the variety of models available because they were proven in various studies to more accurately estimate evaporation compared to other methods and because they incorporate easily measured parameters (see Table 4.1). Additionally, the fact that these methods required inputs from different mediums enables the potential identification of the suitability of different methods to perform better based upon a comparison between the methods under different surface and boundary conditions Each of these four methods comprise the four methods used in the analysis as part of this research which will be described below.

The sensible heat balance and heat pulse (SHB+HP) approach allows for the continuous measurement of soil water evaporation. In this approach, the measured temperature at two depths and the change in heat storage between these depths are used to compute a heat balance for a soil layer. The latent heat flux with the soil layer (i.e., *E*) is computed based on the residual to the heat balance. This method has shown good results in both field (e.g., Heitman et al., 2008a; Sakai et al., 2011; Xiao et al., 2011, 2012, 2014) and laboratory (Deol et al., 2012; Trautz et al., 2014) studies. The limitation of this method is that it oftentimes does not yield good results for Stage I evaporation conditions (Heitman et al., 2008a; Deol et al., 2012). Xiao et al. (2014) recently showed the applicability of this method to *E* beneath a maize canopy, demonstrating the ability of the method to determine *E* in the presence of vegetation.

Table 4.1. Evaporation methods selected for comparison and evaluation.

Evaporation Model	Nomenclature	Reference	Comments
Sensible Heat Balance and Heat Pulse Method	SHP+HP	Heitman et al., 2008a; Sakai et al., 2011; Xiao et al., 2014; Trautz et al., 2014	Enables determination of *E* only
Micro Bowen Ratio Energy Balance	M-BREB	Ashktorab et al., 1989; Holland et al., 2013	Applicable to determine *ET* (grass covered soil) and *E* (bare soil)
Soil Temperature Difference	TD	Ben-Asher et al., 1983	Applicable to determine of *ET* and *E*
Energy and Water Balance	ENWATBAL	Lascano et al., 1987	Applicable to determine of *ET* and *E*

Holland et al. (2013) summarized a micro Bowen ratio energy balance (M-BREB) succinctly as a scaled down version of a Bowen ratio system that is designed to measure small footprints (2.7 m interrow). Like the Bowen ratio method, model inputs include differences in water vapor concentration and air temperature at two heights above the soil surface at 1 and 6 cm.

Ashktorab et al. (1989) successfully tested the M-BREB method over bare soil, demonstrating the method's applicability to under-canopy *E* estimates. Zeggaf et al. (2008) showed the potential of M-BREB to provide *E* separately from canopy *T* for a full canopy cover of corn crops. The technique was more recently tested in sparse canopy conditions (i.e., vineyard) by Holland et al. (2013) who compared M-BREB estimates to field microlysimeter tests demonstrating good agreement for *ET* associated with grass covered soil (R^2=0.99) and bare soil (R^2=0.89).

The relative evaporation (*RE*) method or temperature difference (*TD*) method developed by Ben-Asher et al. (1983) is an energy balance model in which *E*T or *E* (depending on surface boundary conditions – vegetated or bare soil) is estimated using soil surface temperature measurements, air temperature, and wind speed. The daily minimum and maximum temperatures of the soil surface are compared to the daily minimum and maximum temperature of a saturated and dry soil surface. This method was successfully tested by Ben-Asher et al. (1983) using lysimeters and in a drip irrigated vineyard by Kerridge et al. (2013) under light wind conditions where measured soil evaporation and calculated soil evaporation were in agreement (R^2=0.74).

The energy and water balance model described by Lascano et al. (1987) was developed to compute water and energy balances both at the soil surface and at the plant canopy. This method addresses the need to compare both energy and water balances for validation. Inputs to the model include: soil (water retention, hydraulic conductivity, number and thickness of soil layers, initial temperature and water content), plant (leaf conductivity, water potential, root area with time, depth and leaf area index with time), and climate (solar radiation, air temperature, humidity, precipitation and irrigation). Lascano et al. (1987) tested the model in the field (row crops) and model results were within 1 standard deviation of measured values (measured with microlysimeters). They

concluded that the model is a reliable method (measured *E* within 7% for dryland and *ET* within 8% for irrigated land), especially in semiarid areas similar to those used in their study. This method has been shown to produce good agreement in a cotton field (Lascano et al., 1987) and sorghum (Qui et al., 1999) but has problems of slight underestimation of *ET*, which may be due to the development of a dry soil layer in arid dry conditions which introduces errors in the surface temperature and energy balance calculations (Kool et al., 2014).

The purpose of this research is to evaluate the ability of different energy and water balance methods to determine evaporation based on varying boundary and initial conditions. Four models were selected from literature that vary in their input requirements and are relevant to determining under-canopy and bare soil *E* and *ET*. Model performance was compared with a series of four laboratory scale experiments. Experiments varied in their climate, soil and surface conditions to include of surface cover (vegetated vs bare), wind speed (0.25-1.05 m s^{-1}), temperature (18-45^{o}C), and water table conditions. A secondary objective of this research was to evaluate temporal scaling issues associated with the use of data collected for estimating evaporation, especially thermal remotely sensed data.

Research presented herein compares the four selected evaporation models (Table 4.1) with lysimeters measured response to varying environmental and surface conditions using controlled experiments. First, the material and methods used to generate the experimental data is discussed. Then, experimental results are provided and analyzed as a function of the different boundary conditions. Next, the fundamental concepts of the four models selected are presented. Finally, the experimental and modeled results are compared with key findings discussed.

4.3 Material and Methods

In this section, the experimental apparatus is described. This is followed by providing information regarding sand and vegetation materials, and concludes with the experimental procedure.

4.3.1 Experimental Apparatus

Three different two-dimensional soil tanks were constructed. Two with an internal length, width, and height of 45, 9, and 30 cm (hereafter referred to as Tank 1 and Tank 2) and one with an internal length, width, and height of 25, 9.1, and 55 cm respectively (hereafter referred to as Tank 3). All were built out of 1.2 cm thick acrylic (specific heat, 1464 J kg^{-1} K^{-1}; thermal conductivity, 0.2 W m^{-1} K^{-1}). Tank 1 and Tank 2 were interfaced with the same open-ended wind tunnel (hereafter referred to as Wind Tunnel 1) constructed out of galvanized steel ducts with an upstream length of 1.82 m and a downstream length of 2.71 m. Tank 1 and Tank 2 along with the interface associated with Wind Tunnel 1 are shown in Figure 4.1.

A series of three 4 ft T5 high output fluorescent light bulbs (6,000 initial lumens and a color temperature of 4800 K) were mounted in parallel above Wind Tunnel 1 and provided representative solar radiation in an amount sufficient for biological growth. The light source (96-watt HydroFarm FLP24) was mounted 83.5 cm above the soil surface. The bulbs were cycled on and off for 12-hour periods (8 a.m. to 8 p.m.) enabling replication of the diurnal cycle.

Tank 3 was connected to a wind tunnel on both the upstream and downstream boundaries with an open-ended wind tunnel (Figure 5.). As with the wind tunnel associated with the dual tank set up (Figure 4.1), the wind tunnel established with Tank 3 (hereafter referred to as Wind Tunnel 2) was constructed out of the same material with the dimensions shown in Figure 5.2. Air flow through both wind tunnels occurred by inducing an air current via a 15.2 cm diameter Pro DB6GTP

in-line duct fan (Suncourt, Inc.; USA). This fan was located downstream and the air speed being induced across the surface of the tank was controlled by a VS200 variable speed controller (Suncourt, Inc.; USA). The wind speed induced across the surface was measured using a 167-12 stainless steel pitot-static tube (Dwyer Instruments, Inc.; USA, accuracy of ± 5%). Code written by Dr. Andrew Trautz enabled data collection using a CR1000 (Campbell Scientific; USA) data logger interfaced with a computer and downloaded using a PC200W program. Data was collected every 60 minutes. Five Infrared Salamander Model FTE 500-240 ceramic radiative heaters (Mor Electric Heating Assoc., Inc.; USA) were connected to the upstream base of Wind Tunnel 2 (Figure 4.2) in order to enable a continuously heated air stream or diurnal heating based upon experimental needs. An infrared temperature sensor (Exergen Corporation; USA) enabled regulation of the climate conditions (i.e., temperature) through interfacing with a 2104 temperature control system (Chromalox; USA).

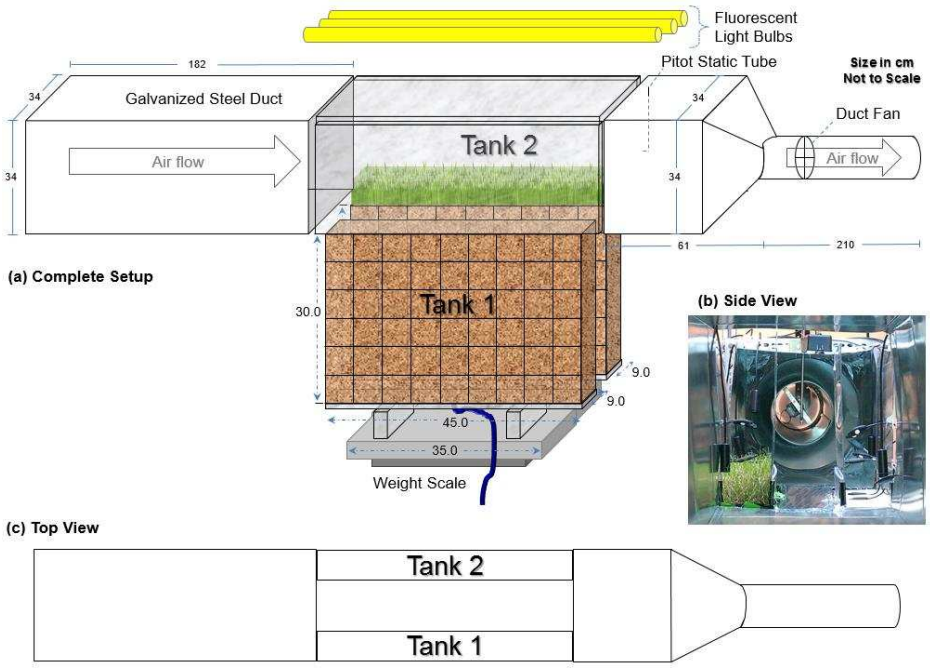

Figure 4.1. Sketch of Tank 1 and Tank 2 interfaced with Wind Tunnel 1 providing a side view and top view of the experimental apparatus.

Tank 1, 2 and 3 were outfitted with sensors installed horizontally at 5 cm increments for measuring soil moisture, temperature, thermal properties, and relative humidity across the width of the tanks and down to a depth of 22.5 cm from the soil surface. All measurements occurred at an interval of 60 minutes and data was stored on Em50 5-channel data loggers (Decagon Devices, Inc.; USA) for easy retrieval. EC-5 dielectric soil moisture sensors (Decagon Devices, Inc.; USA, accuracy = ± 3%) enabled calculation of soil moisture throughout the tank. The two-point α-mixing model developed by Sakaki et al. (2008) enables conversion of an analog-to-digital converter number (ADC count) as recorded by the EC-5 into a volumetric water content. ECT sensors (Decagon Devices, Inc.; USA, accuracy = ± 1 °C) enabled measurement of subsurface temperature and atmospheric temperature at 8.5 cm above the surface for Tank 3.

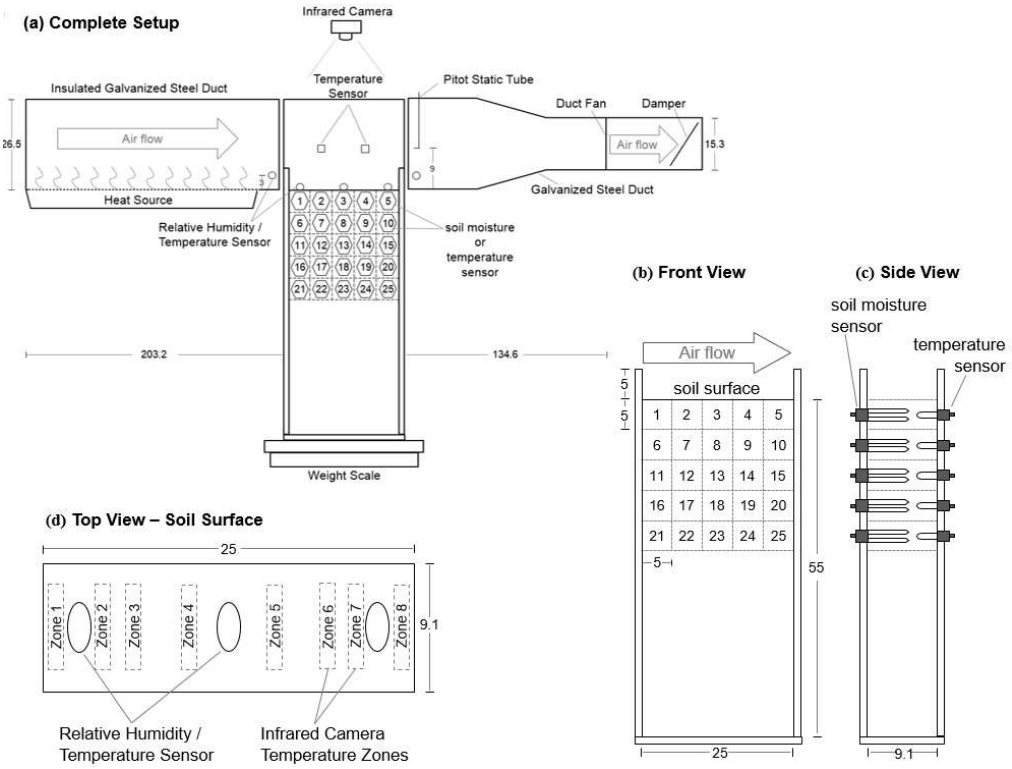

Figure 4.2. Sketch of Tank 3 interfaced with Wind Tunnel 2 providing a side view, top view, and view of primary instrumentation locations similar for all tanks. Tank is used with bare soil.

Thermal property SH-1 sensors (Decagon Devices, Pullman, WA; dual needle, length = 3 cm, spacing = 6 mm, ± 10% accuracy from 0.2 to 2 W m^{-1} K^{-1} for λ, ± 0.001 ^{o}C for temperature) connected to a KD2 Pro™ thermal property analyzer were used to measure thermal conductivity λ (W m^{-1} K^{-1}) and soil temperature (^{o}C) within each soil tank and soil type across (i.e., tightly packed, loosely packet, disturbed mixture, top coarse soil, and fine overlain soil. Soil thermal measurements were made at 60 minute intervals to allow thermal gradients to dissipate. The SH-1 sensor consists of two needles containing a thermistor in one needle and a heating element in the other. A current is passed through the heating element in one needle while the time dependent temperature response is monitored over time in the second needle. A dual needle algorithm (Abramowitz and Stegun, 1972) based on the line heat source analysis described in Carslaw and Jaeger (1959) and Kluitenberg et al. (1993) along with the temperature measurements and knowledge of the heat generated (~22.3 W m^{-1}) during heating (1 min) and cooling cycles (1 min) was used to calculate the λ of the soil (Decagon Devices, 2014).

Heat pulse sensors based upon Heitman et al. (2008) design were emplaced in each tank. The sensor consists of three needles, each containing a thermistor, with the middle needle containing a resistive heater for generating heat pulses connected into an epoxy body. The automatic measurements were made every 60 minutes and written directly to file using LabVIEW software (National Instruments Corp.; USA).

EHTs (Decagon Devices, Inc.; USA, temperature accuracy = ± 1 °C, relative humidity accuracy = ± 3% between 5 and 100%) enabled measurement of both relative humidity and temperature. Sensor were placed in firm contact with the surface, above the soil surface, and in Wind Tunnel 1 and 2 at locations upstream and downstream.

VP-3s (Decagon Devices, Inc.; USA, temperature accuracy = ± 0.3 °C, relative humidity accuracy = ± 2% to 3% based upon temperature and RH) were used to simultaneously measure relative humidity and temperature directly. The sensors were located in the influent and effluent air streams for Wind Tunnel 1 and 2.

An additional source used to obtain surface temperatures was a 320×240 pixel resolution Model 7320 infrared camera (Infrared Cameras, Inc. (ICI); USA, spectral range = 7-14 μm, accuracy = ± 1^{o}C). The software (ICI; USA) that comes with the camera instantaneously applies corrections for transmission, reflection, and emissivity. Beyond the IR camera, a PowerShot Se IS digital camera (Canon; USA) was used to monitor the propagation of the drying front via CameraWindow software (Canon; USA).

Tanks 1, 2, and 3 were placed on a separate 65 kg ± 1 g Model 11209-95 weighting scale (Sartorius Corp.; USA). The measurements were transcribed onto a dedicated computer through LabVIEW software (National Instruments Corp.; USA). The weight measurements were used in a mass balance to determine evaporation rates.

4.3.2 Sand and Vegetation Materials

The same sand was used for all three tanks which was Accusand #30/40 (Accusands, Unimin Corps.; USA, mean grain size = 0.420 to 0.595 mm, uniformity coefficient = 1.2, particle density = 2.65 g cm^{-3}, grain shape = rounded, mineralogical composition = 99.8% quartz). Other select properties of the #30/40 sand are provided in Table 4.2.

Table 4.2. Sand properties for #30/40 Accusand.

					Thermal Conductivity	
Dry Bulk Density ρ (g cm-3)	Air Entry Pressure* h_d (cm H_2O)	Residual Water Content** θ_r (m^3 m^{-3})	van Genuchten Model Parameters*** α (cm^{-1})	n (-)	Dry λ_{dry} (W m^{-1} K^{-1})	Saturated λ_{sat} (W m^{-1} K^{-1})
1.79	22.5	0.016	0.06	20	0.314	3.475

* Based upon graphical interpretation of the SWRC corresponding to the pressure reached when water content transitioned from a constant value to decreasing significantly with small increases in pressure.

**Measured based upon destructive sampling method.

***Parameters determined using RETC based upon experimental data.

Vegetation grown in Tank 2 was Cynadon dactylon (Bermuda grass) and hereafter referred to as grass. This grass is native to more than 80% of the United States based upon the US Department of Agriculture. The Bermuda grass was determined to germinate the most effectively in #30/40 Accusand compared to two other species investigated which included Festuca arundinacea (tall fescue) and Festuca spp. (fine fescue). Two other sands were also investigated which included #110 sand and a mixture of 80% #30/40 and 20% #110 based upon weight in which case neither enabled as successful germination as that of the #30/40 sand. The time of germination was approximately 7 days. Kiniry et al. (2007) summarized additional select properties for Bermuda grass given in Table 4.3.

Table 4.3. Vegetation properties of Bermuda grass.

Leaf Area Index (*LAI*)	Light Extinction Coefficient (*k*)	Radiation Use Efficiency (RUE) of dry biomass [g MJ^{-1}] of intercepted photosynthetically active radiation
0.27 – 2.51	1.0	1.6

4.3.3 Experimental Procedure

The experimental procedures followed were similar for both Tanks 1 and 3 regarding establishing a tank with tight packed homogeneous conditions. Therefore, the discussion that follows is related directly to Tank 3, but applies to Tank 1 as well. Tight packing conditions were pursued evenly throughout the entire depth of the tank. At all times, the water level (using deionized water) was maintained above the sand level to ensure the sand was packed under fully saturated conditions. Tight packing conditions throughout the tank were achieved by placing the sand in 2.5 cm lifts and then pushing the sand down manually as well as tamping all four sides of the tank using a rubber mallet following the same procedures as Sakaki and Illangasekare (2007). Once completely packed with sand event with the surface of the tank, the tank was moved in place on top of the scale. Then sensors were placed on the surface as appropriate.

Upon completion of wet packing Tank 2, grass seeds were placed evenly across the soil surface (not buried) with the soil tank covered with clear plastic wrap. Tank 2 was then placed below grow lamps cycling every 12 hours. Watering occurred every 1 to 2 days using a spray bottle to enable the saturation level to reach just below the surface. Every 5 to 7 days, 1/8 teaspoon of Miracle-Gro All Purpose Plant Food was mixed with 1 gallon of DI water and applied to Tank 2. After roots were at least 1 cm in length and the growth above the soil surface was at least 2 to 3 cm, DI watering transitioned from every 1 to 2 days to every 3 to 5 days and the fertilized amount transitioned from 1/8 tsp to ¼ tsp of fertilized mixed in DI water every 5 to 7 days.

A series of four experiments were conducted to collect data regarding varying environmental conditions. Each experiment occurred over a 20-day period to allow adequate time for completion of Stage 1 evaporation, transition to Stage 2 evaporation and approaching near steady state conditions associated with Stage 2 evaporation. Experiment 1 (hereafter referred to as

EX1) consisted of ambient laboratory temperature maintained. Experiment 2 (hereafter referred to as EX2) consisted of elevated temperatures through use of the ceramic heaters (Figure 4.2) maintained throughout the duration of the experiment. Experiment 3 and 4 (hereafter referred to as EX3 and EX4) occurred under diurnal conditions resulting from 12-hour cycling fluorescent lights used to maintain vegetation growth versus the ceramic heaters of EX2. The dual tank experiment associated with EX3 and EX4 enabled maintaining similar experimental conditions for comparison between bare soil evaporation (EX3 - Tank 1) and evapotranspiration (EX4 - Tank 2). EX1 and EX2 occurred using Tank 3. EX3 and EX4 employed the use of Tanks 1 and 2, respectively.

Important physical, boundary and initial conditions associated with each experiment considered in this study are given in initial conditions are provided in Table 4.4. The water table for each experiment started at the soil surface with the tank fully saturated. The sides and bottom of the tank were no flow boundaries resulting in mass flux of water vapor occurring only through the top of the tanks.

Table 4.4. Experimental boundary and initial conditions.

Experiment	Tank Used	Soil Surface	Porosity ($m^3\ m^{-3}$)	Average Net Radiation ($W\ m^{-2}$)	Average Air Temperature (^oC)	Average Air Relative Humidity (%)	Average Wind Speed ($m\ s^{-1}$)
1	3	Bare	0.324	*	25.9	27	0.71
2	3	Bare	0.320	*	39.8	10	1.10
3	1	Bare	0.345	13.2	22.6	48	1.00
4	2	Grass	0.310				

*Not measured for EX1 or EX2.

4.4 Results and Discussion

The experimental results from the four experiments are discussed in relation to cumulative water loss, saturation, relative humidity, and temperature as each of these serve as inputs or points of comparison for the various evaporation models discussed in the next section. The cumulative water loss due to evaporation in the case of EX1, EX2, and EX3 and the evapotranspiration for EX4 is shown in Figure 4.3. Stage I evaporation denotes a high rate of cumulative water loss and high evaporative demand. EX1 has the least amount of water loss and lowest total evaporation due to a lack of external forcing from elevated temperatures or diurnal fluctuation. The continuous elevated air temperature associated with EX2 causes an increased water loss and a transition almost immediately into Stage II evaporation compared with EX1 where the transition between the two stages occurs around day 3.5. The higher heat causes an increase atmospheric demand driving an increased evaporation rate. However, regardless of the difference in atmospheric boundary conditions, both EX1 and 2 exhibit almost identical evaporation rates later during Stage II evaporation. During this period, vapor-diffusion limited evaporation conditions dominate and with the same soil and relative porosity, the evaporation rates exhibit similar characteristics.

EX3 and EX4 have considerably more cumulative water loss as a function of two factors: (1) Tank 1 and 2 have a 78% increase in surface area and (2) the diurnal effect of the lamp. The bare soil evaporation occurring in EX3 shows an extended period of Stage I evaporation followed by a more gradual transition to Stage II evaporation compared with EX 1 and EX2. EX4 exhibits two different rates of evapotranspiration; however, they are more similar in average value than the difference in evaporation rate averages of EX3 for Stages I and II. For EX4, there are competing effects. Root and grass growth add weight measured from the scale whereas evapotranspiration reduces the weight measured. The grass was well established within Tank 2 leading to minimal

root growth observed through the sides of the tank. Additionally, the grass did grow but not appreciably (average across the surface of the tank = 1.5 cm over the 20-day experiment) based upon visual analysis of photos taken regularly. Therefore, the amount of growth causing an increase in weight is reasonably assumed to minimally impact the measured weight loss. As a result, the measured weight loss is likely the actual *ET* rate minus a few percent. Multiple experiments were conducted under similar conditions associated with EX4 and maintained for over 45 days to identify a point of significant change in evapotranspiration rates and none were identified. The comparison between EX3 and 4 also shows that between days 7 to 14, the initially higher rate of water loss with EX3 during Stage I evaporation reduces below the *ET* rate of EX4 as EX3 transitions into Stage II evaporation. These observed characteristics are compared against the four models to identify their ability to capture these relationships.

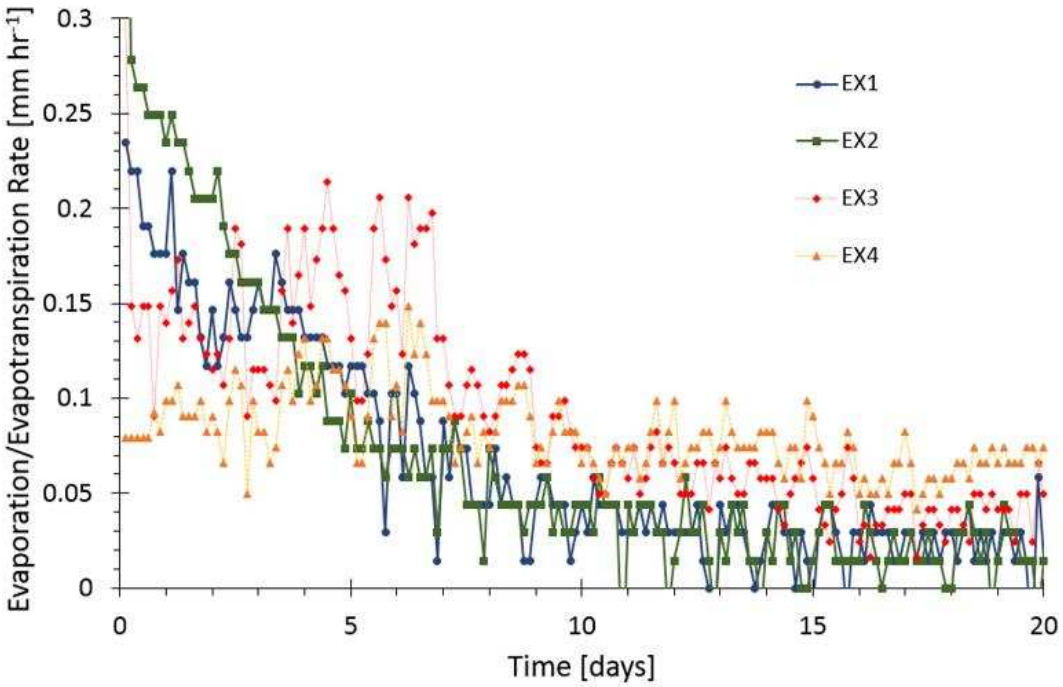

Figure 4.3. Lysimeter analysis for all four experiments providing a comparison of evaporation or evapotranspiration rate based upon ground cover and boundary conditions.

The soil moisture taken as the average of all soil moisture measurements recorded at the same depth are plotted against time in Figure 4.4 for all experiments. The data recorded at 2.5, 7.5 and 12.5 cm bgs are shown. Measured saturation at 17.5 and 22.5 cm remained fully saturated for all experiments and are therefore not shown. The color scheme used in the figure include blue markers denoting 2.5 cm bgs, red markers denoting 7.5 cm bgs, and green markers denoting 12.5 cm bgs. The same color scheme is used for all experiments for ease of comparison. The saturation at 2.5 and 7.5 cm for EX2 decreased more rapidly than all other experiments during Stage I evaporation marked by the steep decline in saturation at both depths. The reduction in saturation at 2.5 cm for EX3 exhibited characteristics similar to both EX1 and EX2 as the experiment cycled between ambient (EX1) and heated (EX2) conditions. At 7.5 cm bgs, saturation of EX3 initially showed a delayed time of significant decrease and then decreased below the residual saturation for EX1 or EX2. The fact that the soil surface was essentially covered by vegetation in EX4 resulted in significantly more saturation remaining in the soil and a less dramatic decrease in saturation at both 2.5 and 7.5 cm bgs when EX4 is compared to all other experiments. At 12.5 cm bgs for all experiments, the transition from fully saturated to decreasing saturation all occurred at about the same time period (~10 days). There was almost no difference between EX1 and EX2 denoting that the elevated temperature did not significantly alter subsurface conditions at 12.5 cm bgs. There was also almost no difference between EX3 and EX4 denoting that the grass roots did not significantly impact soil moisture at a depth of 12.5 cm for the duration of the experiment. This fact gives further validity to the statements above that the measured weight loss over time is representative of the actual *ET* rate. Furthermore, with both set of experiments remaining similar associated with similar experimental apparatus used, the properties of the soil become more significant than atmospheric, boundary layer conditions at a depth of 12.5 cm.

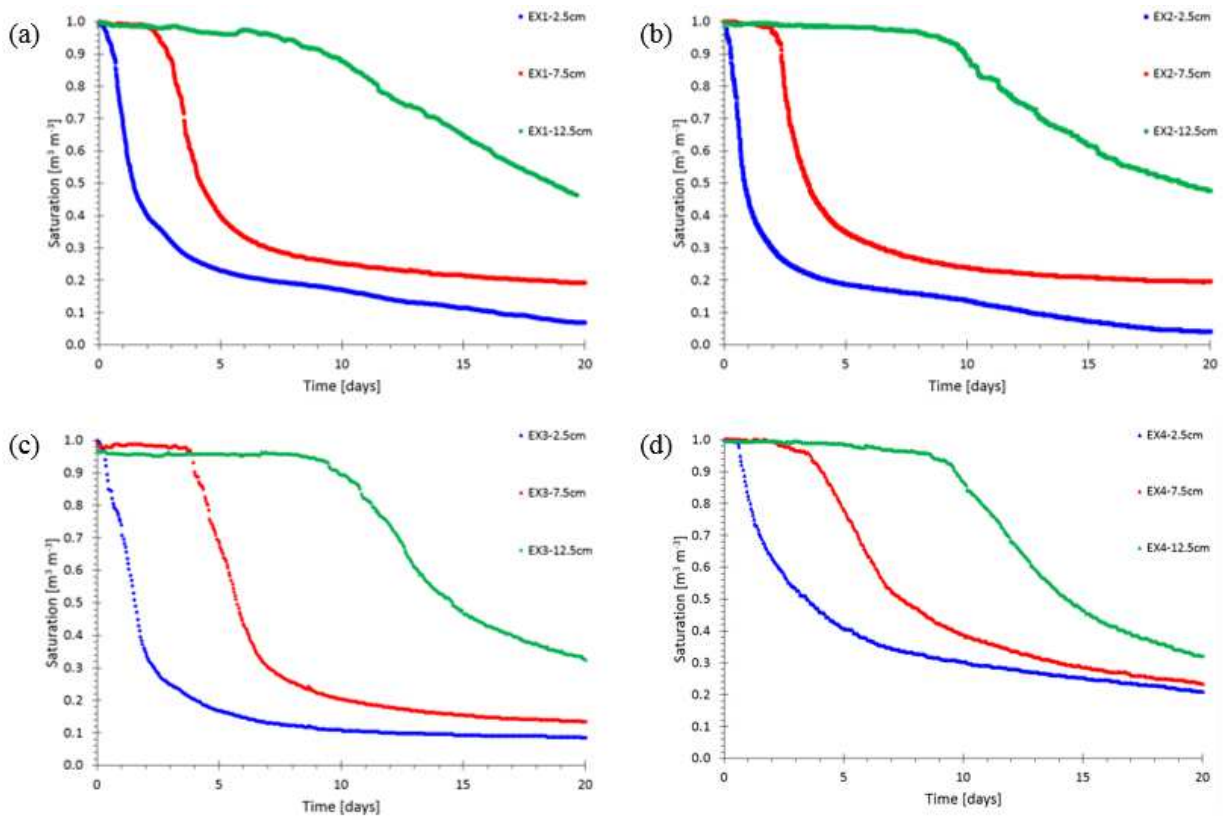

Figure 4.4. Average saturation at 2.5 cm (blue), 7.5 cm (red), and 12.5 cm (green) below ground surface for a) EX1, b) EX2, c) EX3, and d) EX4.

Changes between the stages of evaporation manifest in the difference in temperature between the air and surface (Figure 4.5). Under ambient (EX1) conditions, the difference in temperature is higher during Stage I evaporation (~ 1.7 mm d^{-1}) and decreases during Stage II. During Stage I, evaporative cooling occurs as water in contact with the surface changes phase into water vapor. As a result the surface is cooler than the atmospheric temperature. As the soil surface loses soil moisture and evaporative cooling no longer dominates at about the same time as residual saturation is reached for 7.5 cm bgs (Figure 4.4), the soil surface temperature approaches the air temperature. At this point in the laboratory experiments, the temperature difference stabilized and maintained a similar value. The periodic fluctuations occurring in EX1 are a result of laboratory climate control systems of heating and cooling throughout the day. Due to a continuously heated

air stream in contact with the soil surface (EX2), the temperature difference is significantly higher than all other experiments. However, there is a clear decrease in temperature difference for the first 11 days and then the difference stabilized which again corresponds to the point where residual saturation is reached for 7.5 cm bgs. This decrease is a function of evaporative cooling and the time associated with reaching the near constant temperature difference corresponds to late Stage II evaporation vapor-diffusion dominates compared to atmospheric demand. The temperature differences associated with EX3 and EX4 follow similar trends, however, the time associated with approaching a stabilized temperature difference is prolonged due to the diurnal heating affect and residual saturation is not completely reached at 20 days nor even at 45 days.

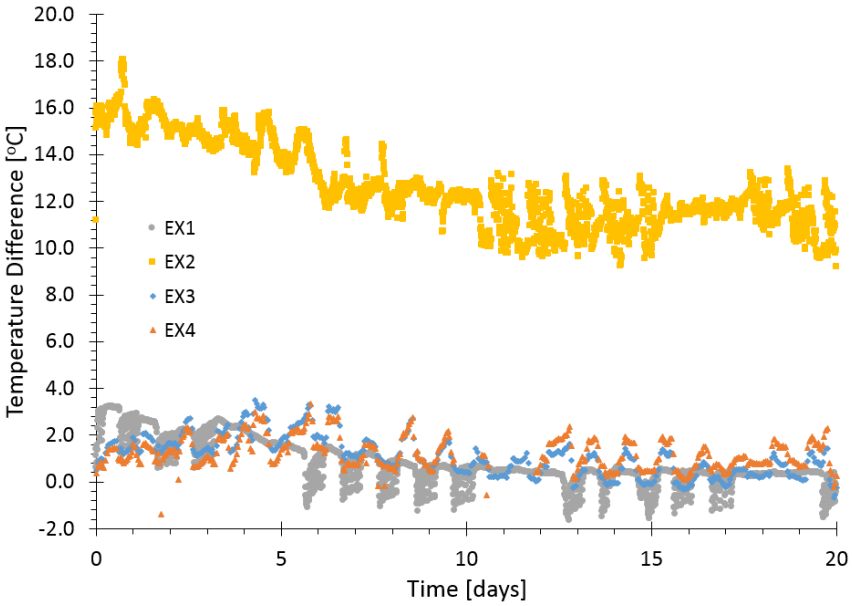

Figure 4.5. Temperature difference between air and surface temperature for EX1 (denoted by circles), EX2 (denoted by squares), EX3 (denoted by diamonds), and EX4 (denoted by triangles).

A comparison of the average relative humidity on the soil surface and in the air stream above the soil provides additional insight to the evaporation behavior (Figure 4.6). With EX1, there is a high, fluctuating relative humidity difference that extends to the time associated with

residual saturation reached at 7.5 cm bgs (Figure 4.4) and where the temperature difference between the air and surface approaches a near constant value (Figure 4.5). At this point, the beginning of the transition to Stage 2 evaporation occurs and is marked by a continuous, significant decrease in difference in relative humidity between the surface and air. Stage 2 evaporation stabilizes at a constant decreased rate at the point where the difference in relative humidity also reaches a near stabilized, constant difference which corresponds to the timing of reaching residual saturation at 7.5 cm bgs and constant temperature difference. The same relationship is clearly seen with EX2; however, less so with EX3 and EX4. The diurnal effect along with the grass covered surface causes prolonged, more constant evaporation to occur. The diurnal impact of evaporation during the heat cycle and potential for condensation during the cool cycle is clearly visible (Figure 4.6) and more pronounced with EX3 compared to EX4.

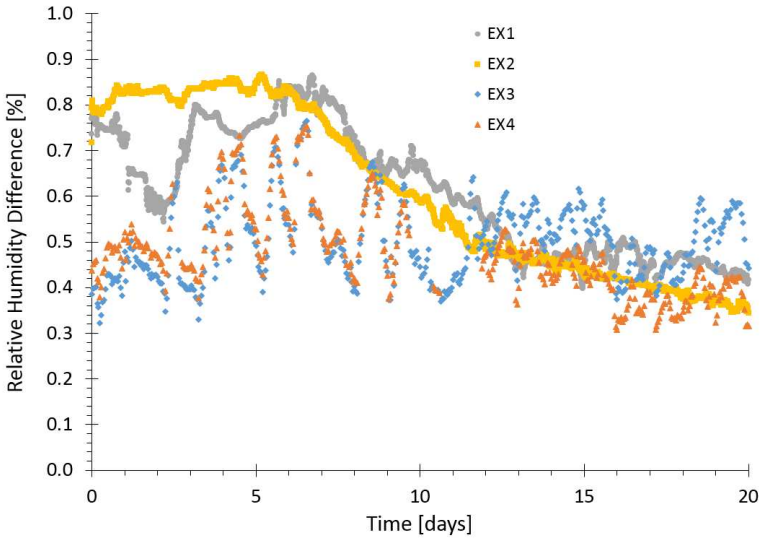

Figure 4.6. Relative humidity difference between surface and air measurements for EX1 (denoted by circles), EX2 (denoted by squares), EX3 (denoted by diamonds), and EX4 (denoted by triangles).

Individually, the relationships examined regarding water weight loss, changes in saturation, temperature difference between air and surface temperatures, and the relative humidity difference between air and surface relative humidity provide the potential to identify Stage I and Stage II evaporation for the boundary conditions investigated with a poorly graded, well sorted sand (>98% quartz). When these characteristics are known regarding the soil of interest, confirmation of the transition between Stage I and II evaporation is possible. Understanding the saturation, temperature, and relative humidity response associated with this transition will help clarify which evaporation model is able to effectively predict either Stage I, Stage II or both evaporation regions.

4.5 Applicability of Evaporation Models

In this study, through measuring subsurface, surface and atmospheric conditions, required inputs for methods of evaporation estimation were collected. There are a variety of evaporation models available and initially investigated as part of this research. Prior modeling efforts by the author compared evaporation rates determined using lysimeters data with those from a surface energy balance presented by Shahraeeni and Or (2010), an energy and water balance discussed by Lascano et al. (1987), a sensible heat balance incorporating the use of in-situ heat pulse probes (e.g., Heitman et al., 2008a; Sakai et al., 2011; Trautz et al., 2014), a soil moisture extraction function by Budyko and Zubenok (1961) which incorporates use of FAO-56 Penman-Monteith, and a soil moisture method by Sellers et al. (1986). Four models were selected based upon reasons previously stated in Section 4.2. These models include: the sensible heat balance and heat pulse method (Heitman et al., 2008a; Trautz et al., 2014; Xiao et al., 2014) hereafter referred to as SHB+HP, micro Bowen ratio energy balance (Ashktorab et al., 1989; Holland et al., 2013) hereafter referred to as M-BREB, a relative evaporation method that incorporates surface

temperatures differences developed by Ben-Asher et al. (1983) hereafter referred to as TD, and an energy and water balance model developed by Lascano et al. (1987) hereafter referred to as ENWATBAL.

The SHB+HP model serves as an approach where the required model inputs come from one heat pulse probe installed with the top needle approximately 3 mm below the soil surface. The SHB+HP model has its foundation in the sensible heat balance equation (Gardner and Hanks, 1966; Heitman et al., 2008a, 2008b; Sakai et al., 2011):

$$LE = H_0 - H_1 - \Delta S \tag{4.3}$$

where L is latent heat of vaporization (J m^{-3}), E is evaporation rate (m s^{-1}), H_o is sensible heat flux at depth 0 (W m^{-2}), H_1 is sensible heat flux at depth 1 (W m^{-2}), and ΔS is change in sensible heat storage between two depths (0 and 1) (W m^{-2}). L is defined based upon Forsythe (1964):

$$L = 2.49463x10^{9} - 2.247x10^{6}T_{mean} \tag{4.4}$$

where T_{mean} is the mean temperature for a given soil depth layer as a function of time. With the use of a three needle heat pulse probe, the sensible heat fluxes based upon Fourier's Law are defined:

$$H_0 = -\lambda_{i+1/2}\frac{T_i - T_{i+1}}{z_i - z_{i+1}} \tag{4.5}$$

$$H_1 = -\lambda_{i-1/2}\frac{T_{i-1} - T_i}{z_{i-1} - z_i} \tag{4.6}$$

where λ is soil thermal conductivity (W m^{-1} ^{o}C^{-1}), T is temperature (^{o}C), z is depth below the surface (m), subscript i is the center needle of the heat pulse probe, subscript i+1 is the bottom needle of the heat pulse probe, and subscript i-1 is the top needle of the heat pulse probe. Ochsner et al. (2001) define ΔS:

$$\Delta S = \sum_{i=1}^{N} C_{i,j-1} \frac{T_{i,j} - T_{i,j-1}}{t_j - t_{j-1}} (z_i - z_{i-1}) \quad (4.7)$$

where C is volumetric heat capacity (J m^{-3} ^{o}C^{-1}), t is time (s), and subscript j denotes the current time step with j-1 referring to the previous time step. C may be approximated using Taylor series expansion to eliminate the exponential integration function (Knight and Kluitenberg, 2004):

$$C \approx \frac{q' t_0}{e\pi r^2 \Delta T_{max}} \left(1 - \frac{\varepsilon^2}{8}\left[\frac{1}{3} + \varepsilon\left\{\frac{1}{3} + \frac{\varepsilon}{8}\left(\frac{5}{2} + \frac{7\varepsilon}{3}\right)\right\}\right]\right) \quad (4.8)$$

where q' is the energy per unit length of heater in the probe (W m^{-1}), t_o is duration of the heat pulse (s), r is radial distance from the line source (m) which was determined experimentally as the effective radius of the heat pulse probe, ΔT_{max} is the maximum temperature change per time step (^{o}C), and ε defined by Knight and Kluitenberg (2004):

$$\varepsilon = \frac{t_0}{t_{max}} \quad (4.9)$$

where t_{max} is the time required per time step to reach ΔT_{max}.

The M-BREB model requires inputs from measurements taken below and above the soil surface. The M-BREB model is an adjustment to the tradition Bowen ratio, β, method in which β is determined based upon temperature and relative humidity measurements at two different heights near the soil surface. E is determined from the ratio of sensible to latent heat flux (Ashktorab et al., 1989):

$$E = \frac{H\Delta e}{L\gamma\Delta T} \quad (4.10)$$

where H is sensible heat flux (W m^{-2}), Δe is difference of vapor pressure (kPa) at two different heights above the surface for the microsystem, L is latent heat of vaporization for water (J kg^{-1}), γ is the psychrometric constant determined as 0.0548 kPa ^{o}C^{-1} based upon FAO-56 (pg 31-32), and

ΔT is temperature difference (°C) at two different heights (typically 1 cm and 6 cm (Ashktorab et al., 1989); however, at 0.5 cm and 8 cm for research conducted) above the surface for the microsystem. H is determined based upon the bulk equation discussion in Yan et al. (2012) with the addition of incorporating soil surface resistance, r_g (s m^{-1}):

$$H = \rho_a C_p \frac{T_g - T_\infty}{r_{ag} + r_g} \tag{4.11}$$

where ρ_a is density of air (kg m^{-3}), C_p is specific heat of air (J kg^{-1} K^{-1}), T is temperature (°C) with subscript g denoting surface and subscript ∞ denoting air, r_{ag} is aerodynamic resistance (s m^{-1}), and r_g is soil surface resistance (s m^{-1}). The density of air is more completely determines as the moist air density, $\rho_{a,moist}$ (Lu and Likos, 2004):

$$\rho_{a,moist} = \frac{u_d \omega_d}{RT} - 0.611\left(\frac{\omega_d}{\omega_v} - 1\right) exp\left(17.27\frac{T-273.2}{T-36}\right)\frac{\omega_v RH}{RT} \tag{4.12}$$

where u_d is dry air pressure (kPa) taken from local meteorological data in Golden, CO, ω_d is molecular weight of air (0.028966 kg mol^{-1}), R ideal gas constant (m^3 kPa K^{-1} mol^{-1}), T is air temperature (K), ω_v is molecular weight of water vapor (0.018016 kg mol^{-1}), RH is relative humidity of the air (-). The specific heat of air was determined based upon the standard thermodynamic property simplified as:

$$C_p = 0.0002T^2 - 0.07T + 1008 \tag{4.13}$$

Yan et al. (2012) defined r_{ag}:

$$r_{ag} = \frac{1}{u_z k^2} ln\left(\frac{z_{ref} - d_h}{z_h}\right) ln\left(\frac{z_{ref} - d_m}{z_m}\right) \tag{4.14}$$

where u_z is mean wind speed (m s^{-1}), k is von Karman's constant (0.41), z_{ref} is the reference height of measurement for temperature and wind speed (m), d_h and d_m are the zero plane displacement

height for heat flux and momentum flux, respectively (0 m for bare soil (Oke, 1978) and <0.07 for short grass (Monteith and Unsworth, 1990)), and z_h and z_m are surface roughness for heat flux and momentum flux, respectively (0.001 m for soil (Oke, 1978) and 0.002 for short grass (Monteith and Unsworth, 1990)). The soil surface resistance is defined by van de Griend and Owe (1994):

$$r_g = 10e^{0.3563(15-\theta)} \tag{4.15}$$

where θ is volumetric water content (m^3 m^{-3}) measured at 2.5 cm bgs. The difference in vapor pressure, Δe, is further defined as the difference in actual vapor pressure measured at the surface and approximately 9 cm above the soil surface (Figure 4.2). The actual vapor pressure (kPa) is determined as the product of the measured relative humidity and saturated vapor pressure (kPa) based upon temperature.

The TD model developed by Ben-Asher et al. (1983) enables calculating E:

$$E = \left[8.7\left(\frac{\rho_a C_p}{r} + 4\varepsilon\sigma T^3\right)\right](T_d - T_e) \tag{4.16}$$

where ρ_a is density of air (kg m^{-3}), C_p is specific heat of air (J kg^{-1} K^{-1}) based upon the thermodynamic relationship between air temperature and specific heat, r is resistance to heat transport (hrs m^{-1}), e is emissivity (0.95 (Ben-Asher et al., 1983) for soil and 0.98 (Sutherland, 1986) for grass), s is the Stefan-Boltzman constant (2.04×10^{-4} J h^{-1} m^{-2} K^{-4}), T is average surface temperature of dry and evaporating surfaces (K) calculated as the average between the air and soil surface temperature, T_d is temperature of the dry surface (which this research took as the air temperature near the soil surface) (K), and T_e is temperature of the evaporating surface (taken as the surface temperature) (K). The method used to determine ρ_a and C_p is the same as that discussed with the M-BREB model. Resistance to heat transport is determined:

$$r = 0.035u^{-0.96} \quad (4.17)$$

where u is the mean wind speed (m s^{-1}). Model inputs for estimating evaporation required only input from above the soil surface.

The ENWATBAL model based upon Lascano et al. (1987) defines E:

$$E = \frac{\left(AH_g - AH_\infty\right)}{r_{ag} + r_g} \quad (4.18)$$

where AH is absolute humidity (g m^{-3}) with subscript g denoting surface and subscript ∞ denoting air (8 cm above soil surface), r_{ag} is aerodynamic resistance (s m^{-1}) using Eq. 15, and r_g is soil surface resistance (s m^{-1}) using Eq. 16. AH is defined:

$$AH = b \cdot e_a / T_g \quad (4.19)$$

where b is a constant (2.16679 g K J^{-1}), T_g is surface temperature (K), and e_a is the actual vapor pressure (kPa) measured at the surface and air (8 cm above soil surface) with the method to determine unknown parameters (e.g., r_{ag}, r_a, e_a) discussed previously. The ENWATBAL model serves as an approach where the required model inputs come from six different sensors installed below the surface (1x soil moisture sensor), on the surface (1x temperature sensor, 1x relative humidity sensor), and in the air stream above the surface (1x temperature sensor, 1x relative humidity sensor, 1x anemometer).

Table 4.5 provides a summary of all four models and the required emplacement locations for sensors, the type of sensors required and inputs from those sensors to enable model prediction of evaporation. The measured inputs from sensors associated with each experiment were incorporated into each of the four models and compared with the measured evaporation based upon lysimeters data. Figure 4.7 shows this comparison based upon change in evaporation rates over

time (Figure 4.7a) and through a direct comparison between measured and modeled evaporation rates (Figure 4.7b) for EX1.

Table 4.5. Comparison of evaporation models regarding sensor location, property measured, and number of inputs for model operation.

Evaporation Model	Sensor Location	Sensor Type Required Property Measured	Measured Inputs Required
SHP+HP	below soil surface	temperature via heat pulse probe	16: t_o, t_{max}, t_j, t_{j-1}, , q', r, z_i, z_{i-1}, z_{i+1}, $T_{i,j}$, $T_{i,j-1}$, T_i, T_{i-1}, T_{i+1}, T_{mean}, λ
M-BREB	above and below soil surface	air pressure, wind speed, soil moisture at 2.5 cm bgs, relative humidity and temperature at the surface and 8 cm above soil surface	8: θ, z_{ref}, u_z, RH_g, RH_∞, T_g, T_∞, u_d
TD	above soil surface	air pressure, wind speed, relative humidity and temperature at the surface and 8 cm above soil surface	6: u, T_d, T_e, u_d, RH_∞, ε
ENWATBAL	above and below soil surface	wind speed, soil moisture at 2.5 cm bgs, relative humidity and temperature at the surface and 8 cm above soil surface	7: θ, z_{ref}, u_z, RH_g, RH_∞, T_g, T_∞

The SHB+HP model provides the highest level of agreement between measured and modeled evaporation rate compared to the other three models. The TD model has fairly good agreement during Stage I evaporation with increasing model fit with Stage II evaporation. Both the M-BREB and ENWATBAL models significantly under-predict evaporation rates during Stage I and slightly under-predict evaporation during Stage II. Both have similar results due to similar model inputs from the same sensors based upon the equations associated with each model. Previous research using the M-BREB and ENWATBAL models occurred under dry conditions (Lascano et al., 1987; Ashktorab et al., 1989; Holland et al., 2013). Therefore, they were not tested under saturated soil conditions. The underestimation of Stage I evaporation may significantly impact evaporation estimates determined using either method.

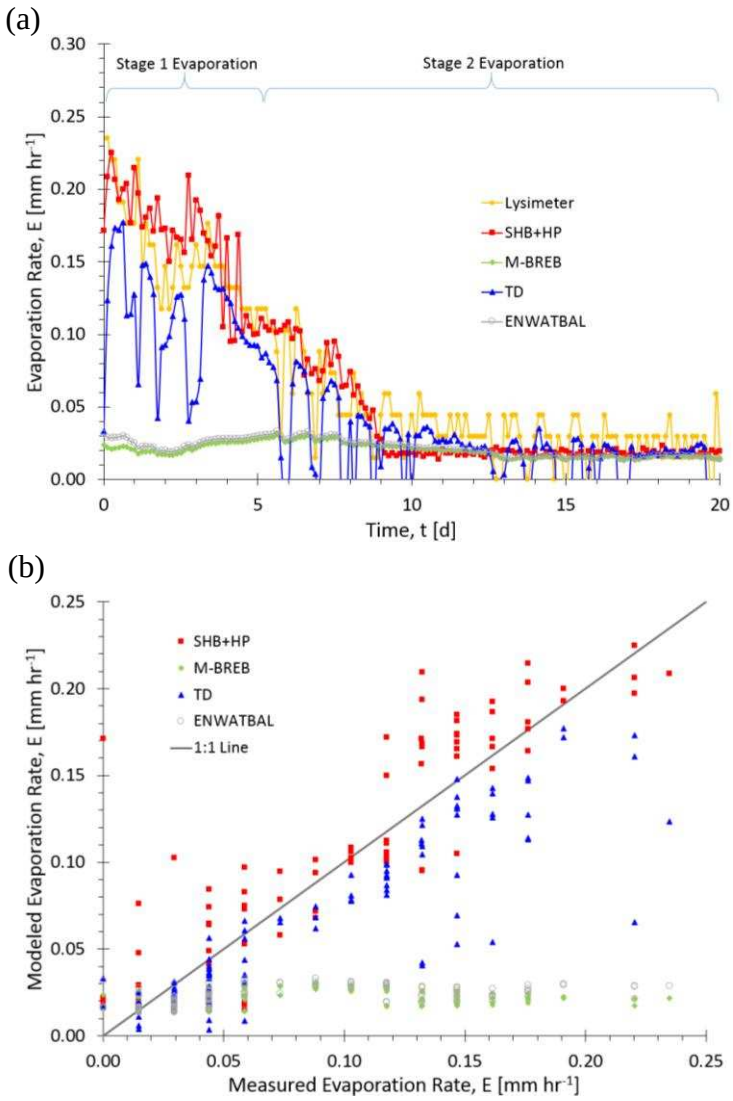

Figure 4.7. Evaporation model comparison associated with ambient conditions (EX1) comparing (a) evaporation rates modeled compared to lysimeter data, and (b) direct comparison between measured and modeled evaporation rates.

The ability of each model to accurately predict evaporation rates with continuously elevated air temperature (EX2) is shown in Figure 4.8. The SHB+HP model is able to effectively model evaporation through both stages of evaporation. However, there is an over-prediction of evaporation rates as Stage 2 evaporation approaches near steady state conditions. The TD model

no longer functions well under continuously elevated temperatures and significantly over-predicts evaporation rates due to the large difference between air and surface measurements. As with EX1, the M-BREB and ENWATBAL models do not enable proper prediction of evaporation rates during Stage 1. Both models only begin to reasonably predict evaporation after Stage 2 evaporation has approached near steady state conditions.

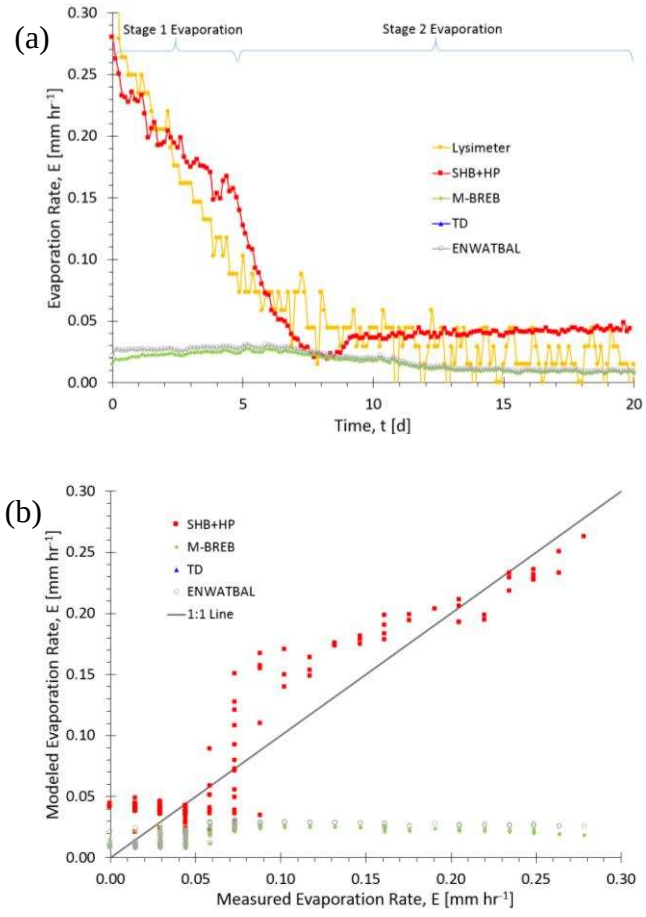

Figure 4.8. Evaporation model comparison associated with elevated air temperature (EX2) comparing (a) evaporation rates modeled compared to lysimeter data, and (b) direct comparison between measured and modeled evaporation rates.

The analysis of the four evaporation models with bare soil evaporation under diurnal conditions (EX3) is shown in Figure 4.9. Both the SHB+HP and TD models are able to effectively

reflect the diurnal fluctuations and capture Stage I and II evaporation regions. These models have more variability along the 1:1 line (Figure 4.9b). As with EX1 and EX2, neither the M-BREB or ENWATBAL models are able to represent Stage I evaporation. A primary reason for this is that both models were developed under dry conditions (Stage II). In fact, a review of the literature identified that if a rain event occurred while either method was being used, then the data from the period of high saturation would be omitted. Furthermore, in the case of diurnal fluctuation, both models significantly under-predict evaporation within Stage II. The increased variability in temperature and relative humidity due to the diurnal cycle caused all models to perform less effectively; however, the overall evaporative trend was captured most effectively by the SHB+HP model followed by the TD model. The reason for more responsiveness of the SHB+HP method results from inputs derived from measurements obtained from analysis of three needles in close proximity to each other (~3 mm between each).

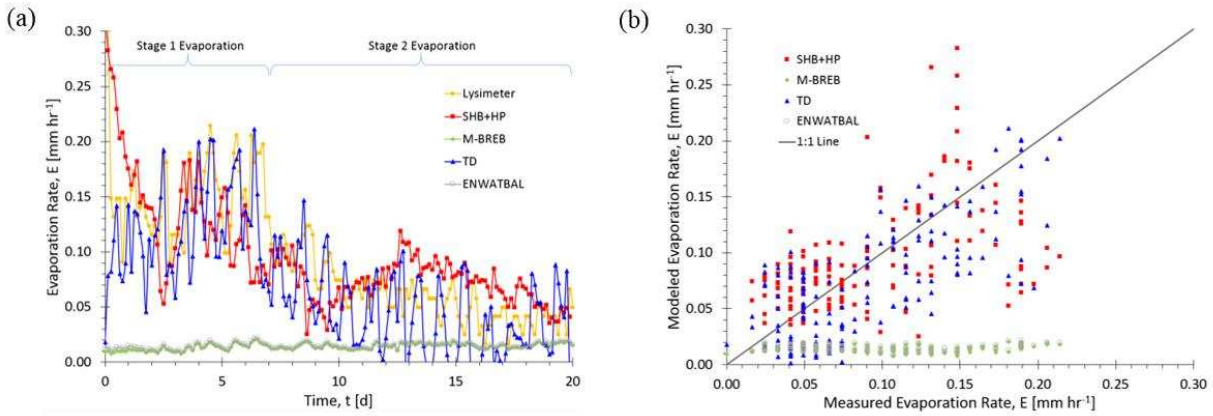

Figure 4.9. Evaporation model comparison associated with diurnal heating of bare soil (EX3) comparing (a) evaporation rates modeled compared to lysimeter data, and (b) direct comparison between measured and modeled evaporation rates.

The final evaluation of the four evaporation models was applied to grass covered sand under diurnal conditions (EX4) and is shown in Figure 4.10. There are two separate evapotranspiration rates observed which match closely to the time associated with Stage I and II for EX3. The SHB+HP model is not able to effectively predict evapotranspiration as a function of the inputs associated with the model. All measurements for the model occur below the soil surface; therefore, only evaporation is measured. However, lysimeters data does provide the *ET* response over time. Within the bounds of the experiment conducted with poorly graded, well sorted high quartz content (>98%) sand, the isolation of *T* is possible through determining the difference between measured *ET* based upon lysimeter and the calculated *E* from the SHB+HP method. The TD model performed the best out of all models and was able to capture the diurnal fluctuation and has fairly good agreement with modeled evapotranspiration. The M-BREB and ENWATBAL models performed inadequately under evapotranspiration conditions and significantly under-predicted *ET* throughout the duration of the experiment. The inability of the models to adequately capture the evapotranspiration response highlights the point that different models are potentially required based upon the land cover in the area of interest.

One additional point of interest conducted as part of this research included an investigation into the effect of temporal sampling frequency on evaporation estimates. A surface energy balance method was used based upon work by Shahraeeni and Or (2010) for EX-1. For specifics regarding this model, the reader is referred to Shahraeeni and Or (2010) as the focus in on interpreting temporal sampling frequency and not further model description. The lysimeter's measured evaporation rates were compared to modeled evaporation rates for sampling frequencies of 3, 6, 12, and 24 hour periods (Figure 4.11). The relationship between modeled and measured evaporation rates significantly changes based upon the sampling frequency: 3-hour (R^2=0.83), 6-

hour (R^2=0.80), 12-hour (R^2=0.60), 24-hour (R^2=0.48). A number of models use daily evaporation rate measurements which may significantly affect the modeled evaporation rate. A higher temporal distribution of data enables hourly and diurnal fluctuations to increase in agreement between measured and modeled evaporation rates.

(a)

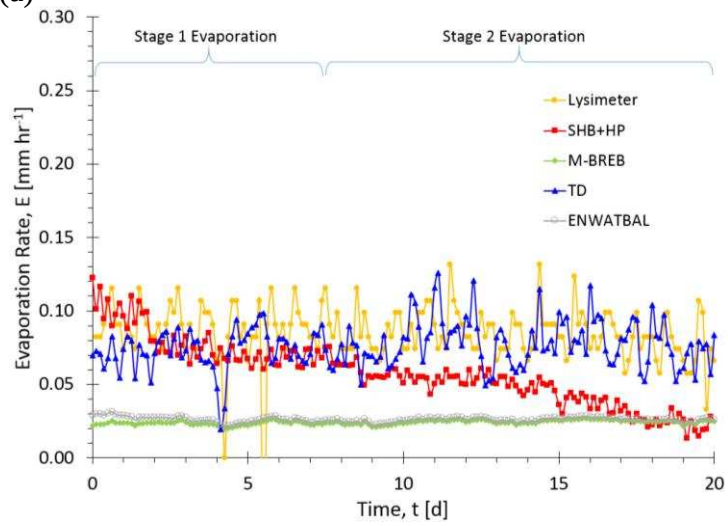

(b)

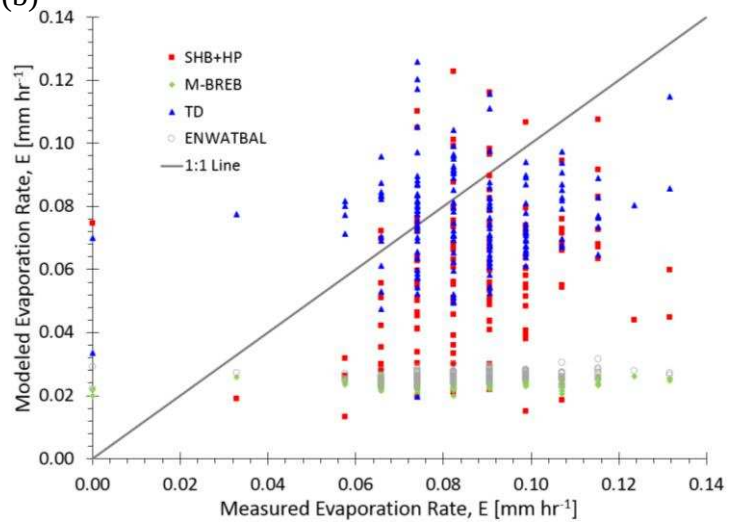

Figure 4.10. Evaporation model comparison associated with diurnal heating of grass covered soil (EX4) comparing (a) evapotranspiration rates modeled compared to lysimeter data, and (b) direct comparison between measured and modeled evapotranspiration rates.

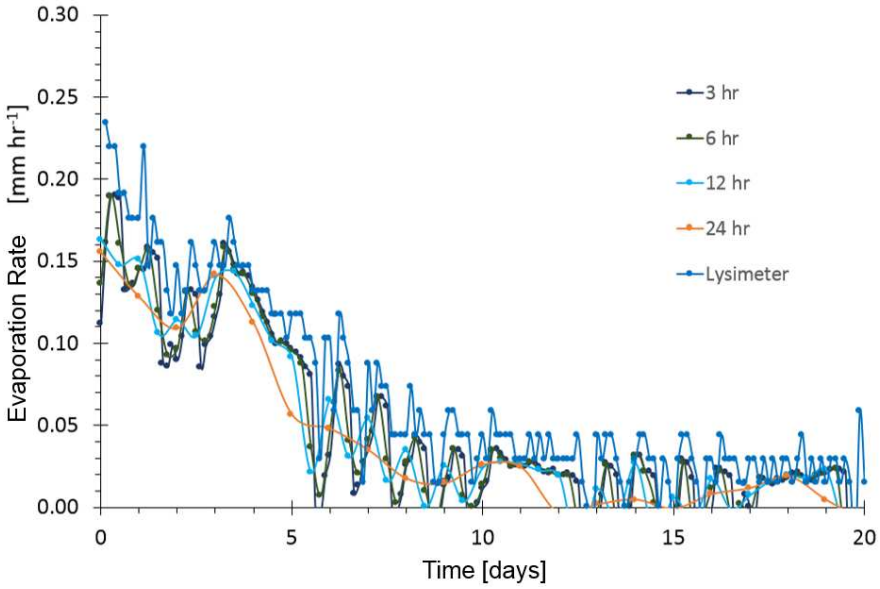

Figure 4.11. Surface energy balance resolved by infrared thermography for different sampling frequencies.

4.6 Conclusions

The purpose of this research was to evaluate the ability of different energy and water balance methods to determine evaporation based on varying boundary and initial conditions. Four models were selected from literature that vary in their input requirements and are relevant to determining under-canopy and bare soil *E* and *ET*. Model performance was compared with a series of four laboratory scale experiment. The conclusion discussed below apply for the boundary conditions investigated with tight packed, poorly graded, well sorted, high quartz content (>98%) sand.

This study investigated enabled understanding that identification of the transition between Stage I and II evaporation is possible through consideration of changes in the rate of cumulative water loss based upon lysimeters measurements, changes in the soil moisture profile at 7.5 cm bgs at the point of inflection in the rate of decreasing saturation from significant decrease in *S* with

minimal change in time to minimal change in *S* during significant changes in time, changes in the temperature difference between air and the ground surface at the point where the difference becomes relatively constant, and at the point where relative humidity on the surface decreases from a constant value. Although one set of relationships enables determination of the transition between Stage I and II evaporation, multiple comparisons provide validity to determination of this transition point which is essential for establishing model performance specific to the different evaporative stages.

The four models were evaluated for their ability to fit measured *E* or *ET* for four experimental conditions (i.e., ambient (EX1), continuous elevated temperature (EX2), diurnal conditions above bare soil (EX3), and diurnal conditions above grass covered soil (EX4). The SHB+HP model consistently performed better than the other models except during EX4 in which the TD model performed better. The reason for this better fit with the SHB+HP model is a function of the measurements derived from subsurface measurements directly below the surface. As a result, the fluctuation in the atmosphere that impact all other models are attenuated. The measurements of the SHB+HP method provide a high level of fidelity in minute changes in measured heat flow which is a significant reason for improved agreement with the various boundary conditions investigated. One other key point is that prior studies (Heitman et al., 2008a; Sakai et al., 2011; Xiao et al., 2014; Trautz et al., 2014) used multiple heat pulse sensor in series to determine evaporation. In this research effort, evaporation was determined through the use of one sensor. Therefore, the number of required sensors to instrument a field for determination of evaporative fluxes decreases significantly saving time and money. Additionally, the difference between measured *ET* based upon lysimeter data and the calculated *E* may provide determination of *T* enabling the SHB+HP model to be used as an *ET* partitioning method.

The TD model was second best with capturing the diurnal fluctuation associated with EX1 and 3 and best with EX4. The relatively high performance of this model to effectively predict evaporation and evapotranspiration demonstrates the flexibility of the model to function given under different boundary conditions. This model was designed by Ben-Asher at al. (1983) with the intent to take surface temperature measurements of completely dry soil and compare those to temperature measurements of drying soil from fully saturated to completely dry conditions. In the case of experiments conducted with this research and based upon previous experimental results, the temperature measurements of completely dry soil were taken as the upstream air temperature measurements prior to the air coming in contact with the soil surface (Figure 4.2a). This is a reasonable assumption as there is no evaporative cooling that occurs from completely dry soil and the soil and air temperature are almost identical (excluding vapor diffusion effects which minimally effect soil surface temperatures compared to evaporative cooling). Therefore, the TD model functions well without the need comparison of two surface temperature measurements (completely dry and evaporating) and can work using upstream air and evaporating soil surface measurements. The point when this model does not work using the altered input temperatures for comparison occurs when the air is continuously heated (EX2). The temperature difference between the air and surface was too great for the model to function in this manner. However, the model may indeed work if the surface temperature of a completely dry soil was measured for comparison with the surface temperature measurement of a drying soil. However, this requires further experimental investigation.

The greatest variability between measured and modeled evaporation rates occurred during Stage I evaporation. The M-BREB and ENWATBAL models consistently under-predicted evaporation during both Stage I and II evaporation regions. Previous research using the M-BREB

and ENWATBAL models occurred under dry conditions (Lascano et al., 1987; Ashktorab et al., 1989; Holland et al., 2013). Therefore, they were not tested under saturated soil conditions. The underestimation of Stage I evaporation may significantly impact evaporation estimates determined using either method.

None of the models performed better under evapotranspiration conditions compared to bare soil evaporation. For selection of the desired model, one must consider ground cover, sensors available and ease of access to required input data for the models. Investigation of the sampling frequency on evaporation rate agreement between measured and modeled relationships leads to the recommendation of a 3-hour sampling frequency of data required as model inputs. The 3-hour sampling frequency allows capture of hourly and diurnal fluctuations. Future work is required toward enabling researchers to require minimal inputs while maximizing modeled to measured evaporation rate agreement through all stages of evaporation. However, for the purposes of future research associated with Tasks 3 and 4, sensor instrumentation used for all future laboratory experiments will include the ability to measure the required inputs for both the SHB+HP and TD models.

4.7 Acknowledgements

This research was funded by the U. S. Army Research Office Award W911NF-04-1-0169, the Engineering Research and Development Center (ERDC), the National Science Foundation (CMMI-1230544 and EAR-1447533), the Edna Bailey Sussman Fund, and the Dorothy Bertine Internship. The author thanks Alec Wallen for support with tank packing and Dr. Andrew Trautz for writing of code for collection of data from various instruments (e.g., Pitot static tube, heat pulse sensor, temperature sensor) via interface between Campbell Scientific CR1000 data loggers and a PC200W program.

4.8 References

Abramowitz, M., and I.A. Stegun. 1972. Handbook of mathematical functions. Dover Publications, Inc., New York.

Ashktorab, W.O.H., K.T. Pruitt, U. Paw, and W.V. George. 1989. Energy balance determinations close to the soil surface using a micro-Bowen ration system. Agric. For. Meteorol. 46(3):259-274. doi:10.1016/0168-1923(89)90068-3

Ben-Asher, J., A.D. Matthias, and A.W. Warrick. 1983. Assessment of evaporation from bare soil by infrared thermometry. Soil Sci. Soc. Am. J. 47(2):185-191. doi:10.2136/sssaj1983.03615995004700020002x

Blight, G.E. 2002. Measuring evaporation from soil surfaces for environmental and geotechnical purposes. Water SA. 28(4):381-394.

Bowen, I.S. 1926. The ratio of heat losses by conduction and by evaporation from any water surface. Phys. Rev. 27(6):779-787.

Brutsaert, W. 1982. Evaporation into the Atmosphere: Theory, History and Applications. D. Reidel Publishing, Dordrecht, the Netherlands.

Budyko, M.I., and L.I. Zubenok. 1961. The determination of evaporation from the land surface, Izv. Akad. Nauk SSSR Ser. Geogr., 6(3), 3-17.

Carslaw, H.S., and Jaeger, J.C., 1959, Conduction of heat in soils, 2nd edition. Oxford, London.

Choudhury, B.J., R.J. Reginato, and S.B. Idso. 1986. An analysis of infrared temperature observations over wheat and calculation of latent heat flux. Agric. For. Meteorol. 37(1):75-88. doi:10.1016/0168-1923(86)90029-8

Cooper, P.J.M., P.J., Gregory, J.H.H. Keatinge, and S.C. Brown. 1987. Effect of fertilizer, variety and location on barley production under rainfed conditions in northern Syria. 2. Soil water dynamics and crop water use. Field Crops Res. 16:67-84.

Daamen, C.C., and L.P. Simmonds. 1996. Measurement of evaporation from bare soil and its estimation using surface resistance. Water Resour. Res. 32:1393-1402.

Das. Y., J.T. Dean, D. Lewis, J.H.J. Roosenboom, and G. Zahaczewsky (Eds). 2001. "Final report of the international pilot project for technology co-operation (IPPTC) for a multi-national technical evaluation of performance of commercial off the shelf metal detectors in the context of humanitarian demining," Tech. Rep. EUR 19719 EN. Published, on behalf of the participants, by the European Commission, Joint Research Centre, Ispra, Italy.

Decagon Devices. 2014. KD2 Pro thermal properties analyzer operator's manual, version 20 June 2014 – 09:11:40. Decagon Devices, Inc., Pullman, WA.

Deol, P., J. Heitman, A. Amoozegar, T. Ren, and R. Horton. 2012. Quantifying nonisothermal subsurface soil water evaporation. Water Resour. Res. 48:W11503. doi:10.1029/2012WR012516

Floret, C., R. Pontanier., and S. Rambal. 1982. Measurement and modelling of primary production and water use in a south Tunisian steppe. J. Arid Environ. 5:77-90.

Forsythe, W.E. 1964. Smithsonian physical table. Smithsonian Institution Publication 4169. Washington, D.C.

Ge, Y., Y. Liang, J. Wang, Q. Zhao, and S. Liu. 2015. Upscaling sensible heat fluxes with area-to-area regression kriging. IEEE Geosci. Remote Sensing Letters. 12(3):656-660. doi:10.1109/LGRS.2014.2355871

Glenn, E.P., A.R. Huete, P.L. Nagler, K.K. Hirschboeck, and P. Brown. 2007. Integrating remote sensing and ground methods to estimate evapotranspiration. Critical Reviews in Plant Sciences. 26(3):139-168. doi:10.1080/07352680701402503

Heitman, J.L., R. Horton, T.J. Sauer, and T.M. DeSutter. 2008a. Sensible heat observations reveal soil-water evaporation dynamics. J. Hydrometeorol. 9:165-171. doi:10.1175/2007JHM963.1

Heitman, J.L., X. Xiao, R. Horton, and T.J. Sauer. 2008b. Sensible heat measurements indicating depth and magnitude of subsurface soil water evaporation. Water Resour. Res. 44:W00D05. doi:10.1029/2008WR006961

Hillel, D., 1998. Environmental Soil Physics. Academic Press, London, UK/San Diego,CA.

Holland, S., J.L. Heitman, A. Howard, T.J. Sauer, W. Giese, A. Ben-Gal, N. Agam, D. Kool, and J. Havlin. 2013. Micro-Bowen ratio system for measuring evapotranspiration in a vineyard interrow. Agric. For. Meteorol. 177:93-100. doi:10.1016/j.agroformet.2013.04.009

Idso, S.B., R.J. Reginato, R.D. Jackson, B.A. Kimball, and F.S. Nakayama. 1974. Three stages of drying of a field soil. Soil Sci. Soc. Am. J. 38, 831–837

Jones, F.E., 1991. Evaporation of water with emphasis on applications and measurements. Lewis Publishers, Chelsea, MI.

Kalma, J.D., T.R. McVicar, and M.F. McCabe. 2008. Estimating land surface evaporation: A review of methods using remotely sensed surface temperature data. Surveys in Geophysics. 29(4-5):421-469.

Kerridge, B.L., J.W. Hornbuckle, E.W. Christen, and R.D. Faulkner. 2013. Using soil surface temperature to assess soil evaporation in a drip irrigated vineyard. Agricultural Water Management. 116(C):128-141.

Kiniry, J.R., B.L. Burson, G.W. Evers, J.R. Williams, H. Sanchez, C. Wade, J.W. Featherstone, and J. Greenwade. 2007. Coastal Bermudagrass, Bahiagrass, and Native Range simulation at diverse sites in Texas. Agron. J. 99:450-461. doi:10.2134/agronj2006.0119

Kluitenberg, G.J., J.M. Ham, and K.L. Bristow. 1993. Error analysis of the heat pulse method for measuring soil volumetric heat capacity. Soil Sci. Soc. Am. J. 57:1444-1451.

Knight, J.H., and G.J. Kluitenberg. 2004. Simplified computational approach for dual-probe heat-pulse method. Soil Sci. Soc. Am. J. 68:447-449. doi:10.2136/sssaj2004.0447.

Kool, D., N. Agam, N. Lazarovitch, J.L. Heitman, T.J. Sauer, and A. Ben-Gal. 2014. A review of approaches for evapotranspiration partitioning. Agric. For. Meteorol. 184:56-70.

Kustas, W.P., and N. Agam. 2013. Soil evaporation. In: Wang, Y.Q. (Ed.), Encyclopedia of Natural Resources. Taylor & Francis, New York.

Lascano, R.J., C.H.M. van Bavel, J.L. Hatfield, and D.R. Upchurch. 1987. Energy and water balance of sparse crop: simulated and measured soil and crop evaporation. Soil Sci. Soc. Am. J. 51:1113-1121.

Lehmann, P., S. Assouline, and D. Or. 2008. Characteristic lengths affecting evaporative drying of porous media. Physical Review E. 77:0563096. doi: 10.1103/PhysRevE.77.056309.

Li, Z.-L., R. Tang, Z. Wan, Y. Bi, C. Zhou, B. Tang, G. Yan, and X. Zhang. 2009. A review of current methodologies for regional evapotranspiration estimation from remotely sensed data. Sensors 9(5):3801-3853. doi:10.3390/s90503801

Lu, N., and W.J. Likos. 2004. Unsaturated soil mechanics. John Wiley & Sons, Inc., Hoboken. p. 429-431.

McCabe, M.F., E.F. Wood, R. Wojcik, M. Pan, J. Sheffield, H. Gao, and H. Su. 2008. Hydrological consistency using multi-sensor remote sensing data for water and energy cycle studies. Remote Sensing of Environment 112(2):430-444. doi:10.1016/j.rse.2007.03.027

Monteith, J.L., and M.H. Unsworth. 1990. *Principles of Environmental Physics*, Edward Arnold, London.

Moradi, A., K.M. Smits, J. Massey, A. Cihan, and J. McCartney. 2015. Impact of coupled heat transfer and water flow on soil borehole thermal energy storage (SBTES) systems: Experimental and modeling investigation. Geothermics. 57:56-72. doi:10.1016/j.geothermics.2015.05.007

Newman, B.D., B.P. Wilcox, S.R. Archer, D.D. Breshears, C.N. Dahm, C.J. Duffy, N.G. McDowell, F.M. Phillips, B.R. Scanlon, and E.R. Vivoni. 2006. Ecohydrology of water-limited environments: A scientific vision. Water Resour. Res. 42(6). doi:10.1029/2005WR004141

Ochsner, T.E., R. Horton, and T. Ren. 2001. A new perspective on soil thermal properties. Soil Sci. Soc. Am. J. 65:1641-1647.

Oke. T.R. 1978. Boundary layer climates. Methuen & Co Ltd. London.

Or, D., P. Lehmann, E. Shahraeeni, and N. Shokri. 2012. Advances in soil evaporation physics – a review. Vadose Zone J. doi:10.2136/vzj2012.0163.

Peters, D.B. 1960. Relative magnitude of evaporation and transpiration. Agron. J. 52:536-538.

Qiu, G.Y., K. Momii, T. Yano, and R.J. Lascano. 1999. Experimental, verification of a mechanistic model to partition evapotranspiration into soil water and plant evaporation. Agric. For. Meteorol. 93(2):79-93. doi:10.1016/S0168-1923(98)00115-4

Ratto, C.R., P.A. Torrione, and L.M. Collins. 2011. Exploiting ground-penetrating radar phenomenology in a context-dependent framework for landmine detection and discrimination. IEEE Trans. Geosci. Remote Sens. 49(5):1689-1700.

Riou, C. 1977. Evaporation du sol nu et repartition des pluies – Relations établies en Tunisie à partire des résultats des cases lysimétriques. Annales de l'INRAT. 50(4). INRAT, Tunisie, 24 pp. (Also published in Cahiers de l'ORSTOM, Sér. Hydrol. XIV(3):285-295.

Sakai, M., S.B. Jones, and M. Tuller. 2011. Numerical evaluation of subsurface soil water evaporation derived from sensible heat balance. Water Resour. Res. 47(2). W02547. doi:10.1029/2010WR009866

Sakaki, T., A. Limsuwat, K.M. Smits, and T.H. Illangasekare. 2008. Empirical two-point -mixing model for calibrating the ECH2O EC-5 soil moisture sensor in sands, Water Resour. Res. 44:W00D08.

Sakaki, T., and T.H. Illangasekare. 2007. Comparison of height-averaged and point-measured capillary pressure-saturation relations for sands using a modified Tempe cell. Water Resour. Res. 43(12):W12502. doi:10.1029/2006WR005814

Sellers, P.J., Y. Mintz, Y.C. Sud, and A. Dalcher. 1986. A simple biosphere model (SIB) for use with general circulation models, *J. Atmos. Sci.,* 43(7):505-531, doi:10.1175/1520-0469(1986)043<0505:ASBMFU>2.0.CO;2.

Shahraeeni, E., and D. Or. 2010. Thermo-evaporative fluxes from heterogeneous porous surfaces resolved by infrared thermography. Water Resour. Res. 46. W09511. doi:10.1029/2009WR008455

Smits, K.M., A. Cihan, T. Sakaki, S.E. Howington, J.F. Peters, and T.H. Illangasekare. 2012. Soil moisture and thermal behavior in the vicinity of buried objects affecting remote sensing detection: experimental and modeling investigation. IEEE Transactions on Geoscience and Remote Sensing. doi:10.1109/TGRS.2012.2214485

Stewart, B.A., and E. Burnett. 1987. Water conservation technology and rainfed and dryland agriculture. In: Jorden, W.R. (Ed.), Water and Water Policy in World Food Supplies, A&M University Press, College Station, TX, pp. 355-359.

Sutherland, R.A. 1986. Broadband and spectral emissivities (2-18 μm) of some natural soils and vegegation. J. Atmos. Oceanic Technolo. 3:199-202.

Trambouze, W., P. Bertuzzi, and M. Voltz. 1998. Comparison of methods for estimating actual evapotranspiration in a row-cropped vineyard. Agric. For. Meteorol. 91(3):193-208. doi:10.1016/S0168-1923(98)00072-0

Trautz, A.C., K.M. Smits, P. Schulte, and T.H. Illangasekare. 2014. Sensible heat balance and heat-pulse method applicability to in situ soil-water evaporation. Vadose Zone J. 13(1). doi:10.2136/vzj2012.0215

van de Griend, A.A., and M. Owe. 1994. Bare soil surface resistance to evaporation by vapor diffusion under semiarid conditions. Water Resour. Res. 30:181-188.

van Genuchten, M.T. 1980. A closed-form equation for predicting the hydraulic conductivity of unsaturated soils. Soil Sci. Soc. Am. J. 44(5):892-897.

Xiao, X., J.L. Heitman, T.J. Sauer, T. Ren, and R. Horton. 2014. Sensible heat balance measurements of soil water evaporation beneath a maize canopy. Soil Sci. Soc. Am. J. 78(2):361-368. doi:10.2136/sssaj2013.08.0371

Xiao, X., R. Horton, T.J. Sauer, J.L. Heitman, and T. Ren. 2011. Cumulative evaporation as a function of depth and time. Vadose Zone J. 10:1016-1022. doi:10.2136/vzj2010.0070

Xiao, Z., S. Lu, J.L. Heitman, R. Horton, and T. Ren. 2012. Subsurface soil-water evaporation with an improved heat-pulse probe. Soil Sci. Soc. Am. J. 76:876-879. doi:10.2136/sssaj2011.0052n

Yan, H., C. Zhang., H. Oue, and H. Sugimoto. 2012. Comparison of different methods for estimating soil surface evaporation in a bare field. Meteorol. Atmos. Phys. 118:143-149. doi:10.1007/s00703-012-0213-9

Zeggaf, A.T., S. Takeuchi, H. Dehghanisanij, H. Anyoji, and T. Yano. 2008. A Bowen ratio technique for partitioning energy fluxes between maize transpiration and soil surface evaporation. Agronomy J. 100(4):988-996. doi:10.2134/agronj2007.0201

CHAPTER 5 HEAT AND MASS TRANSFER BEHAVIOR FROM DISTURBED AND MIXED SOILS: LABORATORY SCALE EXPERIMENTAL AND ANALYTICAL INVESTIGATION

As with previous chapters, prior to any discussion regarding the specifics of this chapter, the intellectual contribution of this portion of the research is specified along with identification of the author's contribution to the work. This research increases knowledge in the field of research regarding heat and mass transfer as affected by subsurface soil heterogeneities near the land-atmosphere boundary using laboratory bench scale experiments. Although there have been a variety of studies investigating vertical textural contrasts (e.g., Or et al., 2012) as well as subsurface heterogeneity (e.g., Lassen et al., 2015), no study was identified that examined the combined effect of vertical and horizontal textural contrasts that occur due to landmine emplacement in both homogeneous and layered soil environments. Six different experiments were performed that included varying boundary and initial conditions as well as soil surface conditions enabling comparison between heat and mass transfer processes as a function of the varying conditions. The robust experimental data sets collected with high spatial and temporal resolution are a significant contribution that serve as a repository for future research efforts undertaken to verify modeling efforts against measured characteristics (e.g., temperature, soil moisture, relative humidity). Additionally, analytical modeling of evaporation from the undisturbed (tight packed) and disturbed (loose packed) regions across the surface enabled identification of the relative contribution to overall evaporation under ambient conditions. The data sets generated and analysis of contribution from each region to total evaporation applies to poorly graded, well sorted sand of high quartz content (>98%) with bare soil surface conditions. All experimental and analytical work was completed by the author of this dissertation. The experimental work enabled direct comparison of

modeled evaporation. Additional work by the author, involved developing a user's guide for individual pressure transducer sensors used in experiments 5 and 6. This user guide was made available to all members of the CESEP research group and is listed in Appendix A.

5.1 Abstract

Soil disturbances caused by landmine emplacement significantly alter heat and mass transfer processes. The contrast between the original parent soil material and the disturbed soil created that is placed back into a dug hole to cover and bury a landmine changes the physical properties of the soil. These changes and the resulting contrasts in saturation and temperature between the surrounding undisturbed soil and disturbed soil above the landmine provide the basis of detection for numerous technologies. The algorithms employed by the technologies to enable detection are in turn based upon an understanding of the physical process of heat and mass transfer in the subsurface environment where a landmine is emplace. Therefore, there is a continual need to increase understanding of the various physical processes effected through landmine emplacement. Despite this fact, there are very few studies dedicated to studying the physical changes that occur and are associated with heat and mass transfer affects. An experimental and analytical investigation was conducted to evaluate the impact of the physical properties that change due to landmine burial processes on both a homogenous and a layered soil. Six experiments were conducted under varying initial and boundary conditions. Results demonstrate that soil disturbance and mixing increases evaporation and water loss compared to undisturbed soil conditions. When disturbed soil is adjacent to a tightly packed undisturbed soil, higher evaporation occurs from the tightly packed soil compared to the loose disturbed soil. Additionally, slightly higher evaporation rates occur from upstream soils than downstream, based upon atmospheric demand. Measured and

analytically modeled evaporation rates exhibited a high level of agreement regarding these finding under ambient conditions.

5.2 Introduction

Understanding heat and mass transfer occurring near the soil surface is of interest across disciplines (e.g., atmospheric science, hydrology, industry). The flux across this boundary requires consideration of energy transfer, phase change, and liquid-water displacement (Shokri et al., 2010) and are affected by hydraulic and thermal processes of the soil (e.g., capillarity). One discipline that is greatly affected by the understanding of land-atmosphere fluxes is mine detection. When a mine is buried in the ground, the soil conditions are altered through the process of mine emplacement. Parent, undisturbed soil is removed causing an altered, disturbed soil. The original parent soil and the disturbed soil that is placed back into the hole above the mine vary in terms of their hydraulic and thermal properties and therefore environmental behavior. These soil changes (disturbance vs. no disturbance) result in differences in saturation and temperature between the surrounding undisturbed soil and disturbed soil above the mine and provide the basis of detection for numerous technologies (e.g. ground penetrating radar, thermal imagery, chemical sniffing) (Maksymonko et al., 1995; Phelan and Webb, 1997; Bruschini and Gros, 1998; English, 2000; Deans et al., 2001; Wang et al., 2013; Krueger et al., 2015; Shire et al., 2015; Yip et al., 2015). The algorithms employed by the technologies to enable detection are in turn based upon an understanding of the physical process of heat and mass transfer in the subsurface environment where a landmine is emplace. Therefore, there is a need to increase our understanding of the how the soil disturbance effects the soil moisture and temperature in the vicinity of a mine as well as the mass flux at the soil surface.

Research on vertical textural contrast in porous media has been conducted by Lehmann and Or (2009), Nachshon et al. (2011) and Shokri and Or (2013). Lehmann and Or (2009) investigated evaporation and capillary pumping across the vertical textural contrasts between two sands, finding that the evaporation rate in a heterogeneous soil is greater than that in a homogeneous soil. Capillary pumping is defined as the capillary pressure difference between large pores at the drying front and fine pores at the surface which induces liquid flow. However to date, no research has been identified that considered the impact of multiple vertical and horizontal textural contrasts that ensue from landmine emplacement both in homogeneous soil and in soil with an initial coarse layer overlying a finer layer (i.e., a typical soil profile). With a layered soil that is impacted by mine emplacement activities, the soil that is removed may result in a mixed soil dependent on the depth of the top coarse layer.

Prior to conducting the experimental investigations associated with this chapter, visualization of the transport processes that occur along a vertical textural contrast within a loose and tightly packed soil is reviewed. Initially during Stage I evaporation, the packing conditions have relatively negligible impact on evaporation as both regions remain hydraulically connected with the surface. Therefore, both regions exhibit the same evaporation rate. However as drying continues two significant events occur that contribute to the loose disturbed soil no longer remaining hydraulically connected with the surface. These events include water loss from the loose soil due to evaporation (loose packing enables more evaporation as a result of less capillarity compared to the tight, undisturbed soil) and capillary pumping occurs from the loose disturbed soil into the tight undisturbed soil. This capillary pumping occurs below the surface as the loose soil is now under diffusion-limited interaction with the atmosphere. The capillary pumping from the loose soil to the tightly packed soil enables the tightly packed soil to remain hydraulically

connected to the surface for a longer period than if the soil had no disturbance. Therefore, the tight packed soil exhibits a higher evaporation rate than the loose packed soil. As drying continues, the tight packed region loses direction hydraulic connection with the surface. At this point both regions are in Stage II evaporation with the tight undisturbed soil experiencing a rapid rate of decrease in evaporation. The evaporation rates between both the regions then approach the same evaporation rate. The difference in elevation of the drying front between the two soil regions is directly related to the air entry pressure of each soil.

Translating these concepts to an originally layered undisturbed soil that is then impacted by landmine burial procedures, the response differs from that discussed above. The fundamental conditions of consideration include the soil water retention curve (SWRC) of the parent soils as well as the SWRC based upon the soil mixture resulting from digging through the layered soil, having the soil mix, and then placing the soil mixture back in the dug hole to bury the landmine. The driving factor for subsurface water flow is based upon capillarity. However with a layered parent soil configuration, the pore space of the tight packed coarse top layer of soil may in fact be larger than the pore space associated with the loose packed soil mixture. Under these conditions, capillary flow may reverse from that previously discussed and result in water flow from the undisturbed coarse layer into the disturbed binary mixture. In fact from work described in Chapter 3, any mixture between a coarse and fine sand regardless of percentage of coarse and find sand parent components results in finer pore space of the mixture compared to the coarse parent sand. This is a function of the fine grains occupying the inter-pore space between the larger sand grains. It is important to acknowledge that the loss of water from the coarse top layer of soil will result primarily from evaporation; however, capillary pumping may likely occur at the boundary between the coarse tight soil and the loose mixture.

The primary focus of the study was to improve our current understanding of the characteristics associated with and the effects of soil disturbances on evaporation behavior at both soil-soil and soil-atmospheric interfaces. In this study, to better understand the effect of heterogeneous porous surfaces on the coupled water-vapor-heat flow processes in the shallow subsurface, we conducted six laboratory experiments performed under varying hydraulic and thermal boundary conditions using bench scale physical models and a unique low velocity porous media/wind tunnel, allowing for better control and gathering of accurate data at scales of interest not easily conducted in the field. Research presented herein compares lysimeter measured evaporation with analytically modeled evaporation for the purpose of identifying individual region (i.e., tight and loose) contribution to overall evaporation. First, material and methods used to generate the experimental data is discussed. Then, experimental results are provided and analyzed as a function of the different boundary conditions. Next, fundamental concepts of the analytical model selected are presented. Finally, the experimental and modeled results are compared with key findings discussed.

5.3 Material and Methods

In this section, the experimental apparatus is described, sand materials, and experimental procedures.

5.3.1 Experimental Apparatus

Three different two-dimensional soil tanks were constructed. Two with an internal length, width, and height of 45, 9, and 30 cm (hereafter referred to as Tank 1 and Tank 2) and one with an internal length, width, and height of 25, 9.1, and 55 cm respectively (hereafter referred to as Tank 3). All were built using 1.2 cm thick acrylic (specific heat, 1464 J kg^{-1} K^{-1}; thermal conductivity,

0.2 W m^{-1} K^{-1}). Tank 1 and Tank 2 were interfaced with the same open-ended wind tunnel (hereafter referred to as Wind Tunnel 1) constructed out of galvanized steel ducts with an upstream length of 1.82 m and a downstream length of 2.71 m. Tank 1 and Tank 2 along with the interface associated with Wind Tunnel 1 are shown in Figure 5.1.

A series of three 4 ft T5 high output fluorescent light bulbs (6,000 initial lumens and a color temperature of 4800 K) were mounted in parallel above Wind Tunnel 1 and provided representative solar radiation. The light source (96-watt HydroFarm FLP24) was mounted 83.5 cm above the soil surface. The bulbs were cycled on and off for 12-hour periods (8 a.m. to 8 p.m.) enabling replication of the diurnal cycle.

Tank 3 was connected on both the upstream and downstream boundaries with an open-ended wind tunnel (Figure 5.2). As with the wind tunnel associated with the dual tank set up (Figure 5.1), the wind tunnel established with Tank 3 (hereafter referred to as Wind Tunnel 2) was constructed out of the same material with the dimensions shown in Figure 5.2. Air flow through both wind tunnels occurred by inducing an air current via a 15.2 cm diameter Pro DB6GTP in-line duct fan (Suncourt, Inc.; USA). This fan was located downstream and the air speed being induced across the surface of the tank was controlled by a VS200 variable speed controller (Suncourt, Inc.; USA). The wind speed induced across the surface was measured using a 167-12 stainless steel pitot-static tube (Dwyer Instruments, Inc.; USA, accuracy of ± 5%). Code written by Dr. Andrew Trautz enabled data collection using a CR1000 (Campbell Scientific; USA) data logger interfaced with a computer and downloaded using a PC200W program. Data was collected every 60 minutes. Five Infrared Salamander Model FTE 500-240 ceramic radiative heaters (Mor Electric Heating Assoc., Inc.; USA) were connected to the upstream base of Wind Tunnel 2 (Figure 5.2) in order to enable a continuously heated air stream or diurnal heating based upon experimental needs. An

infrared temperature sensor (Exergen Corporation; USA) enabled regulation of the climate conditions (i.e., temperature) through interfacing with a 2104 temperature control system (Chromalox; USA).

Tank 1, 2 and 3 were outfitted with sensors installed horizontally at 5 cm increments for measuring soil moisture, temperature, thermal properties, and relative humidity across the width of the tanks and down to a depth of 22.5 cm from the soil surface. All measurements occurred at an interval of 60 minutes and data was stored on Em50 5-channel data loggers (Decagon Devices, Inc.; USA) for easy retrieval. EC-5 dielectric soil moisture sensors (Decagon Devices, Inc.; USA, accuracy = ± 3%) enabled calculation of soil moisture throughout the tank. The two-point α-mixing model developed by Sakaki et al. (2008) enables conversion of an analog-to-digital converter number (ADC count) as recorded by the EC-5 into a volumetric water content. ECT sensors (Decagon Devices, Inc.; USA, accuracy = ± 1 °C) enabled measurement of subsurface temperature and atmospheric temperature at 8.5 cm above the surface for Tank 3.

Tank 1 and 2 were outfitted with individual tensiometers for measuring water pressure at 2.5 cm and 7.5 cm below ground surface (bgs) across the width of the tank. Measurement of the water pressure coupled with measurements of soil water saturation (EC-5 sensors) enables accurate depiction of soil water retention curves (SWRC) based upon the different subsurface soil conditions (i.e., different layered soil and disturbed soil mixture as shown in Figure 5.1). Although small cell experiments are used to provide soil water retention curves, the conditions of the small cell experiments will vary in porosity and density which we know from Task 1 have a significant influence on the SWRC and the thermal conductivity-water content (λ -θ) relationship. Therefore, the importance of being able to acquire these relationships for the exact experimental conditions used to gather all other data cannot be overstated as this leads to the ability to identify parameters

based upon measured SWRC such as van Genuchten parameters that are used in a variety of analytical and numerical models - such as predicting thermal conductivity in the Lu and Dong (2015) model discussed as part of Task 1. Tensiometers (SoilMoisture Equipment Corp., Goleta, CA; small porous cups, diameter = 0.64 cm, length = 3 cm; air-entry value = 51 kPa) were installed vertically and connected to pressure transducers (Omega Engineering, Inc., Stamford, CT; Model PX26, ± 1% psi for range 0-250 psi; operating temperature = -40^{o}C to 85^{o}C). Automatic measurements were made every 60 minutes and written directly to file using LabVIEW software (National Instruments Corp.; USA). Data was monitored and recorded using a CR1000 data logger (Campbell Scientific; Logan, UT).

Thermal property SH-1 sensors (Decagon Devices, Pullman, WA; dual needle, length = 3 cm, spacing = 6 mm, ± 10% accuracy from 0.2 to 2 W m^{-1} K^{-1} for λ, ± 0.001 ^{o}C for temperature) connected to a KD2 Pro™ thermal property analyzer were used to measure thermal conductivity λ (W m^{-1} K^{-1}) and soil temperature (^{o}C) within each soil tank and soil type across (i.e., tightly packed, loosely packet, disturbed mixture, top coarse soil, and fine overlain soil. Soil thermal measurements were made at 60 minute intervals to allow thermal gradients to dissipate. The SH-1 sensor consists of two needles containing a thermistor in one needle and a heating element in the other. A current is passed through the heating element in one needle while the time dependent temperature response is monitored over time in the second needle. A dual needle algorithm (Abramowitz and Stegun, 1972) based on the line heat source analysis described in Carslaw and Jaeger (1959) and Kluitenberg et al. (1993) along with the temperature measurements and knowledge of the heat generated (~22.3 W m^{-1}) during heating (1 min) and cooling cycles (1 min) was used to calculate the λ of the soil (Decagon Devices, 2014).

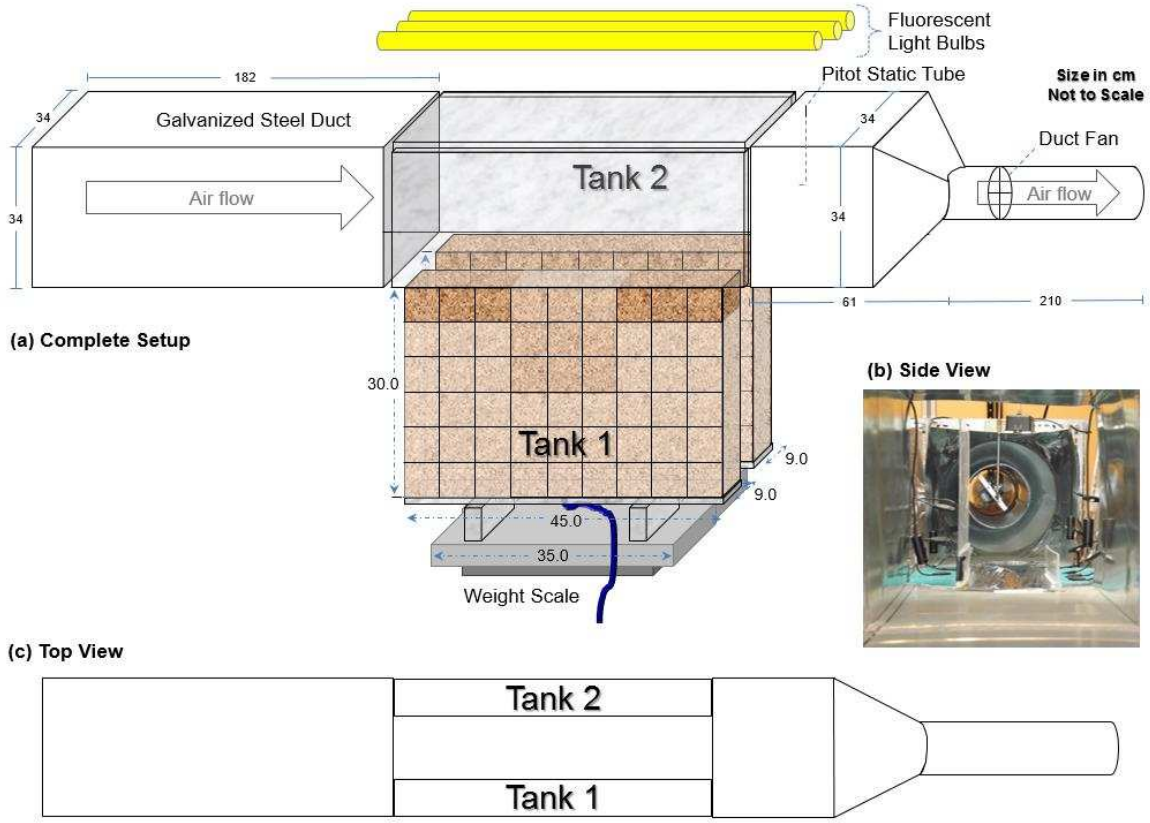

Figure 5.1. Sketch of Tank 1 and Tank 2 interfaced with Wind Tunnel 1 providing a side view and top view of the experimental apparatus. The top layer of #12/20 coarse sand is shown as the darkest shading ( ), the underlying #110 sand is shown as the lightest shading ( ), and the disturbed, loose mixture of #12/20 and #110 sand is shown in the center of Tank 1 ( ).

Heat pulse sensors based upon Heitman et al. (2008) design were emplaced in each tank. The sensor consists of three needles, each containing a thermistor, with the middle needle containing a resistive heater for generating heat pulses connected into an epoxy body. The automatic measurements were made every 60 minutes and written directly to file using LabVIEW software (National Instruments Corp.; USA).

EHTs (Decagon Devices, Inc.; USA, temperature accuracy = ± 1 °C, relative humidity accuracy = ± 3% between 5 and 100%) enabled measurement of both relative humidity and

temperature. Sensor were placed in firm contact with the surface, above the soil surface, and in Wind Tunnel 1 and 2 at locations upstream and downstream.

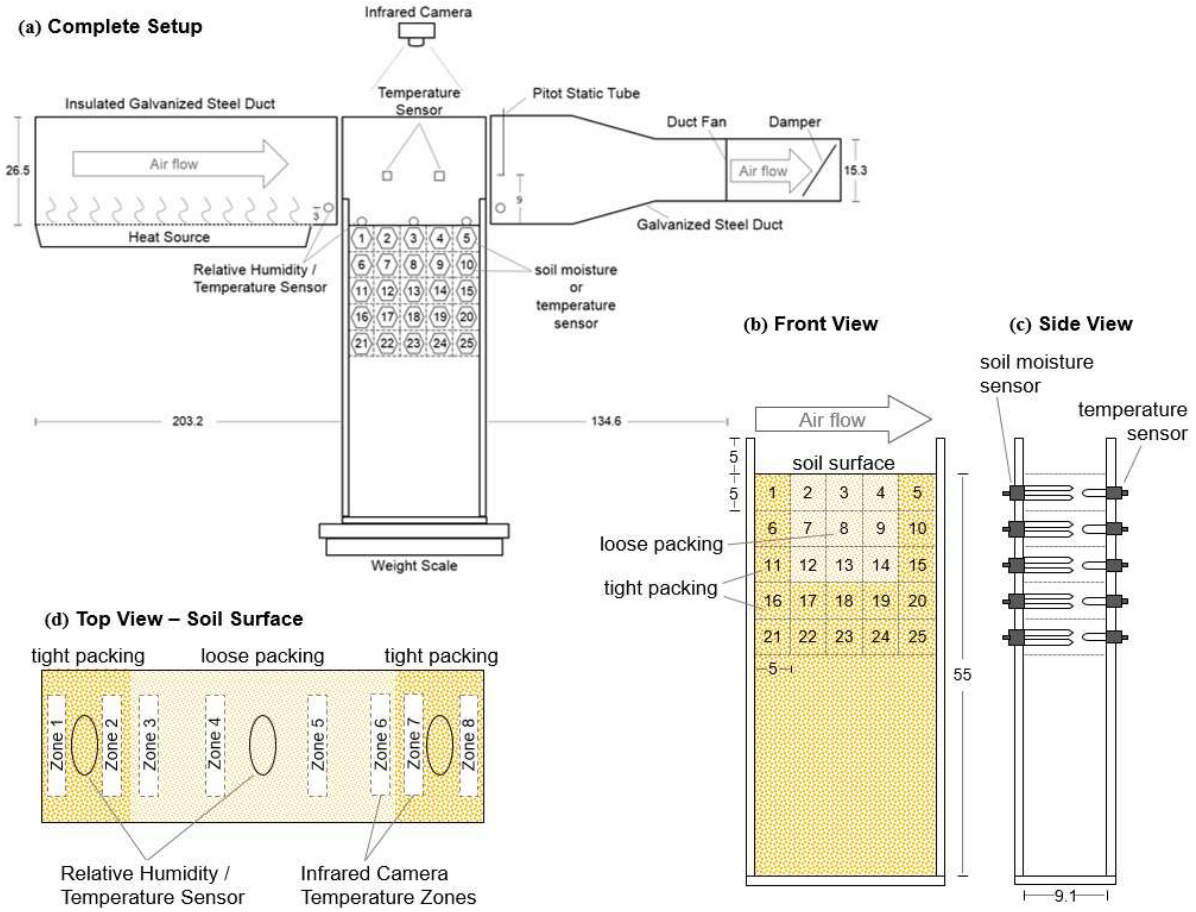

Figure 5.2. Sketch of Tank 3 interfaced with Wind Tunnel 2 providing a side view, top view, and view of primary instrumentation locations similar for all tanks. Tank is used with #30/40 sand. Tight and loose packing (disturbed sand conditions) are shown.

VP-3s (Decagon Devices, Inc.; USA, temperature accuracy = ± 0.3 °C, relative humidity accuracy = ± 2% to 3% based upon temperature and RH) were used to simultaneously measure

relative humidity and temperature directly. The sensors were located in the influent and effluent air streams for Wind Tunnel 1 and 2.

An additional source used to obtain surface temperatures was a 320×240 pixel resolution Model 7320 infrared camera (Infrared Cameras, Inc. (ICI); USA, spectral range = 7-14 μm, accuracy = ± 1^{o}C). The software (ICI; USA) that comes with the camera instantaneously applies corrections for transmission, reflection, and emissivity. Beyond the IR camera, a PowerShot Se IS digital camera (Canon; USA) was used to monitor the propagation of the drying front via CameraWindow software (Canon; USA).

Tanks 1, 2, and 3 were placed on a separate 65 kg ± 1 g Model 11209-95 weighting scale (Sartorius Corp.; USA). The measurements were transcribed onto a dedicated computer through LabVIEW software (National Instruments Corp.; USA). The weight measurements were used in a mass balance to determine evaporation rates.

5.3.2 Sand Materials

Three different sands were used in the experiments associated with this work. Tank 1 and 2 used #110 and #12/20 sand. Sand properties associated with both sands are provide in Section 3.3.2 and Table 3.1. Select properties of the binary mixture based upon the parent sands (i.e., #110 and #12/20) are provided in Table 5.1. Tank 3 used Accusand #30/40 (Accusands, Unimin Corps.; USA, mean grain size = 0.420 to 0.595 mm, uniformity coefficient = 1.2, particle density = 2.65 g cm^{-3}, grain shape = rounded, mineralogical composition = 99.8% quartz). Other select properties of the #30/40 test sand are provided in Table 5.1.

Table 5.1. Sand properties as characterized by Smits and Limsuwat (2009) for #30/40 Accusand and for the loose mixture of #12/20 and #110 parent sands.

Packing Conditions	Sand	Dry Bulk Density (g cm^{-3})	Air Entry Pressure (cm H_2O)	Residual Water Content (m^3 m^{-3})	Van Genuchten Model Parameters*	
					α (cm^{-1})	n (–)
Tight	#30/40	1.79	16.1	0.028	0.04	20.53
Loose	#30/40	1.54	9.6	0.024	0.06	20.00
Loose	Mixture (#12/20 & #110)	1.70	70.8	0.008	0.01	6.95

*Parameters determined using RETC based upon experimental data

The soil water retention curves (SWRC) for tight and loose packed conditions are shown in Figure 5.3 for experiments conducted in Tank 3. The SWRC for tight packed parent sands (#12/20 and #110) and the loose packed, disturbed mixture are shown in Figure 5.4 for experiments conducted in Tank 1 and 2. Experiments similar to those discussed in Chapter 3 were conducted to obtain the SWRC with the nuance of no tamping or disturbance of the small cell apparatus in order to obtain loose packing conditions.

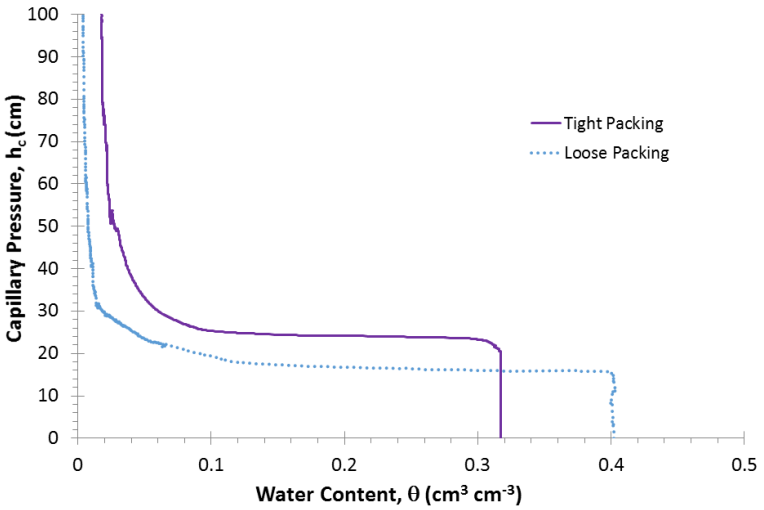

Figure 5.3. Soil water retention curve (SWRC) for #30/40 Accusand for tight and loose packing conditions.

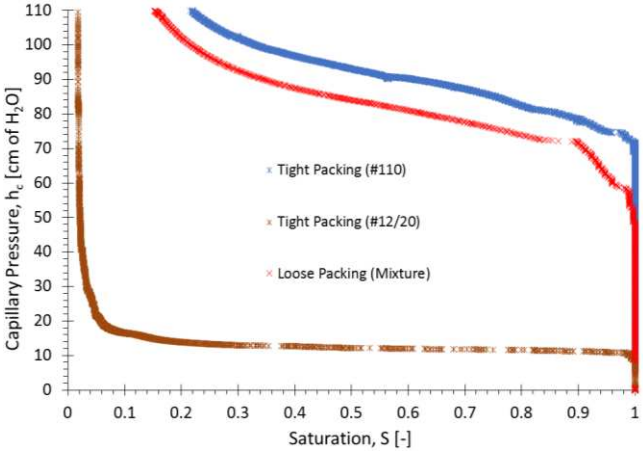

Figure 5.4. Soil water retention curve (SWRC) for tight packing conditions for #12/20 and #110 sands and for loose packing conditions of the mixture of the two sands.

5.3.3 Experimental Procedure

The experimental procedures followed were similar for both Tanks 1 and 3 regarding establishing a tank with a disturbed soil surrounded by an undisturbed, tight packed soil. Therefore, the discussion that follows is related directly to Tank 3, but applies to Tank 1 as well. Tight packing conditions were pursued evenly throughout the tank up to the point that only the top 15 cm of the tank remained to be packed. At all times, the water level (using deionized water) was maintained above the sand level to ensure the sand was packed under fully saturated conditions. With 15 cm left to pack to reach the soil surface, two baffles were pushed at least 7 cm into the tight packed soil at locations to purposefully isolate the middle 15 cm x 15 cm cell of the tank. This region represents the same dimensions associated with a hole dug for emplacement of an antipersonnel mine. The outer boundaries were then packed under tight conditions to the surface level. Tight packing conditions throughout the tank were achieved by placing the sand in 2.5 cm lifts and then pushing the sand down manually as well as tamping all four sides of the tank using a rubber mallet following the same procedures as Sakaki and Illangasekare (2007). At that point, the tank was

moved in place on top of the scale in order to set the conditions for minimal disturbance of the tank for the purpose of packing the center section under loose packing conditions. The sand was gently placed in the center section through pouring the sand at a slow, relatively constant rate until the sand was level at the surface with the tight packed regions. Extreme care was taken to remove the baffles with minimal disturbance to the tank. Once the baffles were removed, sensors were placed on the surface as appropriate and data recording for the experiment began

With respect to Tank 1 and Tank 2 (Figure 5.1), each consisted of fine-grained #110 sand in the bottom 25 cm of the tank overlain by coarse-grained #12/20 sand in the top 5 cm of each tank. Tank 2 was tightly packed throughout the entire tank. Tank 1 was tightly packed except for the middle portion which was a mixture of the parent sands that made up the layered soil profile. With a depth of 10 cm of #110 and 5 cm of #12/20, the mixture was a C3F7 mixture based upon 1/3 coarse sand and 2/3 fine sand. The binary mixture was loosely added to the tank without compaction. As with Tank 3, Tank 1 and 2 were wet-packed with deionized (DI) water. However, for the dual tank apparatus, non-toxic blue dye (envision Environmental Eduction, LLC; USA) was added to the DI water in the ratio of 40 mL of dye for every 9,570 mL of DI water for the purpose of enabling visualization of the drying front propagation in both tanks throughout the experiment. This is significant because future research efforts focused on numerical modeling of soil moisture movement may be compared to the observations as a check and balance if the physics of the model is captured properly. Figure 5.5a shows Tank 1 with both tight packed regions in place and the baffles enabling the disturbed region to remain available for loose packing. Figure 5.5b shows Tank 1 with all the disturbed, mixture in place. Extreme care was taken during the removal of the baffles to maintain the sharp boundary between the tight packed boundary and the disturbed mixture.

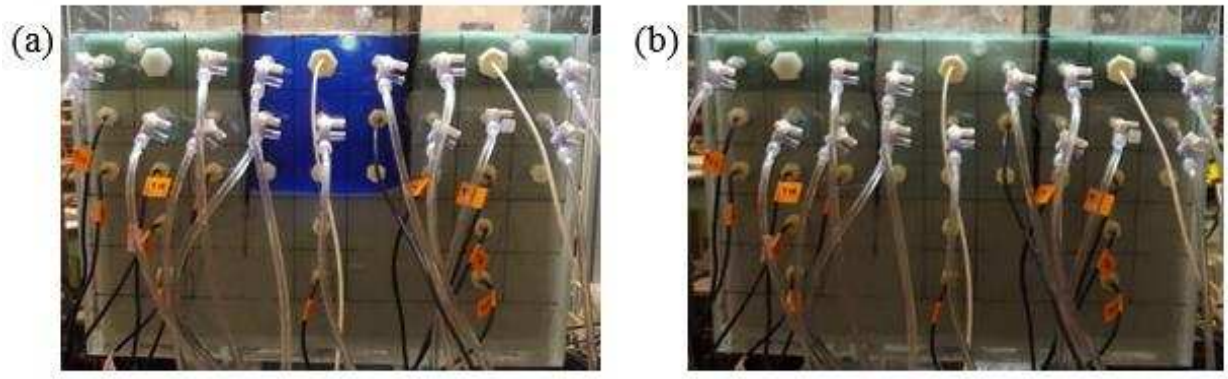

Figure 5.5. Tank 1 preparation for experimentation showing the (a) tight packed regions of #110 sand in the bottom 25 cm of the tank overlain by #12/20 sand in the top 5 cm of the tank and the (b) loose packed, disturbed inclusion of the C3F7 binary mixture in the center of the tank. Note that the metal baffles used to separate the tight and loose packed regions were removed prior to the beginning of the experiment.

5.3.4 Experimental Summary

A total of six experiments were conducted under varying boundary conditions (e.g. air temperature, relative humidity, wind velocity) and initial conditions (i.e., saturation) as summarized in Table 5.2 and Table 5.3. The first four experiments were conducted using Tank 3 (Figure 5.2). The fifth and sixth experiments were conducted simultaneously using the apparatus shown in Figure 5.1 with the fifth experiment performed using Tank 2 and the sixth experiment using Tank 1. The first experiment (EX-1) was run under ambient conditions; the average temperature and relative humidity in the headspace above the soil surface was 22^{o}C and 0.19 respectively. In the second experiment (EX-2), the incoming air was continuously heated, using the temperature control system described in Section 5.3.1, with the average headspace temperature and relative humidity recorded as 45^{o}C and 0.10 respectively. Temperature was maintained with a range of approximately ±5.63^{o}C of the mean value. The third experiment (EX-3) simulated diurnal conditions by cycling the heating control system between two set temperatures (24 and 50°C) at 12

hour time increments. These first three experiments were initially fully saturated throughout the entire soil tank; evaporation was then allowed to occur freely throughout the duration of each experiment. In the fourth experiment (EX-4), a constant water table was maintained at a depth of 20.6 cm using a constant head device. The headspace temperature was maintained at approximately constant value of 66.1^{o}C and relative humidity of 0.01. Each experiment was run for 20 days. EX-4, the lowered water table experiment, followed the above procedures except that upon completion of the packing process, a constant head device attached to the tank was lowered to a depth of 20.6 cm. This allowed free drainage from the tank, establishing the final, steady state water table conditions. The fifth experiment (EX-5) was conducted under diurnal conditions established with the use of the overhead fluorescent light bulbs (Figure 5.1) and consisted of the tight packed layered soil configuration. The sixth experiment (EX-6) was conducted under the same conditions as EX-5 as a function of the dual tank set up and consisted of tight packed layered soil on the boundary and below the disturbed mixture in the center. Although the focus of this research was on the impact of soil disturbance and mixing, EX-5 enabled a point of comparison between the undisturbed conditions (EX-5) with the impact of soil disturbance akin to the impact of mine emplacement (EX-6).

Table 5.2. Average characteristics and conditions of Experiments 1-6.

Experiment	Average Headspace Temperature (°C)	Average Headspace Relative Humidity (%)	Average Surface Temperature (°C)	Average Wind Velocity (m s^{-1})	Initial Water Table Depth (cm)
EX-1	22.9	0.19	22.3	0.755	0
EX-2	57.5	0.10	32.5	1.094	0
EX-3*	50.2 / 24.0	0.2 / 0.12	29.8 / 22.5	0.986 / 0.710	0
EX-4	66.1	0.01	28.5	1.0532	20.6
EX-5	21.7	0.16	21.7	1.783	0
EX-6	22.4	0.16	21.1	1.783	0

*Diurnal heating cycle; therefore, values shown correspond to on/off cycle.

Table 5.3. Summary of final soil porosities for disturbed and mixed experiments.

	Porosity		
Experiment	Loose Packing[1]	Tight Packing (Sides)[2]	Tight Packing (Bottom)[3]
EX-1	0.440	0.319	0.319
EX-2	0.417	0.320	0.321
EX-3	0.449	0.318	0.315
EX-4	0.452	0.314	0.317
	C3F7 Disturbed Mixture	Tight Packed #12/20 (Top Layer)	Tight Packed #110 (Underlying Layer)
EX-5	None	0.327	0.369
EX-6	0.360	0.357	0.346

5.4 Experimental Results and Discussion

The results and discussion are presented in two parts. First, the focus is on the disturbed soil experiments of EX1-4. After that discussion, the focus transitions to the layered and disturbed soil experiments of EX5-6. For the discussion of results from EX1-4, experimental results for EX-1 are presented in full and then significant nuances are highlighted as a function of the varying boundary conditions for the other three experiments. Observed trends as well as differences between experiments are noted. Results from EX-1 (ambient conditions) are presented including graphs and summary tables of measured relative humidity and temperature, as well as calculated saturation from measured soil water content. Then, evaporation rates are compared as determined from weight loss and IR data. The discussion and results from EX5-6 are presented together as a function of both experiments conducted simultaneously using the dual tank apparatus (Figure 5.1). This effort enabled direct comparison of almost identical boundary conditions except for those at the surface based upon Tank 1 including a mixture and Tank 2 containing tight packed layered soil without the loose mixture.

The primary focus of the study was to improve our current understanding of the characteristics associated with and the effects of soil disturbances on evaporation behavior at both soil-soil and soil-atmospheric interfaces. The following in depth discussion of the experimental results of EX-1 provides an overview of the datasets generated for this study in terms of: cumulative evaporation, evaporation rate, soil moisture, subsurface temperature, relative humidity, and surface temperature. This section also provides a baseline for the discussion that will follow on the complex processes occurring within the soil (loose and tight packed regions) and atmosphere and at their interfaces (subsurface packing conditions and soil-atmosphere).

5.4.1 Evaporation based on Weight Data for EX1 (Ambient Conditions)

Total cumulative water loss which corresponds to cumulative evaporation (Figure 5.6) was determined from the continuous weight measurements made using the scale described earlier in Section 5.3.1. Cumulative weight measurements will not allow for the evaporation rates from each of the differently packed regions to be determined; for this, a surface energy balance (SEB) model was employed and will be discussed later. Stage I evaporation can be identified by the constant slope of the cumulative evaporation curve (Figure 5.6). The high evaporation rates are sustained by flow driven by high atmospheric demand (Yiotis et al., 2004; Lehmann and Or, 2009). The weight oscillation observed may be due to changes in atmospheric pressure within the laboratory where the experiments were performed. Stage II evaporation, often referred to as the falling-rate stage, involves the evaporation rate quickly decreasing as the drying front retreats beneath the soil surface, severing the hydraulic connection. This causes evaporation to become vapor diffusion limited (Van Brakel, 1980; Yiotis et al., 2004; Lehmann et al., 2008). Stage II is identified in the cumulative evaporation curve as the portion where the water loss as a function of time is no longer

linear. The smaller rate of gradual cumulative water loss is characteristic of vapor diffusion limited Stage II evaporation.

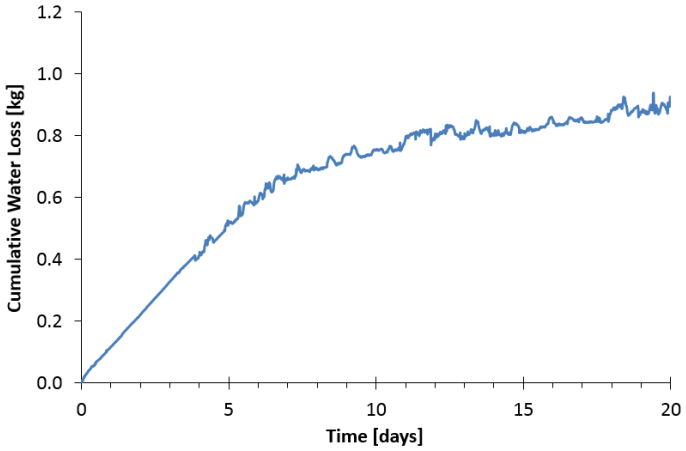

Figure 5.6. Cumulative water loss from EX-1.

5.4.2 Evaporation based on Drying Front Visualization for EX1 (Ambient Conditions)

The drying front marks the plane (when idealized) or interface that separates the fully saturated and partially saturated regions. The drying front can be used as a rough way of determining what stage of evaporation may be occurring (Lehmann et al., 2008; Shokri et al., 2010). Figure 5.7 enables visualization of the drying front propagation over the 20-day experiment as observed from the digital photographs taken of the soil tank on an hourly basis. The rate at which the drying front retreats throughout the tank is dependent on the soil hydraulic properties, which in this case differ based on the packing conditions (i.e. loose or tight packing). In EX-1, the water table and hence the drying front was initially located at the soil surface. The depth of the drying front increased rapidly in the loose packed region through day 5.5 (~10 cm) with less change from day 5.5 to day 25 (~6 cm). The slower rate of the drying front's propagation in the loosely packed sand region after day 5.5 is the result of vapor diffusion limited Stage II

evaporation. The retreat in the tight packed region trailed behind that of the loose packed region and was always higher than that of the loose packed region for two primary reasons. First, the air entry pressure of the tight packed sand is higher than the loose packed sand, 16.1 and 9.6 cm, respectfully (Table 5.1). Second, capillary pumping, resulted in the lateral movement of water from the loose packed to the tight packed regions and enabled the tight packed region to remain saturated longer than the loose packed region.

The change in the rate of drying front propagation can be used to roughly determine the change in the evaporative stage. As shown by Assouline et al. (2013), once the depth of the drying front reaches the depth associated with the air entry pressure, the evaporation rate changes from Stage I to Stage II. The rate of cumulative water loss during Stage I evaporation (Figure 5.6) corresponds to the rapid water loss which is visualized in terms of the drying fronts in Figure 5.7.

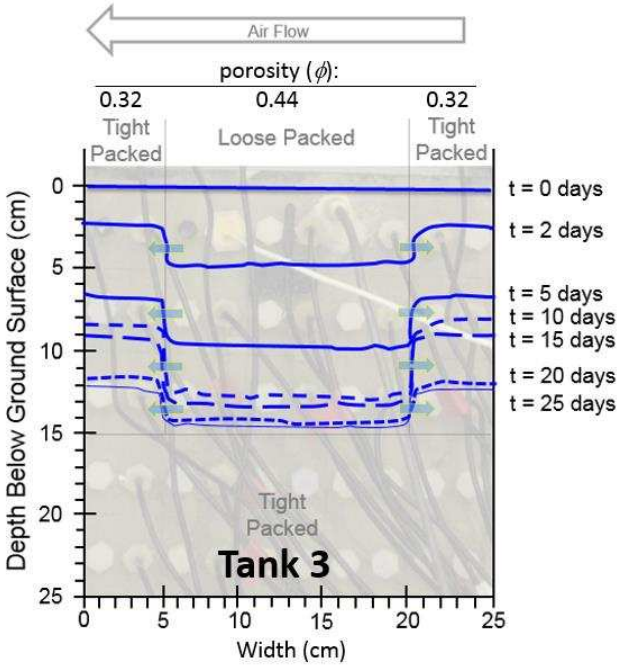

Figure 5.7. Drying front propagation within a heterogeneously packed sand tank under ambient conditions. Porosities shown for different packed regions. Arrows below the surface indicate direction of capillary pumping.

5.4.3 Surface Temperature of EX1 (Ambient Conditions)

The surface energy balance model employed in this study uses time-dependent surface and air temperature measurements (Figure 5.8). Temperatures fluctuated approx. ± 1°C in conjunction with the ambient room temperature due to the laboratory's climate control system. The average surface temperatures for the tight and loosely packed soils were similar, varying by less than 0.5°C. The initially cool surface temperature, approximately 2°C lower than the ambient headspace temperature, is the result of evaporative cooling associated with Stage I evaporation. As the drying front retreats into the soil (Stage II), the temperature of the soil surface increases due to the absence of evaporative cooling associated with the phase change close to the surface (Yiotis et al., 2007). This increase in temperature coincides with the same time identified by the change in rate of increase in cumulative water loss (Figure 5.6).

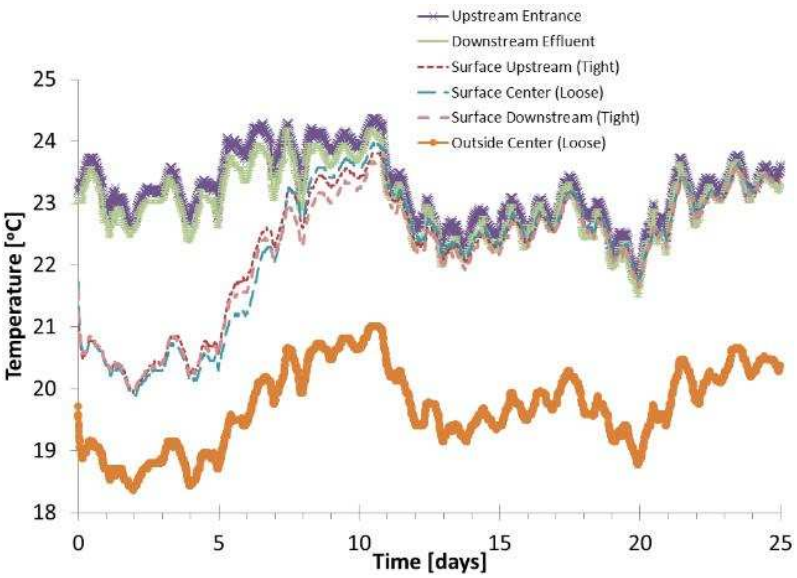

Figure 5.8. Surface and atmospheric temperatures. Temperature measured across the surface length, head space, influent and effluent air upstream and downstream of the soil surface, and outside on the front of the tank.

5.4.4 Relative Humidity of EX1 (Ambient Conditions)

The relative humidity data collected from sensors located in the headspace (Figure 5.2) contributed directly to air density calculations in the SEB model. Figure 5.9 portrays the humidity of the three soil packings and headspace upstream and downstream of the tank. The relative humidity remains at approx. 100% everywhere on the soil surface (i.e. upstream tight, loose and downstream tight) until day 8 when the loose soil surface humidity begins to decline. This time corresponds to the transition of the loose soil to Stage II evaporation. The loose packed center exhibited a steep rate of decrease in relative humidity from day 8 to 10.9 reaching a final, residual surface relative humidity of about 45% at day 20. The downstream tight packed region exhibited a gradual, relatively constant rate of decrease with the upstream tight packed region following approximately four days later. The preferential subsurface water flow from the loose center to the upstream tight packed region is evident due to the RH decreasing in the upstream tight packed region later than the downstream tight packed region. The reason for this preferential flow relates to the direction of flow of air above the soil surface. The upstream soil was exposed to a larger evaporative demand than the downstream soil in terms of both temperature and RH. This then enhanced the evaporation rate from the upstream soil lowering the demand downstream.

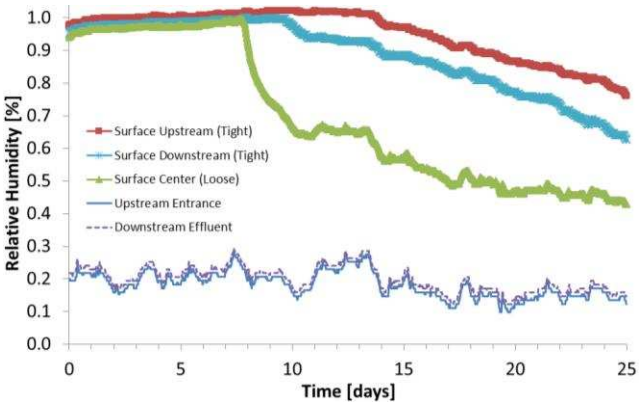

Figure 5.9. Relative humidity at the soil surface and above the soil surface for EX-1.

5.4.5 Saturation of EX1 (Ambient Conditions)

As mentioned in the material and methods section, the initial saturation conditions for EX-1 was fully saturated. At the start of the experiment, water was then allowed to evaporate freely. Figure 5.10 shows the degree of saturation as a function of time for the tight and loosely packed soil regions at the depths of 2.5, 7.5, and 12.5 cm below ground surface (bgs). As expected, the degree of saturation decreased faster in the loosely packed region than the tightly packed regions. Residual saturation at 2.5 cm bgs was reached in both the tight and loose packed regions by the completion of the experiment. At 7.5 and 12.5 cm bgs, the soil remained fully saturated (S=100%) for the first 2 days, corresponding to Stage I evaporation. At approx. 2 days, the soil in the loose region began to drain, rapidly decreasing the degree of saturation 7.5 cm bgs. In the tightly packed region, the soil 7.5 cm bgs remained fully saturated until approx. days 4 and 5.5 for the downstream and upstream tight regions, respectively. The immediate decrease in saturation 2.5 cm bgs (Figure 5.10a) denotes that the soil surface experienced drying almost immediately. For this experiment, there was very little Stage I evaporation.

5.4.6 Subsurface Temperature of EX1 (Ambient Conditions)

Temperature was measured throughout the sand tank as shown in Figure 5.11 and exhibits specific characteristics associated with each stage of evaporation. During the early part of the experiment (0-5 days), temperature throughout the depth and across the length of the tank remain relatively constant (±1°C). The observed differences in temperature between sensors with depth are well within the accuracy of the sensors. As the soil dried, the temperature increased. Temperatures across the length of the tank at the same depths remained almost identical while during Stage I evaporation. As the drying front retreated earlier in the loosely packed center, there was a corresponding increase in temperature sooner than in the tightly packed regions.

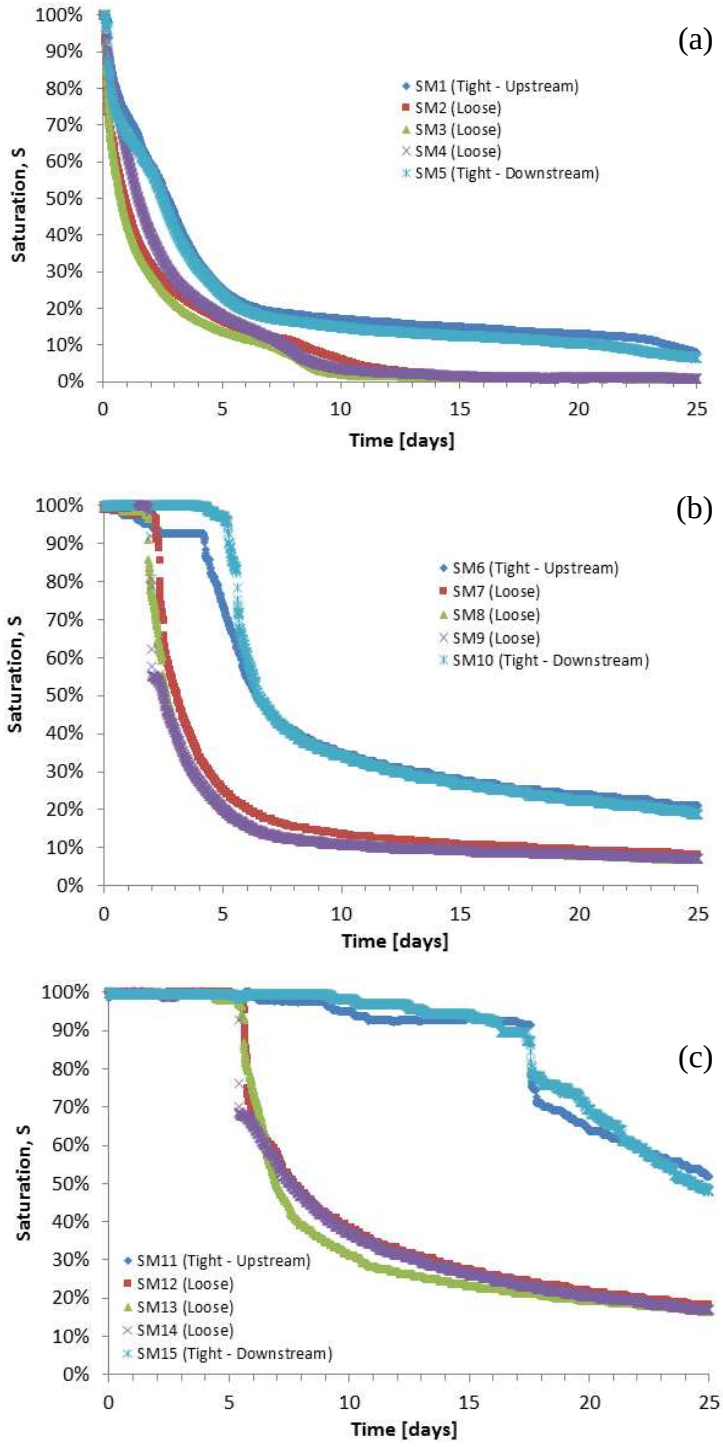

Figure 5.10. Soil moisture profiles across the length of the soil tank at varying depths within the heterogeneous packed region at (a) 2.5 cm bgs, (b) 7.5 cm bgs, and (c) 12.5 cm bgs.

.

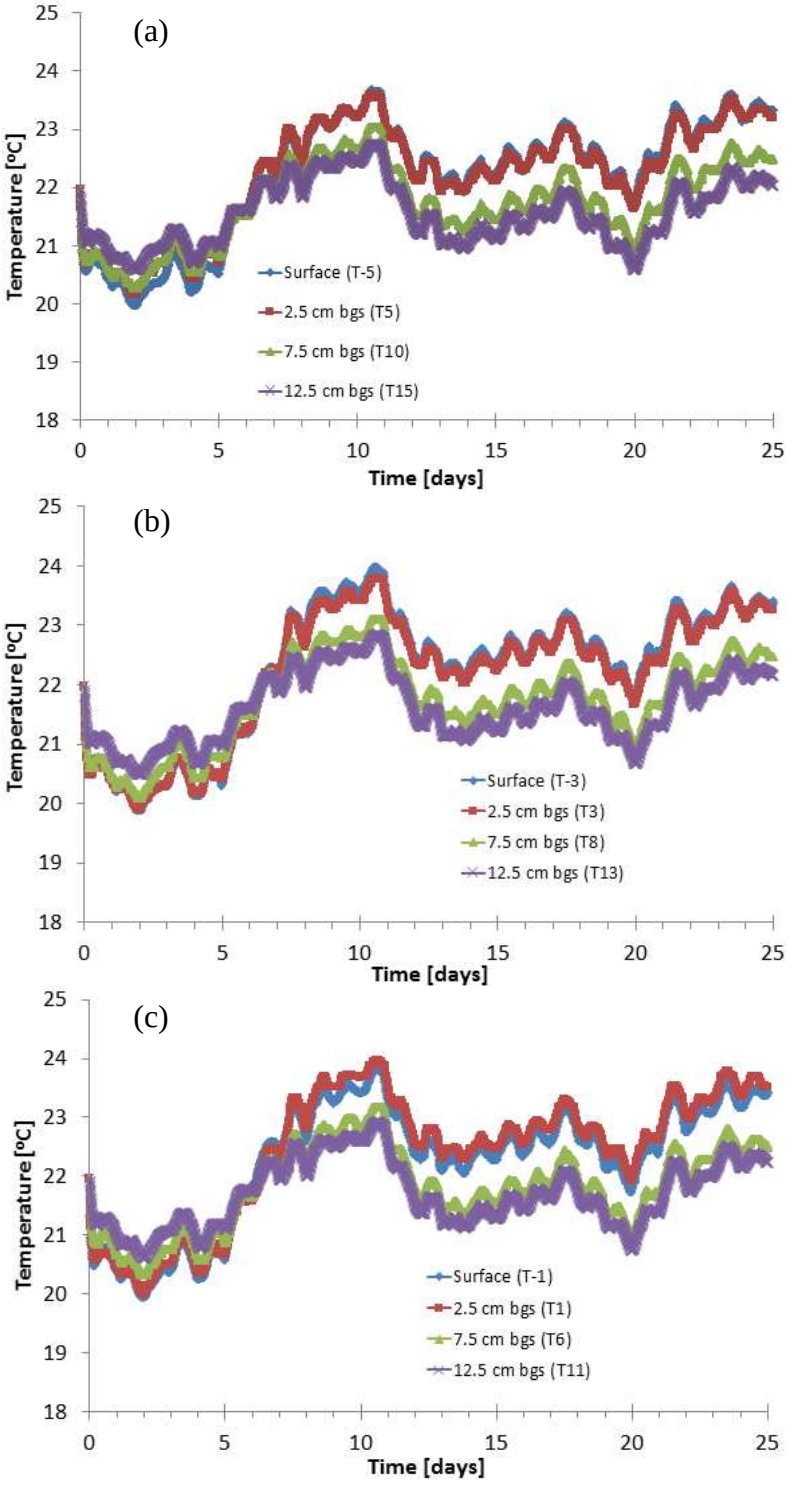

Figure 5.11. Measured temperature as a function of time for different packing regions within the soil tank for EX-1. Each graph (a-c) is associated with a column of sensors: (a) downstream tight packed region downstream, (b) center loose packed region, and (c) upstream tight packed region.

5.4.7 Experimental Results Comparison with EX-2, EX-3, and EX-4

The following sections provide a comparison between EX-1 as the baseline condition and EX-2, EX-3, and EX-4 to highlight the differences due to the variation in boundary conditions. The focus for the discussion remains centered on the disturbed soil boundaries between the tight packed and loose packed regions. The parameters evaluated between the four experiments conducted include evaporation rates, surface and subsurface temperature profiles, relative humidity, water flow and saturation.

5.4.8 Evaporation Comparison based upon Weight Analysis

The cumulative water loss for the four experiments is shown in Figure 5.12. As seen in the slope of the curves, the cumulative water loss for EX1-3 transitioned from a higher Stage I evaporation rate to a lower and almost constant Stage II evaporation rate at varying times. The higher atmospheric demand of EX-2 (elevated temperature) and EX-3 (diurnal effects) caused more evaporation compared to EX-1. This is consistent with that shown in Trautz et al. (2014).

EX-2 and EX-3 have similar time periods associated with the transition between Stage I, and II evaporation; however, the fluctuation in water loss is greatest in EX-3 due to the diurnal air temperatures. The reason for this is two-fold. First, the elevated temperature associated with both experiments results in an increased atmospheric demand causing more water loss. Second, the diurnal fluctuation in EX-3 could have resulted in condensation enabling increased water loss compared with EX-2. The cumulative water loss evaluated from the change in weight fluctuated by a factor of 10% due to the induced increase in evaporation during the heating cycle and recovery of the system when the heater was turned off. EX-4 (constant water table 20.6 cm bgs) shows a gradual increase in cumulative water loss. EX-4 began in Stage II evaporation and maintained a

relatively constant water loss throughout the experimental duration. The variability in cumulative water loss for EX-4 is due to the constant water table and heated air cycling.

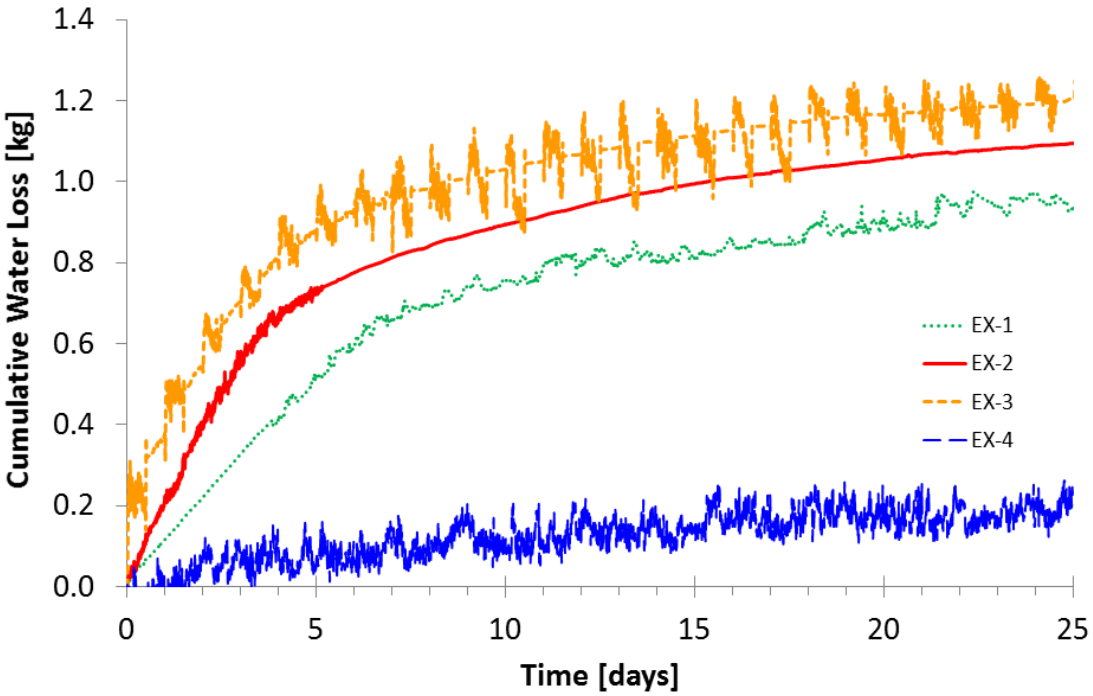

Figure 5.12. Cumulative water loss comparison between the different boundary conditions associated with all four experiments.

5.4.9 Drying Front Visualization Comparison

Visualization of the evaporative front propagation for EX2-4 is provided in Figure 5.13. All experiments showed a more rapid rate of front propagation from day 0 through to the time associated with the transition to Stage II evaporation depicted in Figure 5.12 where the rate of cumulative water loss decreases significantly. Front propagation continued to decrease at a much slower rate through the time associated with saturation reaching residual saturation in the tight packed region at 2.5-cm bgs as shown in Figure 5.15a below.

The front propagation under ambient conditions in Figure 5.7 is slower than those in EX-2. The time to transition to stage two evaporation occurred later due to the lack of continuously heated air above the soil surface and resulted lower atmospheric demand. Comparison between Figure 5.13a and b show that the evaporative front is very similar throughout the depth and over time. The one primary exception is that the movement of the front under diurnal conditions was very consistent from day 5 through to the end of the experiment. The higher atmospheric demand associated with both resulted in an increase rate of reduction in the drying front.

For EX-2, after 2 days, the water table level in the loosely packed region was 5-cm lower than that in the tightly packed region. This trend continued throughout the duration of the experiment. After day 15, the water table level in the loosely packed region reached the interface between the tight and loose packing and remained constant. The water table level in the tight packed region decreased marginally between day 15 to day 20, remaining about 2.5-cm above the level of the water table level in the loosely packed region. These relationships were observed for EX-3 as well. The relationships in relative height of the drying front relate to the air entry pressure of the differently packed regions. The 5-cm difference corresponds to the different in the air entry pressure (Table 5.1). The impact of air entry pressure is apparent when viewing Figure 5.13c.

The constant water table maintained in EX-4 resulted in a smaller change in the depth of the drying front over the experimental duration as shown in Figure 5.13c. The decrease from day 0 to day 5 was due to the packing method (wet packed) and transition period needed to maintaining the constant water table at 20.6 cm bgs. Note that prior to beginning EX-4, the constant head device was lowered to 20.6 cm bgs and maintained at this level for the course of the experiment. An observation specifically shown in Figure 5.13c corresponds to the height of capillary rise for both the tight and loose packed regions denoted as $h_{d,T}$ and $h_{d,L}$ respectively. The air entry pressure

measured as cm of water noted in Table 5.1 is in good agreement with the height of capillary rise above the water table in both regions. The variation between the height of rise and the air entry pressure is a function of the difference in porosities associated with the specific experiments. The $h_{d,L}$ was not influenced by the underlying tight packed region regarding the ultimate height of the capillary fringe in the loose packed center. Therefore, the height of capillary rise is possibly dependent on the air entry pressure of the material in contact with capillary fringe at the boundary layer between fully saturated and unsaturated regions.

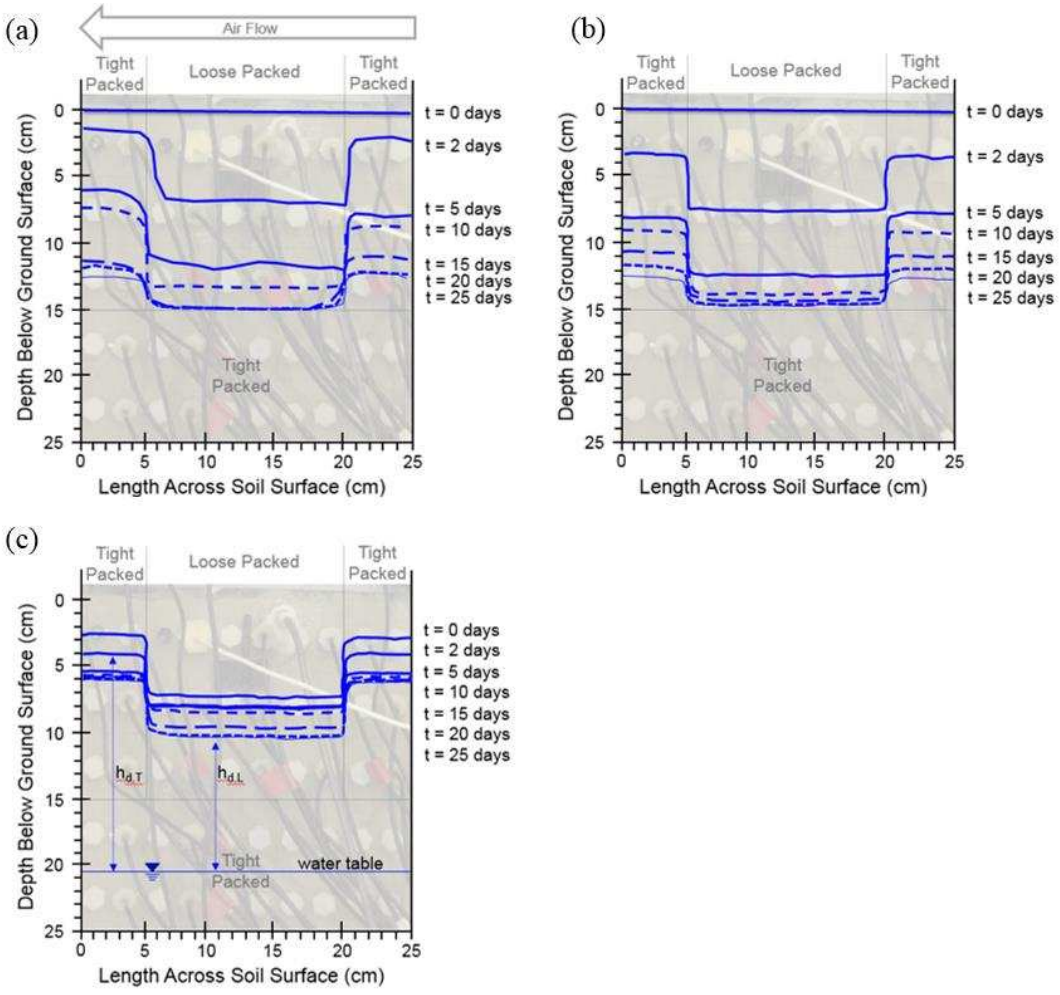

Figure 5.13. Drying front visualization across the length and throughout the depth of the sand tank over the duration of the experiments for (a) EX-2, (b) EX-3, and (c) EX-4. The constant water table and air entry head, h_d, for the tight (T) and loose (L) packed regions are shown in (c).

5.4.10 Surface Temperature Comparison

Soil surface temperature profiles similar to Figure 5.8 were created for each experiment. A similar trend in all experiments was observed which highlighted the temperature in the center loose packed region was typically higher than the temperatures associated with the tight packed regions upon entering Stage II evaporation and continued to experiment completion. The surface temperature measured for the first three experiments mirrored the same relationships displayed in Figure 5.8. Measured temperatures across the surface remain relatively constant through Stage I evaporation. At the beginning of Stage II evaporation, the surface temperatures increased. For the remainder of Stage II evaporation, the surface temperature remained relatively constant.

5.4.11 Relative Humidity Comparison

The relative humidity (RH) at the soil surface associated with the tight and loose packed regions are compared in Figure 5.14. The darker lines (solid or dashed) correspond to the tight packed regions and the lighter lines relate to the loose packed regions for the four experiments. Each pair of lines per experiment includes the line with a higher RH corresponding to tight packed regions and a lower RH corresponding to the loose packed region. The average of the upstream and downstream tight packed regions was plotted for each experiment to simplify the graph for comparison purposes between the four experiments.

Although not shown, the same relationship as shown in Figure 5.9 for EX-1 held true for EX-2 and EX-3 with the upstream tight packed region exhibiting a reduction in RH shortly after the downstream tight packed region. This supports the finding that the subsurface water flowed preferentially from the loose packed region to the upstream tight packed region due to the higher atmospheric demand occurring upstream compared to downstream conditions.

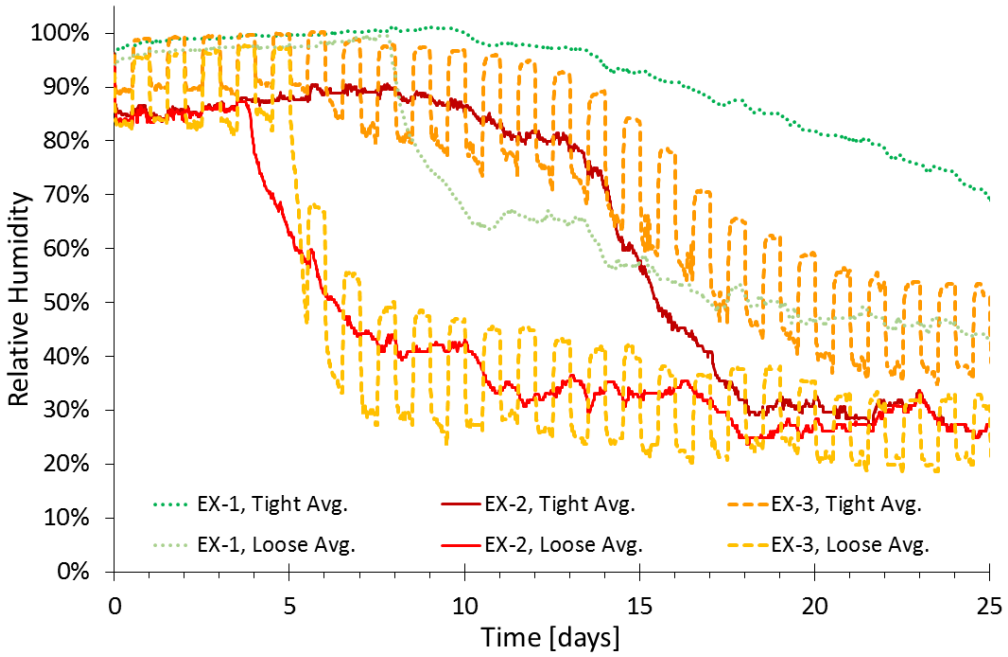

Figure 5.14. Surface relative humidity profile comparisons between differently packed regions between all four experiments.

All experiments exhibit similar characteristics with the loose packed region decreasing in humidity prior to the tight packed regions. The specific time for the decrease in tight and loose packing varied between each experiment corresponding to the environmental conditions. At the point where the rate of change in average surface temperature across the differently packed regions matched the rate of change in the downstream air space temperature, the RH in the tight packed regions began to significantly decrease. For EX-1, EX-2 and EX-3, the time associated with the decrease in RH of the loose regions occurred during Stage II evaporation. The ambient conditions of EX-1 displayed an expected trend of humidity in each region decreasing at a later time period and to a lesser extend as compared to EX-2 due to the absence of the continuously heated air above the surface. EX-3 results fluctuated between EX-1 and EX-2 due to the diurnal conditions corresponding to a fluctuation of about 10% corresponding to the fluctuation in cumulative water

loss. The drop in RH for both the tight and the loose packed regions matched EX-2 results more closely than EX-1 as the periods of heated surface air significantly contributed to the rate of evaporation. Under diurnal conditions, the heating and cooling cycles caused a more gradual decline in RH of the tight packed regions compared to EX-2 as captured by the steady decrease in evaporative front shown in Figure 5.13b.

5.4.12 Saturation Comparison

The average degree of saturation for the tight and loosely packed regions at three different depths (2.5, 7.5 and 12.5 cm bgs) is compared between EX1-4 as shown in Figure 5.15. As with relative humidity in Figure 5.14, each pair of lines per experiment includes the line with a higher saturation corresponding to tight packed conditions and a lower saturation corresponding to loose packed conditions.

Out of the first three experiments, EX-1 exhibited a more gradual decline in saturation with less dramatic transition between stages of evaporation due to the ambient conditions associated with the experiment. EX-3 displayed a reduction in saturation for both tight and packed regions at 2.5-cm bgs in much closer agreement than with other experiments. At 7.5 and 12.5 cm bgs, the saturation for EX-2 and EX-3 were almost identical for both packing regions as shown in Figure 5.15b and c.

Under the constant water table condition (i.e., EX-4), the overall difference between initial and final saturation compared to all other experiments was much smaller for both the tight and loose packed regions. This was a result of maintaining a constant water head at 20.6 cm bgs. Therefore, the capillary rise, based upon air entry pressures of each soil, was maintained at approx. 4.5 cm bgs in the tight packed region and 11 cm bgs in the loose region. As a result, there was water remaining below the surface and above the capillary fringe associated with the air entry head

for the various packed regions. This is evident as the level of saturation decreased at a quicker rate during the first 5 days of the experiment as compared to after. The tight packed saturation at 2.5-cm bgs matched almost exactly the loose packed saturation at 7.5-cm bgs. This correlation matches the difference in air-entry pressure.

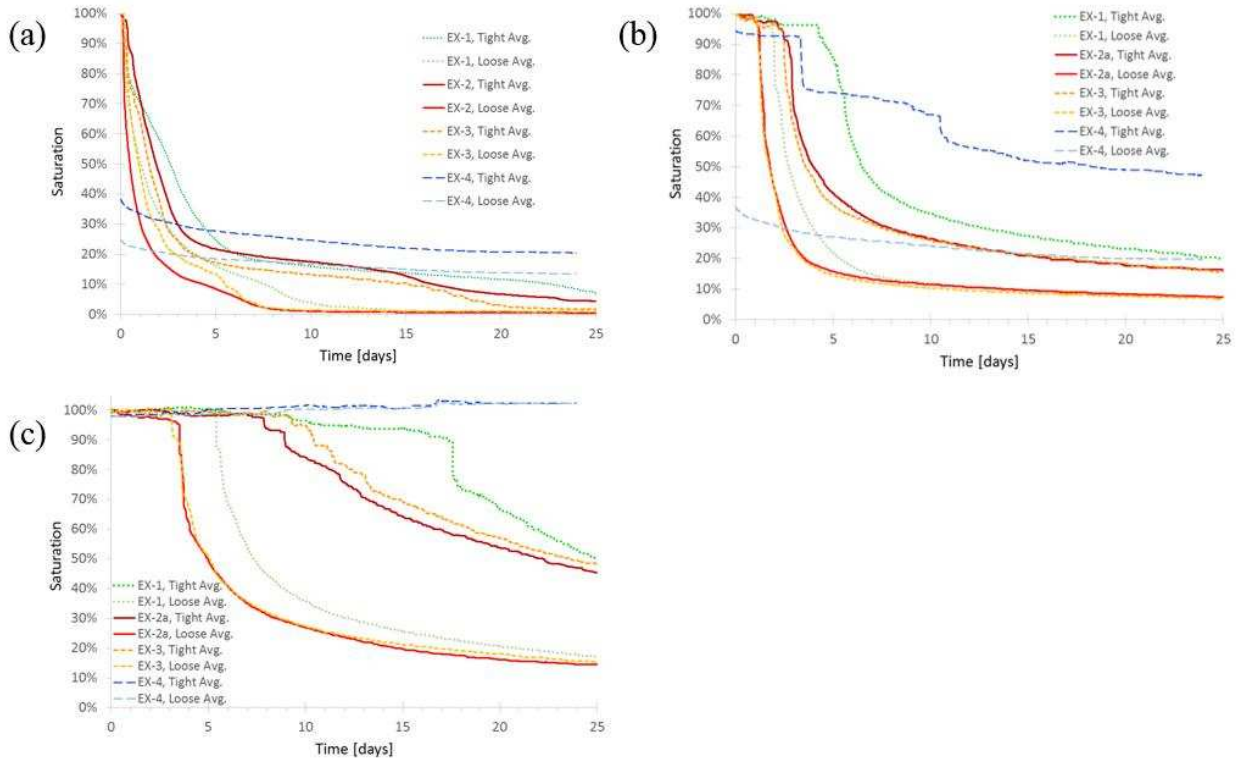

Figure 5.15. Soil moisture profile comparisons between differently packed regions at varying depths within the heterogeneous packing region at (a) 2.5-cm bgs (b) 7.5-cm bgs (c) 12.5-cm bgs.

5.4.13 Subsurface Temperature Comparison

Subsurface temperature profiles across the length and throughout the depth of the sand tank were obtained and compared with those presented in Figure 5.11. Regardless of the type of packed region and depth, the subsurface temperatures remained similar until the saturation as measured at

2.5 cm bgs in the tight packed region, $S_{2.5(T)}$, decreased to the point where the constant rate of steep decrease began to change denoting transition to Stage II evaporation. As with the surface, the subsurface temperatures at all depths increased at a quick rate (rate of increase decreased with depth) between periods of constant rate of decrease in $S_{2.5(T)}$. The correlations between the first three experiments cannot be made with EX-4 due to the different initial conditions.

5.4.14 Soil Mixing Experimental Highlights

Many of the general observations and discussion associated with EX-1 to EX-4 apply to EX5 and EX-6. However, due to different soil types, boundary conditions and tank dimensions, EX-5 (soil layers) and EX-6 (soil layers with mixture) will be compared independently of EX-1 to 4. The robust nature of data collected across the spectrum of soil and atmospheric properties enables use of the generated data sets for many future comparisons.

Cumulative water loss for EX-5 and 6 is shown in Figure 5.16. During Stage I, there is no difference in cumulative water loss. However, at approx. day 5, the cumulative water loss for EX-5 (soil layering) abruptly changes. This is due to the abrupt hydraulic disconnection from the surface. There are no hydraulically connected pathways to the surface resulting in a rapid transition to Stage II evaporation and a very low rate of continued water loss. For EX-6, the soil mixture/disturbance enables a long period of hydraulic connection with the surface resulting in a much large cumulative water loss.

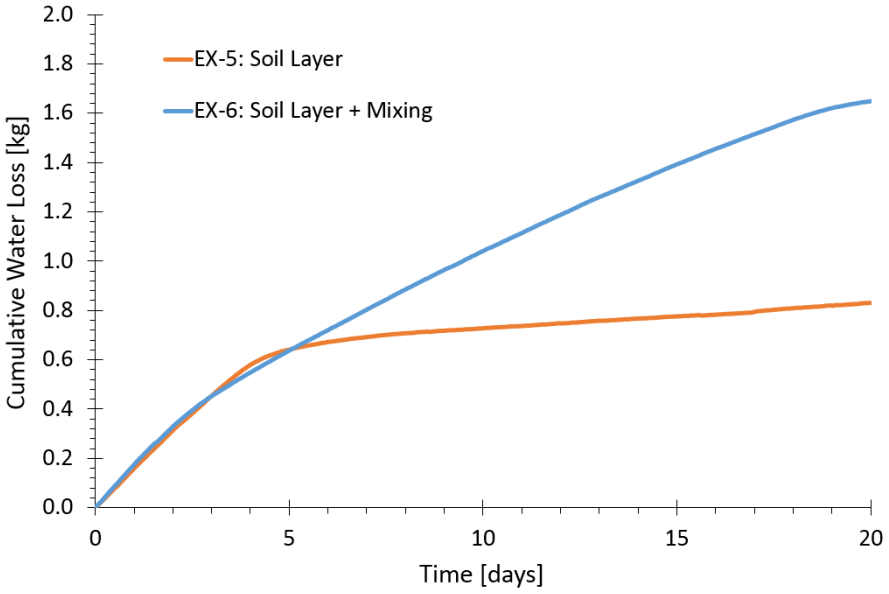

Figure 5.16. Cumulative water loss comparison between the different subsurface conditions associated with EX-5 and EX-6.

A visualization of the drying front is shown in Figure 5.17. For EX-6, although the disturbed center of is indeed loose packed compared to the tight packed coarse (#12/20) sand, it is important to remember that the disturbed center is a binary mixture of the parent coarse #12/20 sand and fine #110 sand – specifically with 1/3 coarse and 2/3 fine sand. As a result, and supported by what we learned from Task 1 (Chapter 3), the binary mixture inherently has finer pore spaces compared to the coarse top layer, resulting in capillary pumping from the coarse and into the mixed soil. The center then remains fully saturated as the coarse sand becomes dry. At that time (approx. day 2), the soil mixture can no longer draw water from the coarse layer which was helping to enable the center to remain fully saturated for a longer time. As a result, between days 5 to 10, the soil mixture dries. No hydraulic pumping occurred from the center mixture into the surrounding tight, fine #110 soil as observed in EX-1 to 4. There are two primary reasons for this. First the air entry pressure of the mixture and the tight #110 sand is very similar (Figure 5.4). Secondly, the #110 sand is not in direct contact with the surface at any location therefore limiting the influence

of atmospheric demand. When compared with EX-5 (layered), and the much slower propagation of the drying front, the impact of the soil disturbance on the significant loss of water is realized.

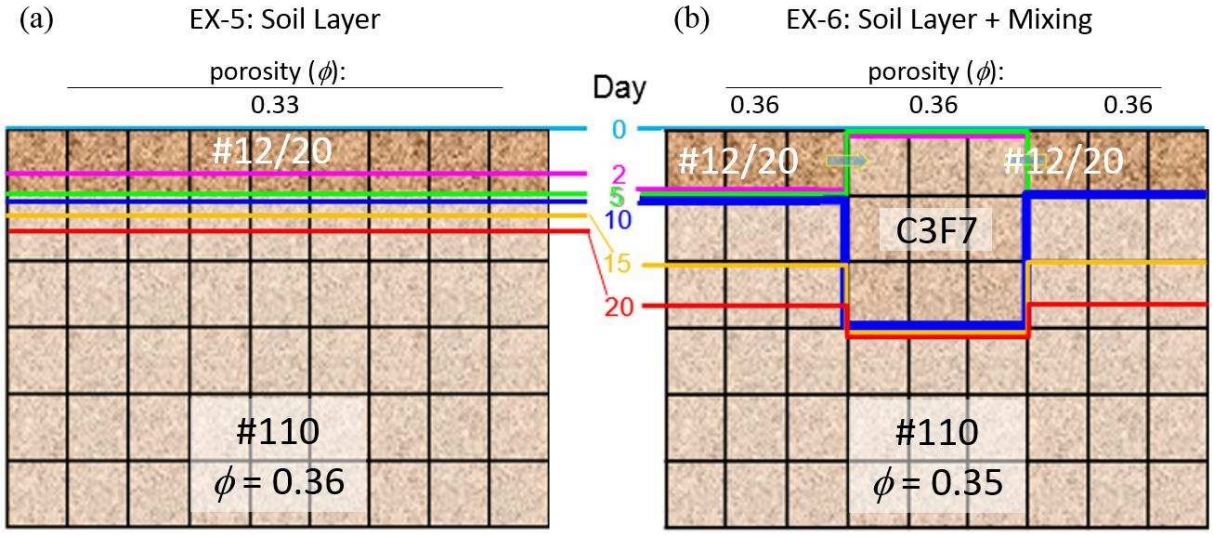

Figure 5.17. Drying front visualization of the propagation over the 20-day experiment for EX-5 and EX-6.

The general trends observed in EX-1 to 4 regarding temperature on and above the soil surface as well as subsurface temperatures were observed with EX-5 and EX-6. However, to highlight a few nuances, the average surface temperatures measured using infrared thermography for both EX-5 and EX-6 are shown in Figure 5.18. The surface temperatures indicate that during Stage I evaporation the surface temperatures were all the same. As each soil region entered Stage II evaporation, temperatures diverged with EX-5 maintaining a higher temperature as the drying front broke hydraulic connection with the surface resulting in a lack of evaporative cooling occurring. The tight packed, #12/20 sand of EX-6 maintained the next highest temperature followed by the coolest temperatures resulting from the C3F7 mixture as expected due to the longer hydraulic connection with the surface. However, for EX-6, as all surfaces regardless of soil

properties entered Stage II evaporation, the surface temperatures became similar again (~day 19.5) and much closer to the same temperature as that of the diurnally induced air temperature (not shown).

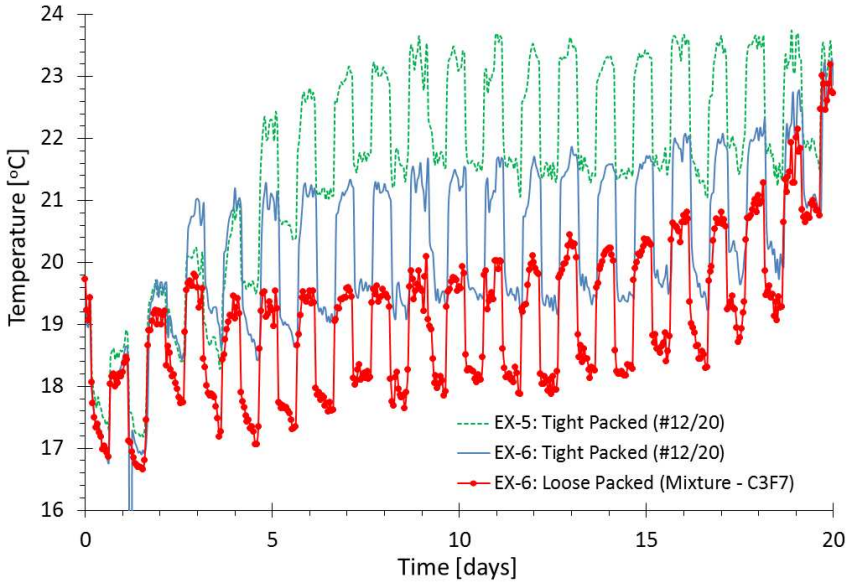

Figure 5.18. Average surface temperatures measured using infrared thermography for each surface soil type (EX-5: tight packed, #12/20; EX6: tight packed, #12/20 and loose packed C3F7 mixture).

The soil degree of saturation as a function of time for EX-5 and 6 is shown in Figure 5.19. The disturbed soil mixture (EX-6) causes a noticeable change in saturation at all depths when compared to layered soil without the disturbance (EX-5). The coarse, top layer drains more rapidly for EX-6, compared to that of EX-5 due to capillary pumping from the coarse soil into the mixed soil. Although the porosity is about the same between the #12/20 top layered soil and the C3F7 mixture, the overall smaller capillary pores in the mixture resulting in smaller pore size diameter enhances lateral water flow from the coarse sand to the C3F7 mixture. The fine grained, #110 sand has approximately the same porosity of the mixture (0.35 and 0.36, respectively). Therefore, both

exhibit a decrease in saturation at about the same time that the top sand layer reaches residual saturation, further suggesting that there is no capillary pumping from the mixture into the adjacent #110 sand. In the case of EX-6, the saturation decreases more rapidly with depth than EX-5. The fine grained-dominated soil mixture enables hydraulic connection to the soil surface and the evaporative demand from the atmosphere. The saturation associated with the mixture is similar throughout the entire mixture regardless of depth demonstrating that the volume of disturbed soil acts as a homogeneous disturbance. The layered soil without the soil disturbance does not enable direct hydraulic connection to the surface after the coarse overlying #12/20 sand drains, resulting in diffusion limited Stage II evaporation.

The ability to simultaneously measure capillary pressure and saturation for EX5-6 enables the development of capillary pressure – saturation relationships for each soil layer. This is important for future modeling efforts.

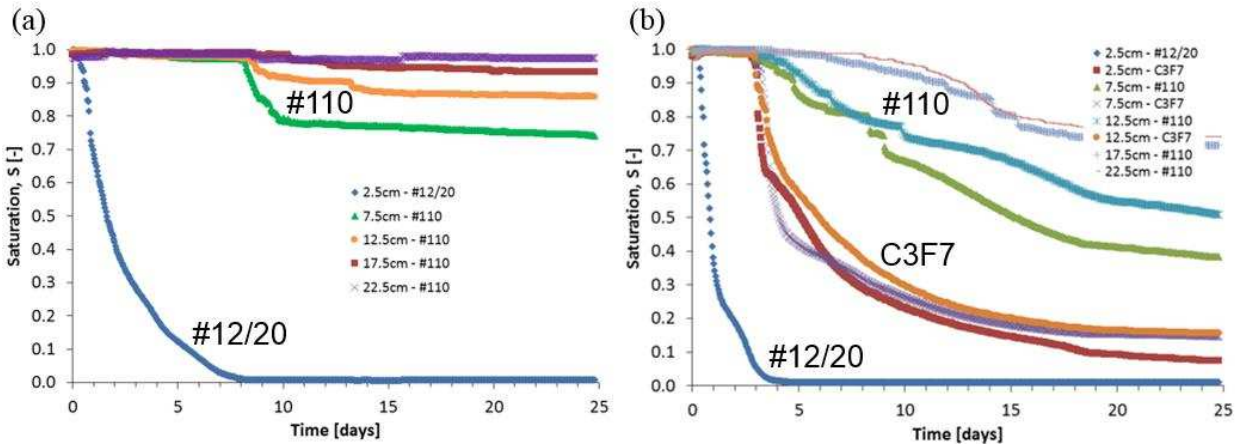

Figure 5.19. Comparison of the soil moisture profile at depths ranging from 2.5 to 12.5 cm below the surface for (a) EX-5 with layered soils and (b) EX-6 with layered soils and a loose binary mixture.

Measurement of capillary pressure within the top 10 cm of both tanks (EX-5 and EX-6) showed that regardless of depth and tank packing conditions, the relationship between the different types of soil (#12/20, #110, and C3F7 mixture) is consistent (Figure 5.20). At 2.5 cm with #12/20 sand, the SWRC is almost identical. At 7.5 cm with #110 sand, the SWRC relationship is similar; however, more complete for the tank with the disturbed soil mixture (EX-6) due to the lower saturation levels observed with EX-6. The C3F7 mixture appears to have the same SWRC regardless of measurements taken at 2.5 cm or 7.5 cm below the surface indicating consistent soil properties maintained through the packing process. As expected, the mixture's SWRC is between that of the parent sands and resembles the shape of the #110 sand more closely than the #12/20 sand as the soil mixture is fine-controlled.

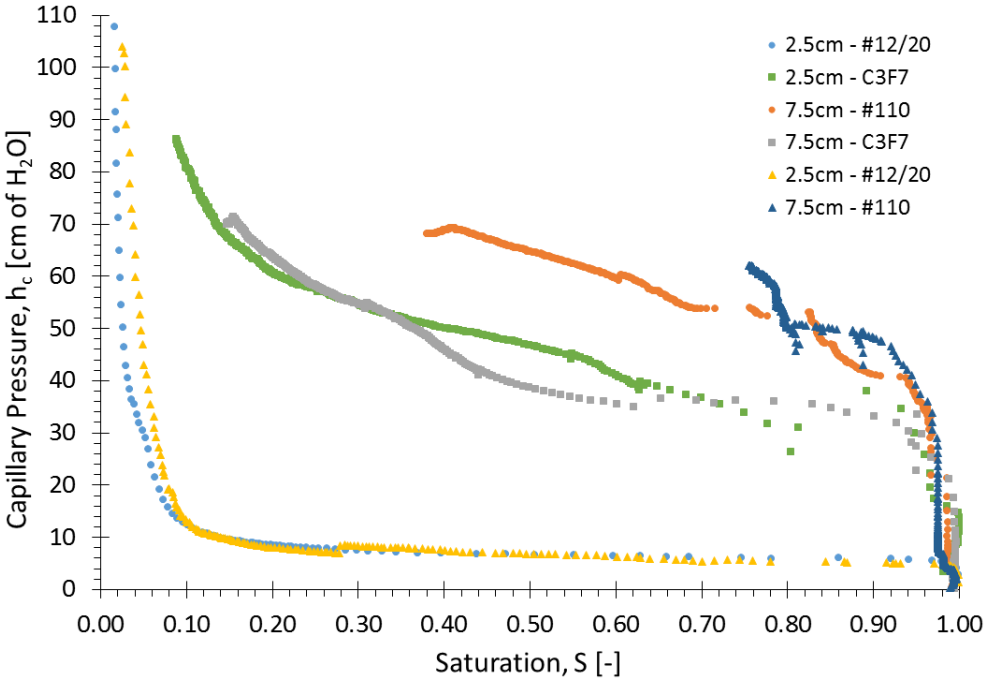

Figure 5.20. Average soil water retention curve (SWRC) based on location and depth (EX-5: triangles / EX-6: circles = tight packed soil & squares = loose packed mixture).

The thermal conductivity-saturation (λ-S) relationship for all soil types is shown in Figure 5.21 for soils associated with EX-5 and EX-6. The measured λ at 2.5 cm for EX-6 in the #12/20 sand and C3F7 mixture have considerably different responses over time. The #12/20 sand exhibits a pronounced decrease in thermal conductivity at approximately the same time as the saturation reaches residual conditions. Although the λ-S relationship is different in the mid-saturation ranges between the top soil layer of #12/20 sand in EX-5 versus EX-6, the saturated λ is about the same for both tanks with the dry λ at almost identical values. Additionally, the point where λ transitions from a gradual decrease to a significant decrease is at the same S for both tanks. The λ-S relationship for the C3F7 mixture (EX-6) is very similar to the #12/20 response of EX-5; however, less overall than the #12/20 response in EX-6. The loose packing associated with the C3F7 mixture results in lower λ throughout the range of S compared to the tighter packed #12/20 sand surrounding the soil disturbance. However, the saturation associated with transition to a rapid decrease in λ is similar.

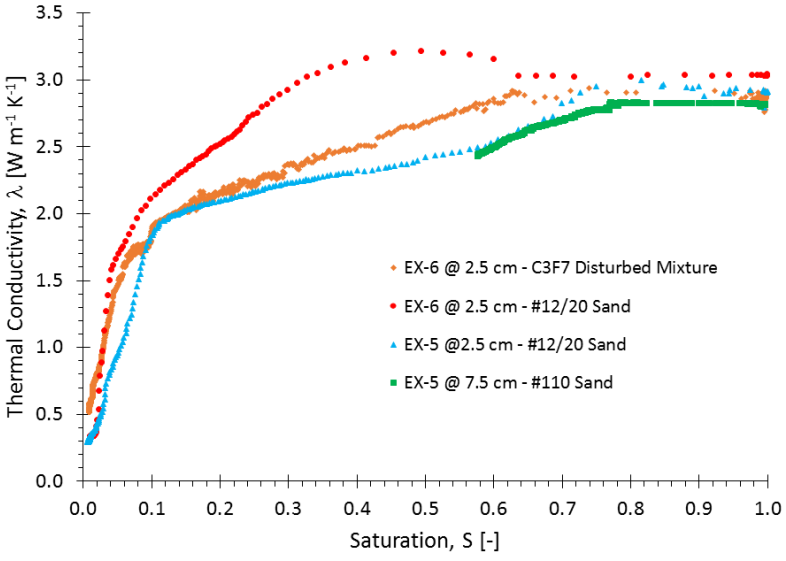

Figure 5.21. Measured thermal conductivity-saturation relationships based upon soil type and location (all measured at 2.5 cm bgs except for #110 sand at 7.5 cm bgs).

5.5 Analytical Model based on Surface Energy Balance (SEB) Theory

The modeling effort discussed herein is based upon work by Shahraeeni and Or (2010) in which evaporative fluxes from heterogeneous porous surfaces are resolved by infrared thermography. Their work was determined for cylindrical coordinates, and therefore required adjustment for the present study resulting in re-deriving fundamental equations in Cartesian coordinates to match the experimental set-up (Figure 5.1). A further modification of the Shahraeeni and Or (2010) model was the incorporation of the temperature dependency of fluid properties (Table 5.3) and the change in effective thermal conductivity with soil moisture. In their research, Shahraeeni and Or (2010) evaluated the impact of a fine, tightly packed column of sand that was surrounded by coarse, tight packed sand. These conditions may be related to those resulting from landmine burial without too much effort (i.e., a loose packed, disturbed soil surrounded by the undisturbed, tight packed soil).

The starting point for development of the method by Shahraeeni and Or (2010) is the surface energy balance (SEB) as stated by Penman (1948) regarding evaporation from bare soil.

$$R_n - G = H + LE \tag{5.1}$$

where R_n is the net radiation flux, G is the soil heat flux, H is the sensible heat flux, and LE is the latent heat flux (all in units of W m^{-2}). LE is the combined effect L which is the latent heat of vaporization (2450 J g^{-1} under atmospheric pressure) and E which is the evaporative flux (W m^{-2}). Eq. 5.1 can be rewritten taking into account heat losses/gains due to evaporation and condensation (LE), net radiation (R_n), soil heat flux (G), and convection (H) (Shahraeeni and Or, 2010):

$$\frac{\rho_w L_w \dot{e}}{\Delta h} + \left(\lambda_{eff} \nabla^2 T_s + \rho_w C_p \frac{DT_s}{Dt} \right) = \frac{\sigma \varepsilon (T_\infty^4 - T_s^4)}{\Delta h} + \frac{h_a (T_\infty - T_s)}{\Delta h} \tag{5.2}$$

where t is time (s), C_p is the soil heat capacity (J kg^{-1}), λ_{eff} is the effective thermal conductivity (W m^{-1} K^{-1}), h_a is the convective heat transfer coefficient (W m^{-2} K^{-1}), T_s is the soil surface temperature (K), T_∞ is the ambient temperature (K), ε is surface emissivity (–), σ is the Stefan-Boltzmann constant (5.67×10^{-8} W m^{-2} K^{-4}), Δh is the thermal decay depth (~ 2 to 3 cm (Gardner and Hanks, 1966)), $\dot{e}$ is the evaporation rate (m s^{-1}), L_w is temperature dependent latent heat of vaporization of water (J kg^{-1}), and ρ_w is temperature dependent water density (kg m^{-3}). A summary of the functions that relate temperature and the temperature dependent fluid properties of interest in this method are found in Table 5.4. The method presented may then be adjusted to determine the specific evaporation rate determined from each region (tight or loose) as well as specific location (upstream or downstream). For more discussion regarding specific equation development and methodology, the reader is referred to Shahraeeni and Or (2010) and Trautz (2015).

In the work of Shahraeeni and Or (2010), the authors assume a constant thermal conductivity value throughout both Stage I and Stage II evaporation. From work associated with Chapter 3, we know that soil thermal conductivity is significantly different when comparing fully saturated and completely dry conditions. Therefore, thermal conductivity was determines using the method presented by Lu and Dong (2015) which is discussed in detail in Chapter 3.

5.6 Analytical Modeling Results and Discussion

The discussion above provides the background regarding the SEB method use for analysis in this research. The results and discussion are presented first regarding comparison with EX-1. Then, a brief discussion occurs regarding the applicability of the model with other experiments conducted. After the discussion of this section, overall conclusions follow.

Table 5.4. Other fluid properties applied in surface energy balance (SEB)*.

Variable	Equation	Reference
Density of Water	$\rho_w = 658.2 + 2.509T_s - 4.6x10^{-3}T_s^2$	Campbell (1985)
Latent Heat of Vaporization	$L_w = \frac{2.495x10^9 - 2.247x10^6(T_s - 273.15)}{\rho_w}$	Forsythe (1964)
Density of Air	$\rho_a = \frac{pM_a}{RT_\infty} - 0.611\left(\frac{M_a}{M_w} - 1\right)\exp\left(17.27\frac{T_\infty - 273.15}{T_\infty - 36}\right)\frac{M_w(RH)}{RT_\infty}$	Lu and Likos (2004)
Dynamic Viscosity of Water	$\mu_a = 1.458x10^{-6}\left(\frac{T_\infty^{1.5}}{T_\infty + 110.4}\right)$	Andreas (2005)
Thermal Conductivity of Air	$\lambda_a = 0.024 + 7.73x10^{-5}(T_\infty - 273.15) - 2.6x10^{-8}(T_\infty - 273.15)^2$	Campbell et al. (1994)
Heat Capacity of Air	$C_{pa} = 1005.6 + 0.017211(T_\infty - 273.15) + 3.92x10^{-4}(T_\infty - 273.15)^2$	Andreas (2005)

* T_s (K): surface temperature, T_∞ (K): ambient temperature, p (Pa): air pressure, M_a (kg mol^{-1}): molecular weight of air, M_w (kg mol^{-1}): molecular weight of water, R (Pa m^3 K^{-1} mol^{-1}): ideal gas constant, RH (–): experimental relative humidity

5.6.1 Evaporation based upon SEB Method for EX1 (Ambient Conditions)

The evaporation rate was determined for each soil region using the method described in Section 5.5. Total cumulative water loss was determined as the summation of the water loss from each region. The calculated evaporation rate related to cumulative water loss from the two tight regions based on location is shown in Figure 5.22 as well as the measured cumulative water loss for comparison purposes.

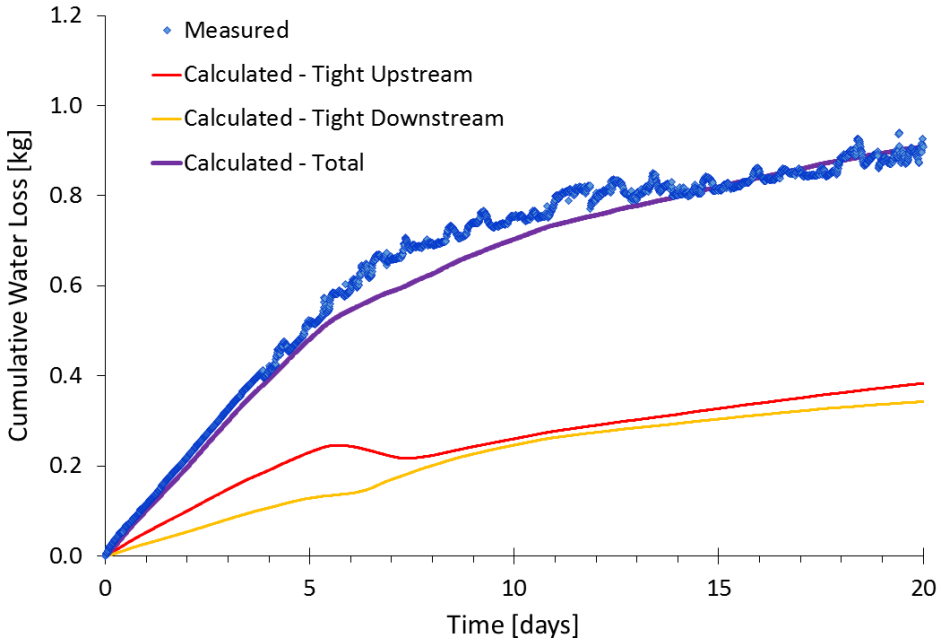

Figure 5.22. Cumulative water loss comparison between measured and calculated values based upon the surface energy balance method under ambient conditions.

Comparison between observed and simulated cumulative water loss shows good agreement (R^2 = 0.987). The tight upstream region contributes slightly more to the overall evaporation compared to the downstream tight packed region due to a higher atmospheric demand present as the airstream initially comes in contact with the upstream soil surface. As evaporation occurs, more water vapor enters the airstream and the demand decreases as the air flows across the surface to the downstream tight packed region.

5.6.2 Evaporation Analysis based upon Surface Temperature Measurements Comparison

The surface energy balance (SEB) method used to determine evaporation for each soil region that was conducted for EX-1 was also conducted for EX-2 to EX-4. However, the SEB method did not effectively predict cumulative water loss for the other experiments. Therefore, on-going research includes the use of soil heat pulse probes and the combined heat-pulse and sensible heat balance method to effectively determine the evaporation rates from each region for EX-2-4.

5.7 Conclusions

The primary research objective of this study was to improve our current understanding of the effects of soil disturbances on evaporation behavior at both soil-soil and soil-atmospheric interfaces. In this study, six laboratory experiments were performed under varying hydraulic and thermal boundary conditions using a unique experimental set up that includes a low velocity wind tunnel interfaced with soil tanks, allowing for better control and gathering of accurate data. The findings summarized here are applicable to poorly graded, well sorted sands.

The comparison between the six experiments yielded a number of observations that held true regardless of the environmental conditions associated with each experiment. Many of these observations enabled determination of the transition between Stage I and II evaporation. For example, all experiments showed a relatively significant decrease in drying front propagation during Stage I evaporation. Front propagation continued to decrease at a much slower rate associated with the time that saturation reached residual saturation in the tight packed region at 2.5 cm bgs. Relative humidity in the loose packed region transitioned to a more gradual decrease at the point where saturation in the loose region reached the residual saturation. The relative humidity in both the loose and tight packed regions stabilized once the saturation in the tight regions decreased to residual saturation. This phenomenon is indicative of the subsurface flow from loose to tight regions. Once the tight packed regions soil moisture levels were significantly reduced, the relative humidity levels at the soil surface quickly decreased.

Soil disturbances in the cases of EX-1 to EX-4 and soil mixtures in the case of EX-6 caused significantly more water loss compared to undisturbed soil conditions (e.g., EX-5). The increased water loss was due to the differences in the soil's physical properties as well as the capillary pumping from the loose to the tight soil regions. Capillary pumping occurred from the coarse soil

into the mixture based upon the finer pore space that exists in the binary mixture. However, the specific contribution of the capillary pumping with respect to evaporation from the surface boundary is not known. Drivers for capillary pumping included both pore space differences in soil along the vertical textural contrast as well as air entry pressure of the parent sand(s) as well as the disturbed sand or mixture as applicable under initially layered soil.

The SEB model used to determine evaporation for the different soil regions from EX-1 enabled identification of the contribution of each region to overall evaporation. Higher evaporation occurred from the upstream tight region than the tight downstream region due to higher atmospheric demand occurring at the point where the dry air came in contact with the soil. The discrepancy between the observed and simulated evaporation rates in EX-2 to EX-4 requires further investigation. The data sets developed from this work will be helpful for future modeling efforts on heat and mass transfer though soils.

Future modeling efforts are improved through comparison with deliberate, thorough experiments that measure the full spectrum of soil moisture, temperature, pressure, relative humidity, and other conditions. The data collected for these experiment is available for future research to further our understanding of changes to subsurface conditions that are affected by soil disturbances associated with events similar to burying landmines.

5.8 Acknowledgements

This research was funded by the U. S. Army Research Office Award W911NF-04-1-0169, the Engineering Research and Development Center (ERDC), the National Science Foundation (CMMI-1230544 and EAR-1447533), the Edna Bailey Sussman Fund, and the Dorothy Bertine Internship. The author thanks Dr. Kathleen Smits for support with tank packing and establishing procedures for individual pressure transducer system calibrations as well as writing code for data

collection of net radiation and Dr. Andrew Trautz for writing of code for collection of data from various instruments (e.g., Pitot static tube, heat pulse sensors, temperature sensors, and individual pressure transducers).

5.9 References

Abramowitz, M., and I.A. Stegun. 1972. Handbook of mathematical functions. Dover Publications, Inc., New York.

Andreas, E.L. 2005. Handbook of physical constants and functions for use in atmospheric boundary layer studies. Cold Regions Research and Engineering Laboratory. ERDC/CRREL M-05-1.

Assouline, S., S.W. Tyler, J.S. Selker, I. Lunati, C.W. Higgins and M.B. Parlange. 2013. Evaporation from a shallow water table: Diurnal dynamics of water and heat at the surface of drying sand. Water Resour Res. 49:4022-4034. doi:10.1002/wrcr.20293

Bruschini, C. and B. Gros. 1998. A survey of current sensor technology research for the Q7 detection of landmines, in sustainable humanitarian demining: trends, techniques and technologies, edited by the Humanitarian Demining Information Center, James Madison University (Co-Editors: D. Barlow, C. Bowness, A. Craib, G. Gately, J.D. Nicoud, J. Trevelyan), Mid Vally Press, Verona, VA. 172-187.

Campbell, G.S. 1985. Soil Physics with BASIC. Elsevier, New York.

Campbell, G. S., J. D. Jungbauer, W. R. Bidlake, and R. D. Hungerford. 1994. Predicting the effect of temperature on soil thermal-conductivity. Soil Sci. 158:307–313.

Carslaw, H.S., and J.C. Jaeger. 1959. Conduction of heat in soils, 2nd ed. Oxford, London.

Deans, J., G. Schmithals, and L.J. Carter. 2001. An analysis of the thermal imaging method for landmine detection using microwave heating. J. Appl. Geophys. 47(2):123-133.

Decagon Devices. 2014. KD2 Pro thermal properties analyzer operator's manual, version 20 June 2014 – 09:11:40. Decagon Devices, Inc., Pullman, WA.

English, T.L. 2000. The quiet Americans: a history of military working dogs. Office of History. 37th Training Wing, Lackland AFB, Texas.

Forsythe, W.E. 1964. Smithsonian physical table. Smithsonian Institution Publication 4169. Washington, D.C.

Gardner, H.R., and R.J. Hanks. 1966. Evaluation of evaporation zone in soil by measuring of heat flux, Soil Sci. Soc. Am. Proc., 30:425-428.

Heitman, J.L., R. Horton, T.J. Sauer, and T.M. DeSutter. 2008. Sensible heat observations reveal soil-water evaporation dynamics, *J. Hydrometeorol.*, 2:165-171, doi:10.1175/2007JHM963.1.

Kluitenberg, G.J., J.M. Ham, and K.L. Bristow. 1993. Error analysis of the heat pulse method for measuring soil volumetric heat capacity. Soil Sci. Soc. Am. J. 57:1444-1451.

Krueger, K.R., McClellan, J.H., and W.R. Scott, Jr. 2015. Efficient algorithm design for GPR imaging of landmines. IEEE Transactions on Geoscience and Remote Sensing. 53(7):4010-4021. doi:10.1109/TGRS.2015.2388786

Lassen, R.N., M. Plampin, T. Sakaki, T.H. Illangasekare, J. Gudbjerg, T.O. Sonnenborg, and K.H. Jensen. 2015. Effects of geological heterogeneity on migration of gaseous CO_2 using laboratory and modeling investigations. Int. J. Greenhouse Gas Control. 43:213-224. doi:10.1016/j.ijggc.2015.10.015

Lehmann, P. and D. Or. 2009. Preferential evaporation and capillary coupling in porous media with textural contrasts, Phys. Rev. E. 80. 046318.

Lehmann, P., S. Assouline, and D. Or. 2008. Characteristic lengths affecting evaporative drying of porous media. Physical Review E. 77:0563096. doi: 10.1103/PhysRevE.77.056309

Lu, N., and W.J. Likos. 2004. Unsaturated soil mechanics. John Wiley & Sons, Inc., Hoboken. p. 429-431.

Lu, N., and Y. Dong. 2015. Closed-form equation for thermal conductivity of unsaturated soils at room temperature. J. Geotech. Geoenviron. Eng., doi:10.1061/(ASCE)GT.1943-5606.0001295, 04015016.

Maksymonko, G.B., B.S. Ware, and D.E. Poole. 1995. Characterization of diurnal and environmental effects on mines and the factors influencing the performance of mine detection ATR algorithms. *Proc. SPIE.* 2496:140-151. doi:10.1117/12.211310

Nachshon, U., N. Weisbrod, M.I. Dragila, and A. Grader. 2011. Combined evaporation and salt precipitation in homogeneous and heterogeneous porous media, Water Resour. Res., 47, W03513, doi:10.1029/2010WR009677.

Or, D., P. Lehmann, E. Shahraeeni, and N. Shokri. 2012. Advances in soil evaporation physics – A review. Vadose Zone J. doi:10.2136/vzj2012.0163

Phelan, J.M., and S.W. Webb. 1997. Environmental fate and transport of chemical signatures from buried landmines: screening model formulation and initial simulations, Sandia National Laboratories Report SAND97-1426, Albuquerque, NM.

Sakaki, T., A. Limsuwat, K.M. Smits, and T.H. Illangasekare. 2008. Empirical two-point -mixing model for calibrating the ECH2O EC-5 soil moisture sensor in sands, Water Resour. Res. 44:W00D08.

Sakaki, T., and T.H. Illangasekare. 2007. Comparison of height-averaged and point-measured capillary pressure-saturation relations for sands using a modified Tempe cell, Water Resour. Res., 43, doi: 10.1029/2006WR005814

Shahraeeni, E., and D. Or. 2010. Thermo-evaporative fluxes from heterogeneous porous surfaces resolved by infrared thermography. Water Resour. Res. 46:W09511. doi:10.1029/2009WR008455

Shire, A., U. Jawarkar, and S. Chavhan. 2015. Overview of buried mines detection using radar bullet. Int. J. Eng. Sci. and Resear. Technol. 4(2):250-254.

Shokri, N. and D. Or. 2013. Drying patterns of porous media containing wettability contrasts. J. Colloid Interface Sci. 391:135-141.

Shokri, N., P. Lehmann, and D. Or. 2010. Evaporation from layered porous media. J. Geophys. Res. 115:B06204. doi:10.1029/2009JB006743

Smits, K.M., and A. Limsuwat. 2009. Characterization of sand properties. CESEP.

Trautz, A.C., 2015. Heat and mass transfer in porous media under the influence of near-surface boundary layer atmospheric flow. Dissertation. Colorado School of Mines, Golden, CO.

Trautz, A.C., K.M. Smits, P. Schulte, and T.H. Illangasekare. 2014. Sensible heat balance and heat-pulse method applicability to in situ soil-water evaporation. Vadose Zone J. 13.

Van Brakel, J. 1980. Mass transfer in convective drying, in *Advances in Drying*, vol. 1. edited by A.S. Mujumdar, pp. 217-267. Hemisphere. Wahington, D.C.

van Genuchten, M. T. 1980. A closed-form equation for predicting the hydraulic conductivity of unsaturated soils, Soil Sci. Soc. Am. J., 44:892–898.

Wang, Y., Q. Song, T. Jin, Y. Shi, and X. Huang. 2013. Sparse time-frequency representation based feature extraction method for landmine discrimination. Progress in Electromagnetics Research. 133:459-475.

Yiotis, A.G., A.G. Boudouvis A.K. Subos, I.N. Tsimpanogiannis, and Y.C. Yortsos. 2004. The effect of liquid films on the drying of porous media. AIChE J. 50:2721-2737.

Yiotis, A.G., I.N. Tsimpanogiannis, A.K. Stubos, and Y.C. Yortsos. 2007. Coupling between external and internal mass transfer during drying of a porous medium. Water Resour. Res. 43:W0640,1012.

Yip, M., M.I. Saripan, K. Wells, and D.A. Bradley. Monte Carlo simulations for the detection of buried objects using single sided backscattered radiation. PLoS ONE. 10(9):e0135769. doi:10.1371/journal.pone.0135769

CHAPTER 6 FIELD SCALE EXPERIMENTAL AND NUMERICAL INVESTIGATION OF DIURNAL FLUCTUATIONS OF HEAT AND WATER DISTRIBUTIONS AROUND LANDMINES IN NATURAL SOIL

Prior to discussion regarding the specifics of this chapter, the intellectual contribution is specified along with identification of the author's contribution to this work. This research increased knowledge in the field of research regarding both thermal and soil moisture response associated with landmine detection. Prior to this effort, no research existed that simultaneously evaluated the impact of soil disturbance, burial depth, and object properties on soil moisture and temperature distributions in the vicinity of a landmine. Specific contributions included identifying both the thermal and soil moisture response to rain events for a disturbed soil location, a shallow and deep buried surrogate mine location, and a shallow buried limestone block with all emplaced in a poorly graded concrete sand similar to that found in Iraq. The findings identified that visual signature of all locations is lost after a rain event. Additionally, precipitation causes the accentuation of thermal contrast above a shallow buried mine both at day and night. However, the thermal contrast of the deep buried mine, disturbed soil location and buried limestone block are attenuated. These finding are significant because they provide relationships to consider that may impact the ability of different detection platforms (e.g., IR) to have signatures diminished or accentuated based upon soil properties and burial depth. However, the most significant contribution of this data is that the high spatial and temporal resolution of the data collected may provide the ability for verification of numerical modeling as part of for future research. All experimental work and analysis of data collected was completed by the author of this dissertation.

6.1 Abstract

The natural environment in which landmines are placed are heterogeneous. These heterogeneities such as differences in soil type, packing and moisture, combined with changes in surface and climate conditions can oftentimes mask the presence of a mine. Understanding the impact of heterogeneity on heat and mass transfer behavior in the vicinity of landmines is paramount to properly identifying landmine locations for demining operations. This study investigates the impact of soil heterogeneity on soil moisture and temperature distributions around buried objects with the goal of increasing our ability to predict the environmental conditions that are most dynamic to mine detection performance. A ten-day field experiment was conducted in which two surrogate anti-personnel landmines at different depths and a limestone block of comparable size were buried. A disturbed soil location without the emplacement of an object, similar in size to those created due to mine burial was also established. The site was instrumented with a series of sensors, monitoring atmospheric, surface and subsurface conditions to include measurements of soil moisture, soil and air temperature, relative humidity, and meteorological conditions such as wind speed and net radiation. Infrared thermal imaging was used to provide continuous profiles of surface temperature conditions. The soil was well characterized in the laboratory to provide good understanding of field conditions for numerical modeling efforts. Experimental results demonstrate distinct behaviors in soil moisture and temperature distributions above and around buried objects that change with climate forcings (i.e., temperature and rain events).

6.2 Introduction

Over 100 million landmines and other undetected explosive remnants of war affect people in more than 80 countries around the world (Miles, 1998; ICRC, 2011; Shire et al., 2015). The Red

Cross estimates that landmines kill about 800 people and injure thousands each month (Andersson et al., 2015) and research regarding the impact of landmines continues to be a point of international concern (e.g., Arcand et al., 2014). As stated by Miller et al. (2004), no unsaturated zone soil contamination is worse from both a human health and environmental perspective than that of buried, unexploded landmines. In addition to those killed by landmines every day, the personnel cost to remove each mine is significant (one mine disposal expert is killed and two injured for every 5000 mines cleared (Walsh and Walsh, 2003)).

Although there are currently a wide variety of landmine detection techniques available (e.g. ground penetrating radar, thermal imagery, chemical sniffing) (Maksymonko et al., 1995; Phelan and Webb, 1997; Bruschini and Gros, 1998; English, 2000; Deans et al., 2001; Wang et al., 2013; Krueger et al., 2015; Shire et al., 2015; Yip et al., 2015), no one detection technique performs with perfect accuracy. One outcome of poor detection performance is a false alarm or in other words, mistaking a buried object, such as a rock, for a landmine. The false alarm rate (i.e., number of false alarms per unit area) is affected by the type of detection technique employed and the environmental conditions in which the mine is placed (MacDonald et al., 2003). Typically, nonthreatening subsurface objects (e.g., rock, soda can, garbage), sensor vibrations, system uncertainty, soil moisture and climate conditions (e.g., temperature, rain, wind) contributes to increasing false alarm rates (FARs) (Ratto et al., 2011). The demand for improvement in technology to increase the find rate or probability of detection (PD) and reduce the FAR drives current research efforts (Bello, 2013).

Environmental conditions in which mines are likely encountered are diverse (Koh and Ballard, 2004) with considerations including redox potential, pH, acidity, soil moisture content, rainfall, heat, cold, fire, shrink/swell soils, saltwater degradation, and plant interferences (Estes at

al., 2011). Surface roughness, subsurface heterogeneity, and soil moisture are environmental conditions that impact landmine detection (Khanafer and Vafai, 2002; Ratto et al., 2011). Soil moisture impacts the permittivity, conductivity, and dielectric contrast of the subsurface environment (Ratto et al., 2011). This is especially important for detection systems that rely heavily on soil moisture impacts. Diurnal thermal fluctuation impacts thermal contrasts at the soil surface to a depth of about 10 cm resulting from the energy exchange with the environment (Garcia-Padron et al., 2002; Moukalled et al., 2006). The contrast between mine and environment increases as the thermal diffusivity and conductivity of a mine decreases (Moukalled et al., 2006) with the most favorable thermal contrast on the surface occurring with 5 wt.% moisture level (Carter et al., 1998).

The presence of a landmine may affect soil hydraulic and thermal properties in a few ways. First, similarly to a rock, a landmine serves as an obstruction to water flow. As a result, moisture directly below a mine decreases more slowly than moisture above the mine during periods of thermal heating of the soil. However, during periods of condensation when the air temperature is cooler than the soil surface, moisture directly above the mine increases. Vapor can accumulate underneath a landmine, condensing, and serving as a location of high moisture. However, above a mine, the moisture is lower as the mine disconnects the pathway for water and vapor flow. Also, if it rains, the water will either flow around the mine or accumulate on top of it. Second, the process of placing the mine disturbs and mixes the soil where the mine is buried. The soil removed to accommodate the landmine is less compact resulting in lower capillarity compared to the parent, compact soil. The disturbed soil also reduces thermal conductivity due to the soil matrix being less compact. With a hole dug for landmine emplacement that included both coarse topsoil and finer underlying soil, the disturbed soil is a mixture of the two parent soils. Both hydraulic and thermal

properties changes significantly due to soil mixtures (Sakaki and Smits, 2015; Wallen et al., 2016). Finally, the emplacement of a landmine disturbs the surrounding soil, changing the soil hydraulic and thermal properties (Das et al., 2001). Some research has focused on examining the interaction of the disturbed soil above the mine with the atmosphere (e.g., Das et al 2001, Garcia-Padron et al., 2002) while other research has examined soil properties around different buried objects (Hendrickx et al., 1999; Ochsner et al., 2001; Smits et al., 2012), no research to date has looked at the effect of the soil disturbance and mixing. Results from Das et al. (2001) demonstrate that soil above and below a landmine differ from that of the surrounding soil due to the disturbed nature of the soil compared to the undisturbed, more compact surrounding soil. Although Smits et al. (2012) examined the thermal and saturation behavior around a buried object, they assumed homogeneous soil conditions and did not consider soil disturbance nor mixing. The thermal signature of a buried object depends on the complex interaction among a soil's water content and the thermal and hydraulic properties of both the soil and the buried object and that temperature contrasts are larger in wet than dry soil (Das et al., 2001; Smits et al., 2012). Borchers et al. (2000) conducted a field study in which soil water content was measured at four total depths above and below a surrogate landmine showing a rapid increase in water content above the mine due to added water and a slower response below the mine with the highest water content recorded directly above the mine. This study assumed homogenous soil throughout, the variability of the soil water content was only caused by temporal variability of weather parameters or by the effect of the mine on water distribution. However, soil water content varies spatially which was not included in this study.

The landmine itself has a tremendous impact on its ultimate detection. Each detection technique applies differently based upon landmine case, explosive material, and soil (Kasban et al., 2010). Considerations regarding detecting buried landmines include the landmines themselves

and their diverse sizes, shapes, composition, and burial depth (Koh and Ballard, 2004; Moukalled et al., 2006). Landmine material makeup (i.e., metal, plastic, wood, fiberglass, bakelite, ceramic, cardboard, concrete, neoprene, and resin) are other characteristics that impact detection probability based upon the detection technology employed (Sai et al., 1998, Estes et al., 2011).

The placement of the mine also has an impact. For example, heat and diffusion parameters of a soil are disturbed through mine emplacement (Garcia-Padron et al., 2002). The depth of burial for the mine alters the mass and momentum properties within the disturbed soil environment. Additionally, the aging of the environment (i.e., wetting drying cycles, changes in soil density, geochemical reactions) in which the landmine is placed impacts the landmine casing as well as differentiation between buried object and surrounding soil (Estes et al., 2011).

Although it is well known that each technology's performance is affected by the environmental conditions in which the mine is placed, most research efforts focus on the response/effectiveness of the technology (e.g., ground penetrating radar (GPR) or vapor explosive detection) rather than the environmental conditions. However, an understanding of different environmental conditions is key to sensor performance. As stated by MacDonald et al. (2003), the only way we can improve the algorithms used for advanced signal processing is to improve our understanding of the environmental response due to soil disturbance associated with landmine burial.

For example, GPR performance is very sensitive to soil water content (English, 2000; Hendrickx et al., 2001; Garcia-Padron et al., 2002; Estes et al., 2011; Ratto et al., 2011; Edwards et al., 2015) as the contrast of the dielectric constant of the soil surrounding the landmine is the basis of detection with GPR. GPR performance changes based upon soil moisture and soil type among other characteristics (Borchers et al., 2000). For example, Hendrickx et al. (2001) showed

that uncertainty in soil water content (coefficients of variability ranging from 10% to 40%) can account for 30 db differences in the strength of GPR reflections and attenuation from a landmine.

While GPR relies predominantly on soil moisture conditions, temperature fluctuations are the basis of detection for infrared (IR) imaging sensors through identification of a temperature difference between the target and background that generates the target signature. IR detector systems are typically capable of discriminating targets with surface temperature differences in the range of 0.3^{o}C (Maksymonko et al., 1995). The variation in soil surface temperature is a result of the differences in soil conditions (e.g., soil disturbance and soil type) in the vicinity of a mine, which results in differences in soil moisture content as well as the thermal properties of the landmines themselves. A buried landmine heats up and cools down at a rate different from the surrounding soil resulting in unequal heat transfer rates manifesting themselves on the surface above the landmine through either a higher or lower surface temperature than the surface temperature at a location away from the landmine. Garcia-Padron et al. (2002) identified a number of environmental conditions that impacted IR detection technology capabilities. Surface characteristics of interest include background clutter which reduces thermal contrast clarity, irregular surface emissivity and reflectivity, shadows on the surface, and vegetation. Subsurface characteristics that impact IR detection capabilities include soil heterogeneity, rocks, and roots. The impact of a mine's thermal properties diminishes as mine burial depth increases which enables an increase in the influence on surface temperature based upon the soil volume above the mine (Garcia-Padron et al., 2002). To date, a field study that comprehensively provides soil moisture and temperature data cannot be found.

A variety of numerical modeling efforts have been undertaken to accurately predict buried landmine locations. The numerical models vary in their level of complexity and how they

incorporate subsurface and surface conditions. For example, Hendrickx et al. (1999) identified high variability in time as well as space with respect to soil water distributions based upon weather conditions and soil type, highlighting that a steady-state or periodic boundary condition approach is not appropriate to study soil water distributions around landmines (Das et al., 2001). A non-steady state two-dimensional heat and mass transfer model was developed by Moukalled and Saleh (2006) demonstrating that the conservative approach presented overcomes mass imbalance problems. Several numerical studies on the thermal signature of buried landmines in soils have been conducted (Baertlein et al., 2001; Kürsat and Baertlein, 2000; Pregowski et al., 2000; Sendur and Baertlein, 2000; Simunek et al., 2001; Khanafer and Vafai 2002; Moukalled and Saleh, 2006) but the effect of soil moisture conditions on the thermal signature of buried landmines is often neglected (Khanafer and Vafai, 2002; Khanafer et al., 2006), incomplete due to sparse data sets (Pregowski et al., 2000) or never compared to experimental results (Sendur and Baertlein, 2000; Kürsat and Baertlein, 2000; Simunek et al., 2001; Moukalled et al., 2006).

Moukalled and Saleh (2006) performed a detailed laboratory experiment on the thermal signature of buried landmines in dry soil. They examined the surface signature changes during heating and cooling using an IR camera, again investigating the responsiveness of the technology and not the soil conditions themselves. In a follow on investigation, they performed a numerical study to determine if there is an optimum moisture content value that maximizes the thermal contrast at the soil surface but did not validate their model with an experimental data set (Moukalled et al., 2006).

Smits et al. (2012) performed a numerical study relating observed and simulated temperature and saturation above and below a buried box in a well, controlled laboratory setting. Their research identified that it is important to take into account water contents far lower than

residual and the effect of temperature on soil water retention function to properly model soil moisture distributions around landmines. The Smits et al. (2012) numerical effort used a two-phase flow model with nonequilibrium mass transfer developed by Smits et al. (2011). The model was then used to show specific temperature and moisture response relative to landmine and limestone block burial.

For any numerical study to be successful, the numerical model developed must be verified against experimental data. The purpose of this research was to generate a data set with high spatial and temporal resolution for the use of comparison with future modeling effort and validation. No previous research exists that simultaneously evaluates the impact of soil disturbance, burial depth, and object properties on the soil moisture and temperature distributions in the vicinity of a landmine. Therefore, the research presented herein investigates all three conditions. It is the hope of the author that the data collected to improve our understanding of the transient behavior of heat and mass flow in the vicinity of buried objects may be used in future efforts to improve models and algorithms used for landmine detection. The impact of the diurnal cycle and precipitation events are investigated as well. In addition to landmine detection, this work is relevant to many applications related to heat and mass transfer though permeable media to include the flux of CO_2 through soil (Raich and Schlesinger, 1992; Di Martino et al., 2016) and local and global water and energy budgets (Liang et al., 1994; Larson et al., 2016).

6.3 Mass and Heat Flow Theory Fundamentals

This section discusses the key governing equations for consideration regarding mass and heat flow in the vicinity of a buried mine. A review of the equations provides insight into the properties that must be measured for the purposes of acquiring the correct inputs for the fundamental relationships.

6.3.1 Mass Flow in Soils

Water movement through soil is approximated by Richards' equation which incorporates both water balance (Darcy's law) and the principle of mass conservation for saturated and partially saturated soil (Richards, 1931):

$$S_s S(\psi) \frac{\partial \psi}{\partial t} + \phi \frac{\partial S(\psi)}{\partial t} = \nabla \cdot [K_s k_r(\psi) \nabla(\psi + z)] + W \quad (6.1)$$

where S_s is the specific storage (m^{-1}), $S(\psi)$ is the water degree of saturation (-), ψ is the water head (m), ϕ is porosity ($m^3\ m^{-3}$), K_s is the water-saturated hydraulic conductivity ($m\ s^{-1}$), k_r is the relative permeability of the media (-), z is the vertical coordinate (m), and W is a source/sink term ($kg\ s^{-1}$). The specific storage (S_s) is defined as the volume of water released by a unit volume of soil due to a unit decrease in hydraulic head. The source/sink term (W) enables release of water into the system based on previously stored water content or removal of moisture from the system (e.g., formation of thin films on the soil grains). The saturation and relative permeability term are based upon van Genuchten (1980):

$$S = S_r + \frac{(1 - S_r)}{[1 + (\alpha\psi)^n]^m} \quad (6.2)$$

$$k_r = \frac{\left[1 - (\alpha\psi)^{n-1}[1 + (\alpha\psi)^n]^{-m}\right]^2}{[1 + (\alpha\psi)^n]^{m/2}} \quad (6.3)$$

where S_r is residual saturation, α (cm^{-1}), n (-) and m (-) are van Genuchten parameters with $m = (1 - 1/n)$.

In the current form of Eq. 6.1, water vapor transport is neglected. Therefore, Eq. 1 is the classical mixed form of Richards' equation which contains pressure and saturation. Vapor transport must be included to reproduce diurnal dynamics of the soil moisture. The diurnal dynamics are controlled by vapor transport, radiation, air temperature, and relative air humidity.

6.3.2 Heat Flow in Soils

The energy balance incorporates heat conduction, convection and surface heat exchange:

$$(\rho_s c_s)_m \frac{\partial T}{\partial t} + (\rho_s c_s)_f \nabla \cdot (vT) = \nabla \cdot (\lambda_e \nabla T) + q_m \quad (6.4)$$

where ρ_s is the soil density (kg m^{-3}), c_s is the soil specific heat capacity (MJ m^{-3} K^{-1}), T is temperature (K), q_m is the source of energy (W m^{-2}) taking into account radiation, and λ_e is effective thermal conductivity (W m^{-1} K^{-1}). Specific heat and thermal conductivity depend on soil moisture (Howington et al., 2006). de Vries (1963) defines soil heat capacity as a weighted average of the mineral, organic, and water components within the soil:

$$c_s = \frac{\phi_m \rho_m c_m + \phi_o \rho_o c_o + \phi_w \rho_w c_w}{\rho_s} \quad (6.5)$$

where ϕ is porosity and the subscripts *m*, *o*, and *w* refer to mineral, organic, and water components, respectively. There are numerous models to determine thermal conductivity; however, the one selected with minimal fitting parameters was developed recently by Lu and Dong (2015):

$$\lambda_e = \lambda_{dry} + \left(1 - \left[1 + \left(\frac{\theta}{\theta_f}\right)^m\right]^{(1/m-1)}\right)(\lambda_{sat} - \lambda_{dry}) \quad (6.6)$$

where *m* is the pore fluid network connectivity parameter related to the pore-size parameter *n* in the van Genuchten (1980) model, and θ_f is the onset of funicular water content corresponding to the highest rate of change in water content between the pendular and hydration regimes. These two variables are fitting parameters whereas λ_{sat} and λ_{dry} are the measured saturated and dry thermal conductivity of the soil.

6.4 Material and Methods

In this section, site selection is described. This is followed by providing information regarding the soil on site. The, the experimental design is explained as well as the experimental methods.

6.4.1 Site Selection

The work of this research focuses on desert environments which occupy approximately 31.5% of the Earth's land surface (Dregne, 1976). Soils in deserts experience less weathering and leaching resulting in coarse textured, shallow soils (Cooke et al., 1993). Therefore, we selected a site field experimentation that mimics a desert environment and consisted of a 10 m-wide by 10 m-long by 2 m-deep volume prepared with poorly graded concrete sand (SP) based upon the Unified Soil Classification (USCS) (Fairley et al., 2014). The soil is well categorized, homogeneous, and free of vegetation.

6.4.2 Description of Soil

The soils were separately characterized using a variety of standard methods in the laboratory based upon 12 core samples taken 0 to approx. 20 cm below ground surface (bgs). A sieve analysis was conducted using standard methods (ASTM, 1987) that identified the soil's uniformity coefficient as approximately 1.8 with a mean particle diameter, d_g, of 0.596 mm. The average saturated hydraulic conductivity for undisturbed soil, K_s, was determined based upon separate constant head hydraulic conductivity experiments conducted in an acrylic column. The column was packed as described in Sakaki et al. (2008). At least three packings were analyzed and in accordance with ASTM (2000), the hydraulic conductivity values were corrected to 20^{o}C. Three separate soil water retention and thermal conductivity test were conducted using a small cell to

determine the saturation-capillary pressure (S-p_c) and saturation-thermal conductivity (S-λ) relationships for both undisturbed and disturbed soil conditions. Additional selected soil properties are provided in Table 6.1.

Table 6.1. Key field soil properties.*

						**		***	
Soil Conditions	ϕ (-)	ρ_p (g cm^{-3})	ρ_B (g cm^{-3})	h_c (cm H_2O)	θ_r (-)	α (cm^{-1})	n (–)	λ_{dry} (W m^{-1} K^{-1})	λ_{sat} (W m^{-1} K^{-1})
Undisturbed	0.38	2.65	1.64	16.75	0.024	0.05	9.09	0.268	2.906
Disturbed	0.47	2.66	1.41	11.24	0.030	0.07	4.14	0.263	2.687

*ϕ = porosity, ρ_p = particle density, ρ_B = dry bulk density, h_c = air entry pressure, θ_r = residual water content
**van Genuchten (1980) model parameters
***Lu and Dong (2015) model inputs: λ_{dry} = dry thermal conductivity, λ_{sat} = saturated thermal conductivity

6.4.3 Experimental Design

The need for careful experimental validation of predictions based upon models was highlighted in numerous research efforts on landmine detection (e.g., Maksymonko et al., 1995; Şendur and Baertlein, 2000; Simunek et al., 2001; Garcia-Padron et al., 2002). The experimental design included evaluation of four different object emplacements: 1) shallow surrogate landmine, 2) deep surrogate landmine, 3) limestone block, and 4) disturbed soil. A schematic of the site set up is shown in Figure 6.1. The shallow mine and limestone block were buried 2.5 cm below the surface while the deep mine was buried 10 cm below the surface. For the fourth test case, a separate hole of the same dimensions as the objects was dug and then backfilled with loose, disturbed soil. Specific characteristics of the surrogate mines and limestone block are provided in Table 6.2. Temperature and soil moisture sensors were placed in the disturbed and undisturbed soil associated with each emplacement location at depths of 2.5, 7.5, 12.5 and 17.5 cm below the ground surface

(bgs). These depths were selected based upon comparison with previous studies (e.g., Miller et al., 2004) and our existing laboratory experimental set up to better transition to future research based upon similar data input. Temperature and relative humidity were measured at both1 cm and 28 cm above the soil surface. Wind speed and direction was measured 51 cm above ground surface. A meteorological station located approx. 48 m from the site provided essential environmental data (e.g., pressure, radiation).

Soil water content was monitored using a total of 17 EC-5 dielectric soil moisture sensors (Decagon Devices, Inc., Pullman, WA; sensor length = 5.5 cm, measurement frequency = 70 MHz, accuracy = 3%, resolution = 0.1%). These sensors measured the dielectric permittivity of the surrounding porous medium in terms of an analog-to-digital converter number (ADC count) which was later converted to soil water saturation using the two-point α-mixing model developed by Sakaki et al. (2008).

Sensors were installed horizontally between the depths of 2.5 and 17.5 cm in 5 cm increments as shown in Figure 6.1. A total of 17 ECT temperature sensors (Decagon Devices, Inc.; USA, accuracy = 0.5^{o}C (5-40^{o}C) and 1.0^{o}C (>40^{o}C), resolution = 0.1^{o}C) were similarly installed horizontally at 5 cm increments between the depths of 2.5 and 17.5 cm (Figure 6.1). Soil moisture and temperature were continuously monitored at 60 minute intervals.

Two relative humidity/temperature sensors (EHT, Decagon Devices, Inc.; USA, temperature: accuracy = 0.5^{o}C (5-40^{o}C) and 1.0^{o}C (>40^{o}C), resolution = 0.1^{o}C, relative humidity: accuracy = 2%, resolution = 0.1%) were installed at 1 and 27.9 cm above the soil surface to obtain near surface and ambient measurements (Figure 6.1). Both sensors were encased in radiation shielding to mitigate potential sensor body heating which could influence measurement fidelity.

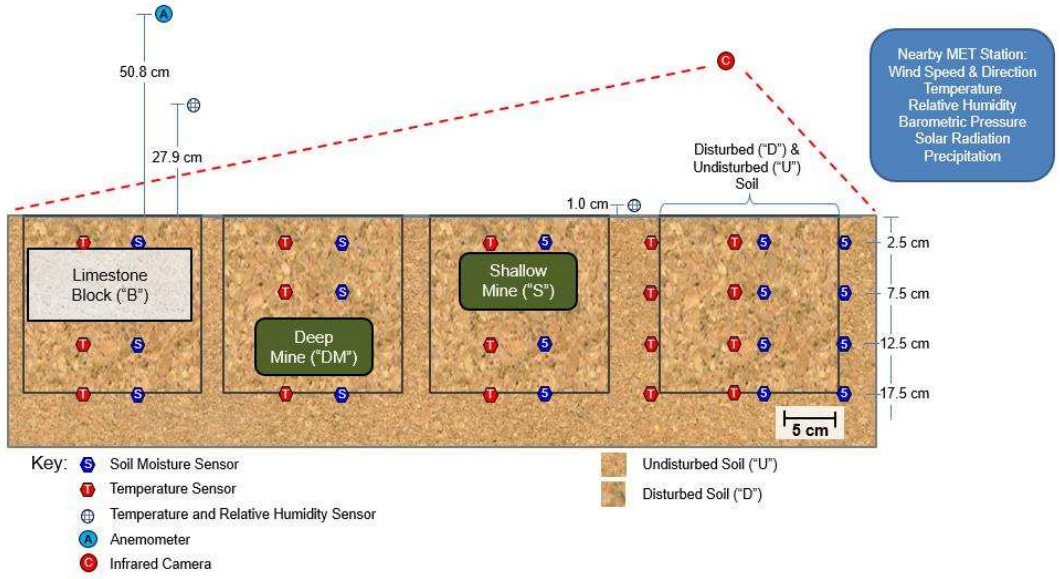

Figure 6.1. Sketch illustrating the experimental set-up to include buried object and sensor locations (cross sectional view).

Table 6.2. Properties of surrogate mines and limestone block.

Object	Property			
	Thermal Conductivity, λ [W m^{-1} K^{-1}]	Specific Heat Capacity, C_p [J kg^{-1} K^{-1}]	Density, ρ [kg m^{-3}]	dimensions
Surrogate Mine*	0.37	1500	1340	d=11.2cm, h=5.6cm explosive weight=550g explosive type=TNT
Limestone Block**	1.9	840	2611	l*w*h 16cm*10cm*7cm

*Values reported by Moukalled et al. (2006).
**Values determined experimentally.

To determine the soil surface temperature in the plot area, two methods were used, an infrared camera and a laser temperature thermometer. Surface temperature was measured over the entire area of interest using a 320×240 pixel resolution Model EX320 infrared camera (FLIR Systems; USA, spectral range = 7.3-13 μm, accuracy = 2^{o}C). The soil surface temperature was

also measured at 10 different locations (Figure 6.2) using a 630-670 nm laser temperature thermometer Model 2265-20 (Milwaukee® Laser Tem Gun™; USA, spectral range = 5.5-14 μm, accuracy = 1.5°C, distance to spot ratio = 1:10). As seen in Figure 6.2, the measurement locations were selected directly above and adjacent to each of the four emplacement locations. The laser thermometer allowed for the collection of data at specific points and confirmation of IR measurements. Temperature measurements were taken approximately every one hour over the course of the experiment (10 days).

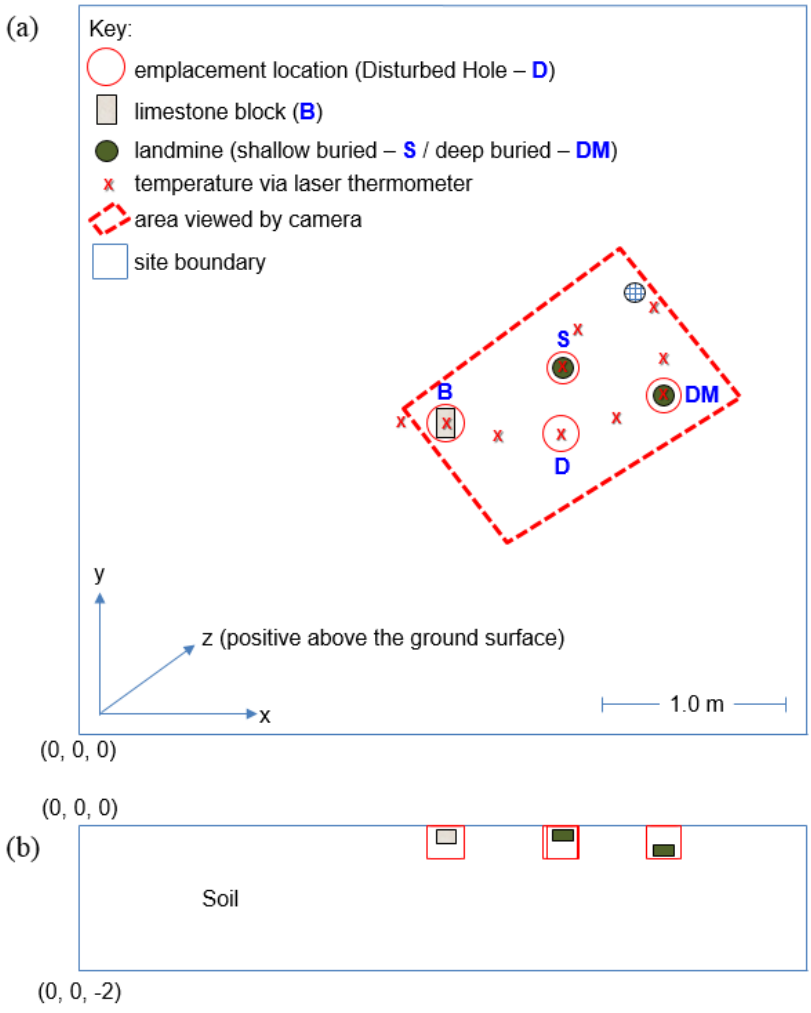

Figure 6.2. Schematic of (a) plan view of site showing emplacement locations, points of temperature acquired via laser thermometer, and infrared camera field of view, and (b) top view of the soil bed. Scale shown on figure.

A local meteorological station provided continuous monitoring (every 5 minutes) of barometric pressure, net radiation, precipitation, ambient temperature, relative humidity, wind speed and direction from 0.5 m and 2 m above the surface. Measured temperature, relative humidity, wind speed and wind direction were in good agreement with measurements made directly at the study site. Therefore, only the barometric pressure and net radiation measured from the meteorological station were used for numerical modeling.

6.4.4 Experimental Methods

The experiment was conducted from 20 to 30 July 2015 (i.e., 10 days) in Vicksburg, MS (32.3361^{o}N, 90.8753^{o}W). Data collection began after the site was prepared with all four emplacement locations established and objects buried with disturbed soil filling all emplacement locations flush with the soil surface. The experiment included three rain events (two periods of applying water manually to the surface followed by one naturally occurring rainfall event) with all occurring between days 4.5 to 5.5. In the first manual rain event (referred to as Rain Event 1 in subsequent figures), 3.5 cm of water was applied over the study site with 8.7 cm applied during the second manual rain event (referred to as Rain Event 2 in subsequent figures). The natural rain event (referred to as Rain Event 3 in subsequent figures) lasted 90 minutes resulting in 1.05 cm applied over the entire site. Throughout the course of the experiment, the sun came in direct contact with the site around 8 am and the site was shaded around 8 am due to sun setting with experimental conditions shown in Table 6.3.

Table 6.3. Summary of diurnal experimental conditions for field experiment.

Time of Day	Average Ambient Temperature (°C)	Average Ambient RH (%)	Average Surface Temperature (°C)	Average Surface RH (%)	Average Wind Speed ($m\ s^{-1}$)	Average Net Radiation ($W\ m^{-2}$)
Day	35.6	50.96	45.1	42.06	0.891	207.7
Night	26.3	83.07	27.2	77.46	0.169	20.1

6.5 Experimental Results

Figure 6.3a shows the average wind speed over the course of the experiment was 0.5 m s^{-1} with a clear diurnal effect of solar forcing on wind speed. For example, there is a considerably higher wind speed during the day due to solar heating. Diurnal fluctuations are also seen in Figure 6b and c (relative humidity and temperature). The three rain events are noted in subsequent figures with the thickness of the line relative to the duration of the rain event. After each rain event (e.g., time = 4.45 days, 4.78 days, and 5.30 days), the range of fluctuation in relative humidity increases and temperature decreases due to an increase in near soil moisture. Figure 6c shows the temperature at 1 and 27.9 cm above the soil surface. The diurnal effect is fairly consistent throughout the duration of the experiments. Analysis will focus on the period from days 3.5 to 7.5 in order to highlight conditions for 24-hours prior to the rain events, during, and two days after the completion of all rain events. The time of day associated with day X.5 is midnight and X.0 is noon. Any gaps in recorded data occur due to either sensor anomalies or a period of not taking measurements.

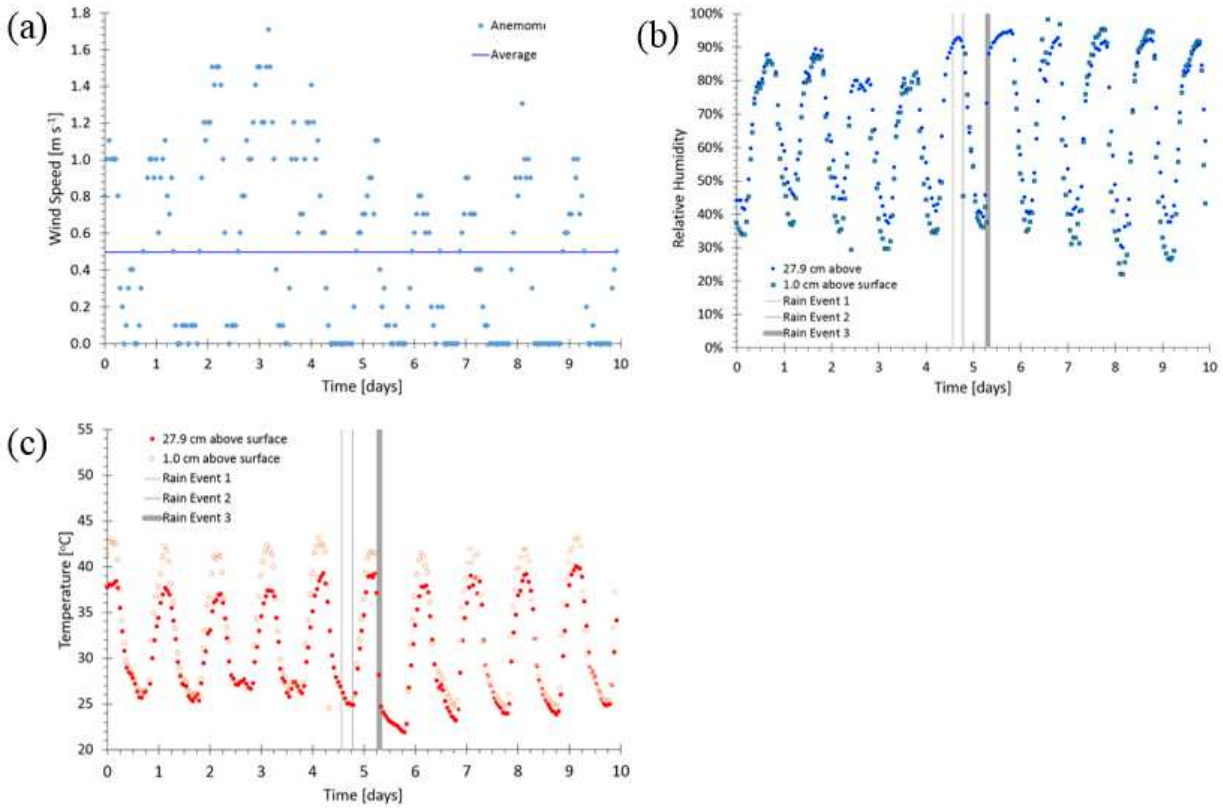

Figure 6.3. Experimental conditions: (a) wind speed, (b) relative humidity, (c) temperature. Note: time zero is 12 pm on day one of the experiment.

6.5.1 Temperature

Figure 6.4a shows the surface temperature measured above each of the four locations of interests (i.e., mines, limestone block, disturbed soil) in comparison to the average temperature measured at all undisturbed locations (6 locations away from the four locations of interest). Figure 6.4b shows the thermal contrast (difference between temperature above each emplacement location and the surrounding undisturbed soil).

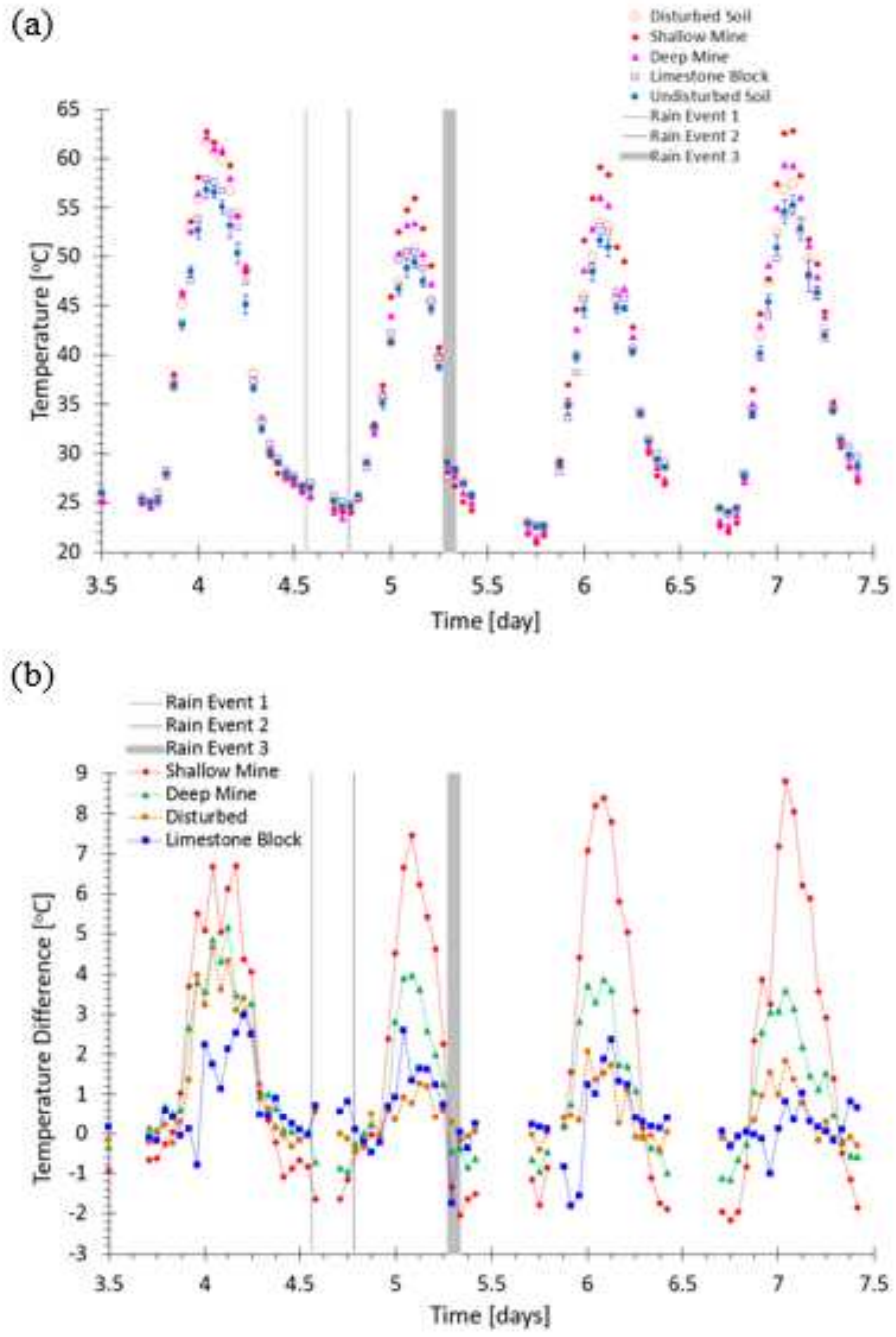

Figure 6.4. Soil surface temperature comparison for emplacement locations: (a) direct temperature measurement, (b) thermal contrast.

In general, the shallow buried surrogate mine displayed the largest thermal contrast (approx. 7.85°C) during the daytime. This was followed by the deep mine and disturbed soil. The

smallest thermal contrast was observed with the limestone block. The largest contrast occurring between 12 to 3 pm, for all buried objects/soil disturbance throughout the entire experiment. The disturbed soil had a larger thermal contrast than the limestone block due to the limestone block serving as a barrier to heat and mass flux. The limestone block absorbed and released heat more restrictively compared to the disturbed.

Prior to any rain events (Figure 6.4), during the night from days 3.5 to 3.9 or days 4.4 to 4.5, for example, there is not a statistically significant difference in surface temperature between the sites. The statistical significance was determined based on the RMSE of the sensors. However, during the day, a statistically significant difference in temperature is observed. The peak temperatures occur between day 4 to 4.2 (12 to 6 pm) seen in Figure 6.4a. The surface temperature above the shallow mine, deep mine, and disturbed soil remain in good agreement and exhibit a significant increase over the undisturbed soil and limestone block. The temperature above the limestone block is generally within the same range as the undisturbed soil.

The rain events significantly altered the thermal contrast above each of the emplacement locations except for the shallow mine. The rain events enabled settling and compaction of the soil in each of the four locations which resulted in changes to the porosity and other associated soil characteristics (e.g., capillarity, thermal conductivity). As a result, the disturbed soil location had a significant decrease in thermal contrast and approached a similar response to that of the limestone block. The thermal contrast associated with the deep mine was reduced slightly compared with the response prior to rain events; however, the shallow mine's thermal contrast increased slightly. The increase for the shallow mine may be a result of the soil compacting and reducing the thickness of the soil layer above the mine. The more compact soil causes more contact between soil grains enabling higher thermal conductivity and heat transfer between the surface and the absorption of

the heat onto the surrogate mine. Rain event 1 and 2 caused a shift in the time associated with being able to identify a thermal contrast for all locations. Prior to the rain events, the first significant thermal contrast was observed at 8 am. After rain events 1 and 2, the first significant thermal contrast was observed at 12 pm.

The first 24 hours that immediately followed rain event 3, portrayed a more pronounced thermal contrast at night for the shallow buried mine and slightly less so for the deep buried mine enabling a thermal signature at night that was not previously distinguishable (i.e., prior to the rain event). The thermal contrast during the day increased slightly for the shallow buried mine due to potentially more compaction of the disturbed soil surrounding and covering the surrogate mine. The disturbed soil maintained a similar thermal contrast to that of the limestone block. Therefore, within 24 hours of completion of all rain events, the disturbed soil and limestone block have a reduced thermal signature compared to either surrogate mine location potentially enabling clearer identification of buried mines both at day and at night.

The second day following rain event 3 (day 6.3 to 7.3) exhibited a decrease in thermal contrast of the limestone block resulting in almost no period during the day which enable an identifiable thermal signature. The peak thermal contrast for the deep mine decreases slightly from 4^{o}C to 3.6^{o}C from day 4.5 to 7.5, whereas the peak thermal contrast for the shallow mine increases from 7.5^{o}C to 8.8^{o}C over the same period. The decrease in thermal contrast associated with an increase in burial depth of the surrogate mine is similar to modeled results by Moukalled et al. (2006). The disturbed soil maintained a slightly higher thermal contrast compared to the buried limestone block. Although not shown, these trends for all emplacement locations persist through to the completion of the experiment.

The previous discussion regarding thermal contrast is more vividly shown with the IR images (Figure 6.5). The figure shows the temperature at the surface at 7:00 a.m. (one hour prior to direct sunlight), 2:00 p.m. (maximum daily temperature) and 9:00 p.m. (no solar light visible). Images are shown for three different times: prior to rain events (day 4.56), during an hour prior to (Figure 6.5a) and during direct solar heating of the site (Figure 6.5b) and no thermal contrast at night (Figure 6.5c). Immediately following rain events, there is no identifiable thermal signature of any emplacement locations at 7:00 a.m. (Figure 6.5d). Only the thermal signature of the shallow buried and deep buried mine are apparent during the heat of the day (Figure 6.5e) with the shallow buried mine having a more significant thermal contrast. This contrast is also apparent at 9:00 p.m. (Figure 6.5f) for both mines in the same relation of strength of signal. About three days after the rain events, there is a thermal signature at 7:00 a.m. (Figure 6.5g) again for both mines with the shallow buried mine having a significantly stronger contrast due to evaporative cooling above the landmine compared to the surrounding soil. This same signature is observed at 9:00 p.m. (Figure 6.5i) but to a lesser extent. The signature of both surrogate mines are again apparent during 2:00 p.m. (Figure 6.5h) with the temperature above the shallow buried mine being considerably hotter than the surrounding soil. However, the signal is very clearly identified whereas the signature from the deep buried mine is observed but the boundaries are less clearly defined. The significance of research presented herein is enabling confirmation of numerical results from Moukalled et al. (2006) that IR technology is better suited for shallow buried mines (i.e., antipersonnel mines). Additionally, the experimental results presented confirm the results of the simulation study by Simunek et al. (2001) that identified a more pronounced thermal signature of buried mines in wet rather than dry soils. To an extent, confirmation of these previously reported results provide increased fidelity regarding selection of operational conditions to follow for demining operations.

Relation to Rain Events	7:00 a.m.	2:00 p.m.	9:00 p.m.
Prior to Rain Events	(a) 	(b) 	(c) 
Immediately After Rain Events (1) – 1:30 am (2) – 6:45 am (3) – 6:30 pm	(d) (1) (2) 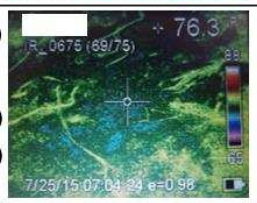	(e) 	(f) (3) 
3 Days After Rain Events	(g) 	(h) 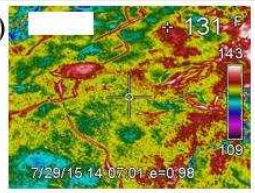	(i) 

Figure 6.5. Infrared thermography of emplacement locations prior to, immediately following, and multiple days after rain events at specific representative times of 7 a.m., 2 p.m., and 9 p.m. Rain events are noted as (1), (2), and (3) with the numbers placed next to the image closest to the rain event occurrence.

The temperature profile from the surface through all four subsurface measurements (Figure 6.1) is shown for each emplacement location in Figure 6.6. A review of all emplacement locations clearly shows that the time of peak temperature shifts to later in the day as depth increases. The temperature profile exhibits an inversion (i.e., where the temperature closer to the soil surface is hotter than further subsurface measurements) during the primary evaporation period (~X.0-X.3, ~12:00-3:00 p.m.). The disturbed soil (Figure 6.6.a) exhibits a smooth transition in temperature at all depths over the diurnal cycle. With regard to the shallow and deep buried mines (Figure 6.6b and c, respectively), the profile is similar to that of the disturbed soil except for the temperature measured directly above the mine. During the day, the temperature is higher above the mines than

at the same location in the disturbed soil. This is due to the surrogate mine's thermal properties and ability to store heat. The soil directly above the mine in conjunction with the surrogate mine result in a localized higher thermal conductivity and resulting temperature. During the night, the temperatures above the surrogate mines are lower than the temperature at the same depth for the disturbed soil location due to the mine serving as a barrier to fluid flow when condensation conditions dominate. Heat capacity and storage are also affected. The temperature just below the surface (2.5 cm) for both the disturbed soil and deep buried mine remain almost identical throughout the duration of the experiment. Therefore except for the temperature directly above a buried surrogate mine, the temperature response of a disturbed soil location effectively reflects a similar temperature response for buried surrogate mines at various depths. A comparison of the thermal response between the shallow buried mine and the buried limestone block (Figure 6.6d) shows a significant difference. The temperature at 2.5 cm bgs for the limestone block is ~10^{o}C less than the shallow mine location during the peak heat of the day. However, there is almost no difference in temperature at 2.5 cm bgs between the limestone block and disturbed soil location at night. The soil heterogeneity represented by the limestone block does alter heat and mass transfer in the vicinity of the block; however, to a varying extent than the surrogate mine. Additionally, the buried limestone block more extensively prohibits heat transfer below due to more completely occupying the hole dug for emplacement (dimensional differences between limestone block and surrogate mines) and representing more inherent natural heterogeneity conditions. Therefore, there is no temperature inversion experience below the limestone block for the 12.5 and 17.5 cm measurements. The fact that the limestone block does not closely resemble the environmental response for either mine burial depth or the disturbed hole further demonstrates the dynamic nature of response associated with background heterogeneities that may exist in areas where landmines

are buried. The ability to distinguish between the typical responses from a more natural versus a manmade disturbance is essential for algorithmic fusion and improvement.

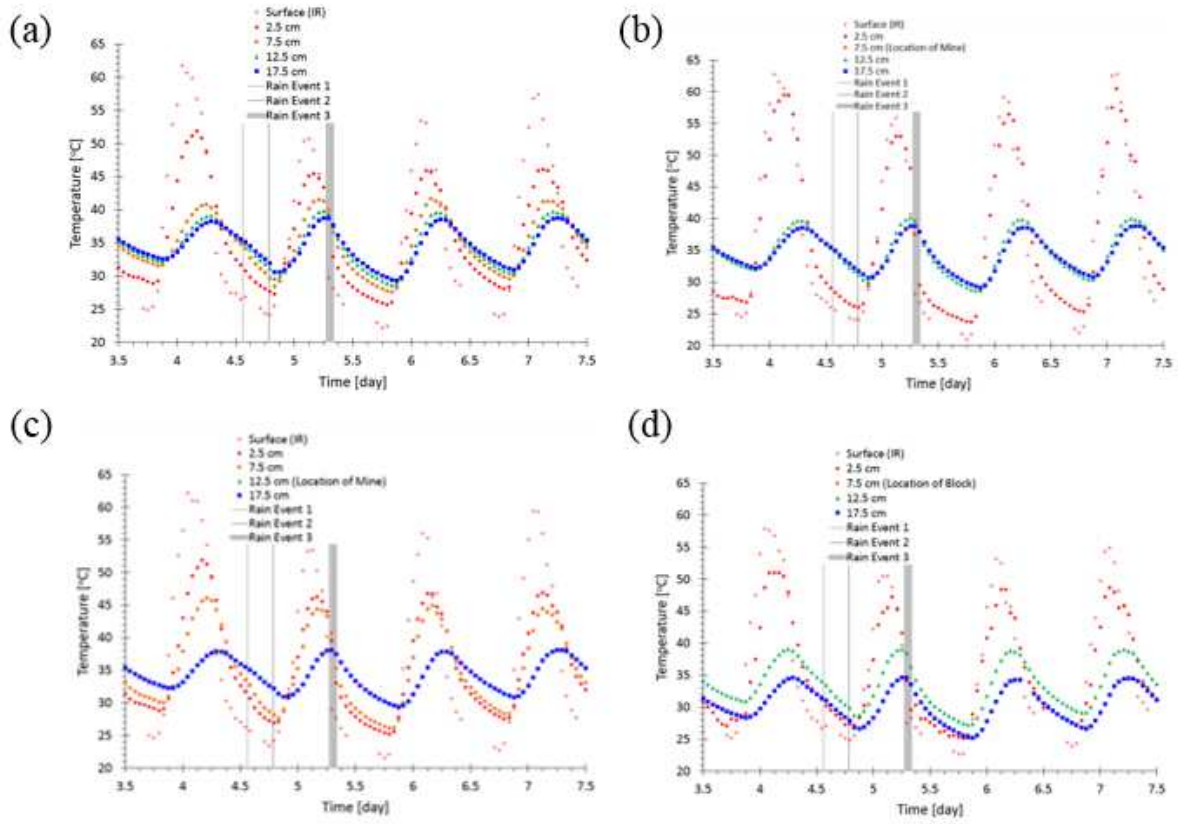

Figure 6.6. Temperature profiles for each emplacement location: (a) disturbed soil, (b) shallow mine, (c) deep mine, and (d) limestone block.

6.5.2 Soil Moisture

Soil moisture is another significant characteristic to measure for a more complete understanding of the impact of rain events associated with variations in burial depth, type of object buried, and disturbed soil. The interaction of the diurnal cycle along with the three rain events is shown for both the temperature and soil moisture at 2.5 cm below the surface for the shallow buried mine, deep buried mine, disturbed soil, and undisturbed soil (Figure 6.7). The temperature

is relatively unaffected by the rain events with the temperature for the deep buried mine, disturbed soil, and undisturbed soil exhibiting similar characteristics. Only the shallow buried mine portrays higher heating during the day and more cooling at night compared to the other emplacement locations. The significance of the rain events is more clearly shown with respect to changes in saturation.

Prior to any rain events, the soil moisture between the different emplacement locations was in good agreement with a slight increase observed during the heat of the day (x.95-x.25) due to the soil's capillary potential and the higher atmospheric demand for moisture. Immediately following rain event 1, saturation increased more significantly in the undisturbed soil due to the lower porosity associated with the tighter packing in relation to the loose soil resulting in higher capillarity. The disturbed soil and shallow buried mine both had an initial increase in saturation by about 10% with the disturbed soil maintaining a constant saturation level through to rain event 2 due to the soil settling as a function of becoming wet and changing physical characteristics slightly. The saturation immediately above the shallow buried mine began decreasing rapidly after the initial increase due to preferential water pathways developing around the boundary of the landmine as explained by Koh et al. (2006). The soil above the deep buried mine displayed a gradual increase without an immediate response to the rain event due to the water infiltrating to lower depths more rapidly and bypassing any immediate retention near the shallow subsurface. The variety of responses of soil moisture with the different emplacement locations and the background undisturbed soil demonstrates the natural environmental variability that is essential to consider in modeling efforts for improved algorithms.

The second rain event resulted in fairly similar increases in saturation as the first rain event for the shallow buried mine, disturbed and undisturbed soil. The deep buried mine had the most

significant increase in saturation by ~15%. The disturbed and undisturbed soil behave almost identically with a gradual decrease after the initial spike in saturation. The deep buried mine's saturation decreased overall interspersed with an increase during the heat of the day. The saturation associated with the shallow buried mine initially increased slightly followed by decreasing rapidly during the heat of the day due to the mines proximity to the surface and ability to store heat resulting in an increased near-surface temperature and evaporation compared to the other emplacement locations.

The third and only regional rain event during the experiment caused an almost identical initial increase in saturation for all emplacement locations compared to the increase from the first rain event. The decrease in saturation (initial increase for the deep buried mine) more closely resembled the response after the first rain event as well. The regional impact of the rain event, time of the event, and diurnal cycle resulted in a prolonged return to pre-saturation conditions for all emplacement locations. The shallow buried mine returned to pre-existing saturation conditions and temperature response within 24 hours of rain event three. The disturbed and undisturbed soil maintained the same relative decrease in saturation with the undisturbed soil exhibiting an initially slower decrease for about one day after rain event three due to the difference in soil properties. Over the next two days, the disturbed soil's saturation reduced slower than that of the shallow buried mine both due to the settling of the soil from precipitation and lack of a buried object in the subsurface to influence heat and mass transfer. At the end of the experiment, the disturbed soil demonstrated good agreement again with the shallow buried mine location. The deep buried mine location resulted in more intense saturation increases during the heat of the day that the other conditions followed by a higher rate of decrease in saturation at ~1500 hrs each day until close to ~2100 hrs when condensation conditions dominated over evaporation. As with the disturbed soil,

the saturation of the deep buried mine location returned to near pre-saturation conditions by the end of the 10-day experiment.

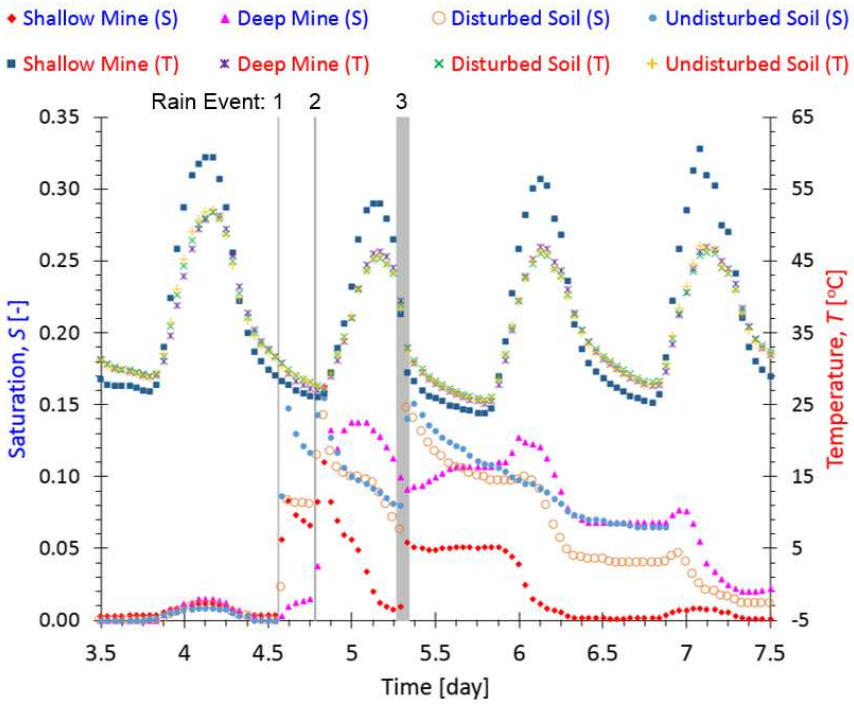

Figure 6.7. Saturation and temperature at 2.5 cm below the surface for comparison of emplacement locations.

As with the temperature discussion above, the saturation profile based upon the four subsurface measurements was evaluated (Figure 6.8). Prior to any rain event, the saturation at each depth was relatively constant with minimal diurnal influence except at 2.5 cm below the surface. After the first rain event, the disturbed soil (Figure 6.8a) exhibited no change in soil moisture except at 2.5 cm below the surface as was the case for the buried limestone block (Figure 6.8d). The saturation measured below the shallow buried mine (Figure 6.8b) decreased by the same percentage at both 12.5 and 17.5 cm below the surface, whereas the saturation below the deep buried mine (Figure 6.8c) increased slightly and then remained almost constant. The saturation above the deep buried mine increased moderately at 2.5 cm and exhibited almost no change at 7.5

cm. As a function of the second rain event and the preexisting increased saturation over the study site, saturation throughout all depths increased almost instantaneously except for 17.5 cm below the surface for the deep buried mine which may be due to water being stored in the soil above and held in the soil matrix with capillary forces exceeding gravitation forces. The saturation levels then decreased with higher rates nearer to the surface except for the shallow mine and at 17.5 cm for the deep mine and limestone block emplacement locations. In both those cases, the saturation levels remained relatively constant. After the third rain event, the saturation continued to remain relatively constant for all depths below buried objects. The saturation in the disturbed soil showed no apparent increase (except for 2.5 cm below the surface) immediately following the rain event and slight decreases at 7.5, 12.5, and 17.5 cm below the surface over the next two days. Of note, the saturation at 12.5 cm is higher than at 17.5 cm for the disturbed soil during the experiment due to changes in subsurface conditions where the overall porosity decreases slightly ~10 cm below the surface due to increased natural packing due to the weight of the above sand. Therefore as the soil properties change near this interface, the lower porosity results in higher capillarity causing an increase in local saturation as seen for all scenarios except the deep buried mine due to the mine displacing the sensor. The dichotomy in response to each rain event requires consideration of subsurface preferential flow pathways, changes in capillarity, and the influence of small heterogeneities in localized porosity changes. These are considerations for modeling efforts.

It is important to note that the observation and deductions made above are applicable for the specific type of soil (SP) in a hot, humid environment similar to climate conditions experienced during the field experiment. Caution must be used to extrapolate these results to other regions and other soil types. Therefore, there is a strong need for a model to investigate the heat and mass transfer changes for the four emplacement locations under varying climate conditions.

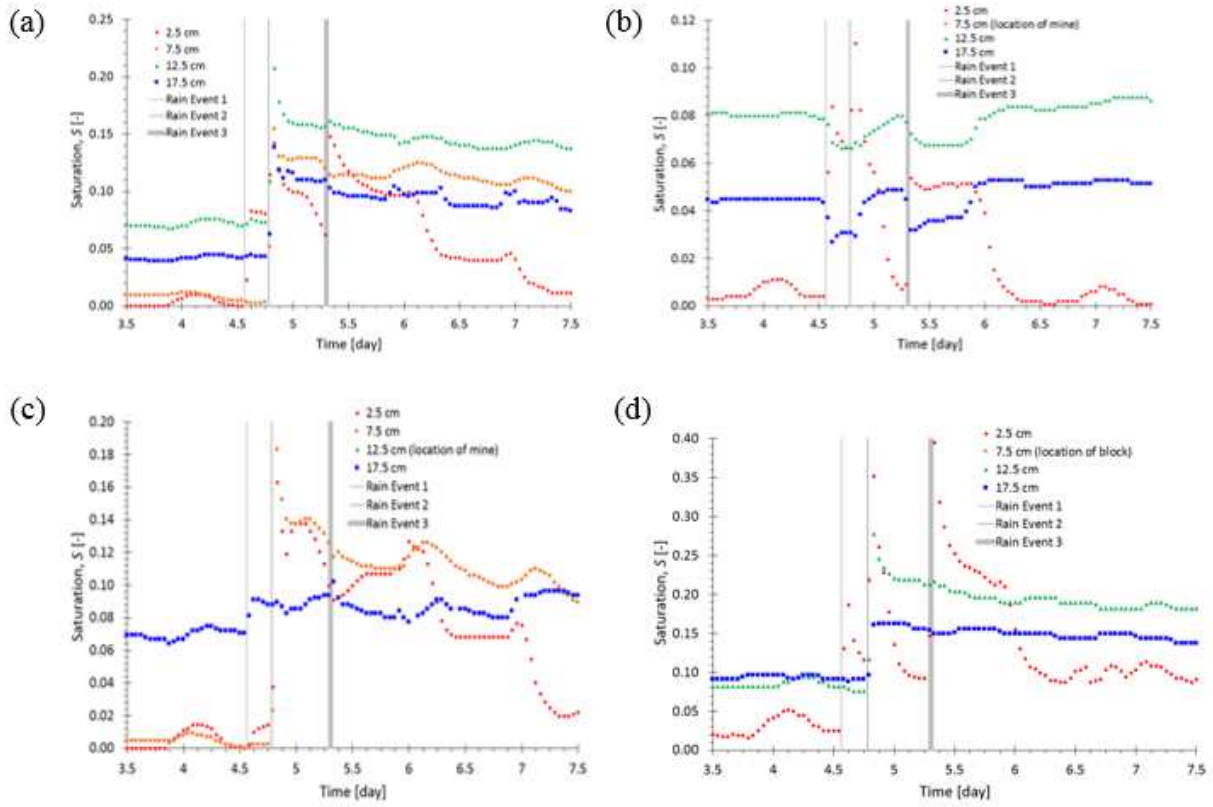

Figure 6.8. Saturation profiles for each emplacement location: (a) disturbed soil, (b) shallow mine, (c) deep mine, and (d) limestone block.

6.6 Conclusions

The purpose of this research was to generate a data set with high spatial and temporal resolution for the use of comparison with future modeling efforts and validation. No previous research exists that simultaneously evaluates the impact of soil disturbance, burial depth, and object properties on the soil moisture and temperature distributions in the vicinity of a landmine. Therefore, the research presented herein investigated all three conditions.

Experimental results enabled a series of significant conclusions related to poorly graded concrete sand with climate conditions associated with Vicksburg, MS from 20 to 30 July 2015.

Saturation events impact the visual signature and thermal contrast of emplacement locations: visual signatures disappear, thermal contrasts for shallow and deep mines are accentuated both during the day and night, and thermal contrasts for the soil disturbance location and limestone block are attenuated. The increase in burial depth of the deep mine results in decreased thermal response to diurnal variation. Soil moisture and thermal behavior of the disturbed soil location closely represent the behavior found with buried surrogate mines except for immediately above the mine location. The impact of changing soil properties due to rain events and depth near the surface must be incorporated for effective modeling in the vicinity of buried objects.

6.7 Acknowledgements

This research was funded by the U. S. Army Research Office Award W911NF-04-1-0169, the Engineering Research and Development Center (ERDC), the G.A. Harris Research Instrumentation Fellowship for Graduate Student Research, and Society of American Military Engineers - Denver Metro Post Professional Development Scholarship. The author wishes to thank, Stacy Howington, Matthew Geheran, Gustavo Galan-Comas, and Ryan North for support that made this field experiment possible and improved this research.

6.8 References

Andersson, Neil, Sergio Paredes, and Cesar Palha da Sousa. "Social cost of land mines in four countries: Afghanistan, Bosnia, Cambodia, and Mozambique." British Medical Journal 16 Sept. 1995: 718+. Academic OneFile. Web. 19 May 2015.

Arcand, J.L., A.S. Rodella-Boitreaud, and M. Rieger. 2014. The impact of land mines on child health: evidence from Angola. Economic development and cultural change. 63(2):249-279.

ASTM. 1987. Standard specification for wire-cloth sieves for testing purposes. ASTM E11-87, p.13-16, *In 1993 Annual Book of ASTM Standards*, Vol. 14.02., ASTM, Philadelphia, PA.

ASTM. 2000. Standard test methods for permeability of granular soils (Constant head). ASTM D2434-68, p.221-225, *In 2006 Annual Book of ASTM Standards*, Vol. 04.08., ASTM, Philadelphia, PA.

Baertlein, B.A., W.J. Liao, and D.H. Chen. 2001. Fusion of acoustic LDV and GPR data. Detection and Remediation Technologies for Mines and Minelike Targets VI. Proc. SPIE. pp.970-978.

Bello, R. 2013. Literature review on landmines and detection methods. Frontiers in Science. 3(1):27-42. doi:10.5923/j.fs.20130301.05

Borchers, B.. Hendrickx, J.M., Das, B.S., and S.H. Hong. 2000. Enhancing dielectric contrast between land mines and the soil environment by watering: modeling, design, and experimental results. *In AeroSense 2000 (pp*. 993-1000). International Soc. Optics and Photonics.

Bruschini, C. and B. Gros. 1998. A survey of current sensor technology research for the Q7 detection of landmines, in sustainable humanitarian demining: trends, techniques and technologies, edited by the Humanitarian Demining Information Center, James Madison University (Co-Editors: D. Barlow, C. Bowness, A. Craib, G. Gately, J.D. Nicoud, J. Trevelyan), Mid Vally Press, Verona, VA. 172-187.

Carter, L.L., M.J. O'Sullivan, Y.J. Hung, and J.C-C. Teng. 1998. Thermal imaging for landmine detection. Detection of abandoned land mines. IEE Conference Publication Number 458:110-114.

Cooke, R.U., A. Warren, and A.S. Goudie. 1993. Desert geomorphology. CRC Press. Frome, England.

Das. Y., Dean, J.T., Lewis, D., Roosenboom, J.H.J., and G. Zahaczewsky (Eds). 2001. "Final report of the international pilot project for technology co-operation (IPPTC) for a multi-national technical evaluation of performance of commercial off the shelf metal detectors in the context of humanitarian demining," Tech. Rep. EUR 19719 EN. Published, on behalf of the participants, by the European Commission, Joint Research Centre, Ispra, Italy.

Deans, J., G. Schmithals, and L.J. Carter. 2001. An analysis of the thermal imaging method for landmine detection using microwave heating. J. Appl. Geophys. 47(2):123-133.

de Vries, D.A. 1963. Thermal properties of soils. p.210-235. *In* W.R. van Wijk (ed.) Physics of plant environment. North-Holland Publishing Co., Amsterdam.

Di Martino, R.M., M. Camarda, S. Gurrieri, and M. Valenza. 2016. Asynchronous changes of CO2, H2 and He concentrations in soil gasses: A theoretical model and experimental results. J. Geophys. Res. Solid Earth.

Dregne, H.E. 1976. Soils of arid regions. Elsevier, New York, p. 250.

Edwards, T.L., C. Cox, B. Weetjens, T. Tewelde, and A. Poling. 2015. Giant African pouched rates (Cricetomys gambianus) that work on tilled soil accurately detect land mines. J. Applied Behavior Analysis. doi:10.1002/jaba.214

English, T.L. 2000. The quiet Americans: a history of military working dogs. Office of History. 37th Training Wing, Lackland AFB, Texas.

Estes, E.J.III, T. Hartshorn, and J. Vallotton. 2011. Landmine materials and environmental soils literature review. Scoping study on the effects of aging on landmines phase 2 presented to the United States Department of State Office of Weapons Removal and Abatement, March 7, 2011.

Fairley, J.R., S.E. Robert, E.S. Berney IV, R.M. Castellane III., L.L. Miller, R.D. Ellison, C.A. Barela, and C.T. Bradley. 2014. Millimeter-wave command wire (CW) phenomenology study. Geotechnical and Structures Laboratory. TR-14-22.

Garcia-Padron, R., D. Loyd, and S. Sjökvist. 2002. Heat and moisture transfer in wet sand exposed to solar radiation – models and experiments concerning buried objects. Subsurface Sensing Technolo. and Applications. 3(2):125-150.

Hendrickx, J.M.H, B.S. Das, and B. Borchers. 1999. Modeling distributions of water and dielectric constants around land mines in homogeneous soils. In *AeroSense'99* (pp. 728-738). International Soc. Optics and Photonics.

Hendrickx, J.M.H., B. Borchers, J. Woolslayer, L.W. Dekker, C. Ritsema, and S. Paton. 2001. Spatial variability of dielectric properties in field soils. In *Aerospace/Defense Sensing, Simulation and Controls* (pp. 398-408). Int. Soc. Optics Photonics.

Howington, S.E., R.C. Berger, E.W. Jenkins, J.P. Hallberg, K.R. Kavanagh, and J.H. Schmidt. 2003. Draft user's manual for groundwater/surface water interaction using ADH. Part of the CHSSI project on High Fidelity Simulation of Littoral Environments.

Howington, S.E., J.F. Peters, J.R. Ballard, T. Berry, L. Lynch, and C. Kees. 2006. A suite of models for producing synthetic, small-scale thermal imagery of vegetated soil surfaces. In *XVI International Conference on Computational Methods in Water Resources*.

International Committee of the Red Cross. Explosive remnants of war. Geneva: ICRC Publications, 2011.

Kasban, H., O. Zahran, S.M. Elaraby, M. El-Kordy, and F.E. Abd El-Samie. 2010. A comparative study of landmine detection techniques. Sens Imaging. 11:89-112. doi:10.1007/s11220-010-0054-x

Khanafer, K., and K. Vafai. 2002. Thermal analysis of buried land mines over a diurnal cycle. IEEE Transactions on Geoscience and Remote Sensing. 40(2):461-473.

Koh, G., and J.R. Ballard. 2004. Disturbed soil signatures for mine detection. Engineer Research and Development Center Hanover NH Cold Regions Research and Engineering Lab.

Krueger, K.R., McClellan, J.H., and W.R. Scott, Jr. 2015. Efficient algorithm design for GPR imaging of landmines. IEEE Transactions on Geoscience and Remote Sensing. 53(7):4010-4021. doi:10.1109/TGRS.2015.2388786

Kürsat, I. and B.A.B. Baertlein. 2000. Numerical simulation of thermal signatures of buried mines over a diurnal cycle. Detection and Remediation Technologies for Mines and Minelike Targets, V. *Proc. SPIE*. 4038.

Larson, M.A., J.C. Refsgaard, K.H. Jensen, M.B. Butts, S. Stisen, and M. Mollerup. 2016. Calibration of a distributed hydrology and land surface model using energy flux measurements. Ag. Forest Meteorol. 217:74-88.

Liang, X., D.P. Lettenmaier, E.F. Wood, and S.J. Burges. 1994. A simply hydrologically based model of land surface water and energy fluxes for general circulation models. J. Geophys. Res.: Atmospheres 99(D7). 14415-14428.

Lu, N., and Y. Dong. 2015. Closed-form equation for thermal conductivity of unsaturated soils at room temperature. J. Geotech. Geoenviron. Eng., doi:10.1061/(ASCE)GT.1943-5606.0001295, 04015016.

MacDonald, J., J.R. Lockwood, J. McFee, T. Altshuler, T. Broach, L. Carin, R. Harmon, C. Rappaport, W. Scott, and R. Weaver. 2003. Alternatives for landmine detection. RAND Science and Technology Policy Institute.

Maksymonko, G.B., B.S. Ware, and D.E. Poole. 1995. Characterization of diurnal and environmental effects on mines and the factors influencing the performance of mine detection ATR algorithms. *Proc. SPIE.* 2496:140-151. doi:10.1117/12.211310

Miles, D. 1998. Confronting the land mine threat. American Forces Press Service.

Miller, T.W., J.M.H. Hendrickx, and B.Borchers. 2004. Radar detection of buried landmines in field soils. Vadose Zone J. 3:1116-1127.

Moukalled, F., and Y. Saleh. 2006. Heat and mass transfer in moist soil, Part I. Formulation and testing. Numerical Heat Transfer, Part B, 49:467-486. doi:10.1080/10407790500510866

Moukalled F., N. Ghaddar, Y. Saleh and Z. Fawaz. 2006. Heat and mass transfer in moist soil, Part II. Application to predicting thermal signatures of buried landmines, numerical heat transfer, Part B: Fundamentals: An international journal of computation and methodology. 49(5):487-512. doi:10.1080/10407790500510965

Ochsner, T.E., R. Horton, and T. Ren. 2001. A new perspective on soil thermal properties. Soil Sci. Soc. Am. J. 65:1641-1647.

Phelan, J.M., and S.W. Webb. 1997. Environmental fate and transport of chemical signatures from buried landmines: screening model formulation and initial simulations, Sandia National Laboratories Report SAND97-1426, Albuquerque, NM.

Pregowski P., W. Swiderski, R.T. Walczak, and K. Lamorski. 2000. "Buried mine and soil temperature prediction by numerical model," in *Detection and Remediation Technologies for Mines and Minelike Targets V*, A.B. Dubey, J.F. Harvey, J.T. Broach, R.E. Dugan, eds., *Proceedings of SPIE.* 4038:1392-1403.

Raich, J.W., and W.H. Schlesinger. 1992. The global carbon dioxide flux in soil respiration and its relationship to vegetation and climate. Tellus B. 44(2):81-99.

Ratto, C.R., P.A. Torrione, and L.M. Collins. 2011. Exploiting ground-penetrating radar phenomenology in a context-dependent framework for landmine detection and discrimination. IEEE Transactions on Geoscience and Remote Sensing. 49(5):1689-1700. doi:10.1109/TGRS.2010.2084093.

Richards, L.A. 1931. Capillary conduction of liquids through porous medium. J. Physics. 1:318-333.

Sai, B., I. Morrow, P. van Genderen. 1998. Limits of detection of buried landmines based on local echo contrasts. Proceedings of 28th European Microwave Conf. Amsterdam, Netherlands.

Sakaki, T., A. Limsuwat, K.M. Smits, and T.H. Illangasekare. 2008. Empirical two-point α-mixing model for calibrating the ECH2O EC-5 soil moisture sensor in sands. Water Resour. Res. 44(4):W00D08. doi:10.1029/2008WR006870

Sakaki, T., and K.M. Smits. 2015. Water retention characteristics and pore structure of binary mixtures. Vadose Zone J. 14(2). doi:10.2136/vzj2014.06.0065

Şendur, İ.K., and B.A. Baerltein. 2000. "Numerical simulation of thermal signatures of buried mines over a diurnal cycle," in *Detection and Remediation Technologies for Mines and Minelike Targets V*, A.C. Dubey, J.F. Harvey, J.T. Broach, R.E. Dugen, eds., *Proceedings of SPIE.* 4038:156-167.

Shire, A., U. Jawarkar, and S. Chavhan. 2015. Overview of buried mines detection using radar bullet. Int. J. Eng. Sci. and Resear. Technol. 4(2):250-254.

Simunek, J., J.M.H. Hendrickx, and B. Borchers. 2001. "Modeling transient temperature distributions around landmines in homogeneous bare soils," in *Detection and Remediation Technologies for Mines and Minelike Targets VI*, A.C. Dubey, J.F. Harvey, J.T. Broach, V. George, eds., *Proceedings of SPIE*. 4394:387-397.

Smits, K.M., A. Cihan, T. Sakaki, and T.H. Illangasekare. 2011. Evaporation from soils under thermal boundary conditions: Experimental and modeling investigation to compare equilibrium and non-equilibrium based approaches. Water Resour. Res. 47(5). W05540.

Smits, K.M., A. Cihan, T. Sakaki, S.E. Howington, J.F. Peters, and T.H. Illangasekare. 2012. Soil moisture and thermal behavior in the vicinity of buried objects affecting remote sensing detection: experimental and modeling investigation. IEEE Transactions on Geoscience and Remote Sensing. doi:10.1109/TGRS.2012.2214485

van Genuchten, M.T. 1980. A closed-form equation for predicting the hydraulic conductivity of unsaturated soils. Soil Sci. Soc. Am. J. 44(5):892-897.

Wallen, B.M., K.M. Smits, T. Sakaki., S.E. Howington, and C. Deepagoda. T.K.K. 2016. Thermal conductivity of binary sand mixtures evaluated through full water content range. Soil Sci. Soc. Am. J. 80. doi:10.2136/sssaj2015.11.0408

Walsh, N.E. and W.S. Walsh. 2003. Rehabilitation of landmine victims – the ultimate challenge. Bulletin of the World Health Org. 81(9):665-670.

Wang, Y., Q. Song, T. Jin, Y. Shi, and X. Huang. 2013. Sparse time-frequency representation based feature extraction method for landmine discrimination. Progress in Electromagnetics Research. 133:459-475.

Yip, M., M.I. Saripan, K. Wells, and D.A. Bradley. 2015. Monte Carlo simulations for the detection of buried objects using single sided backscattered radiation. PLoS ONE. 10(9):e0135769. doi:10.1371/journal.pone.0135769

CHAPTER 7 CONCLUSIONS

Landmines are one of the most prolific, human-made environmental hazards impacting the world. Although there are numerous technologies used to detect buried landmines, none enable a perfect find rate, in part, due to the heterogeneous nature of the environment in which they are buried. Variations in environmental conditions such as soil moisture and climate (e.g. temperature, diurnal fluctuations) impact detection performance. Improved understanding of the environmental conditions associated with minefield emplacement is needed to improve the existing algorithms associated with different detection technologies, thus increasing their performance and probability of detection rates. The ability to collect and analyze soil characteristics for every location where landmines are found is not tenable. Therefore numerical models are oftentimes used to simulate landmine scenarios. These models require an understanding of both the soil environment and climate conditions. However, there is a lack of understanding of the effect of the mine placement on the heat and mass transfer dynamics in the vicinity of the mine. More specifically, very little is known about how the disturbance of the soil itself, due to the placement and burial of the mine effects the soil moisture and temperature conditions in the vicinity of the mine. Soil disturbance is defined as the process in which the soil is removed prior to mine burial and replacement of this now loosely packed and potentially mixed soil around and above the mine itself. The process of disturbing the soil changes its thermal and hydraulic properties and hence the thermal and moisture behavior in the vicinity of the mine, compared to the surrounding, undisturbed soil. In addition to landmine detection, this work is applicable to heat transfer within soil that influences micrometeorological phenomena (Hanks et al., 1967), engineering efforts such as cooling electronic devices with heat pipes and insulating buildings (Bussing and Bart, 1997; Sakaguchi et

al., 2009; Moradi et al., 2015), and agricultural production (Al Nakshabandi and Kohnke, 1964; Usowicz et al., 1996; Lipiec et al., 2007).

The purpose of this research was to better understand the effect of soil disturbance and mixing on heat and mass transfer behavior in the vicinity of buried landmines. This research integrated field and laboratory experimentation with analytical modeling to address four primary tasks: (1) characterization of thermal conductivity of binary sand mixtures, (2) comparison of methods used to calculate evaporation, (3) impact of soil disturbance and mixing on heat and mass transfer behavior in soil at the land-atmosphere interface, and (4) field investigation of the effect of soil disturbance on heat and moisture transfer behavior around buried objects.

7.1 Lessons Learned

A variety of areas regarding landmine research could have been the focus of this dissertation. The selection to study the environmental subcomponents that are affected due to landmine emplacement provided a unique means to enhance our understanding of the impact of burring landmines regarding heat and mass transfer in the shallow subsurface. A summary of key findings and results are included in the subsequent sections for the four primary chapters of this dissertation (i.e., Chapters 3-6) which have been or will be published in peer reviewed journals.

A variety of best practices were adopted regarding the multitude of sensors and systems/equipment used in the ~66 experiments conducted as part of this dissertation. These best practices were codified into user guides that are listed in Appendix A. The final dual tank set up discussed in Chapter 5 with the addition of the individual pressure transducers emplaced in the top two rows of both tanks provides a benchmark for future experimental endeavors. The ability to compare two experimental configurations simultaneously enables more accurate evaluations of altered packed conditions between the tanks. The simultaneous measurement of water content,

thermal properties, and capillary pressure enables generation of soil water retention curves and thermal conductivity-saturation relationships specific to the exact conditions of the current experiment. Therefore, modeling parameters (e.g., van Genuchten, 1980) are able to be determined for the specific conditions from which the experiments are conducted.

Although as stated in the introduction (Chapter 1), it is important to be clear that the conclusions of this research are based on the comparison of experimental results derived from the analysis of manufactured quartz (>98%) sands. Therefore, conclusions may not apply to all soil types or conditions.

7.1.1 Chapter 3 Key Findings

Efforts to continually guide data collection from experiments that more closely replicate natural field conditions required evaluation of mixtures of top soil and subsurface soil. Soil horizons typically include a layer of coarse top soil over a finer subsurface environment. Therefore, the landmine burial process of digging a hole to emplace the landmine causes the creation of a mixture of the coarse and fine soil, considered as a binary mixture. The depth of the interface between the coarse and fine soil results in a variety of different mixing fractions between the two soils. Characterization of the various resulting binary mixtures was essential to understand the environmental response expected within the disturbed mixed soil surrounding the buried landmine. This work provided critical knowledge of the unique thermal behavior of disturbed and mixed soils. Prior to this effort, no research existed that reviewed the impact of binary sand mixtures on the relationship between thermal conductivity (λ) and the degree of saturation (S). The hypothesis associated with the research included in this chapter was that the thermal properties of binary soil mixtures are distinct from that of the parent materials comprising the mixtures and cannot be described by current thermal conductivity-water content (λ-θ) models. Both portions of this

hypothesis were affirmed and the significant results and conclusions associated with this task follow.

- λ-θ relationships for the binary mixtures are distinct from that of the parent materials comprising the mixtures, varying significantly depending on the volume fraction of the fine particles.
- $\lambda-\theta$ is highly dependent on porosity (ϕ) and that systematic changes in the volume fraction of fine particles also systematically changes λ.
- Change in density (ρ) due to the fine fraction or percentage of fines associated with each mixture was shown to affect λ more significantly under saturated conditions with the effect diminishing in the hydration regime.
- Strong correlation exists between density and both dry (λ_{dry}) and saturated (λ_{sat}) thermal conductivity values for the sands tested.
- The Campbell et al. (1994) model did not enable the incorporation of experimentally measured soil properties for the model parameters, but rather worked best when the parameters were fitted to experimental data.
- The Lu and Dong (2015) model worked best when the physically based soil specific parameters were used as best fit parameters
- No current $\lambda-\theta$ models can effectively model thermal conductivity based entirely upon measured characteristics of the binary mixture.

7.1.2 Chapter 4 Key Findings

The second task compared several approaches used to determine evaporation. Further refinement of model development required selection of the most appropriate analytical method for

determination of evaporation. As evaporation from bare soils is one of the governing processes controlling the mass and energy exchanges between the land and atmosphere, several analytical methods for determining evaporation were considered. A series of laboratory experiments via medium sand tanks interfaced with a wind tunnel using homogeneous soil were used to compare actual evaporation based on lysimeter data compared to predicted evaporation for a number of analytical methods. Although there have been many studies comparing the performance of different evaporation models, a comparison for the purpose of selection based upon input approach (i.e., surface and free flow, porous and free flow mediums, or strictly porous medium) was not identified. Selection of the desired method enabled further refinement regarding required sensors to use for future elements of this research through identification of required model inputs. The purpose of this work was to determine a method that can be easily applied to field scale studies of landmine detection, specifically, finding a method that can be applied to disturbed soil conditions. The hypothesis corresponding to this research line of effort was that using remotely sensed soil moisture and temperature data from multiple platforms coupled with in-situ data, will allow us to determine an optimal approach to accurately determine evaporation from soils. Although no one approach was determined optimal for all experimental conditions studied, significant results and conclusions were obtained as follows.

- Identification of the transition between Stage I and Stage II evaporation is possible through consideration of the following: changes in soil moisture at the point of inflection in the rate of decreasing saturation, temperature difference between air and the ground surface at the point where the difference becomes relatively constant and changes in the rate of drying front propagation and depth of drying front propagation compared to air entry pressure head.

- The sensible heat balance and heat pulse (SHB+HP) model (Heitman et al., 2008; Trautz et al., 2014; Xiao et al., 2014) consistently performed better than the other models when isolating measured *E*. In addition, this method allowed for the isolation of transpiration in the vegetated test cases.
- The temperature difference (TD) model (Ben-Asher et al., 1983) performs adequately to estimate evaporation under all boundary conditions except for continuously elevated air temperature when model inputs are taken as influent air temperature and surface temperature.
- Investigation of the sampling frequency on evaporation rate agreement between measured and modeled relationships demonstrates that a 3-hour sampling frequency is most appropriate for the boundary conditions and test soils studied.

7.1.3 Chapter 5 Key Findings

The third task investigated the impact of soil disturbance and mixing on heat and mass transfer behavior at the laboratory scale. This research included laboratory experiments replicating conditions more closely associated with minefield emplacement. Therefore, a medium sand tank was packed with a disturbed center section to represent the conditions associated with a buried mine. Experiments were conducted that further investigated the impact of soil heterogeneity on mass and heat transfer. An analytical model was employed to enable identification of the relative contribution of each region (e.g., tight and loose packing) toward the total evaporation occurring based upon the variety of boundary conditions investigated. Experimental studies then focused on a layered disturbed soil in which the disturbed soil is a binary mixture of the coarse and fine layered soil. The added complexity associated with this analysis more appropriately simulated natural conditions found in arid climates in which landmines are be buried. This work was critical to

understand how the disturbance effects the soil moisture distributions within the soil profile as well as the temperature and moisture conditions at the soil surface, under varying climate conditions. The findings apply to arid environmental in which the soil profile is comprised of poorly graded, well sorted sands with high quartz contents (>98%). The most significant contribution of this research was the acquisition of robust data sets with high spatial and temporal resolution for the use of comparison with future numerical modeling efforts as a means to enable model validation for the multitude of initial and boundary condition investigated. The hypothesis corresponding to this research was that soil moisture and temperature distributions are significantly altered by soil disturbance/mixing, especially in the shallow subsurface where transient boundary conditions at the land/atmospheric interface (e.g. temperature, wind speed, pressure, humidity and evapotranspiration) play a role. Significant results and conclusions associated with this task follow.

- The ability to conduct simultaneous bench scale tests using multiple tanks within the same laboratory framework (i.e., same wind tunnel) enables direct comparison between changing soil (e.g., disturbance) conditions.
- Surface temperature increases consistently coincide with the transition from Stage I to Stage II, regardless of boundary and initial conditions.
- Tightly packed soil regions have higher evaporation rates and longer Stage I evaporation than loosely packed soil regions. In addition, the relative humidity and degree of saturation are greater in the tightly packed soil regions. Stage I evaporation was sustained longer in the tightly packed soil regions than in the loosely packed soil region, in part, due to capillary pumping which is in agreement with the conceptual model developed by Lehmann and Or (2009).

- Soil mixing and disturbance create complex evaporation conditions that can be predicted based on knowledge of the soil hydraulic properties, specifically, the soil water retention behavior of the mixed soils.

7.1.4 Chapter 6 Key Findings

Finally, the fifth task was a field scale proof of concept demonstration. The field experiment simultaneously investigated the relationship between landmines buried at different depths (e.g., shallow and deep) and object (e.g. surrogate landmine, limestone block, disturbed hole) properties. The impact of soil conditions (e.g., porosity, saturation) and atmospheric conditions (e.g., velocity, temperature, relative humidity) were measured for all four emplacement locations. To the author's knowledge, a field study applied to landmine detection previously did not exist that integrated the impact of soil burial depth, object properties, and soil disturbance on subsurface soil moisture and temperature distributions. The significance of this research is embodied in the collection of a robust data set with high spatial and temporal resolution for the use of comparison with future numerical modeling efforts as a means to enable model validation. The application of the experimental results apply to a poorly graded sand similar to that found in arid environments. Findings associated with this task follow.

- Precipitation can impact the visual signature and thermal contrast of object locations: thermal contrasts for shallow and deep mines are accentuated both during the day and night, and thermal contrasts for the soil disturbance location and limestone block are attenuated.
- An increase in object burial depth decreases the temperature contrast at the soil surface, compared to a shallow buried object.

- The impact of rain events on soil thermal and hydraulic properties can be significant and should be incorporated into future research efforts (e.g. modeling) of mine detection scenarios.

7.2 Recommendations for Future Research

This research provides new experimental and analytical model insights into soil moisture and temperature behavior in mixed and disturbed soils in the shallow subsurface, as influenced by changes in surface and atmospheric conditions. This work provides a step towards refining our understanding of heat and mass transfer through unsaturated soils in order to better predict temperature and moisture conditions in the vicinity of buried objects. Recommendations for future research follow.

Although thermal conductivity models were able to capture the thermal conductivity-saturation (λ-S) behavior for binary sand mixtures when properly fitted with experimental data, model improvements are needed to capture the relationship based entirely on physically based soil parameters. Future work studying the effect of binary mixtures from a variety of soils with more grain sizes and at different temperatures is required to enhance our understanding. This research is important as the λ-S relationship serves as an important input to many numerical modeling efforts.

Another significant relationship required for modeling efforts is the ability to effectively predict evaporative fluxes. No one model was identified for the accurate prediction of evaporation under the variety of initial and boundary conditions investigated. Therefore, continued research is required to work toward a more universally accepted evaporation model. Based on the current work, the author proposes that using remotely sensed soil moisture and temperature data from

multiple platforms coupled with data obtained in-situ will allow us to determine an optimal approach to accurately determine evaporation from soils.

The impact of changing soil properties near the land-atmosphere interface due to landmine emplacement activities is significant. However, there are few laboratory disturbed soil studies and none identified that study under layered soil conditions. With the variety of soil environments to understand, more studies are needed to investigate both disturbed and mixed soil environments with the ultimate goal to provide a comprehensive suite of data collected for model verification that ultimately leads to algorithm improvement for mine detection technology platforms. In addition, how to properly apply the knowledge gained at the laboratory scale to the field scale also requires additional research.

Based upon a review of landmine research, further work is recommended to analyze the heat and moisture transfer in different soils with objects buried at different depths under a variety of environmental and surface conditions.

7.3 References

Al Nakshabandi, G., and H. Kohnke. 1965. Thermal conductivity and diffusivity of soils as related to moisture tension and other physical properties. Agric. Meteorol. 2(4):271-279. doi:10.1016/0002-1571(65)90013-0

Ben-Asher, J., A.D. Matthias, and A.W. Warrick. 1983. Assessment of evaporation from bare soil by infrared thermometry. Soil Sci. Soc. Am. J. 47:185-191.

Bussing, W., and H.J. Bart. 1997. Thermal conductivity of unsaturated packed beds – comparison of experimental results and estimation methods. Chem. Eng. Process. 36(2):119-132. doi:10.1016/S0255-2701(96)04176-1

Campbell, G. S., J. D. Jungbauer, W. R. Bidlake, and R. D. Hungerford. 1994. Predicting the effect of temperature on soil thermal-conductivity. Soil Sci. 158:307–313.

Hanks, R.J., H.R. Gardner, and M.L. Fairbourn. 1967. Evaporation of water from soils as influenced by drying with wind or radiation. Soil Sci. Soc. Am. Proc. 31(5):593-598. doi:10.2136/sssaj1967.03615995003100050001x

Heitman, J.L., R. Horton, T.J. Sauer, and T.M. DeSutter. 2008. Sensible heat observations reveal soil-water evaporation dynamics. J. Hydrometeorol. 2:165-171. doi:10.1175/2007JHM963.1

Lehmann, P. and D. Or. 2009. Preferential evaporation and capillary coupling in porous media with textural contrasts, Phys. Rev. E. 80. 046318.

Lipiec, J., B. Usowicz, and A. Ferrero. 2007. Impact of soil compaction and wetness on thermal properties of sloping vineyard soil. Int. J. Heat Mass Trans. 50(19-20):3837-3847. doi:10.1016/j.ijheatmasstransfer.2007.02.008

Lu, N., and Y. Dong. 2015. Closed-form equation for thermal conductivity of unsaturated soils at room temperature. J. Geotech. Geoenviron. Eng., doi:10.1061/(ASCE)GT.1943-5606.0001295, 04015016

Moradi, A., K.M. Smits, J. Massey, A. Cihan, and J. McCartney. 2015. Impact of coupled heat transfer and water flow on soil borehole thermal energy storage (SBTES) systems: experimental and modeling investigation. Geothermics. doi:10.1016/j.geothermics.2015.05.007

Sakaguchi, I., T. Momose, H. Mochizuki, and T. Kasubuchi. 2009. Heat pipe phenomenon in soil under reduced air pressure. Eur. J. Soil Sci. 60(1):110-115. doi:10.1111/j.1365-2389.2008.01095.x

Trautz, A.C., K.M. Smits, P. Schulte, and T.H. Illangasekare. 2014. Sensible heat balance and heat-pulse method applicability to in situ soil-water evaporation, *Vadose Zone J.*, 13(1), doi:10.2136/vzj2012.0215

van Genuchten, M. T. 1980. A closed-form equation for predicting the hydraulic conductivity of unsaturated soils, Soil Sci. Soc. Am. J., 44:892–898.

Xiao, X., J.L. Heitman, T.J. Sauer, T. Ren, and R. Horton. 2014. Sensible heat balance measurements of soil water evaporation beneath a maize canopy. Soil Sci. Soc. Am. J. 78(2):361-368. doi:10.2136/sssaj2013.08.0371

APPENDIX A SENSOR USER GUIDES

Appendix A provides the complete list of sensor user guides developed for systems and sensors used throughout this research. User guides are available upon request at benwallen@earthlink.net.

1. Canon Digital Camera
2. Davis Cup Anemometer
3. Degas Pump
4. ECH$_2$O EC-5 Soil Moisture Sensor
5. ECT Temperature Sensor
6. EHT Relative Humidity and Temperature Sensor
7. Em50 Data Logger
8. Individual Pressure Transducer Systems
9. IR Camera
10. KD2-Pro Thermal Properties Analyzer
11. Laster Temperature Gun Thermometer
12. Pressure Transducer System
13. Sartorius Scale
14. VP-3 Relative Humidity and Temperature Sensor

APPENDIX B PROCEDURES TO DETERMINE EFFECTIVE RADIUS OF HEAT PULSE PROBES

Appendix B contains the laboratory procedures established and followed to determine the effective radius of two different variations of heat-pulse probes.

B.1 Theory

Heat-pulse probes are a relatively new technology that provide an opportunity to estimate soil-water evaporation through measuring changes in soil temperature in response to small measured heat input (Trautz et al., 2014). The heat-pulse probes used in this experiment contain a tri-needle configuration as shown in Figure B.1 as presented by Trautz et al. (2014).

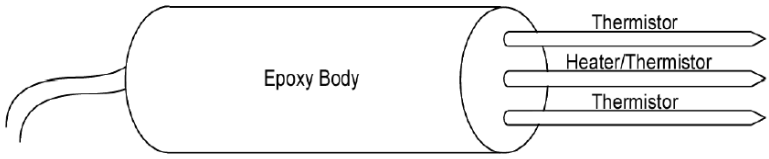

Figure B.1. "Heat-pulse probe design modeled after Heitman et al. (2008). The probe consists of three needles arranged in parallel that project from an epoxy body. Each needle contains a thermister for measuring temperature; the center needle also has a heating element." (Trautz et al., 2014)

The heat generated from the center needle over an 8 second period (the duration of the heat pulse, t_o (s)) at 750 J m^{-1} provides a temperature gradient measured by the top and bottom needle resulting in recording t_{max} (s), the time required to reach the maximum temperature change ΔT_{max} (^oC). These values are used to determine thermal diffusivity, κ (m^2 s^{-1}), and volumetric heat capacity, C (J m^{-3} $^oC^{-1}$) as shown by Eqs. B.1 and B.2.

$$\kappa = \frac{r^2}{4t_{\max}}\left(\frac{t_o}{t_{\max}-t_o}\right)\left[\ln\left(\frac{t_{\max}}{t_{\max}-t_o}\right)\right]^{-1} \quad \text{(B.1)}$$

$$C \approx \frac{q' t_o}{e\pi r^2 \Delta T_{\max}}\left(1-\frac{\varepsilon^2}{8}\left[\frac{1}{3}+\varepsilon\left\{\frac{1}{3}+\frac{\varepsilon}{8}\left(\frac{5}{2}+\frac{7\varepsilon}{3}\right)\right\}\right]\right) \quad \text{(B.2)}$$

where q' (W m^{-1}) is the energy per unit length of heater in the probe (measured value during experiment), e in the natural logarithm base (e = 2.71828) and $\varepsilon = t_o/t_{max}$. Both equations require a value for the radial distance from the line source, r (m). In previous work by Trautz et al. (2014), an r value was assumed as 0.003 m. Both κ and C are affected by small changes in r.

In order to determine the effective radius of the two different variations (3 mm and 6 mm between needles) of heat-pulse probes, two different KD-2 Pro property analyzers (one dual-needle sensor and one single-needle sensor) (Decagon Devices, Inc.) will be used to measure κ and C values. The use of the various probes and sensors will provide all variables required in both equations (1) and (2) except for r which will be calculated through manipulating both equations and solving for r as shown in Eqs. B.3 and B.4.

$$r = \sqrt{\kappa\left[\ln\left(\frac{t_{\max}}{t_{\max}-t_o}\right)\right]\left(\frac{t_{\max}-t_o}{t_o}\right)4t_{\max}} \quad \text{(B.3)}$$

$$r = \sqrt{\frac{q' t_o}{Ce\pi\Delta T_{\max}}\left(1-\frac{\varepsilon^2}{8}\left[\frac{1}{3}+\varepsilon\left\{\frac{1}{3}+\frac{\varepsilon}{8}\left(\frac{5}{2}+\frac{7\varepsilon}{3}\right)\right\}\right]\right)} \quad \text{(B.4)}$$

The value of r calculated under similar conditions from both equations should yield the same number. If this occurs, then the equations and the two KD-2 Pro sensors are validated as well as confirming the effective radius of the heat-pulse probes.

B.2 Procedure

Six heat-pulse probes will be used with four probes having needle spacing of 3 mm and two probes with spacing of 6 mm between probes. A six-quart Stertilite™ container serves to provide the experimental volume through filling #30/40 sand (bulk specific gravity, SG, 2.65 g cm^{-3}) to 8.5 cm from the bottom of the container. In order to compare to k and C measurements to experimentally determined values by Smits et al. (2010) to further validate effective radius calculations, the #30/40 sand will be compacted to a similar porosity, ϕ, of 0.334 cm cm^{-3}. A graduated cylinder will be used to measure the total volume, V_T (cm^3), of water required to fill the Sterilite™ container to 8.5 cm from the bottom. Sand will be added to the container under dry and fully saturated conditions with measurements taken every 30-minutes (to allow ample time for the temperature of the surrounding soil to recover to ambient temperature between heating events) for two and a half hours to confirm similarity in measured values required for input in Eqs. B.1 and B.2. All probes and sensors will be placed in the same manner (vertical) at the same depth (surface plus 2 cm to stabilize the epoxy body housing the needles). From this effort, the effective radius of the heat-pulse probes will be confirmed.

B.2.1. Heat-Pulse Probe (3 mm needle spacing) Dry Experiment (Probe C2036, C2037, C2038, C2039)

Step 1. Using a graduated cylinder, measure the amount of water required to fill a Sterilite™ container to 8.5 cm from the bottom. Mark the water line on the outside of the container with a permanent marker as this provides the line to fill the container with sand for further experiments.

Step 2. Empty the water from the container and dry thoroughly, and calculate the mass, *m* (g), of #30/40 sand (specific gravity, SG, of 2.65 g cm^{-3}) to add to the penned line on the container

in order to achieve a porosity, ϕ, of 0.334. Manipulation of the fundamental porosity Eq. B.5 below yields Eq. B.6 used to determine the mass of sand to add.

$$\phi = \frac{V_T - \frac{m}{SG}}{V_T} \tag{B.5}$$

$$m = (V_T - \phi V_T)SG \tag{B.6}$$

Step 3. Weight a clean, empty stainless steel pan, tare the weight, then add the calculated mass of sand required to achieve the desired porosity.

Step 4. Weigh the empty Sterilite™ container prior to adding sand. Add the calculated mass of #30/40 sand from the stainless steel pan to the container in lifts of 1 cm, compacting each lift via pushing down on the surface with a common pointing trowel with a lift handle. Upon reaching a depth of 4 cm, use the blade of the trowel to push vertically down through the different layers of sand to minimize stratification between lifts and use a rubber mallet to hit the sides to further enable proper compaction to achieve the desired porosity. Once all the sand is added from the stainless steel pan, the sand should be leveled and at the height of the marked pen line. Compact more as necessary to ensure level and at (not above) the marked pen line from step 1. Weigh the Sterilite™ container with sand added to obtain the desired porosity.

Step 5. Write a programming code to enable the datalogger to execute the desired experiment. Connect the probes to a CR1000 datalogger (Campbell Scientific) to control a direct-current power supply to the heat-pulse probes to generate 8 second 750 J m^{-1} heat pulses. Connect the KD-2 Pro sensors to their respective control/power module.

Step 6. Push the four heat-pulse probes into the sand vertically until the epoxy body is about 1 cm below the surface. Place each probe in one of the four corners of the container being sure to keep each at least 5 cm from the sides and other probes and sensors. Push one two-prong

KD-2 Pro sensor into the sand vertically until the epoxy body is about 1 cm below the surface, placing the sensor about 5 cm to the left of center lengthwise and centered widthwise. Push one one-prong KD-2 Pro sensor into the sand vertically until the epoxy body is about 1 cm below the surface, placing the sensor about 5 cm to the right of center lengthwise and centered widthwise. This will disrupt the compacted soil; therefore, take care to minimize the disturbance and then compact the sand once all probes and sensors are in place and stabilized. If needed, use tape across the top to ensure the probes and sensors remain vertical during the experimental runs.

Step 7. Begin the experiment and run for 2 ½ hours in order to obtain five measurements from each heat-pulse probe. Once complete, collect all date from the heat-pulse probes and KD-2 sensors.

Step 8. Upon completion of obtaining all experimental data, remove and wash probes and sensors with deionized water.

B.2.2. Heat-Pulse Probe (6 mm needle spacing) Dry Experiment (Probe C2040, 2041)

Step 9. Weight the Sterilite™ container to determine how much sand was lost due to removal of the probes and sensors. Be sure to remove tape if any was used to stabilize the probes and sensors as noted at the end of step 6 above.

Step 10. Add the required amount of sand (original weight with sand minus weight measured in step 9) to bring the weight of the container with sand back to the original weight to obtain the same porosity. Smooth and compact as necessary to level the sand at the marked pen line.

Step 11. Write a programming code to enable the datalogger to execute the desired experiment. Connect the two probes to a CR1000 datalogger (Campbell Scientific) to control a

direct-current power supply to the heat-pulse probes to generate 8 second 750 J m^{-1} heat pulses. Connect the KD-2 Pro sensors to their respective control/power module.

Step 12. Push the two heat-pulse probes into the sand vertically until the epoxy body is about 1 cm below the surface. Place each probe 5 cm from the sides (left and right respectively), centered widthwise and 5 cm away from the sensors. Push one two-prong KD-2 Pro sensor into the sand vertically until the epoxy body is about 1 cm below the surface, placing the sensor about 5 cm to the left of center lengthwise and centered widthwise. Push one one-prong KD-2 Pro sensor into the sand vertically until the epoxy body is about 1 cm below the surface, placing the sensor about 5 cm to the right of center lengthwise and centered widthwise. This will disrupt the compacted soil; therefore, take care to minimize the disturbance and then compact the sand once all probes and sensors are in place and stabilized. If needed, use tape across the top to ensure the probes and sensors remain vertical during the experimental runs.

Step 13. Begin the experiment and run for 2 ½ hours in order to obtain five measurements from each heat-pulse probe. Once complete, collect all date from the heat-pulse probes and KD-2 sensors.

Step 14. Upon completion of obtaining all experimental data, remove and wash probes and sensors with deionized water. Remove the sand from the Sterilite™ container, wash and dry the container thoroughly in preparation for running the experiment under saturated conditions.

B.2.3. Heat-Pulse Probe (3 mm needle spacing) Saturated Experiment (Probe C2036, C2037, C2038, C2039)

Step 15. Weight a clean, empty stainless steel pan, tare the weight, then add the calculated mass of sand required to achieve the desired porosity of 0.334 cm^3 cm^{-3}.

Step 16. Wet pack the Sterilite™ container to the marked pen line using the #30/40 sand and deionized water. Add sand to the container in 1 cm depth increments maintaining approximately 5 cm of water above the sand surface to ensure saturation and a uniform bulk density throughout. Compact each sand layer via pushing down on the surface with a common pointing trowel with a lift handle. Upon reaching a depth of 4 cm, use the blade of the trowel to push vertically down through the different layers of sand to minimize stratification between lifts and use a rubber mallet to hit the sides to further enable proper compaction to achieve the desired porosity. Once all the sand is added from the stainless steel pan, the sand should be leveled and at the height of the marked pen line. Compact more as necessary to ensure level and at (not above) the marked pen line from step 1. Ensure the water line above the sand is 1.5 cm above the sand to maintain the sand in a fully saturated condition during the experiment. Mark the water line on the outside of the container with a permanent marker. Weigh the Sterilite™ container with sand added to obtain the desired porosity and water at 1.5 cm above the sand.

Step 17. Use the previously developed programming code to enable the datalogger to execute the desired experiment. Connect the probes to a CR1000 datalogger (Campbell Scientific) to control a direct-current power supply to the heat-pulse probes to generate 8 second 750 J m^{-1} heat pulses. Connect the KD-2 Pro sensors to their respective control/power module.

Step 18. Push the four heat-pulse probes into the sand vertically until the epoxy body is about 1 cm below the surface. Place each probe in one of the four corners of the container being sure to keep each at least 5 cm from the sides and other probes and sensors. Push one two-prong KD-2 Pro sensor into the sand vertically until the epoxy body is about 1 cm below the surface, placing the sensor about 5 cm to the left of center lengthwise and centered widthwise. Push one one-prong KD-2 Pro sensor into the sand vertically until the epoxy body is about 1 cm below the

surface, placing the sensor about 5 cm to the right of center lengthwise and centered widthwise. This will disrupt the compacted soil; therefore, take care to minimize the disturbance and then compact the sand once all probes and sensors are in place and stabilized. If needed, use tape across the top to ensure the probes and sensors remain vertical during the experimental runs.

Step 19. Begin the experiment and run for 2 ½ hours in order to obtain five measurements from each heat-pulse probe. Once complete, collect all date from the heat-pulse probes and KD-2 sensors.

Step 20. Upon completion of obtaining all experimental data, remove and wash probes and sensors with deionized water.

B.2.4. Heat-Pulse Probe (6 mm needle spacing) Saturated Experiment (Probe C2040, 2041)

Step 21. Weight the Sterilite™ container to determine how much sand was lost due to removal of the probes and sensors. Be sure to remove tape if any was used to stabilize the probes and sensors as noted at the end of step 18 above.

Step 22. Add the required amount of sand (original weight of sand with water minus weight measured in step 21) to bring the weight of the container with sand back to the original weight to obtain the same porosity. Smooth and compact as necessary to level the sand at the marked pen line and ensure that the water level is at the marked water line from step 16.

Step 23. Use the previously developed programming code to enable the datalogger to execute the desired experiment. Connect the two probes to a CR1000 datalogger (Campbell Scientific) to control a direct-current power supply to the heat-pulse probes to generate 8 second 750 J m^{-1} heat pulses. Connect the KD-2 Pro sensors to their respective control/power module.

Step 24. Push the two heat-pulse probes into the sand vertically until the epoxy body is about 1 cm below the surface. Place each probe 5 cm from the sides (left and right respectively),

centered widthwise and 5 cm away from the sensors. Push one two-prong KD-2 Pro sensor into the sand vertically until the epoxy body is about 1 cm below the surface, placing the sensor about 5 cm to the left of center lengthwise and centered widthwise. Push one one-prong KD-2 Pro sensor into the sand vertically until the epoxy body is about 1 cm below the surface, placing the sensor about 5 cm to the right of center lengthwise and centered widthwise. This will disrupt the compacted soil; therefore, take care to minimize the disturbance and then compact the sand once all probes and sensors are in place and stabilized. If needed, use tape across the top to ensure the probes and sensors remain vertical during the experimental runs.

Step 25. Begin the experiment and run for 2 ½ hours in order to obtain five measurements from each heat-pulse probe. Once complete, collect all date from the heat-pulse probes and KD-2 sensors.

Step 26. Upon completion of obtaining all experimental data, remove and wash probes and sensors with deionized water. Remove the sand from the Sterilite™ container, wash and dry the container.

B.3 Data Analysis

The focus of the data analysis is three-fold. First, compare all date from the heat-pulse probes. Determine the statistical significance between the five measurements for each probe and their agreement in measurements to each other for both dry and saturated conditions. Second, compare all date from the KD-2 sensors. Validate that both sensors provide the same measured values for κ and C. Compare these values to the calculated values by Smits et al. (2010) for both dry and saturated conditions. Finally, determine the effective radius for each heat-pulse probe and evaluate the similarities between each probe to assess statistical significance between measurement for both dry and saturated conditions.

B.4 References

Heitman, J.L., R. Horton, T.J. Sauer, and T.M. DeSutter. 2008. Sensible heat observations reveal soil-water evaporation dynamics. J. Hydrometeorol. 9: 165-171.

Smits, K.M., T. Sakaki, A. Limsuwat, and T.H. Illangasekare. 2010. Thermal conductivity of sands under varying moisture and porosity in drainage-wetting cycles. Vadose Zone J. 9.

Trautz, A.C., K.M. Smits, P. Schulte, and T.H. Illangasekare. 2014. Sensible heat balance and heat-pulse method applicability to in situ soil-water evaporation. Vadose Zone J. 13(1). doi:10.2136/vzj2012.0215

APPENDIX C PERMISSIONS

Appendix C contains the permission from the managing editor of *Soil Science Society American Journal* (SSSAJ) for reprinting of the paper published in SSSAJ for inclusion as Chapter 3 as part of this dissertation. A screen capture of the permission is provided below.

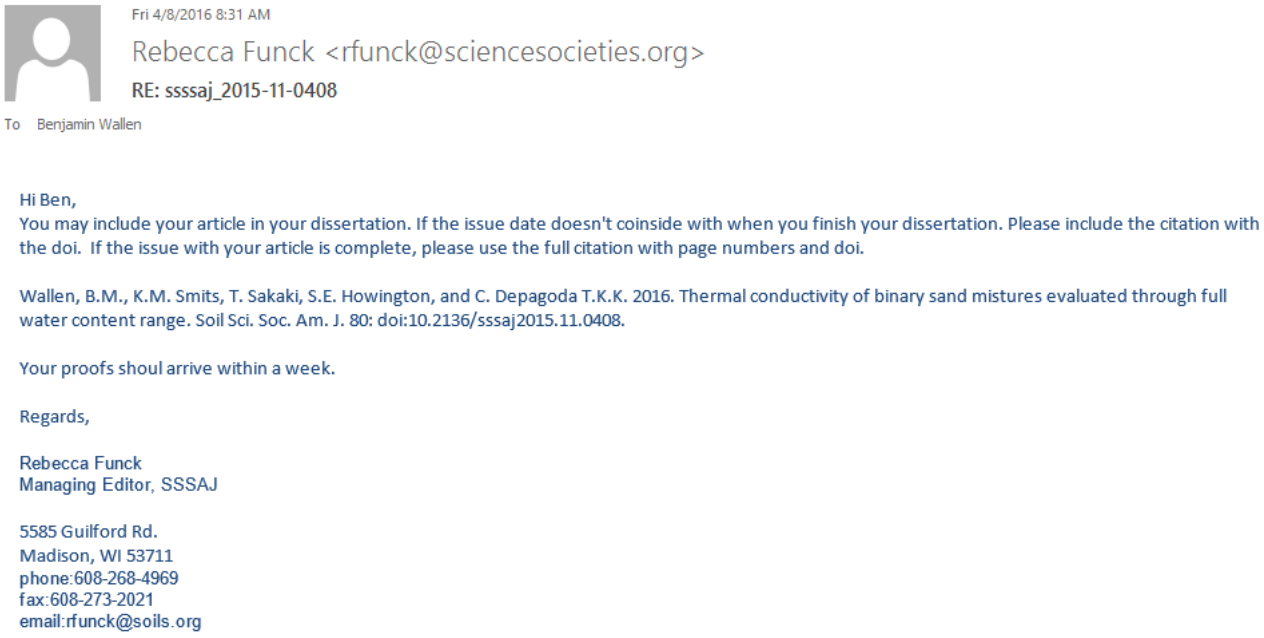

Fri 4/8/2016 8:31 AM

Rebecca Funck <rfunck@sciencesocieties.org>

RE: ssssaj_2015-11-0408

To Benjamin Wallen

Hi Ben,
You may include your article in your dissertation. If the issue date doesn't coinside with when you finish your dissertation. Please include the citation with the doi. If the issue with your article is complete, please use the full citation with page numbers and doi.

Wallen, B.M., K.M. Smits, T. Sakaki, S.E. Howington, and C. Depagoda T.K.K. 2016. Thermal conductivity of binary sand mistures evaluated through full water content range. Soil Sci. Soc. Am. J. 80: doi:10.2136/sssaj2015.11.0408.

Your proofs shoul arrive within a week.

Regards,

Rebecca Funck
Managing Editor, SSSAJ

5585 Guilford Rd.
Madison, WI 53711
phone:608-268-4969
fax:608-273-2021
email:rfunck@soils.org

APPENDIX D DETAILS OF SOILS USED IN EXPERIMENTATION

Throughout the process of this dissertation, a number of parent sands as well as binary mixtures were evaluated regarding their soil water retention curve (SWRC) or capillary pressure-water content (h_c-θ) relationship and their thermal conductivity-saturation (λ-S) relationship as described in Chapter 3. The manufacturer provided technical sheet identified these parent sands' uniformity coefficients as approximately 1.2, grain density as 2.65 g cm^{-3}, grain shape as rounded, and mineralogical composition as 99.8% quartz. Sieve numbers (e.g., #12/20, #30/40) enabled identification of the silica sands. Select measured properties of investigated sands are provided in Table D.1. The properties of the sands were measured under two different conditions, loosely packed without compaction and compacted as tight as possible.

Figure D.1 shows the λ–θ and h_c–θ relationships for the different sands tested under tight and loose packed conditions. The van Genuchten parameters were determined experimentally through RMSE analysis.

Table D.1. Select measured properties of investigated sands.

Sand	Parent Sands of Mixture	Packing	ϕ (-)	h_c (cm of H_2O)	θ_r (-)	van Genuchten parameters α (cm^{-1})	van Genuchten parameters n (-)	λ_{dry} ($W\ m^{-1}\ K^{-1}$)	λ_{sat} ($W\ m^{-1}\ K^{-1}$)
#12/20	---	tight	0.318	10.8	0.006	0.081	12.7	0.287	3.383
#110	---	tight	0.337	72.8	0.009	0.011	14.1	0.282	3.241
C9F1	#12/20 & #110	tight	0.261	10.7	0.013	0.075	4.5	0.427	4.396
C9F1	#12/20 & #110	loose	0.337	8.5	0.066	---	---	0.358	3.114
C8F2	#12/20 & #110	tight	0.212	10.5	0.015	0.021	4.0	0.558	4.833
C8F2	#12/20 & #110	loose	0.337	8.1	0.009	---	---	0.356	2.963
C7F3	#12/20 & #110	tight	0.190	52.1	0.006	0.018	4.5	0.529	5.010
C7F3	#12/20 & #110	loose	0.337	7.8	0.013	---	---	0.335	3.648
C5F5	#12/20 & #110	tight	0.237	72.0	0.007	0.013	7.0	0.419	4.815
C5F5	#12/20 & #110	loose	0.337	27.1	0.009	---	---	0.308	3.665
C2F8	#12/20 & #110	tight	0.298	78.0	0.007	0.014	8.5	0.332	3.947
C2F8	#12/20 & #110	loose	0.337	71.0	0.008	0.013	7.0	0.324	3.367
#30/40	---	tight	0.315	22.5	0.016	0.041	21.5	0.314	3.475
#30/40	---	loose	0.403	15.8	0.004	0.059	20.0	0.251	2.695
#50/70	---	tight	0.327	40.5	0.014	0.032	4.9	0.304	3.307
C7F3	#12/20 & #50/70	tight	0.245	30.0	0.006	0.029	6.8	0.418	4.157

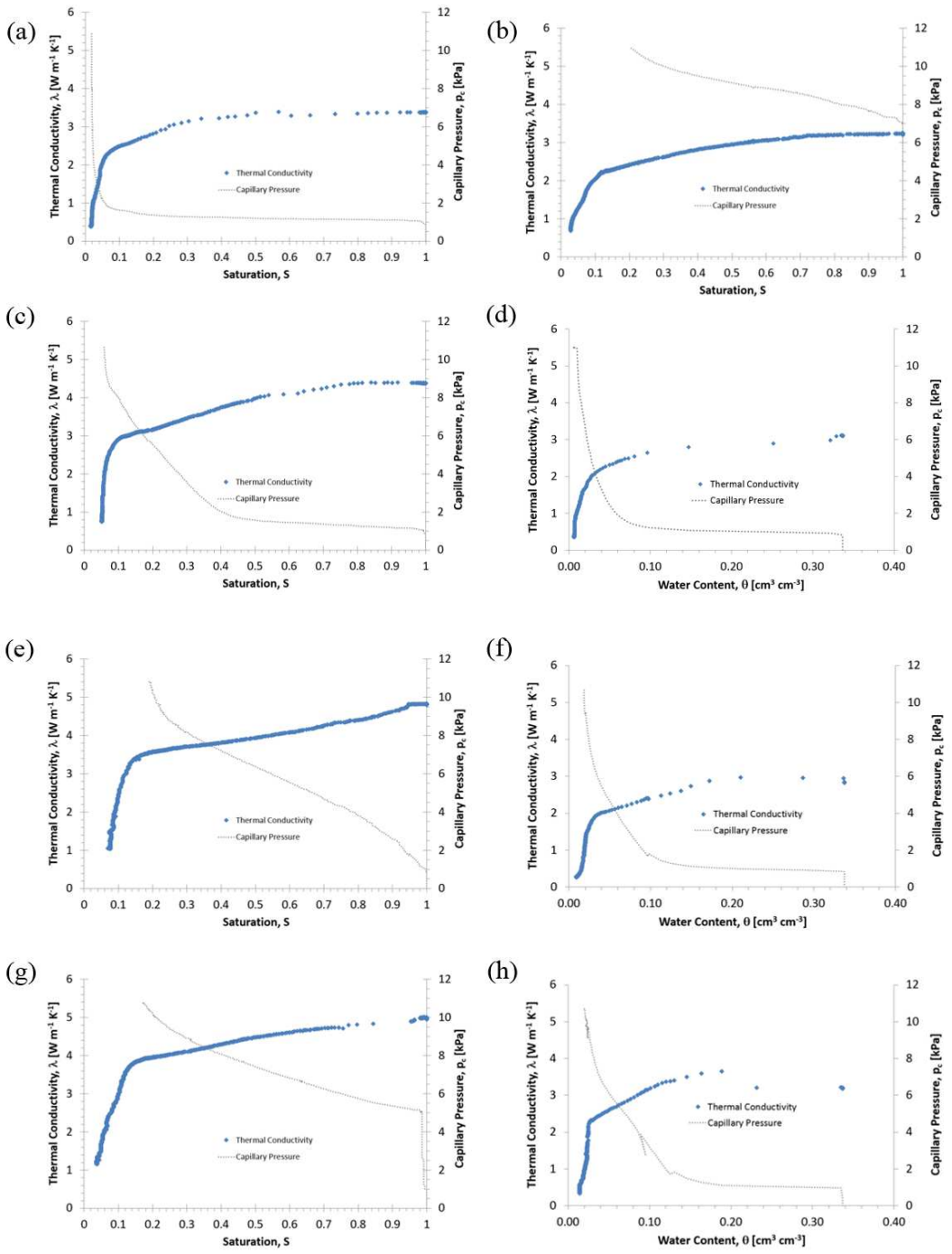

Figure D.1. Thermal conductivity and capillary pressure as a function of water content for (a) #12/20 – tight, (b) #110 – tight, (c) C9F1 – tight, (d) C9F1 – loose, (e) C8F2 – tight, (f) C8F2 – loose, (g) C7F3 – tight, (h) C7F3 – loose, (i) C5F5– tight, (j) C5F5 – loose, (k) C2F8 – tight, (l) C2F8 – loose, (m) #30/40 – tight, (n) #30/40 – loose, (o) #50/70 – tight, (p) C7F3 {#12/20 & #50/70} – tight. Unless otherwise stated, the binary mixtures are comprised of parent sands #12/20 and #110. The notation for the binary mixtures denote % coarse followed by % fine sand.

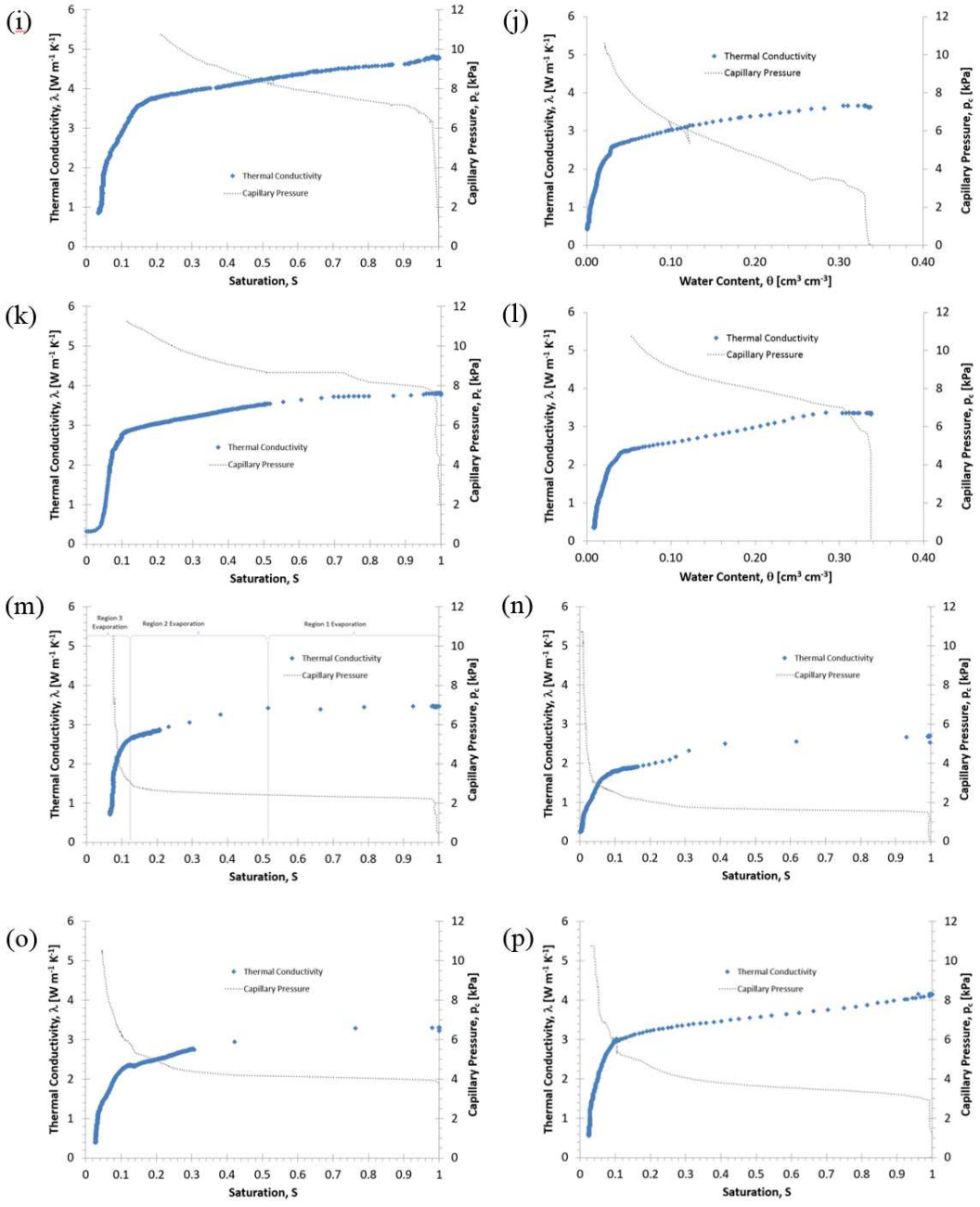

Figure D.1. Continued.

APPENDIX E SUPPLEMENTAL ELECTRONIC FILES

Appendix E contains the electronic files incorporated into this dissertation. The files are comprised of the processed data used in association with each chapter of this manuscript. The data sets include information (e.g., temperature, soil moisture, relative humidity, wind speed, etc.) obtained using the variety of sensors associated with the experimental apparatus or site instrumentation. The files are presented in order of use with the associated dissertation chapters.

File Name	Dissertation Chapter for Which Data is Used	Specific Experiments Addressed
Ch3_BinaryMixtures.xlsx	Seven experimental data sets are used in the research presented in Chapter 3	C10F0
		C9F1
		C8F2
		C7F3
		C5F5
		C2F8
		C0F10
Ch4_EvaporationComparison.xlsx	Four experimental data sets are used in the research presented in Chapter 4	Ambient
		Elevated Temperature
		Diurnal – Bare Soil
		Diurnal – Vegetation
Ch5_Disturbed&MixedSoil.xlsx	Six experimental data sets are used in the research presented in Chapter 5	Ambient
		Elevated Temperature
		Diurnal
		Water Table
		Diurnal – Layered
		Diurnal – Layered+Mix
Ch6_FieldExperiment.xlsx	One experimental data set used with four different emplacement locations in the research presented in Chapter 6	Shallow Buried Mine
		Deep Buried Mine
		Shallow Limestone Block
		Disturbed Soil Location